IN SITU X-RAY ABSORPTION SPECTROSCOPIC STUDY OF NANOPARTICLE CATALYSTS

A Thesis Submitted to the College of

Graduate and Postdoctoral Studies

In Partial Fulfillment of the Requirements

For the Degree of Doctor of Philosophy

In the Department of Chemistry

University of Saskatchewan

Saskatoon

By

Yali Yao

PERMISSION TO USE

In presenting this thesis/dissertation in partial fulfillment of the requirements for a Postgraduate degree from the University of Saskatchewan, I agree that the Libraries of this University may make it freely available for inspection. I further agree that permission for copying of this thesis/dissertation in any manner, in whole or in part, for scholarly purposes may be granted by the professors who supervised my thesis/dissertation work or, in their absence, by the Head of the Department or the Dean of the College in which my thesis work was done. It is understood that any copying or publication or use of this thesis/dissertation or parts thereof for financial gain shall not be allowed without my written permission. It is also understood that due recognition shall be given to me and to the University of Saskatchewan in any scholarly use which may be made of any material in my thesis/dissertation.

Requests for permission to copy or to make other uses of materials in this thesis/dissertation in whole or part should be addressed to:

Head of the Department of Chemistry

University of Saskatchewan

Saskatoon, Saskatchewan

S7N 5C9, Canada

ABSTRACT

X-ray absorption spectroscopy (XAS) is sensitive to the oxidation state and coordination environment of an element and places few constraints on the samples, thus it is a useful technique for the characterization of metal nanoparticles with short-range order. With recent advances in XAS techniques, it is now possible to study materials under *in situ* conditions. As the synthesis and many catalytic reactions involving nanoparticles occur in solution, *in situ* XAS is a powerful technique to study the structures and speciation of nanoparticles under real reaction conditions. Fe@Fe_xO_y core@shell nanoparticles have been widely studied for environmental remediation and catalysis due to their low cost, relatively low toxicity and magnetic recovery advantages. Using *in situ* XAS, this thesis details investigations into the oxidation mechanisms of Fe@Fe_xO_y nanoparticles, the formation of Fe@Fe_xO_y/Pd and Fe@Fe_xO_y/Cu nanoparticles, the penetrability of hollow Fe oxide shells via galvanic exchange reactions between the Fe(0) core within the hollow Fe oxide shell and Pd(II) salts, and the metal speciation in these nanoparticles during catalytic reactions.

First, Fe@Fe_xO_y nanoparticles were synthesized by the reduction of Fe salts in methanol or water/methanol mixtures using a $NaBH_4$ reducing agent under nitrogen gas. Polyvinylpyrrolidone stabilizers and different volume ratios of methanol to water were used to control the sizes of the resulting Fe@Fe_xO_y nanoparticles. The relative oxidation kinetics of these different sizes of Fe@Fe_xO_y nanoparticles were monitored by *in situ* Fe K-edge X-ray absorption near-edge structure (XANES) spectra. These Fe@Fe_xO_y nanoparticles were also applied as catalysts for the hydrogenation of a variety of alkenes, and their catalytic abilities were compared with Fe nanoparticles synthesized in a tri(hexyl)tetradecylphosphonium chloride ionic liquid. Then, Fe@Fe_xO_y nanoparticles were reacted with different molar ratios of Pd(II) and Cu(II) by galvanic exchange reactions to form Fe@Fe_xO_y/Pd and Fe@Fe_xO_y/Cu bimetallic nanoparticles with different morphologies. The reduction processes of Pd(II) and Cu(II) toward the formation of Fe@Fe_xO_y/Pd and Fe@Fe_xO_y/Cu bimetallic nanoparticles were studied through using *in situ* Pd L_3-edge and Cu K-edge XANES spectra. *In situ* XANES results also show that these Fe@Fe_xO_y nanoparticles can re-reduce oxidized Pd in Suzuki-

Miyaura cross-coupling reactions. As catalysts for the hydrogenation of 2-methyl-3-buten-2-ol, Fe@Fe_xO_y/Pd nanoparticles are shown to have a higher catalytic activity in ethanol compared to water for hydrogenation reactions, and *in situ* XANES experiments reveal that these nanoparticles are more stable in ethanol solutions, whereas further oxidation of the Fe cores occurs in the presence of water. 50:1 or 20:1 Fe@Fe_xO_y/Pd nanoparticles could also be used as magnetically recoverable catalysts.

Finally, Fe nanoparticles were also obtained by thermal decomposition of Fe pentacarbonyl in the presence of air-free 1-octadecene with oleylamine at 180 °C. Starting with these Fe nanoparticles, *in situ* high temperature Fe K-edge XANES spectroscopy was used to monitor the formation of hollow Fe oxide nanoparticles from Fe nanoparticles. The core-void-shell Fe-Fe_xO_y intermediates during the formation of hollow Fe oxide nanoparticles were captured. Utilizing the incompletely oxidized Fe cores in these core-void-shell structures to reduce Pd(II) to Pd(0), the penetrability of hollow Fe oxide shells was studied.

ACKNOWLEDGEMENTS

I would like to sincerely thank my supervisors Dr. Robert W. J. Scott and Dr. Yongfeng Hu for their valuable guidance throughout my PhD program. Thank you for the knowledge, advice, patience, encouragement and forgiveness. I also thank my advisory committee members, Drs. Ron Steer, Timothy Kelly and Derek Peak for their valuable suggestions throughout my PhD program.

I appreciate the opportunity to carry out my PhD study at University of Saskatchewan given by Dr. Robert W. J. Scott and the Department of Chemistry. I thank the National Science and Engineering Research Council of Canada for providing the financial support.

Also, I would like to thank all the past and present Scott group members, Dr. Atal Shivhare, Dr. Mahesh Gangishetty, Dr. Abhinandan Banerjee, Aimee Maclennan, Jiaqi Liang, Sudheesh Kumar Veeranmaril, Vy Phung, Michael-Roy Durr, William Barett, Brandon Chivers, Kazeem Sulaiman and Maryam Alyari. Thank you for all the help and happy time. Additionally, I would like to thank the scientists and their associates at Canadian Light Source, Dr. Yongfeng Hu, Dr. Ning Chen, Dr. Jian Wang, Dr. Tom Regier, Dr. Qunfeng Xiao, Dr. Weifeng Chen and Aimee Maclennan for their help in carrying out beamline experiments and data analysis.

My thanks also go to the laboratory managers. Drs. Alexandra Bartole-Scott and Adrian Clark for their guidance in teaching Chem 112 and Chem 115. I would like to express my gratitude to many staff in the Department of Chemistry, Leah Hildebrandt, Bonita Wong, Garth Parry, Tracey Friesen, Linda Duxbury, Ronda Duke and Pia Wennek, for their invaluable help.

Finally, I would like to thank my family members for their support and encouragement to finish my PhD study.

DEDICATIONS

I would like to dedicate this thesis to my supervisors

Dr. Robert W. J. Scott and Dr. Yongfeng Hu.

TABLE OF CONTENTS

CHAPTER 7

LIST OF TABLES

LIST OF FIGURES

LIST OF SCHEMES

LIST OF ABBREVIATIONS

acac	Acetylacetonate
CLS	Canadian Light Source
CTF	Covalent Triazine Framework
DMSA	*Meso*-2,3-dimercapto Succinic Acid
EDX	Energy Dispersive X-ray
EELS	Electron Energy Loss Spectroscopy
EXAFS	Extended X-ray Absorption Fine Structure
FID	Flame Ionization Detector
GC	Gas Chromatograph
HAADF	High Angle Annular Dark Field
HRTEM	High Resolution TEM
HXMA	Hard X-ray Micro-Analysis Beamline
IL	Ionic Liquid
IR	Infrared Spectroscopy
JCPDS	Joint Committee on Powder Diffraction Standards
MB	Methylene Blue
NMR	Nuclear Magnetic Resonance
NPs	Nanoparticles

NSERC	National Sciences and Engineering Research Council of Canada
P[6,6,6,14]Cl	Tri(hexyl)tetradecylphosphonium Chloride
PEEK	Polyether Ether Ketone
ppm	Parts per Million
PVP	Poly(vinylpyrrolidone)
PXRD	Powder X-ray Diffraction
PZS	Poly(cryclotriphosphazene-*co*-4,4'-sulfonyldiphenol)
SAD	Selected Area Diffraction
SGM	Spherical Grating Monochromator Beamline
SHE	Standard Hydrogen Electrode
STEM	Scanning Transmission Electron Microscopy
SXRMB	Soft X-ray Micro-characterization Beamline
TEM	Transmission Electron Microscopy
TEY	Total Electron Yield
TOFs	Turnover Frequencies
UV-Vis	Ultraviolet and Visible
XANES	X-ray Absorption Near Edge Structure
XAS	X-ray Absorption Spectroscopy
XPS	X-ray Photoelectron Spectroscopy

CHAPTER 1

1.1 Introduction

Catalysts are used widely in chemical reactions and in industry, because they can provide an alternative reaction pathway in which the activation barriers of a reaction are lowered and the reaction rate is increased.[1] Particles with average sizes of less than 100 nanometers have attracted extensive interest in the field of catalysis, because their nanoscale features can dramatically change the properties of the materials, and thus they can show impressive catalytic abilities.[2] Generally, catalysis is classified into three main categories: homogeneous, heterogeneous and enzymatic types. Heterogeneous catalysts are distinguished from homogeneous or enzymatic catalysts by the presence of different phases, usually solid catalysts with the reactions of gaseous or liquid reactants over their surfaces. Precious metal nanocatalysts constitute an important branch of heterogeneous catalysis including Ag, Au, Pd, Pt, Rh, Ir, Ru, Os and Re. Among these metals, Pd is relatively cheap and stable, and Pd nanocatalysts have been found to be very active for many catalytic reactions, such as Suzuki cross-coupling reactions,[3] alkyne and alkene hydrogenation reactions[4] and oxygen reduction reactions.[5]

To further decrease the cost in catalysis, tremendous research efforts have been devoted to developing non-precious metal nanocatalysts, such as Fe, Co, Ni and Cu nanoparticles (NPs).[6] These 3d transition metals are naturally abundant, therefore, they have relatively low cost. Fe, in particular, is one of the most abundant metals on earth, and consequently one of the least expensive metals.[7] In addition, Fe is relatively non-toxic compared with many other transition metal catalysts, and Fe or Fe oxide NPs may be magnetically recovered.[8] Fe NPs have emerged as a potential candidate for many catalytic reactions, such as hydrogenations,[9-11] hydrodeoxygenations,[12] Haber-Bosch[13,14] and Fischer-Tropsch reactions.[15]

This section begins with a description of the synthesis and characterization of NPs and bimetallic NPs with an emphasis on Fe NPs. Characterization of metal speciation by X-ray absorption spectroscopy (XAS) and *in situ* XAS development are also introduced. Finally, my overall research objectives and the organization and scope of this thesis are discussed.

1.2 Synthesis of Nanoparticle Catalysts

1.2.1 Monometallic Nanoparticle Catalysts

Monometallic NPs can be prepared by physical and chemical methods as shown in Figure 1.1. Physical methods to prepare NPs usually need high temperatures, vacuum conditions or expensive equipment, while chemical methods provide more simple ways to synthesize NPs under mild conditions. Here, two chemical methods, chemical reduction and thermal decomposition, are introduced using the synthesis of Fe NPs as examples.

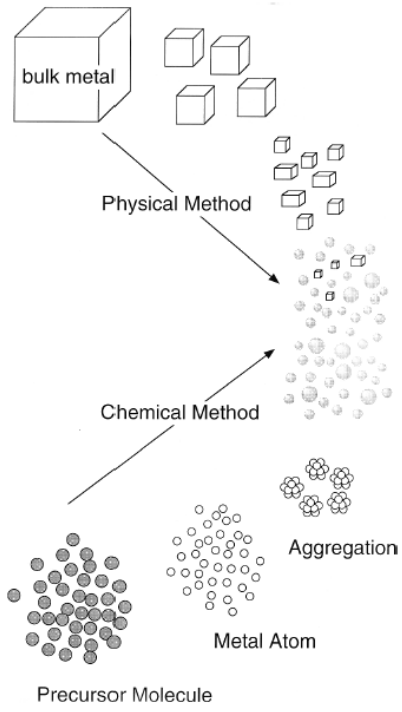

Figure 1.1. Schematic illustration of preparative methods of metal NPs. (Reproduced from Reference 16 with permission of The Royal Society of Chemistry (RSC) on behalf of the European Society for Photobiology, the European Photochemistry Association and the RSC. Copyright (1969) Royal Society of Chemistry.)

1.2.1.1 Chemical Reduction

Chemical reduction is a simple and fast method for the fabrication of metal NPs. The reduction of ferric or ferrous salts by $NaBH_4$ under inert gas is one of the most widely used methods for the synthesis of Fe NPs. The reaction equations are as follows:[17]

$$n\ FeSO_4(aq) + 2n\ NaBH_4(aq) + 6n\ H_2O(l) \rightarrow (Fe)_n(s) + n\ Na_2SO_4(aq) + 2n\ B(OH)_3(aq) + 7n\ H_2(g) \quad \textbf{(1.1)}$$

$$2n\ FeCl_3(aq) + 6n\ NaBH_4(aq) + 18n\ H_2O(l) \rightarrow 2\ (Fe)_n(s) + 6n\ NaCl(aq) + 6n\ B(OH)_3(aq) + 21n\ H_2(g) \quad \textbf{(1.2)}$$

However, small amounts of oxygen or even oxygen-free water in the synthesis can oxidize the zero-valent Fe NPs by the following reactions:[17]

$$2\ Fe(s) + O_2(g) + 2\ H_2O(l) \rightarrow 2\ Fe(OH)_2(s) \quad \textbf{(1.3)}$$

$$Fe(s) + 2\ H_2O(l) \rightarrow Fe(OH)_2(s) + H_2(g) \quad \textbf{(1.4)}$$

Fe^{2+} can be further oxidized to Fe^{3+} in the presence of oxygen:

$$4\ Fe(OH)_2(s) + 2\ H_2O(l) + O_2(g) \rightarrow 4\ Fe(OH)_3(s) \quad \textbf{(1.5)}$$

$Fe(OH)_3$ can also dehydrate to form FeOOH:

$$Fe(OH)_3(s) \rightarrow FeOOH(s) + H_2O(l) \quad \textbf{(1.6)}$$

Therefore, after the synthesis of zero-valent Fe NPs, a thin layer of an Fe oxide shell typically forms on the surface of zero-valent Fe NPs to give rise to $Fe@Fe_xO_y$ (core@shell) NPs (Figure 1.2), in which the oxide shell can protect the zero-valent Fe core against excessive rapid oxidation.[18]

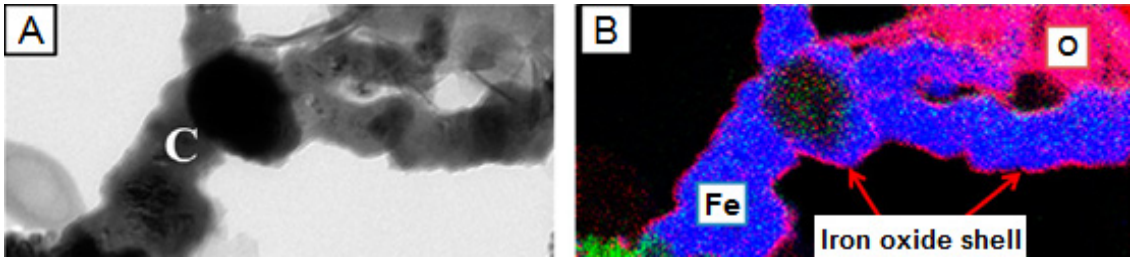

Figure 1.2. (A) Bright-field TEM image of Fe@Fe_xO_y NPs. (B) Corresponding EDX map. (Adapted with permission from Reference 18. Copyright (2015) American Chemical Society.)

As shown in Figure 1.2, the resulting Fe or Fe@Fe_xO_y NPs also exhibit a strong tendency to aggregate due to their high surface energies and magnetic interactions.[17] Many efforts have been devoted to the dispersion of Fe NPs. For example, He and Zhao used water-soluble starch as stabilizers to reduce the average sizes of Fe NPs from tens of nanometers to 14.1 nm in diameter.[19] Fu *et al*. synthesized Fe NPs with sepiolite clays as supports.[20] The resulting Fe NPs with sizes in the range of 10-50 nm can be dispersed on the sepiolite supports without aggregation. Saleh *et al*. used poly(methacrylic acid)-block-poly(methyl methacrylate)-block-poly(styrensulfonate) to modify the surfaces of Fe NPs and disperse them.[21] Poly(vinylpyrrolidone) (PVP) is a common polymer which has been widely used to stabilize NPs.[22] It has relatively low cost and low toxicity, and it is soluble in water and other polar solvents.[22,23] It can be a potential stabilizer to disperse both Fe NPs and Fe oxide NPs.

Besides using stabilizers, the polarity of solvents can also influence the aggregation and final size of NPs. Gacem and Diao synthesized PVP-coated Rh NPs by varying the water-to-methanol ratio in the synthetic solutions.[24] They showed that PVP-coated Rh NPs have strong tendency to aggregate and grow in high polarity solvents, and stability toward aggregation and growth can be gained by adding a lower polarity solvent to the reaction media. They proposed a mechanism to elucidate the reason for the formation of large sizes of Rh NPs in high polarity solvents: large amounts of small Rh NPs formed rapidly, followed by a slow particle aggregation step. Their studies can explain that why Sun *et al*. reported the average sizes of Fe NPs are 70.2 nm synthesized only in water,[25] while Hudson *et al*. synthesized the Fe NPs with average sizes around 50 nm in 7:3 water to methanol mixtures.[26]

Another alkali metal borohydride has been used to reduce Fe salts is $LiBEt_3H$.[27] The reaction generally proceeds according to the following equation:

$$2n\ FeCl_3(aq) + 6n\ LiBEt_3H(l) \rightarrow 2\ (Fe)_n(s) + 6n\ LiCl(aq) + 3n\ H_2(g) + 6n\ BEt_3(aq) \quad \textbf{(1.7)}$$

However, using alkali metal borohydrides as reducing agents can introduce the impurities of borates as byproducts.[26,28,29] Hudson *et al*. revealed the presence of 3.3 wt% of boron in every 100 mg of Fe NP products by ICP-MS analysis; notably a complete absence of Fe boride species was confirmed by X-ray Photoelectron Spectroscopy (XPS).[26] Ni *et al*. reported a facile one-step method to prepare Fe NPs by reducing Fe salts with hydrazine hydrate in strong alkaline conditions, and showed that almost no impurities were introduced into final products.[30] First, $Fe(OH)_3$ formed in the alkaline media, then $Fe(OH)_3$ was reduced by N_2H_4 following Equation 1.8:

$$4n\ Fe(OH)_3(s) + 3n\ N_2H_4(l) \rightarrow 4\ (Fe)_n(s) + 12n\ H_2O(l) + 3n\ N_2(g) \quad \textbf{(1.8)}$$

However, the above reaction has to be conducted in a closed system, because N_2H_4 may decompose in an open system before reducing the $Fe(OH)_3$:[30]

$$3\ N_2H_4(l) \rightarrow 4\ NH_3(g) + N_2(g) \quad \textbf{(1.9)}$$

Other methods to synthesize Fe NPs by chemical reduction include the reduction of Fe(III) acetylacetonate by ascorbic acid in the absence of water,[31] and the reduction of $\{Fe(N[Si(CH_3)_3]_2)_2\}_2$ by H_2 at 3 bar pressures at 150 °C.[32] The $HN[Si(CH_3)_3]_2$ ligands produced during the synthesis are able to stabilize the resulting Fe NPs.

1.2.1.2 Thermal Decomposition

Thermal decomposition reactions happen at high temperature and involve the decomposition of various organometallic compounds in high boiling point solvents to form their respective zero-valent NPs. This has been another widely used method for the synthesis of Fe NPs. The most common method is to thermally decompose Fe pentacarbonyl in 1-octadecene containing oleylamine or in octyl ether with oleic acid[33-35] according to the following equation:

$$n\ Fe(CO)_5(l) \rightarrow (Fe)_n(s) + 5n\ CO(g) \quad \textbf{(1.10)}$$

For example, Peng *et al*. synthesized 13 nm Fe NPs by thermal decomposition of 0.7 mL of $Fe(CO)_5$ in 20 mL of air-free octadecene with 0.3 mL of oleylamine at 180 °C.[36] The particle size could be effectively tuned by the amount of oleylamine added; for example, Fe NPs with average sizes of 15 nm were obtain using half as much oleylamine stabilizer in the synthesis. Thus the sizes of Fe NPs can be controlled by the amount of oleylamine stabilizer in the mixture.

High boiling point solvents can also allow one to further oxidize the as-synthesized Fe NPs by trimethylamine oxide or oxygen gas at high temperature to form hollow maghemite or magnetite NPs by the Kirkendall effect.[34,36] As illustrated in Figure 1.3, at high temperature, Fe atoms diffuse to the surface of the NPs faster than O atoms diffuse inward from the surfaces of the NPs, leaving vacancies behind, which come together to form hollow spaces within the NPs. Fe atom diffusivities are exponentially dependent on the temperature. As shown in Figure 1.4, the Fe NPs formed are only partially hollow after 12 h oxidation at 80 °C by 20% oxygen, and are almost completely hollow after 1h oxidation at 150 °C. At 350 °C the Fe NPs are totally oxidized within 1 h of oxidation to form hollow structures.

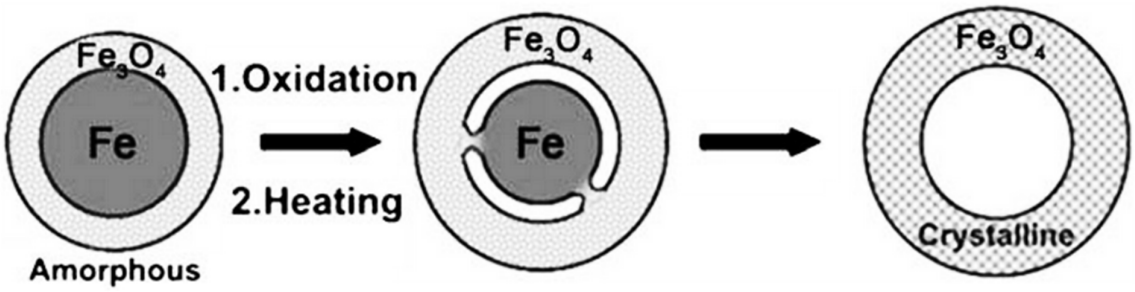

Figure 1.3. Synthesis of core-shell-void Fe-Fe_3O_4 and hollow Fe_3O_4 NPs from Fe-Fe_3O_4 NP seeds. (Reprinted with permission from Reference 36. Copyright (2007) WILEY-VCH Verlag GmbH & Co. KGaA, Weinheim.)

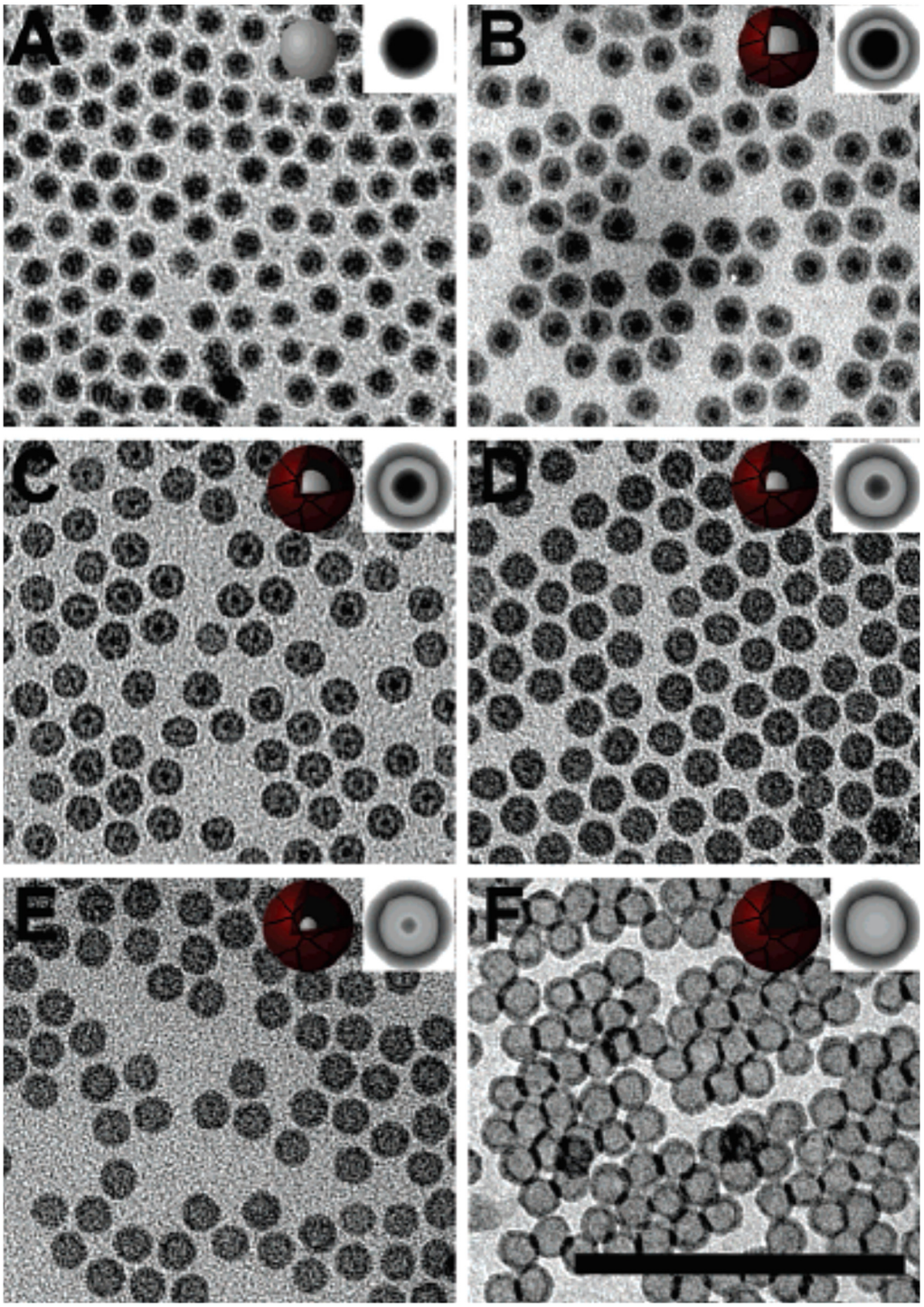

Figure 1.4. TEM micrographs of Fe/Fe oxide NPs exposed to dry 20% oxygen: (A) < 1 min at room temperature; (B) 1h at 80 °C; (C) 12 h at 80 °C; (D) 5 min at 150 °C; (E) 1 h at 150 °C; (F) 1 h at 350 °C on a substrate. (Reprinted with permission from Reference 34. Copyright (2007) American Chemical Society.)

1.2.2 Bimetallic Nanoparticle Catalysts

Bimetallic NPs have attracted tremendous interest from researchers because of their synergistic properties that are difficult to achieve by single-component NPs.[37,38] Co-reduction and successive reduction of two metallic precursors are two common strategies to synthesize bimetallic NPs. Co-reduction involves simultaneous reduction of two metallic precursors, which can give alloy NPs if the reduction rates are similar. Successive reduction involves the growth of a second metal on the surface of pre-formed metal NP seeds. This strategy normally gives rise to core@shell bimetallic NPs.[39]

Galvanic exchange reactions also provide a simple method to synthesize core@shell bimetallic NPs, and occur when the metals in a NP are displaced by the reduction of other metal ions with a higher electrochemical reduction potential than the displaced metal.[40,41] Fe(0) has a relatively low standard electrode potential (Table 1.1), thus zero-valent Fe NPs have been used as precursors to seed, reduce and support other metals with more positive electrochemical potentials for the synthesis of bimetallic NPs by galvanic exchange reactions (Figure 1.5).[42,43]

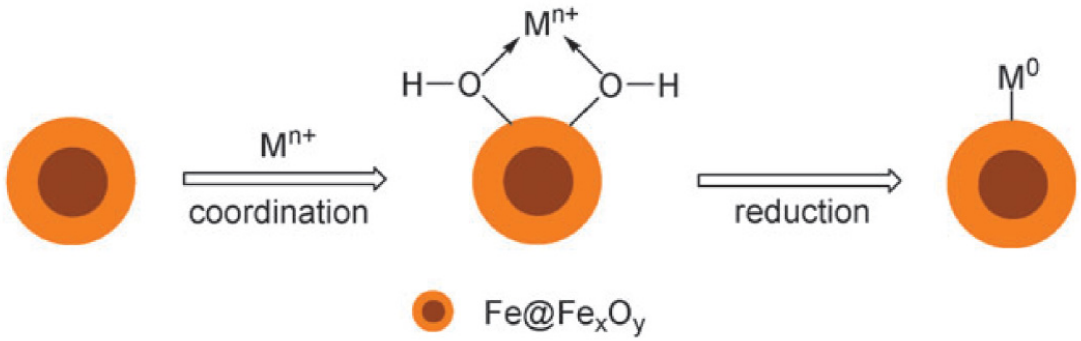

Figure 1.5. The deposition of metallic domains onto the surface of $Fe@Fe_xO_y$ NPs by galvanic exchange reactions. (Reproduced from Reference 43 with permission of The Royal Society of Chemistry. Copyright (2010) Royal Society of Chemistry.)

Table 1.1. Standard reduction potentials at 298.15 K.[42]

Reduction half-reaction	E^o/V
$Fe^{2+} + 2e^- \rightarrow Fe$	-0.44
$Fe^{3+} + 3e^- \rightarrow Fe$	-0.04
$Fe^{3+} + e^- \rightarrow Fe^{2+}$	+0.77
$Co^{2+} + 2e^- \rightarrow Co$	-0.28
$Ni^{2+} + 2e^- \rightarrow Ni$	-0.23
$Cu^{2+} + 2e^- \rightarrow Cu$	+0.34
$Ru^{2+} + 2e^- \rightarrow Ru$	+0.45
$Cu^{+} + e^- \rightarrow Cu$	+0.52
$Ag^{+} + e^- \rightarrow Ag$	+0.80
$Rh^{3+} + 3e^- \rightarrow Rh$	+0.80
$Pd^{2+} + 2e^- \rightarrow Pd$	+0.92
$Pt^{2+} + 2e^- \rightarrow Pt$	+1.20
$Au^{3+} + 3e^- \rightarrow Au$	+1.52
$Au^{+} + e^- \rightarrow Au$	+1.83

A number of bimetallic NPs, such as FePd,[43] FeCu,[44,45] FeRu[46] and FePt,[47] have been successfully synthesized by galvanic exchange methods and applied as catalysts for various catalytic reactions. For example, Zhou *et al*. showed that FePd NPs have improved activity over commercial Pd/C powders under identical reaction conditions for Suzuki-Miyaura cross-coupling reactions and the Fe supports can re-reduce any leached Pd after the reactions.[43] Moores' group investigated the morphologies of FeCu NPs with different Fe:Cu mass ratios and applied FeCu NPs for the heterogeneous catalysis of azide-alkyne click reactions in water.[44,45] They also synthesized FeRu NPs and used them for the catalytic transfer hydrogenation of ketones.[46] The existence of Fe in the bimetallic NPs can allow for magnetic recovery of the catalysts from reaction solutions by simple application of an external magnet.

For example, FeRu NPs could be used up to five times for the transfer hydrogenation of acetophenone with no appreciable decrease in yield by magnetic recovery and recycling of the NPs. Shi *et al*. used SiO_2-supported Fe NPs to reduce Pt(II) on their surfaces and showed that the resulting bimetallic NPs are highly selective in catalyzing the hydrogenation of carbonyl groups in cinnamaldehyde.[47]

1.3 Characterization of Nanoparticle Catalysts

1.3.1 Transmission Electron Microscopy, Energy Dispersive X-ray Spectroscopy and Powder X-ray Diffraction

1.3.1.1 Transmission Electron Microscopy (TEM)

TEM operates on the same basic principles as a light microscope to image the transmission of a focused beam through a sample. However, TEM uses electrons instead of light as the light source. The small de Broglie wavelength of electrons make it possible to get atomic resolution by TEM. Therefore, TEM is a vital characterization tool for directly imaging nanomaterials to obtain information about their sizes, shapes and distribution. High-voltage TEM has been widely used to image nanomaterials, as the wavelength of electrons is related to the acceleration voltage, and low wavelength electrons provide better resolutions and greater sample penetration. However, high-voltage TEMs can also cause sample damage in systems that include organic compounds, thus typically moderate voltage TEMs are used such that images can be obtained with no damage to the sample.

Bright field imaging is the most common mode used to collect TEM images. In this mode, the image results from a decrease in intenisty of the direct electron beam by its interaction with the sample. A NP specimen for imaging is normally prepared by drying a diluted sample drop of the NP solution on a copper grid with a thin layer of carbon. When the beam travels through a specimen, sample regions will backscatter the electrons and appear dark in the image, while regions with no sample in the beam path will appear bright. The resulting image is a simple two dimensional projection of the sample. Dark areas in the image are due to both mass-thickness and diffraction contrast. Thick areas of the sample, areas containing heavy atoms and

crystalline areas appear with dark contrast. For example, Figure 1.4 shows the formation of hollow Fe oxide NPs from Fe NPs. The as-synthesized Fe NPs are dark in contrast with the background (Figure 1.4 A).[35] As the oxidation of the Fe NPs takes place, a thin layer of Fe oxide formed on the surface of Fe core. Because the Fe oxide layer is much thinner than the Fe core, it is lighter than the Fe core (Figure 1.4 B). However, as the Fe oxide layer grows and the Fe core shrinks, they gradually show similar dark contrast (Figure 1.4 C and D). Finally, as one approaches the formation of hollow Fe oxide NPs, the Fe core became much lighter than the Fe oxide shell.

For crystalline NPs, high resolution TEM (HRTEM) can be used to identify their crystal structures, measure lattice parameters and examine crystal defects. A selected area diffraction (SAD) aperture located below the sample holder on the TEM column allows to collect a diffraction pattern for a specified region of a sample using phase contrast. For example, HRTEM image allows the identification of the *d*-spacing for adjacent lattice fringes of Au_{oct}@PdPt NP, as shown in Figure 1.6.[39] The SAD pattern is similar to a X-ray diffraction pattern, but instead shows spots from electron diffraction as the electrons sample a very small nanometer size area of the sample.

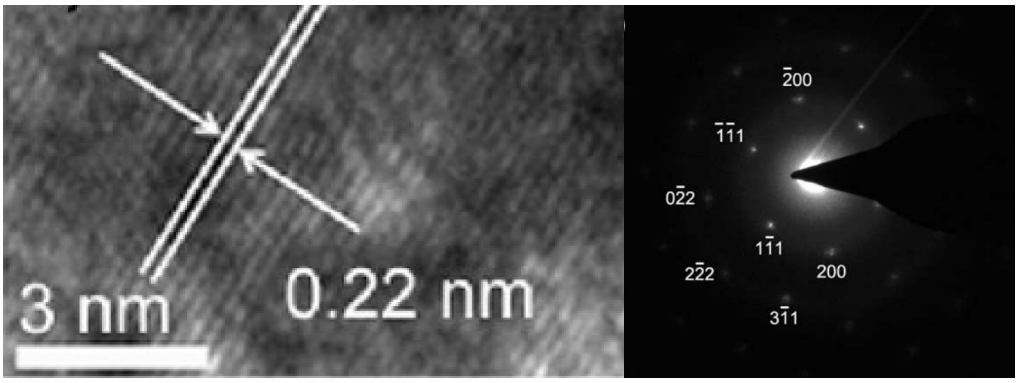

Figure 1.6. (Left) HRTEM of Au_{oct}@PdPt NP. (Right) Its SAD pattern. (Reprinted with permission from Reference 39. Copyright (2013) American Chemical Society.)

Scanning TEM (STEM) combines the principles of TEM and scanning electron microscopy. A very fine focused beam of electrons rather than the broad parallel beam used in TEM is scanned across a sample in a raster pattern to get either bright field images or dark field

images. Transmitted electrons collected in the STEM give bright field images which are similar to those collected in bright-field TEM. STEMs can also collect the scattered electrons from the samples by a high angle annular dark field (HAADF) detector. Because a HAADF image is formed from high angle scattering of electrons from the atomic nuclei, its signal is directly proportional to the mass-thickness and particularly the atomic number of the sample. Thus, it can be used to distinguish and contrast different elements with moderate differences of atomic number in a sample; heavier elements will scatter more electrons and thus appear much brighter in the image. For example, as shown in Figure 1.7, [$Ru_{10}Pt_2$] NPs are barely visible on mesoporous silica under bright-field conditions, however, they stand out clearly under HAADF conditions because of the high atomic number contrast.[48]

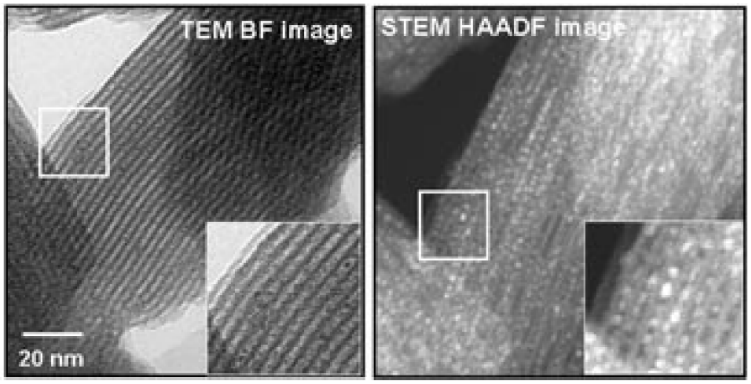

Figure 1.7. A comparison of bright-field and HAADF images of identical areas of catalyst: NPs of [$Ru_{10}Pt_2$] supported on mesoporous silica. (Reprinted with permission from Reference 48. Copyright (2004) WILEY-VCH Verlag GmbH & Co. KGaA, Weinheim.)

1.3.1.2 Energy Dispersive X-ray Spectroscopy (EDX)

Given the large promise of bimetallic or multimetallic NPs for catalysis and other fields, it is important to determine their compositions and structures. This can be particularly challenging in catalysis given that high catalytic activities are typically gained by using small NPs with a large percentage of their atoms on the surface. In addition, many bimetallic or mutlimetallic NPs are synthesized with metals with close atomic numbers, such as Au/Pd bimetallic NPs and Au/Pd/Pt trimetallic NPs. In such cases, it is hard to image bimetallic or multimetallic structures with conventional TEMs or even HAADF STEMs. Coupling TEM or

STEM with EDX spectroscopy or electron energy loss spectroscopy (EELS) can allow one to determine elemental composition and distribution of NPs via elemental mapping. EELS is an analytical technique that measures the change in kinetic energy of electrons after they have interacted with a specimen.[49] EELS tends to work best at relatively low atomic numbers ranging from carbon through the 3d transition metals, and has the energy resolution to potentially give both composition and speciation information. As the bimetallic NPs studied in this thesis contain precious metals, such as Pd, EDX spectroscopy is mainly used to characterize bimetallic NPs in this thesis. EDX spectroscopy can allow for the collection of elemental composition maps of NPs, but does not have the energy resolution to allow for speciation information to be obtained.

When a sample is bombarded by an electron beam in TEM or STEM, an electron originally positioned in the inner shell of an atom can be ejected and leaves behind a core hole. To return the atom to a lower energy state, an electron from a higher energy level falls into the core hole, and an X-ray is emitted to balance the energy difference between the two electrons' states. The relative abundance of emitted X-rays versus their energy can be measured by an EDX detector. The emitted X-rays are named according to the shell in which the initial core vacancy occurs and the shell from which an electron drops to fill that vacancy. For example, and electron falling from the L (n=2) shell to the K (n=1) shell emits a K_α X-ray, while an electron falling from the M (n=3) shell to the K shell emits a K_β X-ray. Because L is the adjacent energy shell of the K shell, K_α radiation will always be more intense than K_β radiation. Similarly, M shell to L shell transition emits L_α X-rays. The energies of the X-rays are characteristic of the difference in energy between the two shells which is specific to a given emitting element, thus EDX allows the elemental composition of the sample to be measured.[50] As shown in Figure 1.8 A, a TEM image only allows information about the sizes of the NPs, while EDX spectra gives information about chemical composition of these NPs.[50] In this specific example, a wide area EDX spectra was collected which shows that the elements Co, Fe and O are present (Figure 1.8 B), while the C and Cu peaks likely come from the TEM grid. Using EDX spectroscopy combined with STEM (which uses a very focused, single pixel beam), it is possible to collect EDX spectra for every pixel of an image. This in turn allows one

to obtain two dimensional elemental maps by using distinct element-specific peaks in the EDX spectra as a measure of the relative concentration of a certain element. For example, HAADF-STEM-EDX maps clearly show the distribution of Au, Pd and Pt in trimetallic Au@Pd@Pt NPs as shown in Figure 1.9 C.[52] The elemental maps and the cross-sectional compositional line profiles (Figure 1.9 C and D) reveal the NPs have triple-layered nanostructures with Au cores, Pd inner layers and dendritic Pt outer shells.

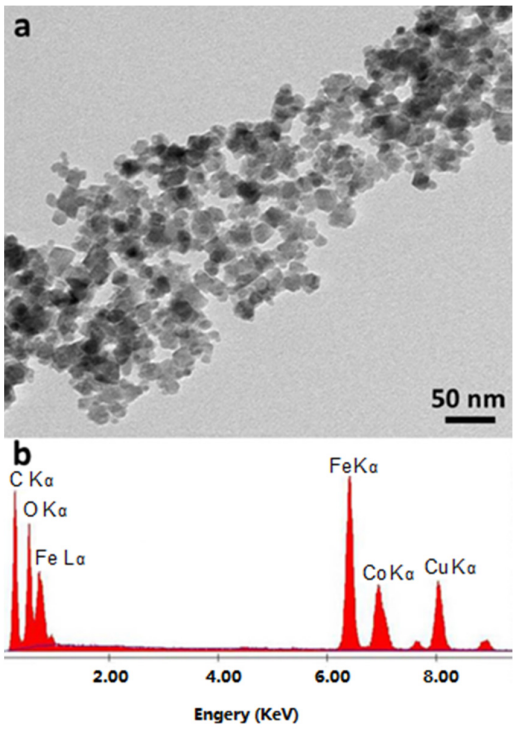

Figure 1.8. (A) TEM image of $CoFe_2O_4$ NPs. (B) Its corresponding EDX spectra. (Adapted with permission from Reference 51. Copyright (2013) Springer.)

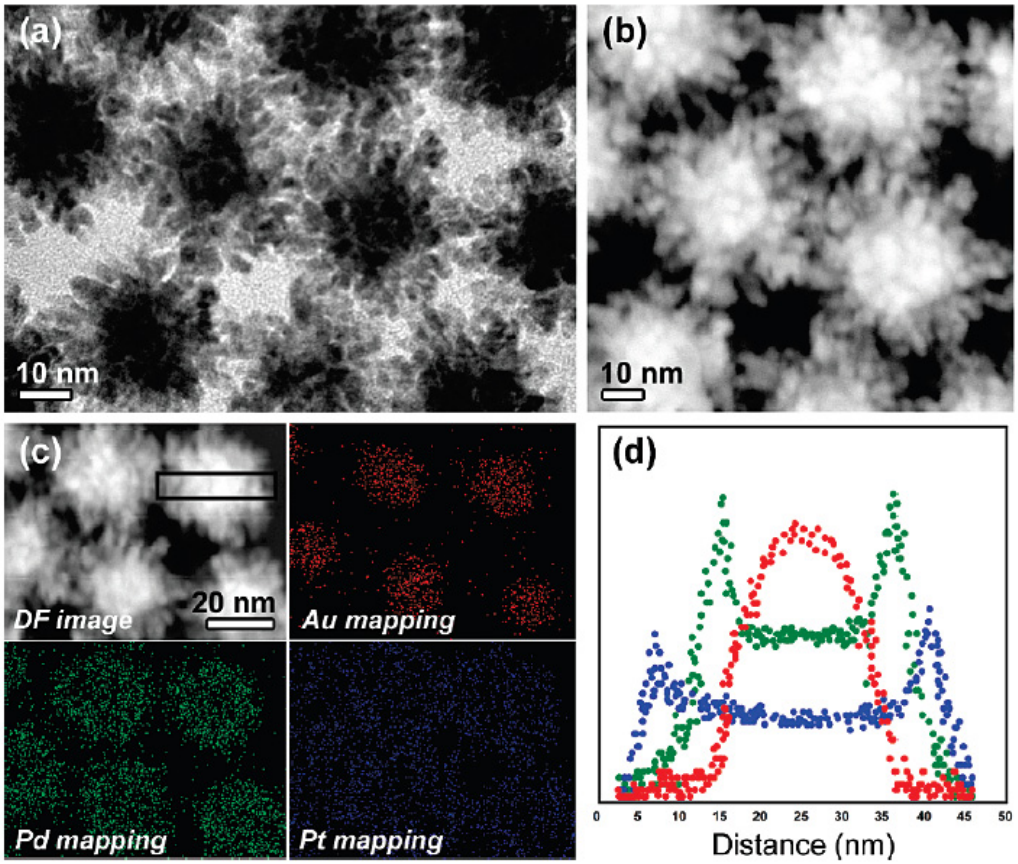

Figure 1.9. (A) TEM image of Au@Pd@Pt NPs. (B) HAADF-STEM image of Au@Pd@Pt NPs. (C) HAADF-STEM-EDX mapping images of Au@Pd@Pt NPs. (D) Cross-sectional compositional line profiles of the square area in Figure C. (Reprinted with permission from Reference 51. Copyright (2010) American Chemical Society.)

1.3.1.3 Powder X-ray Diffraction (PXRD)

When an X-ray beam hits a crystal, a diffraction pattern with many sharp spots are generated, which is similar to the SAD pattern as shown in Figure 1.6 B. These spots reflects the periodic atomic order in the crystal. A finely ground crystalline powder contains a large number of crystallites which are oriented randomly, and when an X-ray beam illuminates these crystallites rather than a single crystal, the effect is that each of the spots is spread out into a ring in the resulting diffraction pattern.[53] Each compound has its unique atomic order and produces a distinctive diffraction pattern. Both of the positons and the relative intensity of the rings in a diffraction pattern indicate a particular phase of a material (*i.e.* a unique

"fingerprint"). Figure 1.10 shows the PXRD results of Fe oxide NPs synthesized by reducing $FeSO_4$ with different reducing agents.[54] Through comparing their distinctive peaks with the reference diffraction patterns from the Joint Committee on Powder Diffraction Standards (JCPDS) database, it reveals that the main phase is γ-Fe_2O_3. The broad peaks are due to the small sizes of the crystallites.

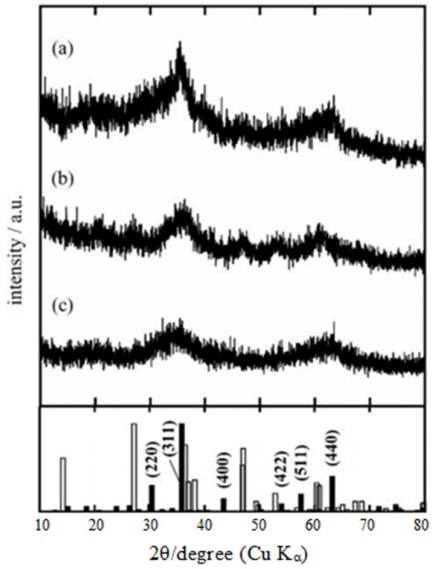

Figure 1.10. PXRD patterns of the Fe oxide NP samples prepared with $NaBH_4$ (a), N_2H_4 (b), and NaH_2PO_2 (c) as reducing agent. Standard pattern for γ-Fe_2O_3 (JCPDS# 39-1336) is shown by solid bars with Miller indices, and that of γ-FeOOH (JCPDS# 44-1415) by open bars. (Reprinted with permission from Reference 44. Copyright (2006) Elsevier.)

The breadth of the PXRD peaks can also be used to calculate the average sizes of crystallites using the Debye-Scherrer Formula (Equation 1.11):[55]

$$D = \frac{0.9\ \lambda}{\beta\ cos\theta} \qquad \textbf{(1.11)}$$

Where λ is the wavelength of the X-ray used, β is the full width at half maximum of the peak in radians (radian = $\pi\theta/180$), θ is the diffraction angle and D is the average size of crystallites.

However, many NPs are polycrystalline, and thus the crystallite size might be smaller than the particle size. Lattice strain results from displacements of the unit cells about their normal

positions, which can also broaden the XRD peaks. Williamson-Hall plots can be used to separate the XRD broadening effects of strain and crystallite size in nanomaterials.[56]

1.3.2 X-ray Absorption Spectroscopy (XAS)

XAS is inherently a short-range structural probe and places few constraints on the samples, thus it is valuable for detecting the composition and structure of a nanoscale material in many different environments. XAS is the measurement of transitions from core electronic states of the metal to upper excited electronic states and finally to the continuum (*i.e.* photoionization).[57] The former is known as X-ray Absorption Near Edge Structure (XANES) which encompasses the region approximately 50 electron volts (eV) before and after the absorption edge (the sudden increase in absorption), and the latter as Extended X-ray Absorption Fine Structure (EXAFS) spectroscopy which refers a region with energy higher than ~50 eV above the absorption edge (Figure 1.11).

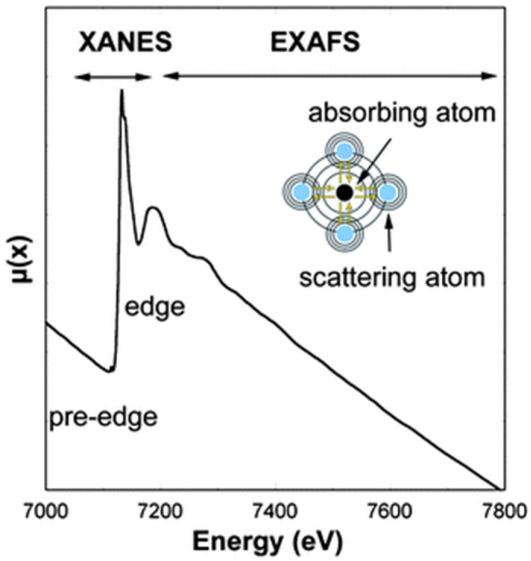

Figure 1.11. XAS spectrum at the Fe K-edge. (Reproduced from Reference 58 with permission of The Royal Society of Chemistry. Copyright (2010) Royal Society of Chemistry.)

The X-ray source typically used is a synchrotron, which provides a full range of X-ray wavelengths. A monochromator typically uses Bragg diffraction to select a particular energy.[59] When a sample of interest is bombarded with X-rays of definite energy in an X-ray absorption

experiment, three common measurement modes can be carried out, transmission, fluorescence and Auger emission, as shown in Figure 1.12:

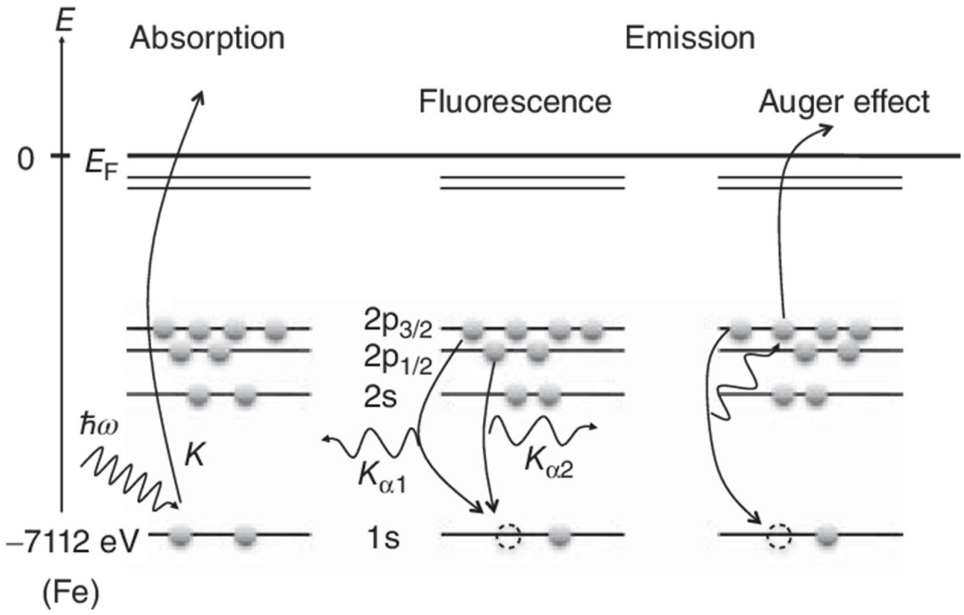

Figure 1.12. Schematic representation of X-ray measurements of a Fe 1s electron (*i.e.* K edge). (Left) Absorbance, (middle) fluorescence and (right) Auger effect emission mechanisms. (Reprinted with permission from Reference 60. Copyright (2016) Wiley-VCH Verlag GmbH & Co. KGaA.)

1. Transmission Geometry

When an X-ray beam of given energy (E) passes through a homogeneous sample with thickness x, it is attenuated (Figure 1.13). This attenuation is due to the absorption of X-ray, which can be described by Lambert-Beer's Law (Equation 1.12):[61]

$$I(E) = I_0(E)e^{-\mu(E)x} \quad \textbf{(1.12)}$$

Where $I_0(E)$ and $I(E)$ are the incident and transmitted X-ray intensities which can be measured by the corresponding ionization chambers, and $\mu(E)$ is the absorption coefficient which describes how strongly X-rays are absorbed as a function of X-ray energy E, as shown in Equation 1.13.[62]

$$\mu(E)x = \ln(I_0(E)/I(E)) \quad \textbf{(1.13)}$$

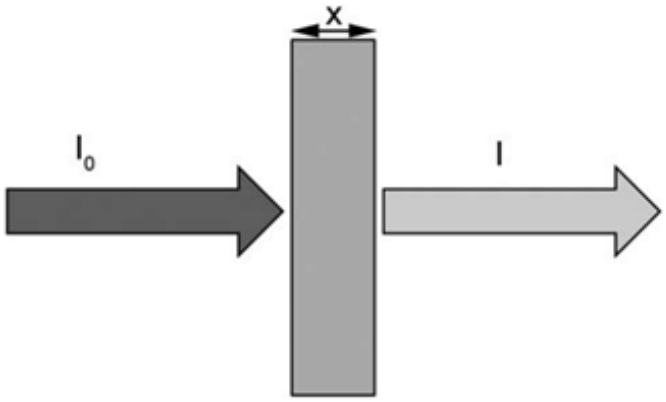

Figure 1.13. Transmission X-ray absorption measurements. (Reproduced from Reference 55 with permission of The Royal Society of Chemistry. Copyright (2010) Royal Society of Chemistry.)

2. Fluorescence measurement

Transmission measurements are useful for uniformly concentrated samples, which have reasonable thickness such that a good portion of the X-rays can pass through the samples. For thick or dilute samples, or for low-energy X-ray edges, fluorescence measurements are commonly used. When an atom absorbs an X-ray, a core electron is excited and leaves a vacancy in one of its core orbitals (Figure 1.12 middle). This vacancy can be filled by an electron from a higher level, and the difference between the two levels results in the emission of fluorescent X-ray with lower energy in a random direction (*i.e.* X-rays emitted in all directions). A detector placed perpendicular to the direction of the beam can measure some of these photons, and the intensity of the X-ray fluorescence signal (I_f) compared to the X-ray intensity upstream of the sample (I_0) can be described by Equation 1.14.[63]

$$\mu(E) \propto I_f(E)/I_0(E) \qquad \textbf{(1.14)}$$

3. Total electron yield measurement

When an electron from a higher level fills the vacancy, the energy released in this process may eject a second electron (Figure 1.12 right). By monitoring the flux of these secondary ejected electrons ($I_e(E)$), the total electron yield (TEY) signals can be measured, as shown in Equation 1.14. Since the escape depth of electrons is generally low, the TEY measurements

are intrinsically sensitive to the region close to the sample surface.[62] TEY signals increase as atomic number decreases, so it is more useful for light elements. TEY signals are normally collected under vacuum conditions.

$$\text{TEY} \propto I_e(E)/I_0(E) \quad \textbf{(1.15)}$$

The energy for an XAS measurement depends on the binding energies of electrons in the core orbitals of the absorbing elements. The nomenclature of the absorption edges is shown in Table 1.2 below, where the column on the right indicates which core orbital the electron was originally excited from.

Table 1.2. Absorption edges.

Edge	Core Electron State
K	1s
L_1, L_2, L_3	2s, $2p_{1/2}$, $2p_{3/2}$
M_1, M_2, M_3, M_4, M_5	3s, $3p_{1/2}$, $3p_{3/2}$, $3d_{3/2}$, $3d_{5/2}$

1.3.2.1 X-ray Absorption Near Edge Structure (XANES) Spectroscopy

The XANES regime is the transition of a core electron to the lowest unoccupied valence state. This transition follows dipole allowed selection rules ($\Delta l = \pm 1$ and $\Delta J = 0, \pm 1$). Using Fe as an example, the outer shell electron configuration of Fe(0) is $3d^6 4s^2$, thus the Fe K-edge is the transition from the 1s orbital to 4p orbital, the L_1-edge is 2s→4p, the L_2 edge is $2p_{1/2}$→3d, and the L_3 edge is $2p_{3/2}$→3d.

XANES is an extremely sensitive technique to study the oxidation state of an element and the coordination chemistry around the absorbing atom. In general, the absorption edge shifts when the oxidation state of an element changes resulting from shielding effects.[64] As shown in Figure 1.14, the absorption edge of Fe K-edge XANES shifts to higher energy upon an increase in their oxidation states. As the loss of electrons leads to a higher oxidation state of Fe, more energy is required to excite an electron from a core orbital. Similarly, higher electronegativity

of neighboring atoms can more strongly withdraw electron density from the atom being probed, which will result in decreased screening of the positive nucleus and cause a shift of the absorption edge to higher energy. For example, O is more electronegative than S, therefore, although both Fe oxalate (FeC_2O_4) and FeS_2 have Fe(II) centers, the absorption edge of FeC_2O_4 in which Fe(II) is coordinated with O shifts to higher energy than that of FeS_2. Any peaks below the absorption energy are pre-edge peaks, which are sensitive to the coordination chemistry around the absorber atom. The pre-edge peaks of Fe K-edge XANES are related to "forbidden" 1s→3d quadrupole electronic transitions.[66] The pre-edge peak intensity for Fe species with tetrahedral symmetry is larger than those for octahedral symmetry due to a large amount of 3d-4p hybridization in tetrahedral environments.[67] As shown in Figure 1.14, the intensity of the pre-edge peak of magnetite, Fe_3O_4, around 7113 eV is high, because some of the Fe in magnetite is in a tetrahedral coordination environment.[68]

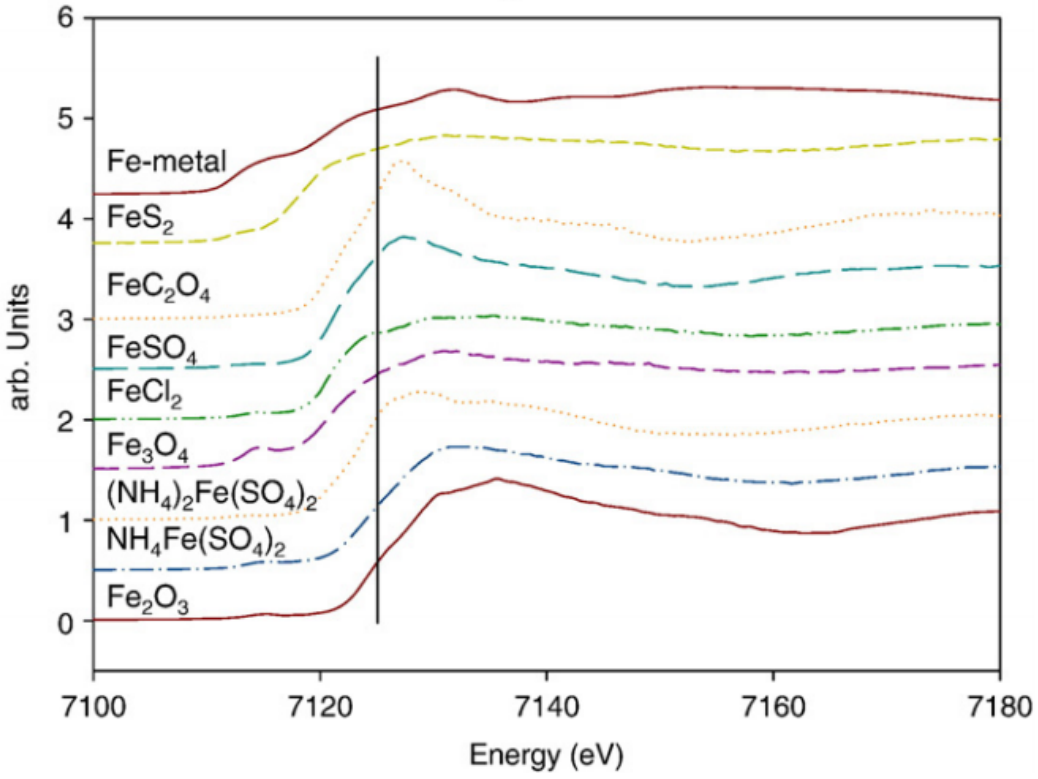

Figure 1.14. Fe K-edge XANES of Fe metal and several Fe oxides, showing a clear relationship between edge position and formal valence state and coordination environment. (Reprinted with permission from Reference 65. Copyright (2008) Elsevier.)

L_2 and L_3 edges can be very sensitive to the d-band occupancy of transition metals, as they directly probe the number of vacancies in the d band. For example, as shown in Figure 1.15, the absorption edge of Pd L_3-edge XANES shifts to a lower energy upon reduction of Pd(II) salts to Pd(0).[69] The outer shell electron configuration of Pd(0) is nominally $4d^{10}5s^0$, so the intensity of the absorption edge of Pd L_3-edge XANES is also affected by the oxidation state of the species. For Pd(0), the 4d band is nearly full, so the intensity of the transition from $2p_{3/2}$ to 4d is low. Pd(II) has a d^8 configuration, and thus more vacancies are in the 4d band, therefore, the intensity of the L_3 absorption edge for Pd(II) species is much higher. As shown in Figure 1.15, the oxidation state of Pd in the *in situ* AuPd NPs is close to Pd(0), which indicates Pd(II) gets reduced during the oxidation of crotyl alcohol. A slightly higher energy of Pd in the AuPd NPs than the Pd(0) bulk phase is likely due to an electronic effect occurring between Au and Pd in the NPs.[69]

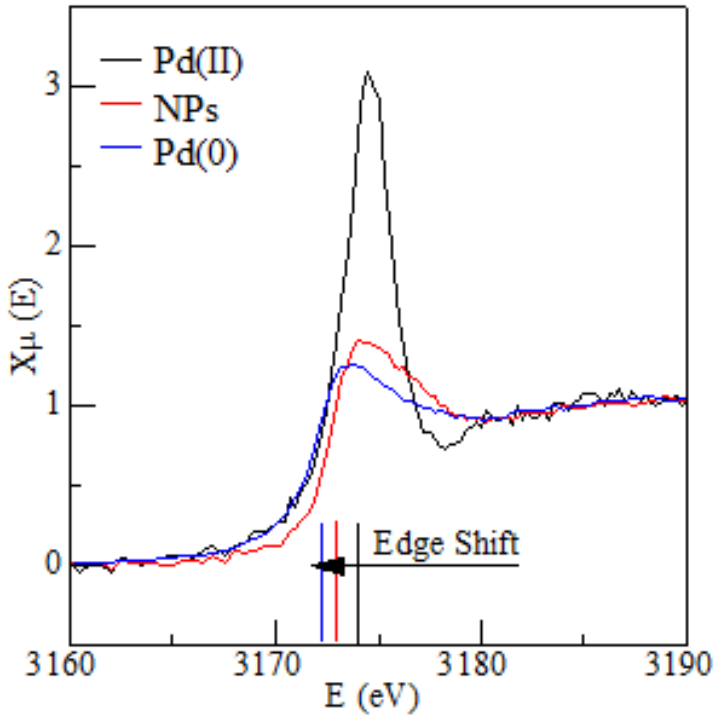

Figure 1.15. Pd L_3-edge XANES spectra comparing Pd(II), NPs formed *in situ* after the addition of crotyl alcohol to 1:3 Au:Pd(II) in water in a 250:1 substrate:metal ratio, and pure Pd metal. (Adapted with permission from Reference 69. Copyright (2013) American Chemical Society.)

For an unknown sample, its oxidation state and crystal phase can be understood through comparing its XANES spectrum with the spectra of standards. If a sample is a mixture of phases, linear combination fitting provides a simple way to distinguish the presence of different phases and to semi-quantitatively determine the atomic fraction of each one. For example, Figure 1.16 on the left shows the normalized XANES spectra of a sample containing Fe and three standards, Fe foil, FeO and Fe_3O_4. Linear combination fitting shows that the unknown sample consists of approximately 6% Fe(0), 11% FeO and 83% Fe_3O_4, and that the resulting sum of the reference spectra is nearly a perfect fit for the actual sample (Figure 1.16 right). If a linear combination fitting fails to find a good match to the data, it suggests that there is a constituent in the sample that is not in the standards.[63] Therefore, linear combination fitting requires a strong library of standards for all chemical species that may be in a mixture. Rather than guessing at the possible maximum number of standard species to linearly combine to fit the spectrum of an unknown mixture, principal component analysis coupled with linear combination analysis can provide a statistical basis for choosing the appropriate number of standards for linear combination fitting.[70] Principal component analysis considers the statistical variance within an experimental data set composed of a group of unknown samples.[71]

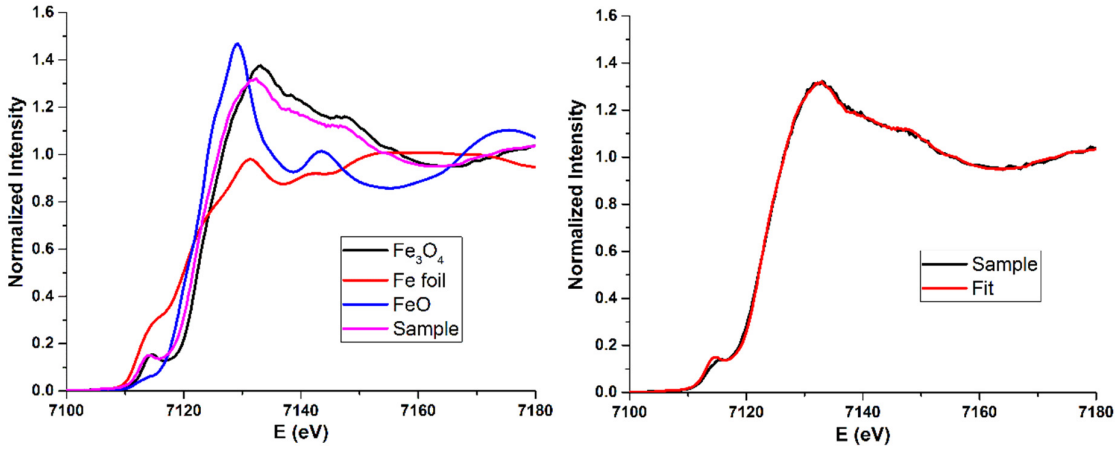

Figure 1.16. (Left) Normalized K-edge Fe spectrum of sample along with Fe foil, FeO and Fe_3O_4 standards. (Right) Normalized sample spectrum together with a linear combination of 6% Fe(0), 11% FeO and 83% Fe_3O_4.

1.3.2.2 Extended X-ray Absorption Fine Structure (EXAFS) Spectroscopy

As the X-ray energy increases in an XAS scan, the excited electron will be ejected out of the atom to create a photoelectron. The ejected photoelectron wave will be scattered by the neighboring atoms creating an interference pattern between the outgoing photoelectron wave and back-scattered waves. These waves will interfere either constructively or destructively, which leads to oscillations in the absorption spectrum above the absorption edge. These oscillations are known as EXAFS. Since the oscillations are created by the interference of the waves with neighboring atoms, EXAFS spectroscopy can be used to determine both the number and elemental composition of neighboring atoms, their distance from the absorbing atom and the thermal or structural disorder of their positons. To get this information, first, we need to extract the EXAFS signal χ(E) from the XAS spectrum. The EXAFS signal, as a function of energy, χ(E) is described by Equation 1.16:

$$\chi(E) = (\mu(E) - \mu_0(E))/\Delta\mu_0(E) \quad \textbf{(1.16)}$$

Where μ(E) is measured absorption coefficient, μ_0(E) represents the absorption coefficient of an isolated atom, which is typically fitted with cubic spline function and $\Delta\mu_0$(E) is the absorption jump (J) at the edge energy, as shown in Figure 1.17 A.

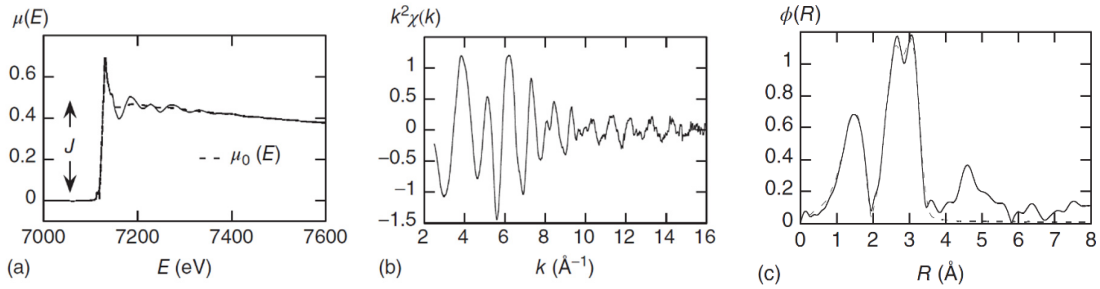

Figure 1.17. (A) Experimental X-ray absorption spectrum of Fe_3O_4 NPs. The free-atom absorption coefficient (dashed line) and jump at the edge energy are indicated. (B) Extracted EXAFS signal with a k^2 weight. (C) *R*-space. (Adapted with permission from Reference 60. Copyright (2016) Wiley-VCH Verlag GmbH & Co. KGaA.)

Because of the wave nature of the produced photoelectron, χ(E) is normally converted to χ(k) using Equation 1.17:

$$k = \sqrt{\frac{2m_e(E-E_0)}{\hbar^2}} = 0.512\sqrt{E-E_0} \quad \textbf{(1.17)}$$

Where k is the photoelectron wave vector, $\hbar$ is the reduced Planck constant, m_e is the effective mass of electron, and E and E_0 are the measured absorption energy and absorption edge energy, respectively.

The full EXAFS equation can be expressed using Equation 1.18 below:

$$\chi(k) = S_0^2 \sum_i \frac{N_i S_i(k) f_i(k)}{kR_i^2} e^{-2R_i/\lambda(k)} e^{-2\sigma_i^2 k^2} sin[2kR_i + \delta_c(k) + \delta_i(k)] \quad \textbf{(1.18)}$$

Where S_0^2 is the amplitude reduction factor, N_i is the coordination number for atom type i, $S_i(k)$ is the amplitude reduction function, $f_i(k)$ is the EXAFS amplitude function for atom type i, R_i is the absorber-backscatterer distance for atom type i, $\lambda(k)$ is the photoelectron mean free path function, σ_i^2 is the Debye-Waller factor which represents the mean-square deviation in R_i, $\delta_c(k)$ is the EXAFS absorber phase shift function and $\delta_i(k)$ is the EXAFS backscatterer phase shift function. Since the $e^{-2\sigma_i^2 k^2}$ factor in the EXAFS equation causes $\chi(k)$ to drop off in amplitude with k, $\chi(k)$ is often multiplied by k, k^2, or k^3 to result in a plot with more uniform amplitude.[47] This is called k-weighting, and an example is shown in Figure 1.17 B.

In the full EXAFS equation, the first term $S_0^2 \sum_i \frac{N_i S_i(k) f_i(k)}{kR_i^2} e^{-2R_i/\lambda(k)} e^{-2\sigma_i^2 k^2}$ represents the amplitude of the waves, while $sin[2kR_i + \delta_c(k) + \delta_i(k)]$ represents the phase of the waves. Therefore, increasing the number of nearest neighbors (N_i) increases the amplitude, while increasing R_i increases the frequency and decreases the amplitude, and larger σ^2 values decreases the amplitude at high k.

A Fourier transform of the EXAFS k-space can convert the data to R-space. However, the resulting R-space plot is one that has no phase shift correction, and the peaks typically shift to lower R values than would be expected from their bond distances. For example, as shown in Figure 1.17 C, the Fe-O peak is at around 1.6 Å, whereas the typical Fe-O distance is around 2.15 Å. Therefore, interatomic distances cannot be determined by directly measuring the position of Fourier transform peaks in the R space EXAFS plot, but rather should be obtained

from fitting. By using a known model crystal structure which has a structure which would be representative of the sample, one can fit EXAFS data by simulating EXAFS spectra of the model structure, and thus can potentially determine best-fit values for the coordination number of each shell (*N)*, the atomic distances between absorber and scattering atoms (*R*), the static and thermal disorder in the positon of the scattering atoms (σ^2), as well as the phase shift(s). At room temperature thermal disorder is moderate, thus σ^2 is normally in the range of $0.0015 \leq \sigma^2 \leq 0.0080$ Å^2, and typical values at the top of the range are seen in nanoscale systems which have a larger amount of static disorder. EXAFS can determine atomic distances (*R*) with high accuracy, so a typical accuracy for *R* is better than ± 0.02 Å.[72]

EXAFS fitting results can help us understand the sizes and structures of NPs. For example, several groups have reported the correlation between the coordination number of NPs and their sizes.[73-75] As NPs get smaller, a large fraction of absorbing atoms occupy under-coordinated surface sites, and thus the average coordination number around absorbing atoms drops as a function of NP size. EXAFS can also be used to give information about the morphology of bimetallic NPs. For example, Maclennan *et al.* reported that in AuPd bimetallic NPs, low Pd-Pd and high Au-Au coordination numbers suggests that Pd tends to be on the surface and Au in the core. Large Pd-Au coordination number can be used to indicate greater alloying in bimetallic AuPd NPs.[69]

1.3.2.3 *In Situ* X-ray Absorption Spectroscopy

The term *in situ* (which means "on site") has been used to describe the collection of spectra of a sample in the same environment in which it has been treated.[76] *In situ* spectroscopic studies can aid the rational design of new and efficient catalysts by providing fundamental information about catalytic structure and surface species under controlled environments.[77] *In situ* spectroscopic characterization of catalysis can be performed by an arsenal of spectroscopic techniques: Raman spectroscopy,[78] infrared spectroscopy (IR),[79] nuclear magnetic resonance (NMR) spectroscopy,[80] ultraviolet and visible spectroscopy (UV-Vis),[81] Mössbauer spectroscopy[82] and X-ray absorption spectroscopy (XAS),[83] among others.[84,85] Given the many advantages of XAS which have been mentioned earlier in Section 1.3.2 along with the

improvement of X-ray optics, detectors, user-friendly software and the increased accessibility of XAS user facilities, more *in situ* XAS experiments have been carried out to study nanocatalysts.

To measure the samples under controlled conditions, scientists need to develop specific cells. Since many catalytic reactions occur in solutions, various *in situ* liquid cells have been designed. For example, Kumar and coworkers have demonstrated the use of a millifluidic chip for time-resolved mapping of the growth of gold nanostructures from solution using *in situ* XAS.[86] As shown in Figure 1.18 A and B, the millifluidic chip used consists of a serpentine channel with dimensions of 2mm (width) × 0.15 mm (height) ×220 mm (length) with two inputs and a single output. The precursor reagents, $HAuCl_4$ and *meso*-2,3-dimercapto succinic acid (DMSA) were dispended within the chip at a flow-rate of 10 mL/h using fully automated syringe pumps. The reaction starts at zone 1, and *in situ* XAS fluorescence data could be collected at different positions on the chip during the reaction by mounting the chip onto a metal stage in the path of the synchrotron beam and allowing the beam to pass through the desired zone on the chip (Figure 1.18 A and C).

(A) (B)

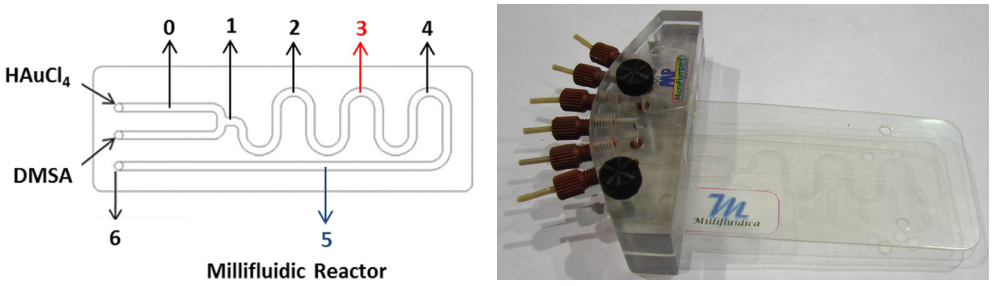

(C)

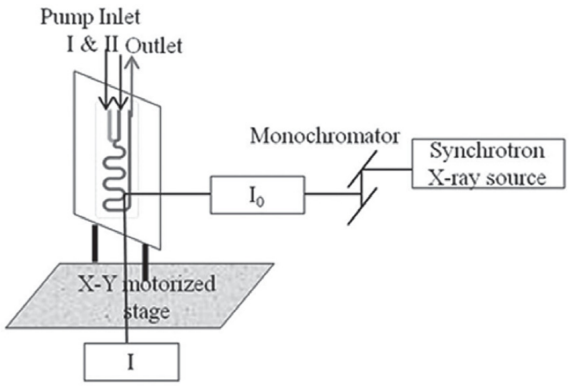

Figure 1.18. (A) Millifluidic chip marked with different zones where *in situ* XAS was performed. (B) Photograph showing the millifluidic chip with serpentine channels connected to the manifold. (C) *In situ* XAS analysis at different zones within the millifluidic channel. (Reprinted with permission from Reference 83. Copyright (2013) American Chemical Society.)

Lee's group reported another designed *in situ* XAS liquid cell, and they used it to quantitatively track the local structure of monodispersed Pd NPs during a Suzuki coupling reaction.[87] As shown in Figure 1.19, a Suzuki coupling reaction catalyzed by Pd NPs was carried out in an external glass reactor, then the reaction solution was circulated through the *in situ* flow cell via a peristaltic pump and PTFE tubing at 60 °C. *In situ* Pd K-edge XAS fluorescence data was collected every 5 min. Using a similar setup, through changing the PTFE cell to a specially designed quartz cuvette, Yao *et al*. have successfully tracked the nucleation pathway in the synthesis of Pt nanocrystals in solution by combining *in situ* Pt L_3-edge XAS and UV-Vis spectra.[88] To reach the optimum absorption thickness and good signal-to-noise

data for XAS and simultaneous UV-Vis measurements, the cuvette has a path length of 8 mm with 100 μm transparent quartz windows in the X-ray direction and 4mm path length in the UV-Vis direction.

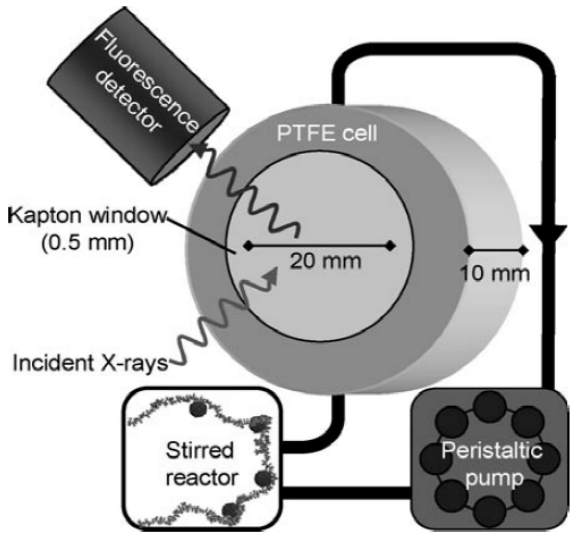

Figure 1.19. Recirculating reactor setup for operando fluorescence XAS. (Reprinted with permission from Reference 87. Copyright (2010) WILEY-VCH Verlag GmbH & Co. KGaA, Weinheim.)

A simple *in situ* liquid cell as shown in the inset of the Figure 1.20 was designed by us in conjunction with Jeffrey Miller (Purdue Univeristy). SPEX CertiPrep Disposable XRF X-Cell sample caps purchased from Fisher Scientific can be used as liquid cells, and different sized and shaped insertions fabricated out of polyether ether ketone (PEEK) or polypropylene are used to adjust the volume of the cell. During an *in situ* XAS measurement, the liquid cell is covered by a 4μm Ultralene window with the sample inside and the cell is then placed on a sample holder in an aluminum box filled with He, as shown in Figure 1.20. The aluminum box is mounted on a magnetic stirrer and a magnetic stir bar can be added to the liquid cell to allow efficient mixing of reaction precursors and to help prevent photoreduction events from occurring by continuously changing the sampling volume. Various *in situ* XAS studies have been carried out in such a cell. For example, Maclennan *et al*. have used this setup to study the *in situ* formation of AuPd core-shell NPs and evaluate their stability toward oxidation during

the catalytic oxidation of crotyl alcohol in aqueous solutions.[69] Liu *et al*. studied the stability of Ag nanoprisms functionalized with thiol-terminated poly(ethylene glycol) by *in situ* Ag L_3-edge XANES.[89] Shivhare *et al*. monitored the reaction of Pd(II) acetate with $Au_{25}(SC_8H_9)_{18}^-$ clusters by *in situ* Pd L_3-edge XANES, and found that Pd(II) acetate was converted to Pd(II) thiolate species through the reaction with S atoms in the staple motifs (-S-Au-S-Au-S-) of the $Au_{25}(SC_8H_9)_{18}^-$ clusters as determined from the changes in the XANES spectra.[90] Most of the *in situ* XAS studies in this thesis are also based on the use of this liquid cell along with further development of cells that allow for *in situ* sample addition.

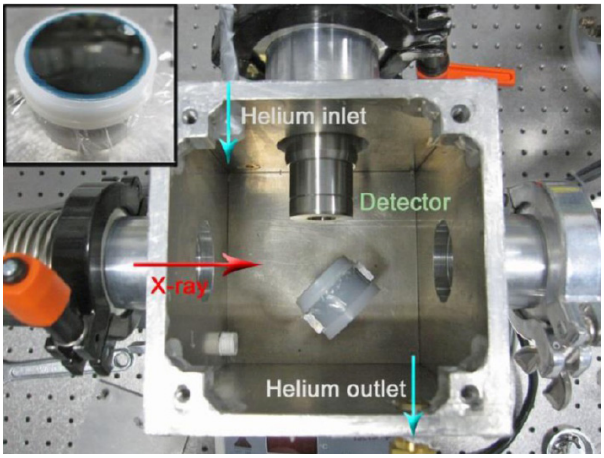

Figure 1.20. A simple *in situ* liquid cell on the SXRMB beamline at the Canadian Light Source. The inset shows a solution of Ag nanoprisms in the sample cell used for the measurements. (Reprinted with permission from Reference 89. Copyright (2013) American Chemical Society.)

There has also been a great deal of development *in situ* liquid cells for high temperature and/or high pressure reactions. To achieve high temperatures and/or high pressures, these *in situ* liquid cells are normally much more complicated than the cells introduced above. As shown in Figure 1.21, Testemale and coworkers have designed a cell which consists of a resistive furnace and an internally heated helium-pressurized autoclave with cold walls and can vary the temperature and the pressure up to 500 °C and 2000 bar, respectively, for aqueous studies.[91,92] 0.2 mL of sample can be loaded in a sapphire tube, and three Be windows allow one to collect both transmission and fluorescence data.

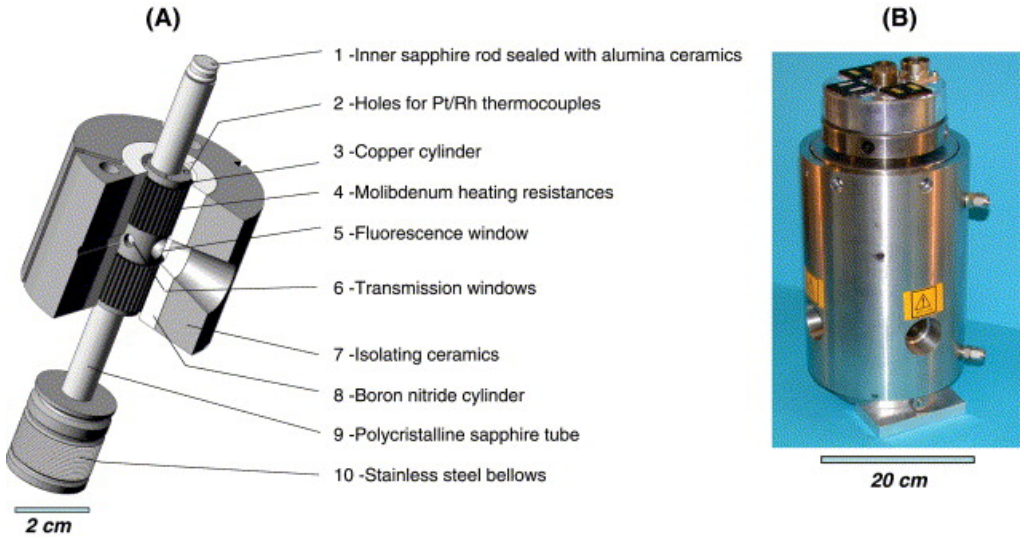

Figure 1.21. (A) Scheme of a X-ray optical cell. (B) High temperature-pressure reactor used for XAS measurements. (Reprinted with permission from Reference 92. Copyright (2005) Elsevier.)

The cell introduced above is pressurized with He gas. Karim *et al*. introduced an *in situ* high temperature-pressure XAS cell which allows the flow of H_2. As shown in Figure 1.22, the cell body is fabricated out of stainless steel and heated by resistive heating cartridges. A flow reactor is used to contain the aqueous sample, and a H_2/He mixture can be delivered through the reactor by a mass flow controller. The *in situ* XAS reaction cell is capable of probing catalysts under reaction conditions in aqueous phase up to 1100 psig and 400 °C.[93] Through using this setup, Tupy *et al*. studied the structural changes of NiPt/C and NiPt/γ-Al_2O_3 nano-catalysts by *in situ* EXAFS during aqueous phase reforming of ethylene glycol.[94] The results show that the NiPt catalysts have mainly Pt surfaces in a H_2 environment, while Ni segregation occurs to produce a Ni-enriched surface during the aqueous phase reforming of ethylene glycol.

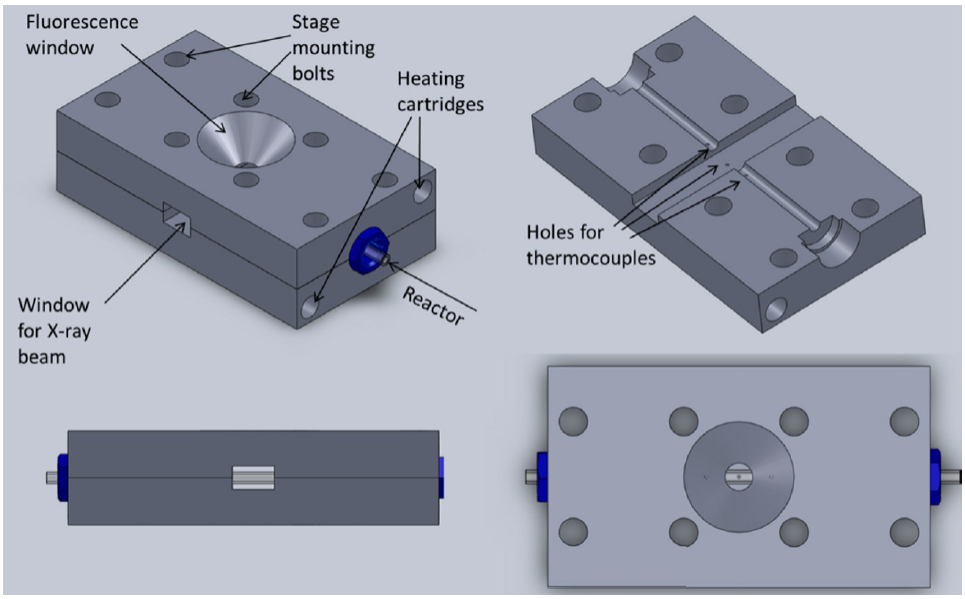

Figure 1.22. Scheme of an operando XAS cell which can be operated up to 1100 psig and 400 °C. (Reprinted with permission from Reference 93. Copyright (2012) American Chemical Society.)

As shown in Figure 1.23, Nelson and Miller developed a general-purpose liquid cell which can be operated up to 250 °C, and allows for liquid samples to be exposed to different gaseous environments.[95] The setup is composed of a small sample cell with diameter *ca.* 1 cm fabricated from a chemically resistant polymer housed inside a heated aluminum block which has machined paths for incoming X-rays, transmitted X-rays and outgoing X-ray fluorescence from the sample (large conical opening). A small magnetic stirring bar can be placed into this cell to mix the reaction precursors. In this thesis, a similar high temperature liquid cell was used to monitor the formation of hollow Fe oxide NPs from as-synthesized Fe NPs via *in situ* Fe K-edge XAS at 180 °C.

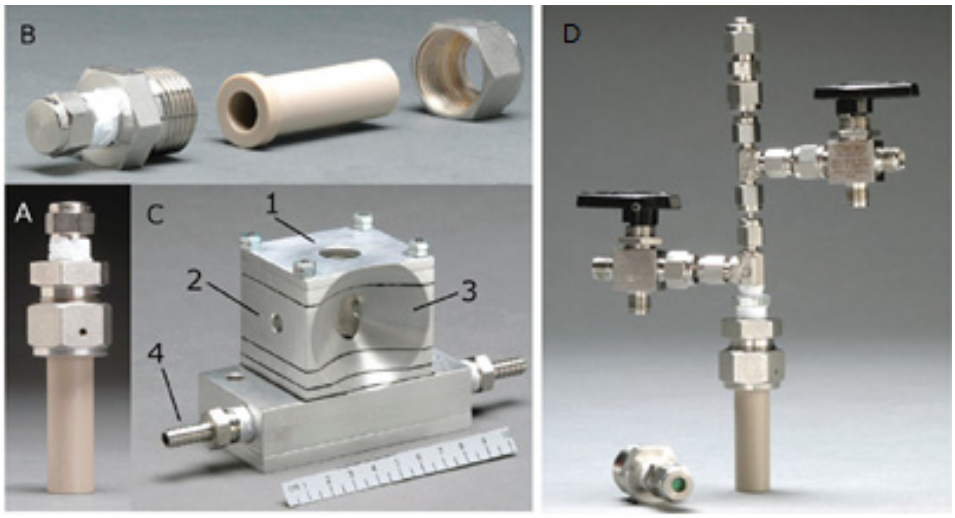

Figure 1.23. (A) An assembled solution XAS sample cell. (B) A disassembled cell. (C) The temperature-controlled mounting block. (D) A cell cap with an injection septum (lower left) and continuous flow manifold (center). (Reproduced from Reference 95 with permission of The Royal Society of Chemistry. Copyright (2011) Royal Society of Chemistry.)

Although many examples have shown that *in situ* XAS is an invaluable tool for studying catalysis under reaction conditions, long exposures of the reaction solutions to X-rays can lead to the possibility of beam-induced photoreduction events.[96,97] For example, some studies have shown that water can decompose under ionizing radiation into a handful of major species, such as hydrated electrons (e_{aq}^-) which can further combine with water to form molecular hydrogen and hydroxide ions.[98] These products may react with the catalysts in the reaction solutions and cause changes in their structures and/or speciation. Therefore, caution must be taken to reduce the rate of photoreduction in the design of *in situ* cell and in spectral measurements, for example, using magnetic stir bars to agitate the reaction solutions or reducing flux or flux density in the measurements. Furthermore, *in situ* studies not only require the design of various *in situ* cells, but also improvements to the setup at beamlines. For example, many catalytic reactions happen very quickly over a period of seconds to minutes. However, a conventional XAS scan normally takes more than ten minutes. To follow the dynamic structural changes of catalysts under reaction conditions, quick-EXAFS methods have been developed to shorten the time for each scan with temporal resolutions below 100 ms.[99] Such methods typically involve

the development of ultra-fast monochromators and detectors that can scan the entire XAS energy range in sub second time ranges.

1.4 My Research Objectives

Compared to XRD which gives information on crystalline components and XPS which is typically performed under ultrahigh vacuum conditions, *in situ* XAS allows us to study nanomaterials and nanocatalysts under reaction conditions without worrying about changes in their speciation upon drying or exposure to air. The objective of this thesis is to show that one can follow the chemistry of Fe based nanomaterials and nanocatalysts in real time using *in situ* XAS.

Reduction of ferric or ferrous ions with sodium borohydride in aqueous solutions is a simple way to prepare Fe@Fe_xO_y NPs, and the resulting NPs have been used for environmental remediation or catalytic studies by many groups.[100-103] However, these Fe@Fe_xO_y NPs have large size distributions and it is difficult to follow the kinetics of their oxidation and relative speciation of Fe in real time. My first research objective was to control the sizes of Fe@Fe_xO_y NPs, and follow the oxidation of Fe@Fe_xO_y NPs by *in situ* XANES. Here, we used PVP as a stabilizer with different molar ratios of methanol to water to control the sizes of Fe@Fe_xO_y NPs. PVP is one of the most common stabilizers in the synthesis of NPs, and it is cheap and soluble in alcohols and water. *In situ* Fe K-edge XAS was carried out under ambient conditions to probe the composition and structural changes of Fe@Fe_xO_y NPs in real time. In addition, the effect of the size of Fe@Fe_xO_y NPs in ethanol for the hydrogenation of alkenes was studied, and their catalytic abilities were compared with Fe NPs synthesized a tri(hexyl)tetradecylphosphonium chloride ionic liquid. The results of these hydrogenation studies are documented in Chapter 6.

Fe has relatively low standard electrode potential, thus Fe@Fe_xO_y NPs can be a versatile support to reduce other metals which have higher standard electrode potentials on their surface by galvanic exchange reactions to synthesize bimetallic NPs. The resulting bimetallic NPs have been used to catalyze various reactions.[43-47,104] However, the morphologies of the resulting bimetallic NPs and their formation processes by galvanic exchange reaction are rarely

studied.[18,105] My second objective was to synthesize Fe@Fe_xO_y supported Pd and Cu NPs by controlling the molar ratios of Fe@Fe_xO_y NPs to Pd(II) or Cu(II) salts and use *in situ* XANES to follow the formation processes of Fe@Fe_xO_y/Pd and Fe@Fe_xO_y/Cu NPs. In addition, the speciation of Fe@Fe_xO_y/Pd NPs for Suzuki-Miyaura cross-coupling reactions was followed under *in situ* conditions. The results of this study are reported in Chapter 3.

Pd NPs have been reported to be catalytically active for a myriad of hydrogenation reactions.[106,107] A variety of supports have also been investigated to further improve the catalytic activity, stability and selectivity of Pd sites in different hydrogenation reactions.[108,109] However, studies of Fe-supported Pd NPs for catalytic hydrogenations are rare. The third objective was to study the catalytic performance of the Fe@Fe_xO_y/Pd NPs synthesized in Chapter 3 for hydrogenation reactions. In Chapter 4, I applied Fe@Fe_xO_y/Pd NPs with different molar ratios of Fe to Pd for the catalytic hydrogenation of 2-methyl-3-buten-2-ol in a solution of either water or ethanol, and studied their ability to both magnetically recover samples from the reaction and agitate samples during the reaction to improve mass transfer of reagents. *In situ* XANES experiments were carried out to study the stability of Fe@Fe_xO_y/Pd in different solvents.

Fe NPs can also be synthesized by a conventional decomposition reaction of $Fe(CO)_5$ in an oleylamine/octadecene solution at 180 °C for 30 min.[33,34] The as-synthesized Fe NPs can further be converted to hollow Fe oxide NPs by the Kirkendall effect.[35,36] With large surface areas and low material density, studies of hollow Fe oxide NPs as catalysts or catalytic supports are promising. Fe oxide shells have been used to prevent the sintering of the catalytically active cores and also allow magnetic recovery of the cores in core@shell bimetallic nanoparticles.[110] However, more studies are required under real reaction conditions on the availability of their interior surface or active cores in bimetallic nanoparticles. Herein, my fourth objective was to study the penetrability of hollow Fe oxide NPs. In Chapter 5, we introduced a simple approach to study the penetrability of hollow Fe oxide shells by galvanic exchange reactions between Fe(0) core in the hollow Fe oxide shell and Pd(II) acetate. First, we used *in situ* high temperature Fe K-edge XANES spectra to monitor the formation of hollow Fe oxide NPs from

Fe NPs. Core-void-shell Fe-Fe oxide NP intermediates were captured at different time intervals to react with Pd(II). The reduction of Pd(II) was characterized by Pd L_3-edge XANES spectra.

1.5 Organization and Scope

This Ph.D. thesis primarily describes the *in situ* X-ray absorption spectroscopic studies of the structures of Fe@Fe_xO_y NPs and bimetallic NPs based on Fe@Fe_xO_y NPs precursors, their formation processes and changes in their speciation during catalytic reactions. It is divided into seven chapters. Chapter 2, 3 and 4 are near verbatim copies of articles published in different journals with minor formatting changes. Chapter 5 and 6 are manuscripts to be submitted in the near future.

Chapter 1 is a brief introduction about the synthesis and characterization of monometallic and bimetallic NPs, and an overview of the main characterization techniques used in this thesis. In Chapter 2, I introduce a simple approach of controlling the sizes of Fe@Fe_xO_y NPs, and show that their oxidation kinetics can be followed by *in situ* XANES. In Chapter 3, different morphologies of Fe@Fe_xO_y-supported Pd and Cu NPs were synthesized by controlling the molar ratios of Fe@Fe_xO_y NPs to Pd(II) or Cu(II) salts, and their formation processes were studied by *in situ* XANES. In Chapter 4, different morphologies of Fe@Fe_xO_y supported Pd NPs synthesized in Chapter 4 were used to catalyze the hydrogenation of 2-methyl-3-buten-2-ol in a solution of either water or ethanol, and their stabilities in the hydrogenation reactions were studied by *in situ* XANES. In Chapter 5, the penetrability of core-void-shell Fe-Fe_3O_4 NPs was studied through the galvanic reactions between the Fe cores and Pd(II). The oxidation of the Fe NPs to form hollow Fe oxide NPs was studied by high-temperature *in situ* Fe K-edge XANES, while the reduction of Pd(II) was characterized by Pd L_3-edge XANES spectra. In Chapter 6, different sizes of Fe@Fe_xO_y NPs synthesized in Chapter 2 have been applied for the catalytic hydrogenation reactions, and the effect of the size of Fe NPs on the catalysis of hydrogenation reactions is studied. Fe K-edge XANES spectra have been used to study the changes of Fe@Fe_xO_y NPs before and after hydrogenation reactions. Finally, in Chapter 7, a summary, outlook and future work are presented.

1.6 References

1. Atkins, P.; de Paula, J. Physical Chemistry. Oxford University Press, **2002**, 908.

2. Cirtiu, C. M.; Dunlop-Brière, A. F.; Moores, A. Cellulose Nanocrystallites as An Efficient Support for Nanoparticles of Pallladium: Application for Catalytic Hydrogenation and Heck Coupling under Mild Conditions. *Green Chem*. **2011**, *13*, 288.

3. Pérez-lerenzo, M. Palladium Nanoparticles as Efficient Catalysts for Suzuki Cross-Coupling Reactons. *J. Phys. Chem. Lett.* **2012**, *3*, 167–174.

4. Semagina, N.; Kiwi-Minsker L. Palladium Nanohexagons and Nanospheres in Selective Alkyne Hydrogenation. *Catal. Lett.* **2009**, *127*, 334–338.

5. Xiao, L.; Zhuang, L.; Liu, Y.; Lu, J. Abruna, H. D. Activating Pd by Morphology Tailoring for Oxygen Reduction. *J. Am. Chem. Soc.* **2008**, *131*, 602–608.

6. Cui, X.; Ren, P.; Deng, D.; Deng, J.; Bao, X. Single Layer Graphene Encapsulating Non-Precious Metals as High-Performance Electrocatalysts for Water Oxidation. *Energy Environ. Sci.* **2016**, *9*, 123–129.

7. Bolm, C.; Legros, J.; Le Paih, J. Zani, L. Iron-Catalyzed Reactions in Organic Synthesis. *Chem. Rev.* **2004**, *104*, 6217–6254.

8. Peng, S.; Lei, C.; Ren, Y.; Cook, R. E.; Sun, Y. Plasmonic/Magnetic Bifunctional Nanoparticles. *Angew. Chem. Int. Ed.* **2011**, *50*, 3158–3163.

9. Phua, P.-H.; Lefort, L.; Boogers, J. A. F.; Tristany, M.; de Vries, J. G. Soluble Iron Nanoparticles as Cheap and Environmentally Benign Alkene and Alkyne Hydrogenation Catalysts. *Chem. Commun* **2009**, *45*, 3747–3749.

10. Rangheard, C.; Fernández, C. de J.; Phua, P.-H.; Hoorn, J.; Lefort, L.; de Vries, J. G. At the Frontier between Heterogeneous and Homogeneous Catalysts: Hydrogenation of Olefins and Alkynes with Soluble Iron Nanoparticles. *Dalton Trans.* **2010**, *39*, 8464–8471.

11. Kelsen, V.; Wendt, B.; Werkmeister, S.; Junge, K.; Beller, M.; Chaudret, B. The Use of Ultrasmall Iron(0) Nanoparticles as Catalysts for the Selective Hydrogenation of Unsaturated C-C Bonds. *Chem. Comm.* **2013**, *49*, 3416–3418.

12. Kandel, K.; Anderegg, J. W.; Nelson, N. C.; Chaudhary, U.; Slowing, I. I. Supported Iron Nanoparticles for the Hydrodeoxygenation of Microalgal Oil to Green Diesel. *J. Catal.* **2014**, *314*, 142–148.

13. Liu, H.; Liu, C.; Li, X.; Cen, Y. Effect of An Iron Oxide Precursor on the H_2 Desorption Performance for an Ammonia Synthesis Catalyst. *Ind. Eng. Chem. Res.* **2003**, *42*, 1347–1349.

14. Wang, D.; Astruc, D. The Recent Development of Efficient Earth-Abundant Transition-Metal Nanocatalysts. *Chem. Soc. Rev.* **2017**, *46*, 816–854.

15. Wang, C.; Zhai, P.; Zhang, Z.; Zhou, Y.; Ju, J.; Shi, Z.; Ma, D.; Han, R. P. S.; Huang, F. Synthesis of Highly Stable Graphene-Encapsulated Iron Nanoparticles for Catalytic Syngas Conversion. *Part. Part. Syst. Charact.* **2015**, *32*, 29–34.

16. Toshima, N.; Yonezawa, T. Bimetallic Nanoparticles–Novel Materials for Chemical and Physical Applications. *New J. Chem.* **1998**, *22*, 1179–1201.

17. Li, X.-Q.; Elliott, D. W.; Zhang, W.-X. Zero-Valent Iron Nanoparticles for Abatement of Environmental Pollutants: Materials and Engineering Aspects. *Crit. Rev. Environ. Sci. Technol.* **2006**, *31*, 111–122.

18. Masnadi, M.; Yao, N.; Braidy, N.; Moores, A. Cu(II) Galvanic Reduction and Deposition onto Iron Nano- and Microparticles: Resulting Morphologies and Growth Mechanisms. *Langmuir* **2015**, *31*, 789–798.

19. He, F.; Zhao, D. Preparation and Characterization of A New Class of Starch-Stabilized Bimetallic Nanoparticles for Degradation of Chlorinated Hydrocarbons in Water. *Environ. Sci. Technol.* **2005**, *39*, 3314–3320.

20. Fu, R.; Yang, Y.; Xu, Z.; Zhang, X.; Guo. X.; Bi, D. The Removal of Chromium(VI) and Lead(II) for Groundwater Using Sepiolite-Supported Nanoscale Zero-Valent Iron (S-NZVI). *Chemosphere* **2015**, *138*, 726–734.

21. Saleh, N.; Phenrat, T.; Sirk, K.; Dufour, B.; Ok, J.; Sarbu, T.; Matyjaszewski, K.; Tilton. R. D.; Lowry, G. V. *Environ. Sci. Technol.* **2005**, *39*, 2489–2494.

22. Koczkur, K. M.; Mourdikoudis, S.; Polavarapu, L.; Skrabalak, S. E. Polyvinylpyrrolidone (PVP) in Nanoparticle Synthesis. *Dalton Trans.* **2015**, *44*, 17883–17905.

23. Lu, G.; Li, S.; Guo, Z.; Farha, O. K.; Hauser, B. G.; Qi, X.; Wang, Y.; Wang, X.; Han, S.; *et al*. Imparting Functionality to A Metal-Organic Framework Material by Controlled Nanoparticle Encapsulation. *Nat. Chem.* **2012**, *4*, 310–316.

24. Gacem, N.; Diao, P. Effect of Solvent Polarity on the Assembly Behavior of PVP Coated Rhodium Nanoparticles. *Colloids Surf. A* **2013**, *417*, 32–38.

25. Sun, Y.-P.; Li, X.-Q.; Cao, J.; Zhang, W.-X.; Wang, H. P. Characterization of Zero-Valent Iron Nanoparticles. *Adv. Colloid Interface Sci.* **2006**, *120*, 47–56.

26. Hudson, R.; Riviere, A.; Cirtiu, C. M.; Luska, K. L.; Moores, A. Iron-Iron Oxide Core-Shell Nanoparticles are Active and Magnetically Recyclable Olefin and Alkyne Hydrogenation Catalysts in Protic and Aqueous Media. *Chem. Comm*. **2012**, *48*, 3360–3362.

27. Takeuchi, K. J.; Marschilok, A. C.; Bessel, C. A.; Dollahon, N. R. Synthesis, Characterization, and Catalytic Use of Acicular Iron Particles. *J. Catal.* **2002**, *208*, 150–157.

28. Zhang, L.; Manthiram, A. Fabrication and Magnetic Properties of Chains Composed of

Spherical Iron Particles. *IEEE. Trans. Magn.* **1996**, *32*, 4481–4483.

29. Arellano, J. S.; Vega, A. K.; Rosendo-Andrés, E.; Diaz-Becerril, T.; Romano-Trujillo, R.; Oliva, A. I.; de la Cruz, W.; Lugo, J. M.; Morales-Ruiz, C. *et al*. Influence of HCl on the NPs-CdSe Synthesis Prepared by the Colloidal Method. *J. Appl. Res. Technol.* **2016**, *14*, 225–231.

30. Ni, X.; Su, X.; Zheng, H.; Zhang, D.; Yang, D.; Zhao, Q. Studies on the One-Step Preparation of Iron Nanoparticles in Solution. *J. Cryst. Growth.* **2005**, *275*, 548–553.

31. Nene, A. G.; Takahashi, M.; Somani, P. R. Fe_3O_4 and Fe Nanoparticles by Chemical Reduction of $Fe(acac)_3$ by Ascorbic Acid: Role of Water. *World J. Nano Sci. Eng.* **2016**, *6*, 20–28.

32. Lacroix, L.-M.; Lachaize, S.; Blon, A. F.; Respaud, M. Ultrasmall Iron Nanoparticles: Effect of Size Reduction on Anisotropy and Magnetization. *J. Appl. Phys.* **2008**, *103*, 07D521.

33. Peng, S.; Wang, C.; Xie, J.; Sun, S. Synthesis and Stabilization of Monodisperse Fe Nanoparticles. *J. Am. Chem. Soc.* **2006**, *128*, 10676–10677.

34. Hyeon, T.; Lee, S. S.; Park, J.; Chuang, Y.; Na, H. B. Synthesis of Highly Crystalline and Monodisperse Maghemite Nanocrystallites without a Size-Selection Process. *J. Am. Chem. Soc.* **2001**, *123*, 12798–12801.

35. Cabot, A.; Puntes, V. F.; Shevchenko, E.; Yin, Y.; Balcells, L.; Marcus, M. A.; Hughes, S. M.; Alivisatos, A. P. Vancancy Coalescence during Oxidation of Iron Nanoparticles. *J. Am. Chem. Soc*. **2007**, *129*, 10358–10360.

36. Peng, S.; Sun, S. Synthesis and Characterization of Monodisperse Hollow Fe_3O_4 Nanoaprticles. *Angew. Chem. Int. Ed.* **2007**, *46*, 4155–4158.

37. Weir, M. G.; Knecht, M. R.; Frenkel, A. I.; Crooks, R. M. Structural Analysis of Pd/Au Dendrimer-Encapsulated Bimetallic Nanoparticles. *Langmuir* **2010**, *26*, 1137–1146.

38. Costi, R.; Saunders, A. E.; Banin, U. Colloidal Hybrid Nanostructures: A New Type of Functional Materials. *Angew. Chem. Int. Ed.* **2010**, *49*, 4878–4897.

39. Kang, S. W.; Lee, Y. W.; Park, Y.; Choi, B.; Hong, J. W.; Park, K.; Han, S. W. One-Pot Synthesis of Trimetallic Au@PdPt Core-Shell Nanoparticles with High Catalytic Performance. *ACS Nano* **2010**, *4*, 6725–6734.

40. Zhang, Y.; Diao, W.; Monnier, J. R.; Williams, C. T. Pd-Ag/SiO_2 Bimetallic Catalysts Prepared by Galvanic Displacement for Selective Hydrogenation of Acetylene in Excess Ethylene. *Catal. Sci. Technol*. **2015**, *5*, 4123-4132.

41. Calver, C. F.; Dash, P.; Scott, R. W. J. Hydrogenations with Ag-Pd Catalysts Prepared by Galvanic Exchange Reactions. *ChemCatChem* **2011**, *3*, 695-697.

42. Haynes, W. M. CRC Handbook of Chemistry and Physics. 96th ed. CRC Press: Cleveland, OH, **2010**.

43. Zhou, S.; Johnson, M.; Veinot, J. G. C. Iron/Iron Oxide Nanoparticles: A Versatile Support for Catalytic Metals and Their Application in Suzuki-Miyaura Cross-Coupling Reactions. *Chem. Commun*. **2010**, *46*, 2411–2413.

44. Hudson, R.; Li, C.-J.; Moores, A. Magnetic Copper-Iron Nanoparticles as Simple Heterogeneous Catalysts for the Azide-alkyne Click Reaction in Water. *Green Chem*. **2012**, *14*, 622–624.

45. Ishikawa, S.; Hudson, R.; Masnadi, M.; Bateman, M.; Castonguay, A.; Moores, A.; Li, C.-J. Cyclopropanation of Diazoesters with Styrene Derivatives Catalyzed by Magnetically Recoverable Copper-Plated Iron Nanoparticles. *Tetrahedron* **2014**, *70*, 6162–6168.

46. Hudson, R.; Chazelle, V.; Bateman, M.; Roy, R.; Li, C.-J.; Moores, A. Sustainable Synthesis of Magnetic Ruthenium-Coated Iron Nanoparticles and Application in the Catalytic Transfer Hydrogenation of Ketones. *ACS Sustain. Chem. Eng*. **2015**, *3*, 814–820.

47. Shi, Y.; Yuan, Z.; Wei, Q.; Sun, K.; Xu, B. Pt-FeO_x/SiO_2 Catalysts Prepared by Galvanic Displacement Show High Selectivity for Cinnamyl Alcohol Production in the Chemoselective Hydrogenation of Cinnamaldehyde. *Catal. Sci. Technol*. **2016**, *6*, 7033-7037.

48. Thomas, J. M.; Midgley, P. A.; Yates, T. J. V.; Barnard, J. S.; Raja, R.; Arslan, I.; Weyland, M. The Chemical Application of High-Resolution Electron Tomography: Bright Field or Dark Field? *Angew. Chem. Int. Ed.* **2004**, *43*, 6745–6747.

49. Egerton, R. F. Electron Energy-Loss Spectroscopy in the TEM. *Rep. Prog. Phys.* **2009**, *72*, 016502.

50. Goldstein, J.; Newbury, D. E.; Joy, D. C.; Lyman, C. E.; Echlin, P.; Lifshin, E.; Sawyer, L.; Michael, J. R. Scanning Electron Microscopy and X-ray Microanalysis. *Springer*, **2003**.

51. Liu, X.; Liu, S.; Han, M.; Zhao, L.; Deng, H.; Li, J.; Zhu, Y.; Krusin-Elbaum, L.; O'Brien, S. Magnetoelectricity in $CoFe_2O_4$ Nanocrystal-P(VDF-HFP) Thin Film. *Nanoscale Res. Lett*. **2013**, *8*, 374.

52. Wang, L.; Yamauchi, Y. Autoprogrammed Synthesis of Triple-Layered Au@Pd@Pt Core-Shell Nanoparticles Consisting of Au@Pd Bimetallic Core and Nanoporous Pt Shell. *J. Am. Chem. Soc*. **2010**, *132*, 13636–13638.

53. Janecek, M.; Kral, R. Modern Electron Microscopy in Physical and Life Sciences. InTech, **2016.**

54. Iida, H.; Nakanishi, T.; Takada, H.; Osaka, T. Preparation of Magnetic Iron-Oxide Nanoparticles by Successive Reduction-Oxidation in Reverse Micelles: Effects of Reducing Agent and Atmosphere. *Electrochim. Acta*. **2006**, *52*, 292–296.

55. Hall, B. D.; Zanchet, D.; Ugarte, D. Estimating Nanoparticle Size from Diffraction Measurements. *J. Appl. Cryst*. **2000**, *33*, 1335–1341.

56. Williamson, G. K.; Hall, W. H. X-ray Line Broadening from Field Aluminium and Wolfram. *Acta. Metall*. **1953**, *1*, 22–31.

57. Yano, J.; Yachandra, V. K. X-ray Absorption Spectroscopy. *Photosynth. Res.* **2009**, *102*, 241–254.

58. Ortega, R.; Direct Speciation Analysis of Inorganic Elements in Single Cells using X-ray Absorption Spectroscopy. *J. Anal. At. Spectrom.* **2011**, *26*, 23–29.

59. Newville, M. Fundamentals of XAFS. University of Chicago, **2004**.

60. Faivre, D. Iron Oxides: From Nature to Applications.Wiley-VCH Verlag GmbH & Co. KGaA, **2016**, 398.

61. Agarwal, B. K. X-ray Spectroscopy. Springer-Verlag, **1989**, 314.

62. Gaur, A.; Shrivastava, B. D.; Nigam, H. L. X-ray Absorption Fine Structure (XAFS) Spectroscopy – A Review. *Proc. Indian. Natn. Sci. Acad.* **2013**, *79*, 921–966.

63. Calvin, S. XAFS for Everyone. CRC Press, **2013**.

64. Shulman, R. G.; Yafet, Y.; Eisenberger, P.; Blumberg, W. E. Observation and Interpretation of X-ray Absorption Edges in Iron Compounds and Proteins. *Proc. Natal. Acad. Sci.* **1976**, *73*, 1384–1388.

65. Fittschen, U. E. A.; Meirer, F.; Streli, C.; Wobrauschek, P.; Thiele, J.; Falkenberg, G.; Pepponi, G. Characterization of Atomospheric Aerosols using Synchrotron Radiation Total Reflection X-ray Fluorescence and Fe K-edge Total Reflection X-ray Fluorescence X-ray Absorption Near-Edge Structure. *Spectrochim. Acta Part B* **2008**, 6*3*, 1489–1495.

66. Henderson, G. S.; Groot, F. M. F. D.; Moulton, B. J. A. X-ray Absorption Near-Edge Structure (XANES) Spectroscopy. *Rev. Mineral. Geochem.* **2014**, *78*, 75–138.

67. Yamanoto, T. Assignment of Pre-Edge Peaks in K-edge X-ray Absorption Spectra of 3d Transition Metal Compounds: Electric Dipole or Quadrupole? *X-Ray Spectrom.* **2008**, *37*, 572–584.

68. Bora, D. K.; Braun, A.; Erat, S.; Safonova, O.; Graule, T.; Constable, E. C. Evolution of Structural Properties of Iron Oxide Nano Particles during Temperature Treatment from 250 °C-900 °C: X-ray Diffraction and Fe K-Shell Pre-Edge X-ray Absorption Study. *Curr. Appl. Phys.* **2012**, *12*, 817–825.

69. Maclennan, A.; Banerjee, A.; Hu, Y.; Miller, J. T.; Scott, R. W. *In Situ* X-ray Absorption Spectroscopic Analysis of Gold-Palladium Bimetallic Nanoparticle Catalysts. *ACS Catal.* **2013**, *3*, 1411–1419.

70. Beauchemin, S.; Hesterberg, D.; Beauchemin, M. Principle Component Analysis

Approach for Modeling Sulfur K-XANES Spectra of Humic Acids. *Soil Sci. Soc. Am. J.* **2002**, *66*, 83–91.

71. Beauchemin, S.; Hesterberg, D.; Chou, J.; Beauchemin, M. Sinnard, R. R.; Sayers, D. E. Speciation of Phosphorus in Phosphorus-Enriched Agricultrural Soils Using X-ray Near-Edge Structure Spectroscopy and Chemical Fractionation. *J. Environ. Qual.* **2003**, *32*, 1809–1819.

72. Bobyr, E.; Lassila, J. K.; Wiersma-Koch, H. I.; Fenn, T. D.; Lee, J. J.; Nikolic-Hughes, I.; Hodgson, K. O. Rees, D. C.; Hedman, B.; Herschlag, D. High-Resolution Analysis of Zn^{2+} Coordination in the Alkaline Phosphatase Superfamily by EXAFS and X-ray Crystallography. *J. Mol. Biol.* **2012**, *415*, 102–117.

73. Shivhare, A.; Chevrier, D. M.; Purves, R. W.; Scott, R. W. J. Following the Thermal Activation of $Au_{25}(SR)_{18}$ Clusters for Catalysis by X-ray Absorption Spectroscopy. *J. Phys. Chem. C* **2013**, *117*, 20007–20016.

74. Jentys, A. Estimation of Mean Size and Shape of Small Metal Particles by EXAFS. *Phys. Chem. Chem. Phys.* **1999**, *1*, 4059–4063.

75. Benfield, R. E. Mean Coordination Numbers and the Nonmetal-Metal Transition in Clusters. *J. Chem. Soc., Faraday Trans.***1992**, *88*, 1107–1110.

76. Bañares, M. A. Operando Methodology: Combination of *in Situ* Spectroscopy and Simultaneous Activity Measurements under Catalytic Reaction Conditions. *Catal. Today*. **2005**, *100*, 71–77.

77. Somorjai, G. A. Modern Surface Science and Surface Technologies: An Introduction. *Chem. Rev*. **1996**, *96*, 1223–1236.

78. Guerreno-Pérez, M. O.; Bañares, M. A. From Conventional *in Situ* to Operando Studies in Raman Spectroscopy. *Catal. Today*. **2006**, *113*, 48–57.

79. Lercher, J. A.; Veefkind, V.; Vajerwerg, K. *In Situ* IR Spectroscopy for Developing Catalysts and Catalytic Processes. *Vib. Spectrosc*. **1999**, *19*, 107–121.

80. Haw, J. F.; Goguen, P. W.; Xu, T.; Skloss, T. W.; Song, W. G.; Wang, Z. K. *In Situ* NMR Investigations of Heterogeneous Catalysis with Samples Prepared under Standard Reaction Conditions. *Angew. Chem. Int. Ed*. **1998**, *37*, 948–949.

81. Weckhuysen, B. M.; Verberckmoes, A. A.; Debaere, J.; Ooms, K.; Langhans, I.; I.Schoonheydt, R. A. *In Situ* UV-Vis Diffuse Reflectance Spectroscopy-on Line Activity Measurements of Supported Chromium Oxide Catalysts: Relating Isobutane Dehydrogenation Activity with Cr-Spreciation via Experimental Design. *J. Mol. Catal. A: Chem*. **2000,** *151*, 115–131.

82. Niemantsverdriet, J. W.; Delgass, W. N. *In Situ* Mössbauer Spectroscopy in Catalysis. *Top. Catal*. **1999**, *8*,133–140.

83. Anderson, R. M.; Zhang, L.; Loussaert, J. A.; Frenkel, A.; Henkelman, G.; Crooks, R. M. An Experimental and Theoretical Investigation of the Inversion of Pd@Pt Core@Shell Dendrimer-Encapsulated Nanoparticles. *ACS Nano* **2013**, *7*,9345–9353.

84. Brown, M. A.; Jordan, I.; Redondo, A. B.; Kleibert, A.; Wörner, H. J.; van Bokhoven, J. A. *In Situ* Photoelectron Spectroscopy at the Liquid/Nanoparticle Interface. *Surf. Sci*. **2013**, *610*, 1–6.

85. Brückner, A. *In Situ* Electron Paramagnetic Resonance: A Unique Tool for Analyzing Structure-Reactivity Relationships in Heterogeneous Catalysis. *Chem. Soc. Rev*. **2010**, *39*, 4673–4684.

86. Krishna, K. S.; Navin, C. V.; Biswas, S.; Singh, V.; Ham, K.; Bovenkamp, G. L.; Theegala, C. S.; Miller, J. T.; Spivey, J. J.; Kumar, C. S. S. R. Millifluidics for Time-Resolved Mapping of the Growth of Gold Nanostructures. *J. Am. Chem. Soc*. **2013**, *135*, 5450–5456.

87. Ellis, P. J.; Fairlamb, I. J. S.; Hackett, S. F. J.; Wilson, K.; Lee, A. F. Evidence for the Surface-Catalyzed Suzuki-Miyaura Reaction over Palladium Nanoparticles: An Operando XAS Study. *Angew. Chem. Int. Ed*. **2010**, *49*, 1820–1824.

88. Yao, T.; Liu, S.; Sun, Z.; Li, Y.; He, S.; Cheng, H.; Xie, Y.; Liu, Q.; Jiang, Y.; *et al*. Probing Nucleation Pathways for Morphological Manipulation of Platinum Nanocrystals. *J. Am. Chem. Soc*. **2012**, *134*, 9410–9416.

89. Liu, L.; Burnyeat, C. A.; Lepsenyi, R. S.; Nwabuko, I. O.; Kelly, T. L. Mechanism of Shape Evolution in Ag Nanoprisms Stabilized by Thiol-Terminated Poly(ethylene glycol): An *in Situ* Kinetic Study. *Chem. Mater*. **2013**, *25*, 4206–4214.

90. Shivhare, A.; Lee, K. E.; Hu, Y.; Scott, R. W. Following the Reactivity of $Au_{25}(SC_8R_9)_{18}^-$ Clusters with Pd^{2+} and Ag^+ Ions Using *in Situ* X-ray Absorption Spectroscopy: A Tale of Two Metals. *J. Phys. Chem. C* **2015**, *119*, 23279–23284.

91. Testemale, D.; Argoud, R.; Geaymond, O.; Hazemann, J. High Pressure/High Temperature Cell for X-ray Absorption and Scattering Techniques. *Rev. Sci. Instrum*. **2005**, *76*, 043905.

92. Pokrovski, G. S.; Roux, J.; Hazemann, J.; Testemale, D. An X-ay Absorption Spectroscopy Study of Argutite Solubility and Aqueous Ge(IV) Speciation in Hydrothermal Fluids to 500 °C and 400 bar. *Chem. Geol*. **2005**, *217*, 127–145.

93. Karim, A. M.; Howard, C.; Roberts, B.; Kovarik, L.; Zhang, L.; King, D. L.; Wang, Y. *In Situ* X-ray Absorption Fine Structure Studies on the Effect of pH on Pt Electronic Density during Aqueous Phase Reforming of Glycerol. *ACS Catal.* **2012**, *2*, 2387–2394.

94. Tupy, S. A.; Karim, A. M.; Bagia, C.; Deng, W.; Huang, Y.; Vlachos, D. G.; Chen, J. G. Correlating Ethylene Glycol Reforming Activity with *in Situ* EXAFS Detection of Ni Segregation in Supported NiPt Bimetallic Catalysts. *ACS Catal.* **2012**, *2*, 2290–2296.

95. Nelson, R. C.; Miller, J. T. An Introduction to X-ray Absorption Spectroscopy and Its *in Situ* Application to Organometallic Compounds and Homogeneous Catalysts. *Catal. Sci.*

Technol. **2012**, *2*, 461–470.

96. El Omar, A. K.; Schmidhammer, U.; Jeunesse, P.; Larbre, J.-P.; Lin, M.; Muroya, Y.; Katsumura, Y.; Pernot, P.; Mostafavi, M. Time-Dependent Radiolytic Yield of OH• Radical Studied by Picosecond Pulse Radiolysis. *J. Phys. Chem. A*. **2011**, *115*, 12212–12216.

97. Garrett, B. C.; Dixon, D. A.; Camaioni, D. M.; Chipman, D. M.; Johnson, M. A.; Jonah, C. D.; Kimmel, G. A.; Miller, J. H.; Rescigno, T. N. *et al*. Role of Water in Electron-Initiated Processes and Radical Chemistry: Issues and Scientific Advances. *Chem. Rev*. **2005**, *105*, 355–390.

98. George, G. N.; Pickering, I. J.; Pushie, M. J.; Nienaber, K.; Hackett, M. J.; Ascone, I.; Hedman, B.; Hodgson, K. O.; Aitken, J. B. *et al*. X-ray-Induced Photo-Chemistry and X-ray Absorption Spectroscopy of Biological Samples. *J. Synchrotron. Rad*. **2012**, *19*, 875–886.

99. Müller, O.; Nachtegaal, M.; Just, J.; Lützenkirchen-Hecht, D.; Frahm, R. Quick-EXAFS Setup at the SuperXAS Beamline for *in Situ* X-ray Absorption Spectroscopy with 10 ms time resolution. *J. Synchrotron. Rad*. **2016**, *23*, 260–266.

100. Glavee, G. N.; Klabunde, K. J.; Sorensen, C. M.; Hadjipanayis, G. C. Chemistry of Borohydride Reduction of Iron(II) and Iron(III) Ions in Aqueous and Nonaqueous Media. Formation of Nanoscale Fe, FeB, and Fe_2B Powders. *Inorg Chem*. **1995**, *34*, 28–35.

101. Zhang, W. Nanoscale Iron Particles for Environmental Remediation: An Overview. *J. Nanopart. Res*. **2003**, *5*, 323–332.

102. Wang, C. B.; Zhang, W. X. Synthesizing Nanoscale Iron Particles for Rapid and Complete Dechlorination of TCE and PCBs. *Environ. Sci. Technol. Lett.* **1997**, *31*, 2154–2156.

103. Liu, Y.; Choi, H.; Dionysiou, D.; Lowry, G. V. Trichloroethene Hydrodechlorination in Water by Highly Disordered Monometallic Nanoiron. *Chem. Mater.* **2005**, *17*, 5315–5322.

104. Kovács, S.; Zih-Perényi, K.; Révész, Á.; Novák, Z. Copper on Iron: Catalyst and Scavenger for Azide-Alkyne Cycloaddition. *Synthesis* **2012**, *44*, 3722–3730.

105. Zhang, Y.; Diao, W.; Monnier, J. R.; Williams, C. T. Pd-Ag/SiO_2 Bimetallic Catalysts Prepared by Galvanic Displacement for Selective Hydrogenation of Acetylene in Excess Ethylene. *Catal. Sci. Technol*. **2015**, *5*, 4123–4132.

106. Sajiki, H.; Ikaea, T.; Hirota, K. Cleavage of the THP Protecting Group under Pd/C-Catalyzed Hydrogenation Conditions. *Tetrahedron Lett*. **2001**, *42*, 7699–7701.

107. Shen. J.; Semagina, N. Iridium- and Platinum-Free Ring Opening of Indan. *ACS Catal*. **2014**, *4*, 268-279.

108. Yang, S.; Cao, C.; Sun, Y.; Huang, P.; Wei, F.; Song, W. Nanoscale Magnetic Stirring Bars for Heterogeneous Catalysis in Microscopic Systems. *Angew. Chem. Int. Ed*. **2015**, *54*, 2661-2664.

109. He, T.; Liu, L.; Wu, G.; Chen, P. Covalent Triazine Framework-Supported Palladium Nanoparticles for Catalytic Hydrogenation of N-Heterocycles. *J. Mater. Chem. A* **2015**, *3*, 16235-16241.

110. Shevchenko, E. V.; Bodnarchuk, M. O.; Kovalenko, M. V.; Talapin, D. V.; Smith, R. K.; Aloni, S.; Heiss, W.; Alivisatos, A. P. Gold/Iron Oxide Core/Hollow-Shell Nanoparticles. *Adv. Mater*. **2008**, *20*, 4323–4329.

CHAPTER 2

2. *In Situ* X-ray Absorption Spectroscopic Study of the Oxidation of Fe@Fe_xO_y Nanoparticles

This work has been published in *The Journal of Physical Chemistry C*. I have been able to control the sizes of Fe@Fe_xO_y nanoparticles through using different volume ratios of methanol to water solutions and poly(vinylpyrrolidone) stabilizers. Fe K-edge and L-edge X-ray absorption near-edge structure (XANES) spectra have been used to study the composition of Fe@Fe_xO_y nanoparticles. *In situ* Fe K-edge XANES measurements were used to monitor the kinetics of the oxidation processes of Fe@Fe_xO_y nanoparticles in solutions.

This work has been published in *The Journal of Physical Chemistry C*., **2014**, *118*, 22317-22324. Tate Johnson is thanked for assistance with preliminary studies, John Hayes for his assistance with the acquisition of XRD spectra, and Jian Wang for providing the Fe L-edge standards. I also thank Tom Regier, Jay Dynes, and Derek Peak for their invaluable advice and assistance with *in situ* liquid measurements at the Fe L-edges on the SGM beamline. All the experimental work in this paper has been done by myself along with the writing of the first draft of the manuscript. The final manuscript was submitted for publication after revisions by Dr. Yongfeng Hu and Dr. Robert W. J. Scott.

2.1 Abstract

Fe nanoparticles and Fe oxide nanoparticles are among the most commonly studied nanomaterials because of their applications in fields ranging from catalysis to ferrofluids. However, many synthetic methods give Fe nanoparticles with large size distributions, and it is difficult to follow the kinetics of Fe nanoparticle oxidation reactions and the relative speciation of Fe oxidation states in real time. Herein, we introduce a simple approach of controlling the sizes of Fe@Fe_xO_y nanoparticles and a novel method for following Fe@Fe_xO_y nanoparticle oxidation *in situ* in liquid solutions by Fe K- and L-edge X-ray absorption near-edge structure (XANES) spectroscopy. XANES results show that these Fe@Fe_xO_y nanoparticles have similar XANES spectra before exposure to air. *In situ* XANES measurements allow for quantitative oxidation kinetics of different nanoparticle sizes to be followed; results show that the rate of Fe(0) oxidation increases with a decrease in average nanoparticle size. However, the rate of Fe core size depletion was found to be *ca*. 0.022 nm/min for all the nanoparticle systems studied. This suggests similar oxidation mechanisms are at work for all the particle sizes studied, and the differences in Fe(0) oxidation rates is primarily a surface area effect. This work shows that *in situ* liquid cell XANES can be used to follow oxidation state and coordination environment changes in Fe nanoparticle dispersions.

2.2 Introduction

Nanoparticles (NPs) with sizes of less than 100 nm have attracted extensive interest in various fields because their nanoscale features can dramatically change the properties of the materials compared to their bulk counterparts.[1,2] Fe NPs and Fe oxide NPs are among the most commonly studied nanomaterials, and have a myriad of applications in fields ranging from catalysis to ferrofluids.[3-8] In particular, Fe oxide NP systems have recently attracted much interest as catalysts for selective hydrogenation and/or enantioselective hydrogenation reactions.[9,10] Compared with many nanomaterials that are derived from precious metals, Fe is one of the most abundant metals on earth, and consequently one of the least expensive metals.[11] In addition, Fe is relatively non-toxic compared with many other transition metals, and Fe or Fe oxide NPs may be magnetically recovered in catalytic applications.[12] However, due to the

ease of oxidation of Fe NPs, exposure to air typically leads to either complete oxidation to Fe_xO_y NPs, or partial oxidation of the surface to form Fe@Fe_xO_y (core@shell) NPs.[13,14] As such, this system allows for the examination of the mechanism of Fe oxidation (*i.e.* rusting) at nanoscale levels, and has been used to develop hollow Fe_xO_y NPs under certain conditions due to the Kirkendell diffusion effect.[5,15] Typically products of such oxidation reactions are characterized via *ex situ* X-ray diffraction (XRD), transmission electron microscopy (TEM), X-ray photoelectron spectroscopy (XPS), and X-ray absorption spectroscopy (XAS) measurements.[16-18] Herein, we show a novel method of following Fe NP oxidation *in situ* by XAS in liquid solution cells; this allows for one to follow in real time the kinetics of Fe NP oxidation reactions as a function of starting NP size and the speciation of Fe oxidation states.

Over the last twenty years, various methods have been developed to synthesize Fe NPs, such as thermal decomposition,[19-21] sonochemical synthesis,[22-24] reduction of Fe salts and oxides,[25-27] and many other methods.[28-30] Klabunde *et al*. reported a simple way to prepare Fe NPs via reduction of ferric (Fe^{3+}) or ferrous (Fe^{2+}) ions with sodium borohydride in aqueous solutions.[31] Small amounts of oxygen or even oxygen-free water in the synthesis can oxidize zero-valent Fe NPs to give rise to Fe@Fe_xO_y NPs, in which the oxide shell can protect the zero-valent Fe core against excessive rapid oxidation.[32] Many groups have used this simple method to synthesize Fe@Fe_xO_y NPs for environmental remediation or catalytic studies.[33-35] For example, Zhang's group showed that Fe@Fe_xO_y NPs can be used for the transformation of halogenated organic contaminants and heavy metals.[36,37] The Moores' group reported that Fe@Fe_xO_y NPs are active for the hydrogenation of olefins and alkynes under mild conditions.[17] Several groups have shown that Fe@Fe_xO_y NPs can also be precursors to seed, reduce and support another metal to form core-shell bimetallic NPs to catalyze Suzuki-Miyaura cross-coupling reactions (Fe@Fe_xO_y/Pd)[18] or azide-alkyne click reaction (Fe@Fe_xO_y/Cu).[38] However, many of these syntheses give NPs with large size distribution and it is unclear whether the underlying Fe cores are accessible via cracks in the oxide shells or whether Fe speciation changes during hydrogenation and/or galvanic reactions. In addition, Fe speciation information is often obtained by XRD and/or XPS as *ex situ* experiments upon drying the solid materials;[17,18,25,38] XRD only gives information of crystalline components, while XPS

measurements are typically done under ultra-high vacuum conditions, which may change the nature of the materials.

XAS is a powerful tool to probe the composition and structure of a material with short-range order.[39,40] Several groups have carried out *ex situ* studies of the composition and oxidation of Fe@Fe_xO_y NPs. Sun *et al*. and Lin *et al*. reported the transmission mode Fe K-edge X-ray absorption near-edge structure (XANES) spectra and extended X-ray absorption fine structure (EXAFS) of Fe@Fe_xO_y NPs, respectively.[16,41] Signorini *et al*. studied the oxidation of Fe@Fe_xO_y NPs by XAS transmission spectra of Fe and O K-edge.[15] With recent advances in XAS and XPS technology, it has now become possible to analyze materials under *in situ* conditions.[42-45] For example, Anderson *et al*. showed that structural inversion took place for Pd@Pt (core@shell) dendrimer-encapsulated NPs via an *in situ* EXAFS study.[46] Wang *et al*. found that a Rh_1/Co_3O_4 catalyst restructured at reaction temperatures of 220 °C using a Nashner-Adler *in situ* cell which can heat a sample up to 600 °C.[47,48] Wu *et al*. studied the surface composition in bimetallic nanoparticles in a specialized *in situ* grazing-incidence cell.[49,50] There are also some excellent examples of XPS used for *in situ* studies of aqueous samples of nanoparticles by using a liquid microjet.[51,52] Recently, our group studied the mechanisms of AuPd NP-catalyzed oxidation of crotyl alcohol in water by *in situ* XAS using a liquid cell with an X-ray permeable window.[53] In this work, we used similar liquid cells and experimental layout of the synchrotron beamline endstation reported by Liu *et al*.[54] to collect XANES spectra of Fe NPs at the Fe K-edge both before and after exposure to air. Fe L_{II}- and L_{III}-edge *in situ* XANES studies were also carried out using a liquid cell with a 100 nm silicon nitride window within an ultra-high vacuum chamber on the SGM beamline at the Canadian Light Source (CLS).[55]

In this study, we introduce a simple approach to control the sizes of Fe@Fe_xO_y NPs synthesized by the reduction of ferrous (Fe^{2+}) ions with sodium borohydride through using different volume ratios of methanol to water mixture solvents and poly(vinylpyrrolidone) (PVP) stabilizer. XANES has been used to study the composition of as-synthesized Fe@Fe_xO_y NPs and monitor the kinetics of the oxidation processes of Fe@Fe_xO_y NPs with different sizes in solution. Results show that Fe@Fe_xO_y NPs synthesized in different volume ratios of

methanol to water have similar XANES spectra before exposure to air. In addition, results show that the oxidation kinetics of different NP batches can be followed. In all cases, the presence of Fe(0) in the cores can be determined by XANES spectroscopy. TEM images and XRD spectra of oxidized Fe NPs have also been obtained to complement XAS results.

2.3 Experimental Section

2.3.1 Materials

All chemicals were used as received. Fe(II) sulfate heptahydrate was purchased from Sigma-Aldrich. Poly(vinylpyrrolidone) (M. W. 58,000 g/mol) was purchased from Alfa Aesar. Sodium borohydride and methanol (HPLC grade) were purchased from Fisher Scientific. Eighteen MΩ·cm Milli-Q water (Millipore, Bedford, MA) was used for all syntheses.

2.3.2 Synthesis

Fe NPs were produced by the reduction of $FeSO_4 \cdot 7H_2O$ (5.0 mmol) in methanol or water/methanol mixtures (100 mL) using $NaBH_4$ (35 mmol) under nitrogen gas.[31,37] PVP stabilizer and different volume ratios of methanol to water were used to control the sizes of the resulting Fe NPs. First, the PVP (50 mL in methanol) solution was added to an $FeSO_4 \cdot 7H_2O$ solution and the mixture was stirred for 10 min. Then a solution of $NaBH_4$ (10 mL in water) was added dropwise. Solid $NaBH_4$ was added when methanol was the only solvent ($NaBH_4$ can react with methanol vigorously). The molar ratios of PVP (molar mass of monomer unit, 111.1 g/mol) to $FeSO_4 \cdot 7H_2O$ were varied from 4:1 to 32:1 with little change in particle size; 4:1 ratios were used in all XANES experiments. The volume ratios of methanol to water used were 9:1, 4:1 and 1:1. 6 mL of 1 M H_2SO_4 was added to the 100 mL of 50 mM as-synthesized $Fe@F_xO_y$ NPs before oxidation reactions to remove any excess $NaBH_4$. The solution was exposed to air and stirred by a stir bar (1 inch × 3/8 inch) at 800 rpm under room temperature (25 ± 2 °C), and 1.0 mL of the solution was delivered into a liquid cell for XANES measurements.

2.3.3 Characterization

TEM analyses of the NPs were conducted using a Philips CM10 microscope operating at 100 kV. The samples were prepared by drop-casting a small amount of dilute, aqueous sample onto a carbon-coated copper TEM grid (Electron Microscopy Sciences, Hatfield, PA). Average particle diameters were determined by manually measuring more than 100 NPs from each sample using the ImageJ program.[56]

Fe K-edge XANES spectra were measured using the Soft X-ray Microcharacterization Beamline (SXRMB) 06B1-1 (energy range 1700 - 10000 eV; resolution, 3.3×10^{-4} to 1×10^{-4} $\Delta E/E$ with InSb(111) and Si(111) crystals) at the CLS. The measurements were conducted under ambient atmosphere. Lowering the beam flux by defocusing and/or filtering the beam with Kapton filters and stirring the sample via magnetic stirring were used to avoid photoreduction. The liquid cells used for XANES analysis were SPEX CertiPrep Disposable XRF X-Cell sample cups with 4 μm Ultralene window films (purchased from Fisher Scientific, Ottawa, ON). The software Athena was used for data processing.[57,58] X-ray energies were calibrated by reference to the absorption of a Fe standard metal foil assuming a lowest energy inflection point of 7112 eV. The background in each post edge was fit to a cubic spline function while the pre-edge region was fit with a straight line.[53] Fe foil transmission spectrum and fluorescence spectra of $FeSO_4 \cdot 7H_2O$ and $Fe(NO_3)_3 \cdot 9H_2O$ aqueous solutions (50 mM) were measured under the same conditions and used as standards for linear combination analysis XANES fitting in the range of 7100 to 7180 eV. The R-factors on the mismatch between data and fit are all lower than 0.001.

The spherical grating monochromator (SGM) beamline at the CLS was used to collect XANES spectra at the Fe L_2- and L_3-edge from 700 eV to 740 eV in 0.1 eV steps. Fluorescence spectra were measured using multi-element silicon drift detectors. A liquid cell with a 100 nm thick Si_3N_4 membrane was used along with a peristaltic pump to continuously flow the target solution through the interaction region. Data analysis was performed in IGOR Pro 6.2. The transmission spectra of Fe foil, $FeLiPO_4$ and $FePO_4$ were used as standards to calibrate the energies of the samples.

X-ray diffraction analysis was conducted with a Rigaku Rotaflex RU-200 rotating anode X-ray diffractometer using a Cu Kα (λ = 1.5406 Å) X-ray source. Samples were placed in a glass holder and scanned from 20° to 80° with scanning rate at 3.0°/min.

2.4 Results and Discussion

Fe@Fe_xO_y NPs were prepared by reducing $FeSO_4 \cdot 7H_2O$ in the absence and presence of PVP with $NaBH_4$ at room temperature (23 ± 2 °C) using different volume ratios of methanol to water as solvents, following previous literature protocols.[31,37] We note that although Fe@Fe_xO_y is used here for the notation of the oxidized core@shell NPs, the surface of these particles is likely to be hydrated to form Fe hydroxides. TEM images were taken of the particles after exposure to air for 30 minutes. No attempt was made to clean the NP samples as it was desirable to have TEM information that would be comparable to *in situ* X-ray absorption data shown below. As shown in TEM images (Figure 2.1 and Table 2.1), the Fe@Fe_xO_y NPs stabilized by PVP are mostly spherical in shape and particles have a Fe core (dark) and Fe oxide shell (light), and exist as chain-like aggregates. Aggregation may be due to the magnetic properties of the particles or could be a drying artifact.[59,60] When different volume ratios of methanol to water as solvents were used to synthesize Fe@Fe_xO_y NPs, smaller particles were observed for higher volume fractions of methanol. Fe@Fe_xO_y NPs synthesized using methanol as the solvent have very small sizes (2.3 ± 0.6 nm), as shown in Figure 2.1 D, while those synthesized in 9:1, 4:1 and 1:1 methanol/water mixtures are 7.7 ± 1.2 nm, 11.8 ± 2.1 nm, and 16.6 ± 4.9 nm, respectively (Figures 2.1 A-2.1 C). Similar oxide shell thicknesses of 1.4-1.5 nm where seen for each of the particles (with the exception of the small particles synthesized in methanol). PVP can provide steric stabilization for metal NPs through the steric bulk of its framework and bind weakly to the metal NPs surface via functional groups,[61] this likely decreases the growth rate of the originally-synthesized Fe NPs. In order to optimally disperse Fe@Fe_xO_y NPs, a 32× excess of PVP (over Fe(II)) were used in the synthesis; TEM results show that there are no obvious differences when PVP amounts were increased from 4× to 32× the moles of Fe(II). In the absence of PVP stabilizer, the average sizes of Fe@Fe_xO_y NPs also decrease with an increase in the volume fraction of methanol in the solvent mixture; however much larger particle sizes are seen and there is little control of polydispersity of the samples.

The changes of the sizes of NPs according to different ratios of methanol to water may be due to the changes of the dielectric property of the mixed methanol-water solvent.[62]

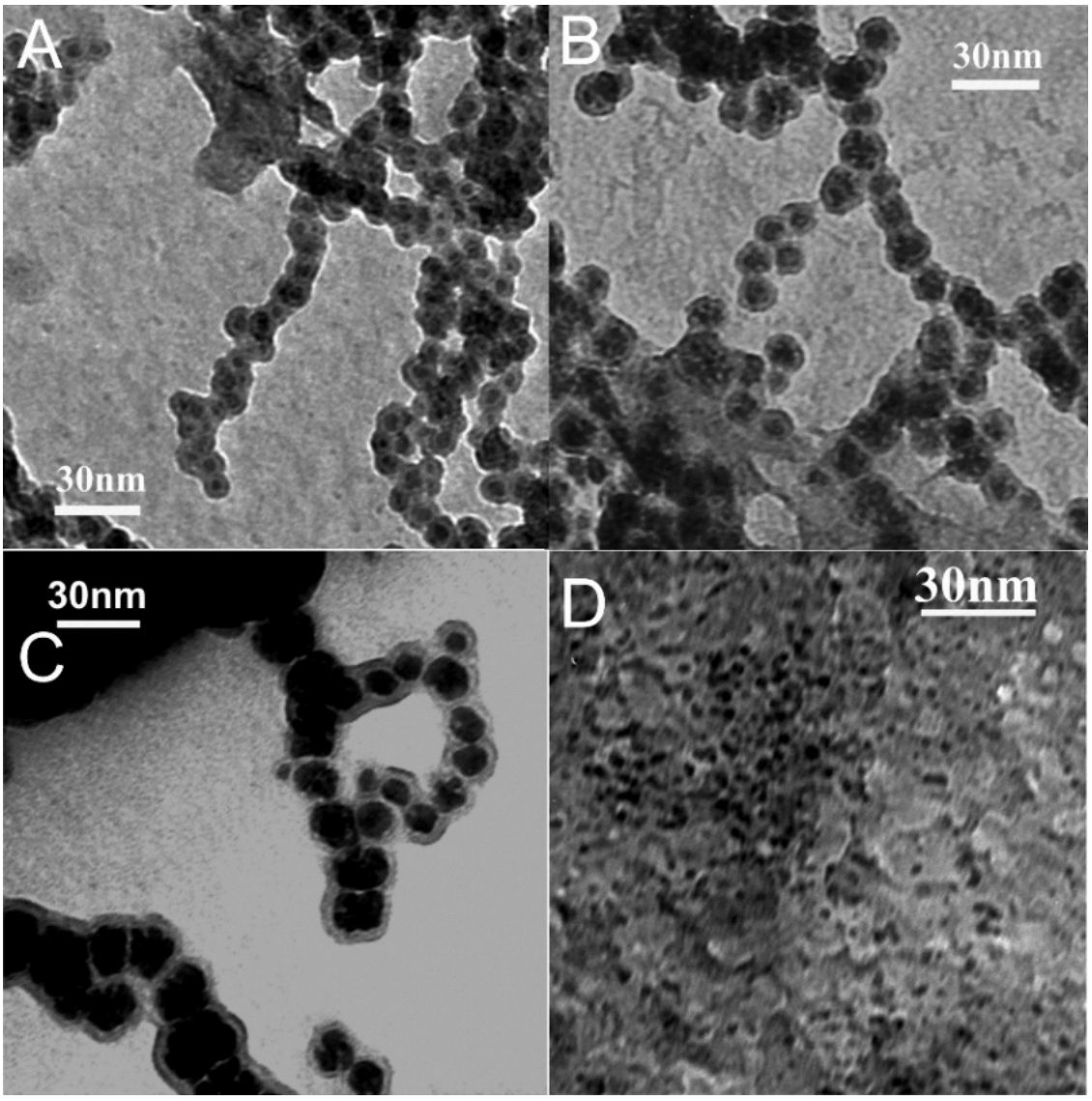

Figure 2.1. TEM images of $Fe@Fe_xO_y$ NPs synthesized in different volume ratios of methanol to water (A) 9:1 methanol/water (v/v) with PVP; (B) 4:1 methanol/water (v/v) with PVP; (C) 1:1 methanol/water (v/v) with PVP; (D) only methanol solvent with PVP.

Table 2.1. Summary of NP Sizes Determined by TEM.

System	NP Diameter	Shell Thickness
Methanol with PVP	2.3 ± 0.6 nm	−
Methanol/water (v/v) 9:1 with PVP	7.7 ± 1.2 nm	1.4 ± 0.4 nm
Methanol/water (v/v) 4:1 with PVP	11.8 ± 2.1 nm	1.5 ± 0.4 nm
Methanol/water (v/v) 1:1 with PVP	16.6 ± 4.9 nm	1.4 ± 0.4 nm

Solution Fe K-edge XANES measurements were conducted to study the oxidation kinetics of Fe@Fe_xO_y NPs, using an *in situ* liquid cell setup identical to the one documented in a previous publication by Kelly and coworkers.[54] Samples were kept under an inert nitrogen atmosphere. As shown in Figure 2.2 A, XANES spectra of as-synthesized Fe@Fe_xO_y NPs synthesized in different volume ratios of methanol to water (v/v 9:1, 4:1 and 1:1) mixtures with the same amounts of PVP are very similar, while the sample synthesized in pure methanol is significantly different. Linear combination fitting was used with $Fe(NO_3)_3$, $FeSO_4$, and zero-valent Fe foil standards (Figure 2.2 B), to measure relative fraction of Fe(III), Fe(II) and Fe(0) in the NPs at different times. The results indicate that there is approximately 80% Fe(0) and 20% Fe(II)/Fe(III) in the NP samples as-synthesized in different volume ratios of methanol to water (v/v 9:1, 4:1 and 1:1) mixtures under nitrogen; while the NPs synthesized in pure methanol has a much lower Fe(0) loading of 45% and correspondingly much higher Fe(II) loading. XANES spectra of as-synthesized Fe@Fe_xO_y NPs synthesized with different amounts of PVP in the same volume ratio of methanol to water mixture are also nearly identical. The results indicate that those Fe@Fe_xO_y NPs have similar surface compositions under inert conditions, which is most likely due to oxidation by water.[55] XANES spectra of Fe(II) and Fe(III) solutions only show very weak pre-edge features around 7113 eV, which are due to the dipole forbidden Fe 1s→3d transition. The relative high pre-edge peaks at 7112 eV in samples are due primarily to the existence of a Fe core in Fe@Fe_xO_y NPs (Figure 2.3). The smaller peak at 7112 eV in the spectrum of NPs synthesized in pure methanol than their counterparts synthesized in water/methanol mixtures indicates these NPs are initially more oxidized; this is likely due to the extremely small size of these NPs.

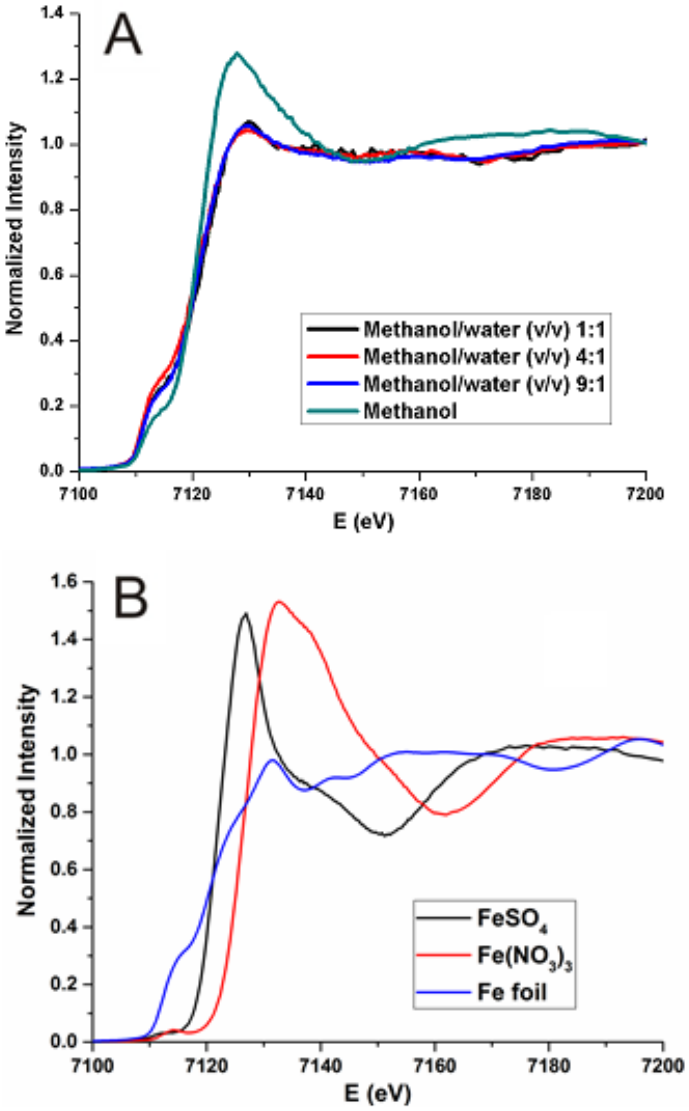

Figure 2.2. Fe K-edge XANES spectra of the (A) as-synthesized Fe@Fe_xO_y NPs and (B) standards.

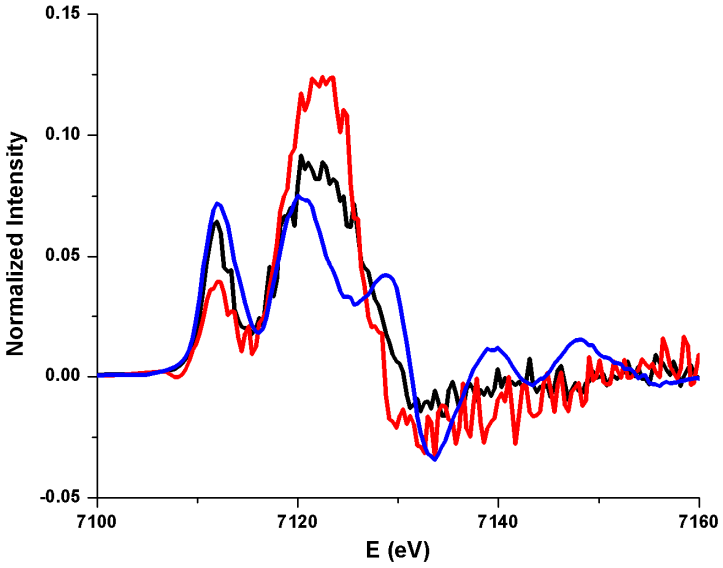

Figure 2.3. Fe K-edge first derivative XANES spectra of the as-synthesized Fe@Fe_xO_y NPs synthesized in methanol/water (v/v) 4:1 mixture (black), as-synthesized Fe@Fe_xO_y NPs synthesized in methanol (red) and Fe foil (blue).

The XANES region is often used to determine the formal oxidation state of the element, because the absorption edge energy increases correspondingly as the oxidations state of the absorption site increases.[43] Figure 2.4 shows the Fe K-edge XANES spectra collected over time upon exposure of the as-synthesized samples of Fe@Fe_xO_y NPs to air, leading to the further oxidation of the particles. As shown in Figure 2.4, upon an increase in the oxidation time, the absorption edge shifts to higher energy, which indicates the Fe@Fe_xO_y NPs are further oxidizing. The data shows that Fe@Fe_xO_y NPs with larger sizes (i.e those synthesized in 1:1 methanol:water mixtures) take longer times to reach a final state. For each sample, the end of oxidation was judged by obtaining two consecutive XANES spectra which were identical (Figure 2.5). The 1st derivative XANES spectra (Figure 2.6) show that the chemical composition of all the Fe@Fe_xO_y NPs reaches a similar final state upon complete ambient air oxidation of the NPs. Linear combination fitting of the XANES spectra in Figure 2.4 using the standards in Figure 2.2 B was attempted to quantify the relative fraction of all three species as a function of time (Table 2.2). Attempts were made to fit the data with a variety of solid Fe oxide standards instead of $Fe(NO_3)_3$ and $FeSO_4$ salts dissolved in water, however the fitting

results suffered when using Fe oxide standards. All fits showed consistent levels of starting Fe(0) in the particles which went down over time; thus results on subsequent fitting results are only mildly influenced by the standards chosen. We are uncertain as to why better fits are obtained with simple Fe salt standards, but it may be due to either the non-identification of more appropriate standards or possibly the existence of defective oxide shells on the surface of the particles, as was seen by Wang *et al*. by EELS measurements.[63] Finally, we should note that some of the Fe(II) and Fe(III) is also leached from the particle surface; the respective spectra are a sum average of both Fe oxide signals from the particle surface and Fe salts dissolved in solution.

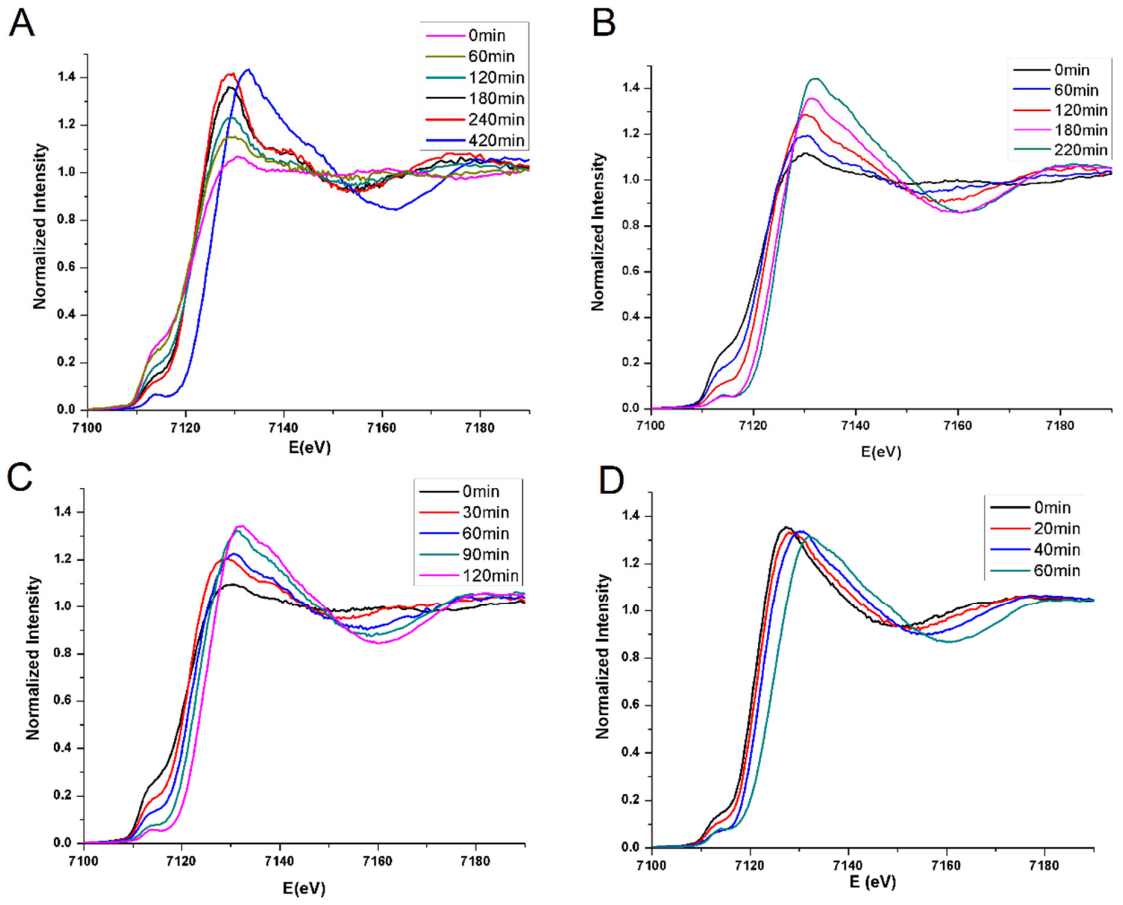

Figure 2.4. Fe K-edge XANES spectra of the oxidation process of Fe@Fe_xO_y NPs synthesized in different volume ratios of methanol to water (A) 1:1 methanol/water (v/v); (B) 4:1 methanol/water (v/v); (C) 9:1 methanol/water (v/v); (D) methanol.

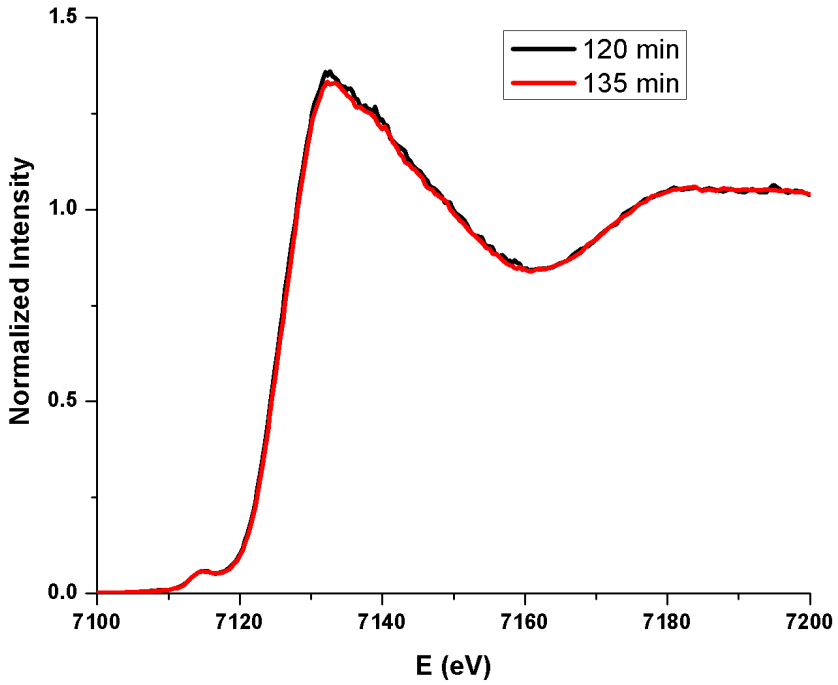

Figure 2.5. Fe K-edge XANES spectra of the Fe@Fe_xO_y NPs synthesized in methanol/water (v/v) 9:1 mixture at different oxidation time.

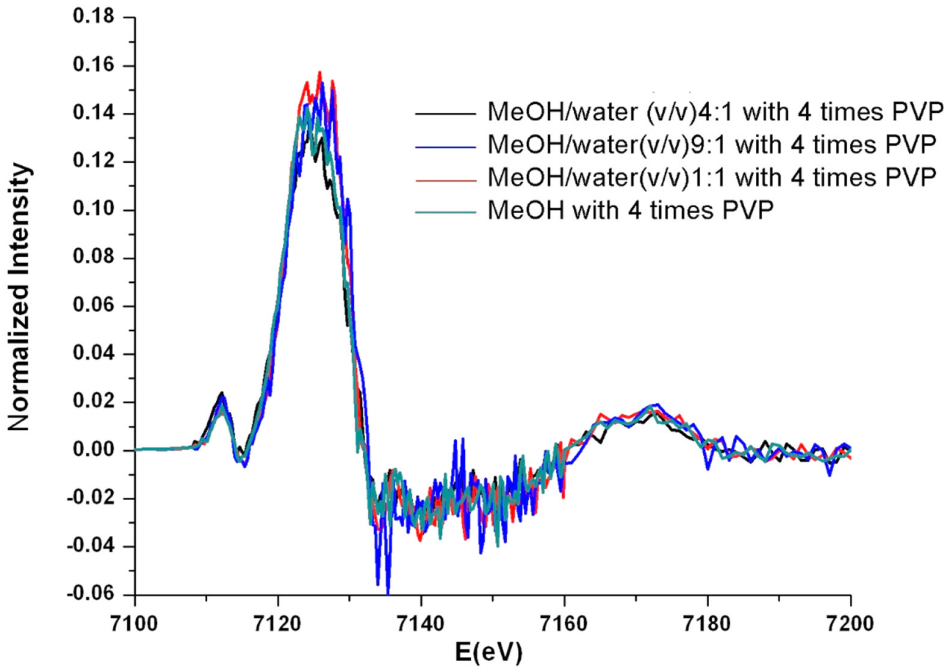

Figure 2.6. Fe K-edge first derivative XANES spectra of Fe@Fe_xO_y NPs after oxidation.

Table 2.2. XANES fitting results showing mole fractions of each Fe standard.

Sample	Oxidation time (min)	Fe(0)%	Fe(II)%	Fe(III)%
Fe@Fe_xO_y NPs synthesized in methanol/water (v/v) 1:1 mixture	0	78(2)	10(1)	12(2)
	60	67(2)	16(1)	18(2)
	120	53(2)	22(1)	25(3)
	180	41(3)	32(2)	26(3)
	240	38(4)	38(2)	24(4)
	420	19(2)	10(1)	71(2)
Fe@Fe_xO_y NPs synthesized in methanol/water (v/v) 4:1 mixture	0	78(2)	15(1)	7(2)
	60	58(2)	23(1)	19(2)
	120	40(2)	27(1)	33(2)
	180	21(1)	20(1)	59(2)
	220	21(2)	18(1)	61(2)
Fe@Fe_xO_y NPs synthesized in methanol/water (v/v) 9:1 mixture	0	78(2)	15(1)	7(2)
	30	54(2)	29(1)	17(2)
	60	45(2)	24(1)	32(2)
	90	28(2)	21(1)	51(2)
	120	18 (2)	16(1)	66(2)
Fe@Fe_xO_y NPs synthesized in methanol	0	45(2)	35(1)	21(2)
	20	28(2)	37(1)	35(2)
	40	24(2)	31(1)	45(2)
	60	27(1)	18(1)	56(2)

Figure 2.7 A shows plots of Fe(0) (in mmol) vs. time for each of the NP samples synthesized in methanol/water mixtures upon oxidation, along with best linear fits for each series. Fe@Fe_xO_y NPs synthesized in pure methanol have much smaller sizes compared with

the other three samples, and showed much further initial oxidation than the other samples (Figure 2.2 A); thus the kinetic oxidation data for this sample was not used in direct comparisons of the relative oxidation kinetics. Fe@Fe_xO_y NPs synthesized in methanol/water mixtures (v/v 9:1, 4:1 and 1:1) have similar initial Fe(0) contents, and their oxidation rates decrease with an increase in NP size. For the three NP samples synthesized in methanol/water mixtures, they have similar starting Fe(0) levels (*ca*. 0.039 mmol Fe(0)); which is about 78% of the initial Fe amount (0.050 mmol). This is most likely due to oxidation by water, but it is possible that trace oxygen has also contributed to surface oxidation. All systems showed linear, zeroth order, kinetics for the oxidation of Fe(0), however, the relative rate constants for oxidation increased from 7.0 x 10^{-5} mmol Fe(0)/min to 2.5 x 10^{-4} mmol Fe(0)/min as the particle size decreased from 16.6 ± 4.9 nm to 7.7 ± 1.2 nm. The standard model for metal oxidation is the Cabrera-Mott model, which predicts an exponential decay of the growth rate (dx/dt) for a two-dimensional Fe surface.[64,65] In order to better compare our results to the standard Cabrera-Mott model, TEM sizes of each of the particles (Table 2.1) were used to estimate the original average amount of Fe in individual particles using Equation 2.1:

$$n = 4\pi R^3/3V_g \quad \textbf{(2.1)}$$

Where V_g is the molar volume of Fe (7.09 cm^3/mol) and R is the radius of a spherical particle. Using the data in Table 2.2, the relative amount of Fe(0) was calculated at each time, and Equation 2.1 was used to calculate the radius of the new core, which was assumed to be spherical. Figure 2.7 B shows the final plot of the Fe(0) core size vs. time as well as linear best fits of the data. The 9:1 and 4:1 methanol/water systems (*ca*. 7.7 and 11.9 nm particles) show similar rates of core oxidation vs. time of *ca*. 0.022 nm/min, while the larger particles formed in 1:1 methanol/water systems had a slightly slower rate of 0.014 nm/min.

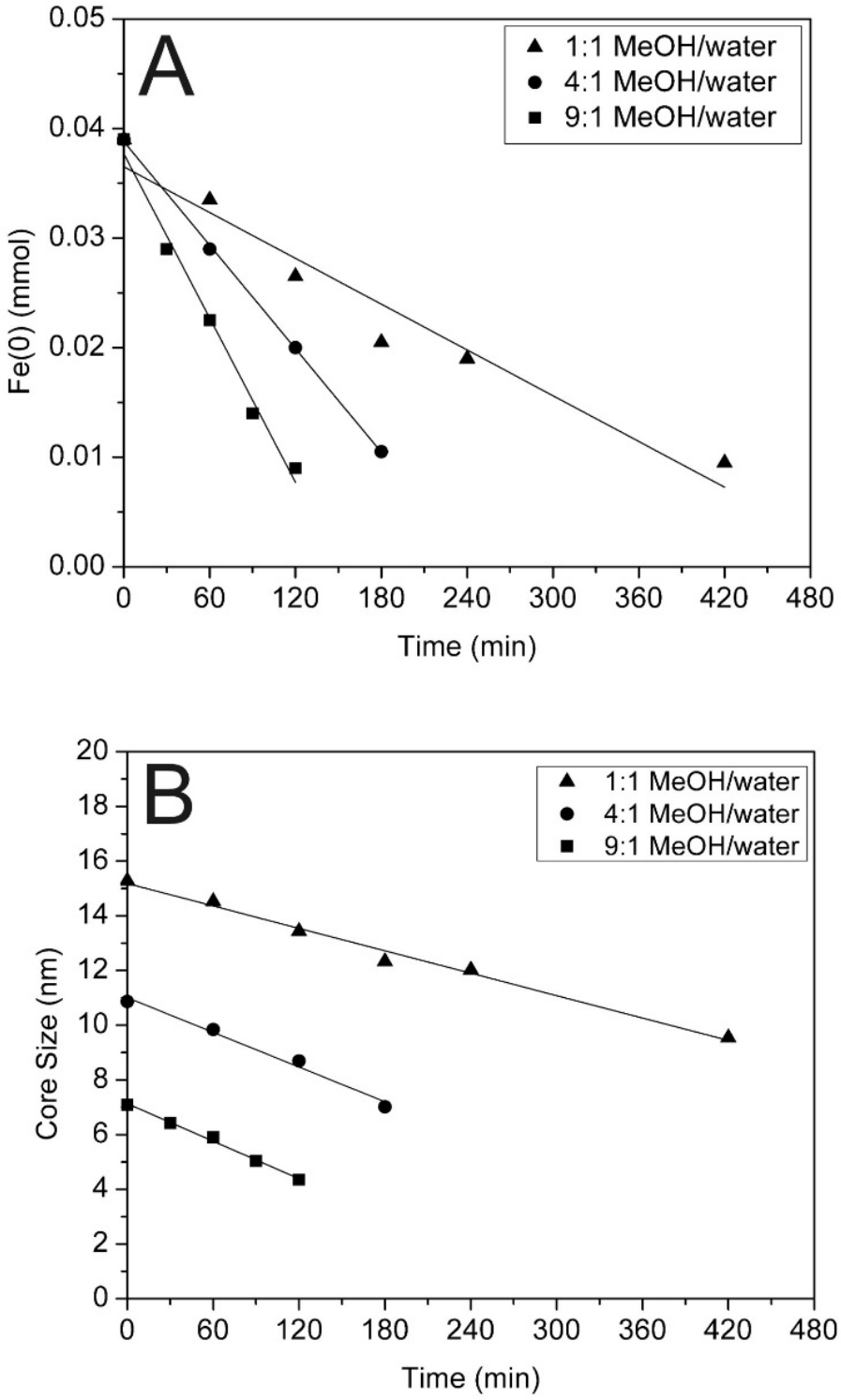

Figure 2.7. (A) Moles of Fe(0) versus oxidation time of Fe@Fe_xO_y NPs synthesized in different volume ratios of methanol to water; (B) Fe(0) NP core size as a function of time.

These numbers are in fair agreement with TEM results after 30 minutes which show similar oxide shell thicknesses for all three systems. Exponential decay of dx/dt as predicted by the Cabrera-Mott theory is not seen in our data set; however, we note that we are not able to follow the kinetics of the initial oxidation before exposure to air. Linderoth *et al*. noted that the Cabrera-Mott theory predicts oxide thickness of 2 nm on 2D Fe surfaces to take 40 s at 295K, while an oxide thickness of 3 nm would take 40 weeks.[66] A greater amount of oxidation is seen in our data, which is not unexpected as 3D NP systems in solution are quite different from 2D surfaces. First, nanoparticle oxidation occurs with a corresponding reduction in surface area which is not seen in 2D systems. In addition, the Kirkendall effect can lead to the formation of void spaces and significant strain can be created in these systems. Pratt *et al*. have shown thicker, anisotropic oxide layers for NP systems, and have attributed this to strain-enhanced ionic conduction.[67] The higher levels of oxidation seen here also suggest that leaching of Fe salts into solution may be contributing to the oxidation rate; this likely accounts for the larger decrease in Fe(0) core size for the largest particles synthesized in 1:1 methanol/water solutions (*i.e*. leaching is exacerbated in solutions with higher water content).

Fe L-edge XAS spectra involve the dipole-allowed Fe 2p→3d transitions, which are much more sensitive to Fe oxidation states than K edge data. Figure 2.8 A shows solution phase Fe L_2-edge and L_3-edge data for Fe@Fe_xO_y NPs synthesized in the 9:1 methanol:water mixture before and after exposure to air for 2 h, whereas Figure 2.8 B shows Fe(0), Fe(II) and Fe(III) standards ($FePO_4$ and $FeLiPO_4$). The Fe L_2-edge (718-725 eV) and L_3-edge (706-713 eV) regions are well resolved as a result of spin-orbit coupling. Additional splitting of L_2-edge and L_3-edge main peaks is due to the degeneracy of Fe d orbitals into e_g and t_{2g} affected by their coordination environment. For the as-synthesized Fe@Fe_xO_y NPs, the positions of the L_2 and L_3 peaks are similar to those of Fe(0) and Fe(II) standards suggesting that the NPs are mostly composed of Fe(0) and Fe(II) which are in agreement with the results from Fe K edge. The XANES spectrum of Fe@Fe_xO_y NPs after oxidation shifts to the higher energy compared with that of as-synthesized Fe@Fe_xO_y NPs, which is likely significant oxidation to Fe(III). This also complements the K edge data which showed copious oxidation of the Fe(0) cores. The L_3-edge spectrum of Fe@Fe_xO_y NPs after oxidation shows two well-resolved peaks at approximately

708.1 and 709.5 eV which is consistent with the L_3-edge spectra of octahedral-coordinated Fe(III) reported by Peak *et al*.[68] Fe L-edge XANES spectra of Fe@Fe_xO_y NPs synthesized in pure methanol before and after oxidation are similar as those of the NPs synthesized in the 9:1 methanol:water mixture. Fe L-edge XANES spectra of Fe@Fe_xO_y NPs synthesized in the 4:1 and 1:1 methanol:water mixtures could not be readily obtained, due to clogging of the sample cell with the larger Fe@Fe_xO_y particles.

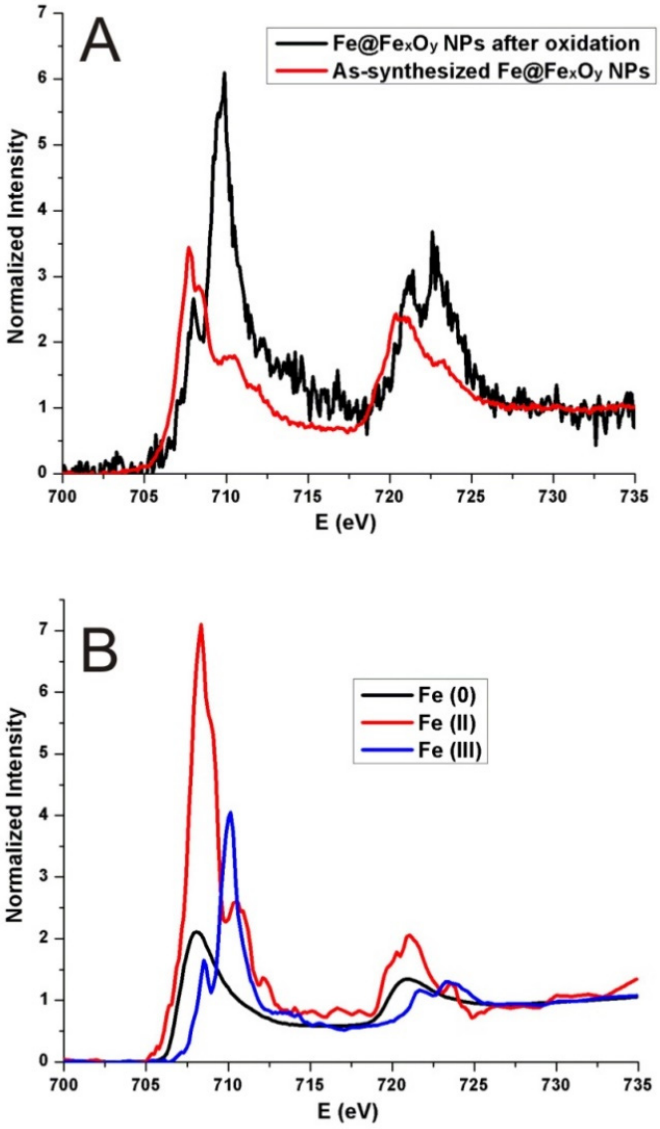

Figure 2.8. Fe L-edge XANES spectra of the (A) Fe@Fe_xO_y NPs synthesized in the 9:1 methanol:water mixture and (B) standards (Fe foil, $FePO_4$ and $FeLiPO_4$).

Powder XRD can complement XAS results by identifying long-range order. Figure 2.9 shows PXRD patterns of the as-synthesized (2.9 A) and oxidized Fe@Fe_xO_y NPs (2.9 B) synthesized in the 1:1 methanol:water mixture. The as-synthesized Fe@Fe_xO_y NPs have peaks at 2θ values of 44.6° and 35.4°, which reveals the existence of both crystalline α-Fe and iron oxide (FeO) which are in agreement with the results reported by others.[16,17] Peak positions of Fe@Fe_xO_y NPs after oxidation are similar to those of pure γ-FeOOH (Figure 2.9.C) which is consistent with the observations of Fe K- and L-edge XANES results. Analysis of the FWHM peaks of the γ-FeOOH PXRD data suggested the PXRD peaks showed both size and strain broadening. Strain in such systems is likely caused by growth of oxide layers on the underlying Fe core.

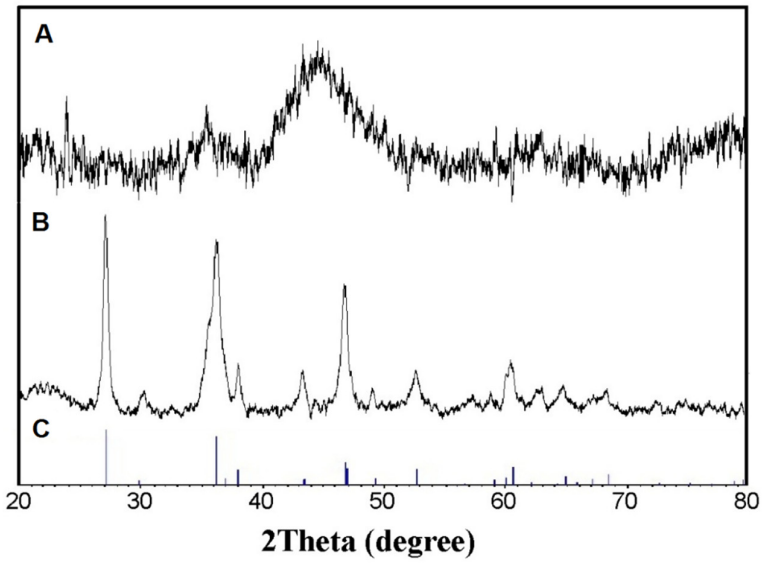

Figure 2.9. XRD patterns of the (A) resulting Fe@Fe_xO_y NPs synthesized in the 1:1 methanol:water mixture and (B) oxidized Fe@Fe_xO_y NPs synthesized in the 1:1 methanol:water mixture. (C) The intensities and positions of pure γ-FeOOH (lines at the bottom) were taken from the JCPDS database.

2.5 Conclusion

We have shown an approach to control the sizes of Fe@Fe_xO_y NPs through using different ratios of methanol to water mixture solvents, and have further shown control of the Fe@Fe_xO_y NP sizes and size distribution using PVP as a stabilizer. Fe K-edge and L-edge XANES spectra

in liquid cells were used to characterize Fe@Fe_xO_y NPs before and after oxidation, and we successfully monitored the oxidation process of Fe@Fe_xO_y NPs by Fe K-edge XANES spectra. XANES results show that these Fe@Fe_xO_y NPs have similar XANES spectra before exposure to air and the rate of oxidation of Fe@Fe_xO_y NPs is slower for larger Fe@Fe_xO_y NPs. However, this is primarily surface area effect; plots of Fe(0) core size vs. time show that all systems proceed with relatively similar kinetics. Together, Fe K-edge and L-edge XANES spectra indicate that these NPs with different sizes finally reach the same octahedral-coordinated Fe(III) oxidation state. XRD results further confirm that these Fe@Fe_xO_y NPs have α-Fe core before oxidation and have a γ-FeOOH shell after oxidation.

This proof of concept work shows that *in situ* liquid cell XANES can be used to follow oxidation state and coordination environment changes in Fe NP dispersions. As such, this work opens the door to controlled corrosion studies of Fe oxidation in different solution environments. In addition, future work will examine the in situ spectroscopy of such Fe@Fe_xO_y NPs for use as redox-active absorbent materials as well as galvanic reactions with other metals to produce supported-NP catalysts. These systems have also been shown by others to be promising hydrogenation catalysts;[9,10,17] *in situ* examinations of Fe oxide NPs under reducing atmospheres should allow for evaluation of the actual Fe speciation under real catalyst operating conditions.

Acknowledgments

The authors acknowledge financial assistance from the National Sciences and Engineering Research Council of Canada (NSERC). XANES experiments described in this paper were performed at the Canadian Light Source, which is supported by the Natural Sciences and Engineering Research Council of Canada, the National Research Council Canada, the Canadian Institutes of Health Research, the Province of Saskatchewan, Western Economic Diversification Canada, and the University of Saskatchewan.

2.6 References

1. Haruta, M.; Kobayashi, T.; Sano, H.; Yamada, N. Novel Gold Catalysts for the Oxidation of Carbon Monoxide at A Temperature far Below 0 °C. *Chem. Lett.* **1987**, *2*, 405–408.

2. Dimitratos, N.; Lopez-Sanchez, J. A.; Lennon, D.; Porta, F.; Prati, L.; Villa, A. Effect of Particle Size on Monometallic and Bimetallic (Au, Pd)/C on the Liquid Phase Oxidation of Glycerol. *Catal. Lett.* **2006**, *108*, 147–153.

3. Reinsch, B. C.; Forsverg, B.; Penn, R. L.; Kim, C.; Lowry, G. V. Chemical Transformations during Aging of Zerovalent Iron Nanoparticles in the Presence of Common Groundwater Dissolved Constituents. *Environ. Sci. Technol.* **2010**, *44*, 3455–3461.

4. Park, T. J.; Sambasivan, S.; Fischer, D. A.; Yoon, W. S.; Misewich, J. A.; Wong, S. S. Electronic Structure and Chemistry of Iron-Based Metal Oxide Nanostructured Materials: A NEXAFS Investigation of $BiFeO_3$, $Bi_2Fe_4O_9$, α-Fe_2O_3, γ-Fe_2O_3, and Fe/Fe_3O_4. *J. Phys. Chem. C* **2008**, *28*, 10359–10369.

5. Peng, S.; Sun, S. H. Synthesis and Characterization of Monodisperse Hollow Fe_3O_4 Nanoparticles. *Angew. Chem. Int. Ed.* **2007**, *46*, 4155–4158.

6. Lu, A.-H.; Salabas, E. L.; Schüth, F. Magnetic Nanoparticles: Synthesis, Protection, Functionalization, and Application. *Angew. Chem. Int. Ed.* **2007**, *46*, 1222–1244.

7. Plaza, R. C.; Arias, J. L.; Espín, A. M.; Jiménez, M. L.; Delgado, A. V. Aging Effects in the Electrokinetics of Colloidal Iron Oxides. *J. Colloid Interface Sci.* **2002**, *245*, 86–90.

8. Pflipsen, C.; Forge, D.; Benali, S.; Gossuin, Y. Improved Stability and Relaxivity of A Commercial Magnetic Ferrofluid. *J. Phys. Chem. C* **2013**, *117*, 20919–20926.

9. Jagadeesh, R. V.; Surkus, A.; Junge, H.; Pohl, M.; Radnik, J.; Huan, H.; Schünemann, V.; Brückner, A.; Beller, M. Nanoscale Fe_2O_3-Based Catalysts for Selective Hydrogenation of Nitroarenes to Anilines. *Science* **2013**, *342*, 1073–1076.

10. Panella, B.; Vargas, A.; Baiker, A. Magnetically Separable Pt Catalyst for Asymmetric Hydrogenation. *J. Catal.* **2009**, *261*, 88–93.

11. Bolm, C.; Legros, J.; Paith, J. L.; Zani, L. Iron-Catalyzed Reactions in Organic Synthesis. *Chem. Rev.* **2004**, *104*, 6217–6254.

12. Zeng, T. Q.; Chen, W. W.; Cirtiu, C. M.; Moores, A.; Song, G. H.; Li, C. J. Fe_3O_4 Nanoparticles: A Robust and Magnetically Recoverable Catalyst for Three-Component Coupling of Aldehyde, Alkyne and Amine. *Green Chem.* **2010**, *12*, 570–573.

13. Wu, W.; He, Q.; Jiang, C. Magnetic Iron Oxide Nanoparticles: Synthesis and Surface Functionalization Strategies. *Nanoscale Res. Lett.* **2008**, *3*, 397–415.

14. Macdonald, J. E.; Veinot, J. G. C. Removal of Residual Metal Catalysts with Iron/Iron Oxide Nanoparticles from Coordinating Environments. *Langmuir* **2008**, *24*, 7169–7177.

15. Signorini, L.; Pasquini, L.; Savini, L.; Carboni, R.; Boscherini, F.; Bonetti, E. Size-Dependent Oxidation in Iron/Iron Oxide Core-shell Nanoparticles. *Phys. Rev. B* **2003**, *68*, 195423.

16. Sun, Y. P.; Li, X. Q.; Cao, J. S.; Zhang, W. X.; Wang, H. P. Characterization of Zero-Valent Iron Nanoparticles. *Adv. Colloid Interface Sci.* **2006**, *120*, 47–56.

17. Hudson, R.; Riviere, A.; Cirtiu, C. M.; Luska, K. L.; Moores, A. Iron-Iron Oxide Core-Shell Nanoparticles are Active and Magnetically Recyclable Olefin and Alkyne Hydrogenation Catalysts in Protic and Aqueous Media. *Chem. Comm.* **2012**, *48*, 3360–3362.

18. Zhou, S.; Johnson, M.; Veinot, J. G. C. Iron/Iron Oxide Nanoparticles: A Versatile Support for Catalytic Metals and Their Application in Suzuki-Miyaura Cross-Coupling Reactions. *Chem. Comm*. **2010**, *46*, 2411–2413.

19. Peng, S.; Wang, C.; Xie, J.; Sun, S. Synthesis and Stabilization of Monodisperse Fe Nanoparticles. *J. Am. Chem. Soc.* **2006**, *128*, 10676–10677.

20. Yoon, T. J.; Lee, H.; Shao, H. L.; Weissleder, R. Highly Magnetic Core-Shell Nanoparticles with A Unique Magnetization Mechanism. *Angew. Chem. Int. Ed.* **2011**, *50*, 4663–4666.

21. Karlsson, M. N. A.; Deppert, K.; Wacaser, B. A.; Karlsson, L. S.; Malm, J.–O. Size-Controlled Nanoparticles by Thermal Cracking of Iron Pentacarbonyl. *Appl. Phys. A. Mater.* **2005**, *8*, 1579–1583.

22. Suslick, K. S.; Fang, M. M.; Hyeon, T. Sonochemical Synthesis of Iron Colloids. *J. Am. Chem. Soc.* **1996**, *118*, 11960–11961.

23. Bang, J. H.; Suslick, K. S. Sonochemical Synthesis of Nanosized Hollow Hematite. *J. Am. Chem. Soc.* **2007**, *129*, 2242–2243.

24. Vijayakumar, R.; Koltypin, Y.; Felner, I.; Gedanken, A. Sonochemical Synthesis and Characterization of Pure Nanometer-Sized Fe_3O_4 Particles. *Mater. Sci. Eng. A* **2000**, *286*, 101–105.

25. Nadagouda, M. N.; Castle, A. B.; Murdock, R. C.; Hussain, S. M.; Varma, R. S. *In Vitro* Biocompatibility of Nanoscale Zerovalent Iron Particles (NZVI) Synthesized Using Tea Polyphenols. *Green Chem.* **2010**, *12*, 114–122.

26. Carroll, K. J.; Pitts, J. A.; Zhang, K.; Pradhan, A. K.; Carpenter, E. E. Nonclassical Crystallization of Amorphous Iron Nanoparticles by Radio Frequency Methods. *J. Appl. Phys.* **2010,** *107*, 09A32.

27. Uegami, M.; Kawano, J.; Okita, T.; Fujii, Y.; Okinaka, K.; Kakuya, K.; Yatagai, S. Toda Kogyo Corp., U.S. Patent Application, **2003**.

28. Choi, C.J.; Dong, X. L.; Kim, B. K. Microstructure and Magnetic Properties of Fe Nanoparticles Synthesized by Chemical Vapor Condensation. *Mater. Trans.* **2001**, *42*, 2046–2049.

29. Elihn, K.; Otten F.; Boman, M.; Kruis. F. E.; Fissan, H.; Carlsson, J. -O. Nanoparticle Formation by Laser-assisted Photolysis of Ferrocene. *Nanostruct. Mater.* **1999**, *12*, 79–82.

30. Kuhn, L. T.; Bojesen, A.; Timmermann, L.; Nielsen, M. M.; Mørup, S. Structural and Magnetic Properties of Core-Shell Iron-Iron Oxide Nanoparticles. *J. Phys.: Condens. Matter.* **2002**, *14*, 13551–13567.

31. Glavee, G. N.; Klabunde, K. J.; Sorensen, C. M.; Hadjipanayis, G. C. Chemistry of Borohydride Reduction of Iron(II) and Iron(III) Ions in Aqueous and Nonaqueous Media. Formation of Nanoscale Fe, FeB, and Fe_2B Powders. *Inorg Chem*.**1995**, *34*, 28–35.

32. Hudson, R.; Hamsaka, G.; Osako, T.; Yamada, Y. M. A.; Li, C. J.; Uozumi, Y.; Moores, A. Highly Efficient Iron(0) Nanoparticle-Catalyzed Hydrogenation in Water in Flow. *Green Chem.* **2013**, *15*, 2141–2148.

33. Ponder, S. M.; Darab, J. D.; Mallouk, T. E. Remediation of Cr(VI) and Pb(II) Aqueous Solutions Using Supported Nanoscale Zero-Valent Iron. *Environ. Sci. Technol.* **2000**, *34*, 2564–2569.

34. Liu, Y. Q.; Majetich, S. A.; Tilton, R. D.; Sholl, D. S.; Lowry, G. V. TCE Dechlorination Rates, Pathways, and Efficiency of Nanoscale Iron Particles with Different Properties. *Environ. Sci. Technol.* **2005**, *39*, 1338–1345.

35. Liu, Y.; Choi, H.; Dionysiou, D.; Lowry, G. V. Trichloroethene Hydrodechlorination in Water by Highly Disordered Monometallic Nanoiron. *Chem. Mater.* **2005**, *17*, 5315–5322.

36. Wang, C. B.; Zhang, W. X. Synthesizing Nanoscale Iron Particles for Rapid and Complete Dechlorination of TCE and PCBs. *Environ. Sci. Technol. Lett.* **1997**, *31*, 2154–2156.

37. Zhang, W. Nanoscale Iron Particles for Environmental Remediation: An Overview. *J. Nanopart. Res*. **2003**, *5*, 323–332.

38. Hudson, R.; Li, C. J.; Moores, A. Magnetic Copper-Iron Nanoparticles as Simple Heterogeneous Catalysts for the Azide-Alkyne Click Reaction in Water. *Green Chem*. **2012**, *14*, 622–624.

39. Ha, D.-H, Moreau, L. M.; Honrao, S.; Hennig, R. G.; Robinson, R. D. The Oxidation of Cobalt Nanoparticles into Kirkendall-Hollowed CoO and Co_3O_4: The Diffusion Mechanisms and Atomic Structural Transformations. *J. Phys. Chem. C* **2013**, *117*, 14303–14312.

40. Moreau, L. M.; Ha, D.-H.; Zhang, H.; Hovden, R.; Muller, D. A.; Robinson, R. D. Defining Crystalline/Amorphous Phases of Nanoparticles through X-ray Absorption Spectroscopy and X-ray Diffraction: The Case of Nickel Phosphide. *Chem. Mater.* **2013**, *25*, 2394–2403.

41. Lin, K. S.; Chang, N. B.;Chuang, T. B. Zero-valent Iron Nanoparticles for Decontamination of Nitrites and Nitrates in Wastewater and Groundwater. *Sci. Technol. Adv. Mater.* **2008**, *9*, 025015.

42. Grunwaldt, J.-D.; Baiker, A. Axial Variation of the Oxidation State of Pt-Rh/Al_2O_3 during Partial Methane Oxidation in A Fixed-Bed Reactor: An *in Situ* X-ray Absorption Spectroscopy Study. *Catal. Lett.* **2005**, *99*, 5–12.

43. Imai, H.; Izumi, K.; Mtsumoto, M.; Kubo, Y.; Kato, K.; Imai, Y. *In Situ* and Real-Time Monitoring of Oxide Growth in A Few Monolayers at Surfaces of Platinum Nanoparticles in Aqueous Media. *J. Am. Chem. Soc.* **2009**, *131*, 6293–6300.

44. Lee, A. F.; Wilson, K. Structure-reactivity Correlations in the Selective Aerobic Oxidation of Cinnamyl Alcohol: *In Situ* XAFS. *Green Chem*. **2004**, *6*, 37–42.

45. Nelson, R. C.; Miller, J. T. An Introduction to X-ray Absorption Spectroscopy and Its *in Situ* Application to Organometallic Compounds and Homogeneous Catalysts. *Catal. Sci. Technol.* **2012**, *2*, 461–470.

46. Anderson, R. M.; Zhang, L.; Loussaert, J. A.; Frenkel, A. I.; Henkelman, G.; Crooks, R. M. An Experimental and Theoretical Investigation of the Inversion of Pd@Pt Core@Shell Dendrimer-Encapsulated Nanoparticles. *ACS Nano* **2013**, *10*, 9345–9353.

47. Wang, L.; Zhang, S.; Zhu, Y.; Patlolla, A.; Shan, J.; Yoshida, H.; Takeda, S.; Frenkel, A. I.; Tao, F. Catalysis and *In Situ* Studies of Rh_1/Co_3O_4 Nanorods in Reduction of NO and H_2. *ACS Catal.* **2013**, *3*, 1011–1019.

48. Nashner, M. S.; Frenkel, A. I.; Adler, D. L.; Shapley, J. R.; Nuzzo, R. G. Structural Characterization of Carbon-Supported Platinum-Ruthenium Nanoparticles from the Molecular Cluster Precursor $PtRu_5C(CO)_{16}$. *J. Am. Chem. Soc.* **1997**, *119*, 7760–7771.

49. Wu, T.; Childers, D. J.; Gomez, C.; Karim, A. M. Schweitzer, N. M.; Kropf, A. J.; Wang, H.; Bolin, T. B.; Hu, Y.; Kovarik, L.; Meyer, R. J.; Miller, J. T. General Method for Determination of the Surface Composition in Bimetallic Nanoparticle Catalysts from the L Edge X-ray Absorption Near-Edge Spectra. *ACS Catal.* **2012**, *2*, 2433–2443.

50. Lee, S.; Lee, B.; Seifert, S.; Vajda, S.; Winans, R. E. Simultaneous Measurement of X-ray Small Angle Scattering, Absorption and Reactivity: A Continuous Flow Catalysis Reactor. *Nucl. Instrum. Methods Phys. Res., Sect. A* **2011**, *649*, 200–203.

51. Brown, M. A.; Jordan, I.; Redondo, A. B.; Kleibert, A.; Wörner, H. J.; van Bokhoven, J. A. *In Situ* Photoelectron Spectroscopy at the Liquid/Nanoparticle Interface. *Surf. Sci.* **2013**, *610*, 1–6.

52. Brown, M. A.; Redondo, A. B.; Jordan, I.; Dyyackaerts, N.; Lee, M.-T.; Ammann, M.; Nolting, F.; Kleibert, A.; Huthwelker, T.; van Bokhoven, J. A. A New Endstation at the Swiss Light Source for Ultraviolet Photoelectron Spectroscopy, X-ray Photoelectron Spectroscopy, and X-ray Absorption Spectroscopy Measurements of Liquid Solutions. *Rev. Sci. Instrum.* **2013**, *84*, 073904.

53. Maclennan, A.; Banerjee, A.; Hu, Y.; Miller, J. T.; Scott, R. W. J. *In Situ* X-ray Absorption Spectroscopic Analysis of Gold-Palladium Bimetallic Nanoparticle Catalysts. *ACS Catal.* **2013**, *3*, 1411–1419.

54. Liu, L.; Burnyeat, C. A.; Lepsenyi, R. S.; Nwabuko, I. O.; Kelly, T. L. Mechanism of Shape Evolution in Ag Nanoprisms Stabilized by Thiol-Terminated Poly(ethylene glycol): an in

Situ Kinetic Study. *Chem. Mater.* **2013**, *25*, 4206–4214.

55. Yang, J. J.; Regier, T.; Dynes, J. J.; Wang, J.; Shi, J. Y.; Peak, D.; Zhao, Y. D.; Hu, T. D.; Chen, Y. X.; Tse, J. S. Soft X-ray Induced Photoreduction of Organic Cu(II) Compounds Probed by X-ray Absorption Near-Edge (XANES) Spectroscopy. *Anal.Chem.* **2011**, *83*, 7856–7862.

56. Abramoff, M. D.; Magalhães, P. J.; Ram, S. J. Image Processing with ImageJ. *Biophotonics Int*. **2004**, *11*, 36–42.

57. Newville, M. IFEFFIT: Interactive XAFS Analysis and FEFF Fitting. *J. Synchrotron Radiat.* **2001**, *8*, 322–324.

58. Ravel, B.; Newville, M. ATHENA, ARTEMIS, HEPHAESTUS: Data Analysis for X-ray Absorption Spectroscopy Using IFEFFIT. *J. Synchrotron Radiat.* **2005**, *12*, 537–541.

59. Li, X. Q.; Ellliott, D. W.; Zhang, W. X. Zero-Valent Iron Nanoparticles for Abatement of Environmental Pollutants: Materials and Engineering Aspects. *Crit. Rev. Env. Sci. Technol.* **2006**, *31*, 111–122.

60. Butter, K.; Bomans, P. H. H.; Frederik, P. M.; Vroege, G. J.; Philipse, A. P. Direct Observation of Dipolar Chains in Iron Ferrofluids by Cryogenic Electron Microscopy. *Nat. Mater.* **2003**, *2*, 88–91.

61. Astruc, D.; Lu, F.; Aranzaes, J. R. Nanoparticles as Recyclable Catalysts: The Frontier between Homogeneous and Heterogeneous Catalysis. *Angew. Chem., Int. Ed.* **2005**, *44*, 7852–7872.

62. Hu, M. A.-C.; Payzant, E. A. P.; Byers, C. H. Sol-Gel and Ultrafine Particle Formation via Dielectric Tuning of Inorganic Salt-Alcohol-Water Solutions. *J. Colloid Interface Sci.* **2000**, *222*, 20–36.

63. Wang, C.; Baer, D. R.; Amonette, J. E.; Engelhard, M. H.; Antony, J. J.; Qiang, Y. Morphology and Electronic Structure of the Oxide Shell on the Surface of Iron Nanoparticles. *J. Am. Chem. Soc.* **2009**, *131*, 8824–8832.

64. Cabrera, N,; Mott, N. F. Theory of the Oxidation of Metals. *Rep. Prog. Phys.* **1949**, *12*, 163–184.

65. Fung, K. K.; Qin, B.; Zhang, X. X. Passivation of α-Fe Nanoparticle by Epitaxial γ-Fe_2O_3 Shell. *Mater. Sci. Eng. A* **2000**, *286*, 135–138.

66. Linderoth, S.; Morup, S.; Bentzon, M. D. Oxidation of Nanometer-Sized Iron Particles. *J. Mater. Sci*. **1995**, *30*, 3142–3148.

67. Pratt, A.; Lari, L.; Hovorka, O.; Shah, A.; Woffinden, C.; Tear, S. P.; Binns, C.; Kroger, R. Enhanced Oxidation of Nanoparticles through Strain-Mediated Ionic Transport. *Nature Mater.* **2014**, *13*, 26–30.

68. Peak, D.; Regier, T. Direct Observation of Tetrahedrally Coordinated Fe(III) in Ferrihydrite. *Environ. Sci. Technol.* **2012**, *46*, 3163–3168.

CHAPTER 3

3. *In situ* X-ray Absorption Spectroscopic Study of Fe@Fe_xO_y/Pd and Fe@Fe_xO_y/Cu Nanoparticle Catalysts Prepared by Galvanic Exchange Reactions

This work has been published in *The Journal of Physical Chemistry C*. In this work, we synthesized Fe@Fe_xO_y/Pd and Fe@Fe_xO_y/Cu nanoparticles by controlling the molar ratios of Fe@Fe_xO_y nanoparticles to Pd(II)/Cu(II) to study their resulting structures and used *in situ* X-ray absorption near edge structure (XANES) spectra to follow the formation processes of Fe@Fe_xO_y/Pd and Fe@Fe_xO_y/Cu bimetallic nanoparticles. *In situ* XANES spectra were also applied to study the changes of Fe@Fe_xO_y/Pd in the catalysis of Suzuki-Miyaura cross-coupling reactions.

This work has been published in *The Journal of Physical Chemistry C*, **2015**, *119*, 21209-21218. This paper has been co-authored with Christian Patzig (2nd author) who did the EDX mapping. Ester Rani Aluri and Ruwaid Rafiuddin are thanked for their assistance with XRD acquisition and Aimee Maclennan for her assistance with the acquisition of XANES spectra. All the experimental work in this paper has been done by myself along with the writing of the first draft of the manuscript. The final manuscript was submitted for publication after revisions by Dr. Yongfeng Hu and Dr. Robert W. J. Scott.

3.1 Abstract

$Fe@Fe_xO_y$ core-shell nanoparticles have been previously shown to be a versatile support for catalytic metals such as Pd and Cu. However, the resulting structure, metal speciation, and performance of such catalysts in catalytic reactions are still poorly understood. Herein, we synthesize $Fe@Fe_xO_y$ supported Pd and Cu nanoparticles by controlling the molar ratios of $Fe@Fe_xO_y$ nanoparticles to Pd(II) or Cu(II) species. Scanning transmission electron microscopy analyses show that Pd or Cu NPs are deposited on the exterior shell of the $Fe@Fe_xO_y$ nanoparticles. *In situ* X-ray absorption near-edge structure (XANES) spectra were used to follow the formation processes of $Fe@Fe_xO_y$/Pd and $Fe@Fe_xO_y$/Cu nanoparticles and the performance of $Fe@Fe_xO_y$/Pd nanoparticles for Suzuki-Miyaura cross-coupling reactions. The results show that different molar ratios of $Fe@Fe_xO_y$ nanoparticles to Pd(II) or Cu(II) lead to different morphologies of the resulting supported-NP structures. *In situ* XANES results show that $Fe@Fe_xO_y$ nanoparticles can effectively fully reduce Pd or Cu salts over the course of ~20 minutes to give small Pd or larger Cu nanoparticles on the surface, and can also re-reduce oxidized Pd in Suzuki-Miyaura cross-coupling reactions.

3.2 Introduction

Nanoparticles (NPs) with sizes of less than 100 nm have attracted extensive interest especially in the catalytic field, because they are often more catalytically active than their bulk counterparts due to their large surface-to-volume ratios, and their electronic properties can change as a function of size.[1,2] Bimetallic NP catalysts are promising because the synergy between two metals can lead to enhanced activity in catalysis or allow for bifunctional properties such as magnetic and plasmonic properties.[3-6] Galvanic exchange reactions provide a very simple and effective method to prepare bimetallic NPs. In a galvanic exchange reaction, the difference of the electrochemical potential between two metals leads to the oxidation and dissolution of the metal "seed" accompanied by reduction of the other metal ions and deposition of the resultant atoms on the surface of the metal "seed".[7] For example, our group has reported that Ag@Pd (core@shell) NPs can be synthesized via a galvanic reaction through the addition of stoichiometric amount of K_2PdCl_4 to Ag NPs,[8] and other groups have similarly

shown that a variety of bimetallic systems can be synthesized via galvanic reactions.[9-11] Interestingly, galvanic reactions have also been shown to take place through metal oxide films in Fe@Fe_xO_y systems with inorganic species, such as Pd(II), Cu(II), Ru (III), Ni(II), As(III), Hg(II), Zn(II) and Pb(II) salts.[12-18] In this study, we focus on monitoring the development of Fe@Fe_xO_y@M (M = Pd, Cu) NPs by following *in situ* XANES spectroscopy of the formation and catalysis of these NPs in solution. Pd and Cu were chosen as several groups have shown that these NP systems have interesting catalytic applications. Results show that both the speciation and metal reduction processes can be followed during synthesis and during subsequent catalytic reactions.

Fe@Fe_xO_y NPs have been widely studied for environmental remediation or catalytic studies due to their low cost, relatively nontoxic nature, and magnetic recovery advantages.[19,20] Several groups have demonstrated that Fe@Fe_xO_y NPs can be synthesized by the sodium borohydride method.[21,22] Others have shown that these core@shell NPs can be used as versatile precursors to seed, reduce and support another metal to form bimetallic NPs by galvanic exchange reactions to catalyze various reactions, such as Suzuki-Miyaura cross-coupling reactions (Fe@Fe_xO_y/Pd),[12] hydrogenation of ketones,[14] azide-alkyne click reactions (Fe@Fe_xO_y/Cu),[13,23] cyclopropanation of styrene deriavtives,[24] and coupling of iodobenzene and thiophenol.[25] In particular, Veinot and coworkers have suggested that a particular advantage of these systems is that the latent Fe core can re-reduce leached metals such as Pd and Cu.[12,26] Following chemical speciation of the added metal in these systems has been difficult, as many of these systems use large polydisperse Fe NP precursors and *ex situ* XPS studies. Recently, we showed that utilizing poly(vinylpyrrolidone) (PVP) stabilizers in various methanol/water mixtures, it is possible to control the sizes of initial Fe NPs and follow the kinetics of the oxidation of the particles to Fe@Fe_xO_y NPs via *in situ* XANES spectroscopy.[27]

X-ray absorption spectroscopy (XAS) has been found to be a valuable technique for the examination of structures of bimetallic NPs as XANES spectroscopy is sensitive to the changes in oxidation state, whereas X-ray absorption fine structure (EXAFS) spectroscopy can provide information about the distances between central and neighboring atoms, the number of neighboring atoms, and the nature of neighboring atoms. Our group has studied the structures

and catalytic activities of bimetallic AuPd NPs synthesized by simultaneous reduction and successive reduction using Pd K-edge and Au L_3-edge XAS data.[28] Results showed that sequentially reduced bimetallic AuPd NPs have surfaces that are significantly enriched in Pd and Au-rich cores, and have higher activity and sensitivity toward oxidation of crotyl alcohol to crotonaldehyde. Moreover, XAS places few constraints on the samples. Considering that many synthetic and catalytic reactions occur in solution, XAS can be employed as a powerful technique to study NP structures and speciation under *in situ* or *operando* liquid conditions.[29-33] For example, Nelson and Miller illustrated that time-dependent XANES can be used to follow the transformation of organometallic catalysts under realistic reaction conditions and study kinetics of metal speciation through linear combination fitting of the XANES spectra.[34] Krishna *et al.* showed *in situ* XAS measurements could be used in microfluidic channels in order to follow time-resolved growth of Au NPs.[35] Also, Anderson *et al.* recently showed that structural inversion took place for Pd@Pt (Core@Shell) dendrimer-encapsulated NPs via an *in situ* EXAFS study.[36]

In this study, we synthesized Fe@Fe_xO_y/Pd and Fe@Fe_xO_y/Cu bimetallic NPs using different molar ratios of Fe@Fe_xO_y NPs to Pd(II) or Cu(II). The final NP structures were investigated by TEM, XRD, energy-dispersive X-ray spectroscopy (EDX) and XAS. *In situ* XANES spectra allowed us to follow the formation processes of Fe@Fe_xO_y/Pd and Fe@Fe_xO_y/Cu bimetallic NPs and the changes of Fe@Fe_xO_y/Pd NPs in the Suzuki-Miyaura cross-coupling reaction. Results show that higher loadings of Pd(II) or Cu(II) salts lead to more Fe oxidation in the Fe@Fe_xO_y NPs and nucleation of the Pd and/or Cu NPs was seen on the surface of the metal oxide shell. However, significantly different morphologies were seen for the final Fe@Fe_xO_y/Pd and Fe@Fe_xO_y/Cu NPs, as Pd formed well-dispersed small NPs, while Cu formed larger NPs. *In situ* XANES studies show that Fe@Fe_xO_y/Pd and Fe@Fe_xO_y/Cu NPs can be formed very quickly, and oxidized Pd in Suzuki-Miyaura cross-coupling reactions is likely re-reduced onto Fe@Fe_xO_y NPs during the course of the reaction. These results are significant as they show that *in situ* XAS measurements can be used as a valuable tool to monitor the formation processes and metal speciation of NPs in their synthetic reactions and catalytic reactions in solutions.

3.3 Experimental Section

3.3.1 Materials

All chemicals were used as received. Fe(II) sulfate heptahydrate and anhydrous Cu(II) sulfate were purchased from Sigma-Aldrich. Poly(vinylpyrrolidone) (M.W. 58,000 g/mol), 4-iodobenzoic acid, benzeneboronic acid, and palladium (II) nitrate hydrate were purchased from Alfa Aesar. Sodium borohydride, ethanol and methanol (HPLC grade) were purchased from Fisher Scientific. Sulfuric acid and sodium carbonate anhydrous were purchased from EMD millipore. All solutions were made using 18.2 MΩ·cm Milli-Q water (Millipore, Bedford, MA).

3.3.2 Synthesis

3.3.2.1 Synthesis of Fe@Fe_xO_y Nanoparticles

Fe@Fe_xO_y NPs were produced as previously reported. Briefly, $FeSO_4 \cdot 7H_2O$ (5.0 mmol) in a water/methanol (v/v) 1:1 mixture (20 mL) was reduced using $NaBH_4$ (25 mmol) under nitrogen gas.[9,11] PVP (20 mmol based on monomer unit) was used to stabilize the resulting Fe NPs. First, PVP (in 10 mL methanol) solution was added to $FeSO_4 \cdot 7H_2O$ solution (in 8.0 mL water) and the mixture was stirred for 10 min. Then a solution of $NaBH_4$ (in 2.0 mL water) was added dropwise. 5.0 mL of 1 M H_2SO_4 was added to the 20 mL of 250 mM as-synthesized Fe NPs before galvanic exchange reactions to remove any excess $NaBH_4$. The Fe oxide shell was formed by exposing the Fe NPs to air for several hours.

3.3.2.2 Synthesis of Fe@Fe_xO_y/Pd and Fe@Fe_xO_y/Cu Bimetallic Nanoparticles

Different molar ratios of Fe@Fe_xO_y/Pd and Fe@Fe_xO_y/Cu bimetallic NPs (50:1, 20:1, and 5:1 Fe:Pd or Fe:Cu ratios) were synthesized by mixing the resulting Fe@Fe_xO_y NP solution with Pd(II) nitrate solution (20 mM) or Cu(II) sulfate solution (20 mM) under nitrogen to stir 30 minutes. *In situ* formation of Fe@Fe_xO_y/Pd and Fe@Fe_xO_y/Cu bimetallic NPs were carried out by flowing Pd or Cu salt solutions (20 mM, 1 mL) by a peristaltic pump into the liquid cell to mix with Fe@Fe_xO_y NPs (200 mM, 2 mL).

3.3.3 Catalytic Reactions

Iodobenzene (1.5 mmol), benzeneboronic acid (2.0 mmol) and sodium carbonate (4.0 mmol) in 2.8 mL ethanol and 5.2 mL of a Fe@Fe_xO_y/Pd NP solution were used for the *in situ* Suzuki-Miyaura cross-coupling reaction at 25 °C.

3.3.4 Characterization

TEM images of the NPs were recorded with a Philips CM10 microscope operated at 100 kV. The samples were prepared by drop-casting one droplet of dilute sample onto a carbon-coated copper TEM grid (Electron Microscopy Sciences, Hatfield, PA). Average particle diameters were measured using the ImageJ program.[37] Scanning transmission electron microscopy analyses (STEM) were done using a high-angle annular dark field (HAADF) detector (Fischione Model 3000, Fischione company) at a camera length of 145 mm, with an FEI Titan 80-300 transmission electron microscope at 300 kV acceleration voltage (FEI). STEM was done in combination with energy dispersive X-Ray spectroscopy (EDXS) using a Super-X EDX (FEI Company) detector that consists of four silicon drift detectors, thus offering a comparably large collection efficiency with a covered solid angle of 0.9 steradians above the sample surface. Element maps of different elements were obtained from the analyzed samples with the commercially available software Esprit (Bruker) by means of spectral imaging (pixelwise EDX spectrum collection). Element maps were derived by evaluating the peak intensity, for example, the area under the K_α edges of all analyzed elements (except for Pd, were the L_α edge was used), with an automatic routine as provided by the software, and plotting the respective intensities in a 2D false color representation. Line scans of the relative peak intensities of chosen elements were obtained as well, in order to monitor relative intensity changes of the elements' K_α peak intensities along specified linear tracks within an as-obtained element map.

Pd K-edge XAS measurements were conducted at the Hard X-ray MicroAnalysis (HXMA) beamline 061D-1 (energy range 5−30 keV; resolution, 1×10^{-4} $\Delta E/E$) at the Canadian Light Source (CLS, 2.9 GeV storage ring, 250 mA current) using the Si (220) monochromator. Fluorescence spectra were measured using a Lytle detector. Fe and Cu K-edge XAS spectra

and Pd L-edge XANES spectra were collected at the Soft X-ray Microcharacterization Beamline (SXRMB) at the CLS. The measurements were conducted under ambient atmosphere for Fe and Cu K-edges, and under helium for Pd L_3-edge measurements. Lowering the beam flux by defocusing and/or filtering the beam with Kapton filters and stirring the sample via magnetic stirring were used to avoid photoreduction problems at the Pd L_3-edge. Liquid cells (SPEX CertiPrep Disposable XRF X-Cell sample cups) were covered with 4 μm ultralene film (purchased from Fisher Scientific, Ottawa, ON) and used for XANES analysis. The data were analyzed using the software package IFEFFIT.[38,39] The R-factors on the mismatch between data and fit for linear combination analysis XANES fitting of Fe K-edge spectra in the range of 7100 to 7150 eV and Cu K-edge spectra in the range of 8970 to 9020 eV are all lower than 0.002. The R-factors for all EXAFS fits are lower than 0.025.

A Rigaku Rotaflex RU-200 rotating anode X-ray diffractometer with a Co Kα (λ = 1.6208 Å) X-ray source was used for X-ray diffraction analysis. Nanoparticles were placed in a glass holder and scanned from 10° to 80° with scanning rate of 3.5°/min.

^{1}H NMR spectra was recorded in DMSO on a Bruker 500MHz Advance NMR spectrometer. Chemical shifts are recorded in parts per million (ppm).

3.4 Results and Discussion

Fe@Fe_xO_y NPs were prepared by reducing $FeSO_4 \cdot 7H_2O$ in the presence of PVP with $NaBH_4$ at room temperature (23 ± 2 °C) using 1:1 volume ratios of methanol to water as solvents following previous literature protocols.[19,21,27] As shown in Figure 3.1, the average sizes of these Fe@Fe_xO_y NPs are 16.0 ± 6.0 nm with *ca*. 3 nm Fe oxide shells on the NPs. Significant particle agglomeration is seen due to magnetic self-assembly of the NPs.[40] The Fe@Fe_xO_y NPs were then exposed to Pd(II) salts for a period of 0.5 h at varying Fe@Fe_xO_y NPs to Pd(II) ratios. When a 50:1 Fe:Pd(II) molar ratio was used to synthesize Fe@Fe_xO_y/Pd NPs, the average sizes of Fe@Fe_xO_y NPs are similar (16.0 ± 3.3 nm), but small NPs are observed, which are likely to be Pd NPs (2.6 ± 0.8 nm) deposited on Fe@Fe_xO_y NPs (Figure 3.1 B). The composition and speciation of these small particles is shown by EDX and XANES analyses below. When the molar ratio of Fe@Fe_xO_y NPs to Pd(II) was decreased from 50:1 to 20:1, Pd NPs were also

seen (2.6 ± 2.3 nm, Figure 3.1 C). It became difficult to continue to identify larger $Fe@Fe_xO_y$ NPs when the molar ratio of $Fe@Fe_xO_y$ NPs to Pd^{2+} was further reduced to 5:1 (Figure 3.1 D); such samples show the limits of conventional TEM analysis of such samples. More monodisperse and smaller $Fe@Fe_xO_y$ NP starting materials could be made by increasing the methanol:water ratios in the synthesis, however, it became increasingly difficult to distinguish Fe vs. Pd domains via conventional bright-field TEM with smaller $Fe@Fe_xO_y$ NPs.

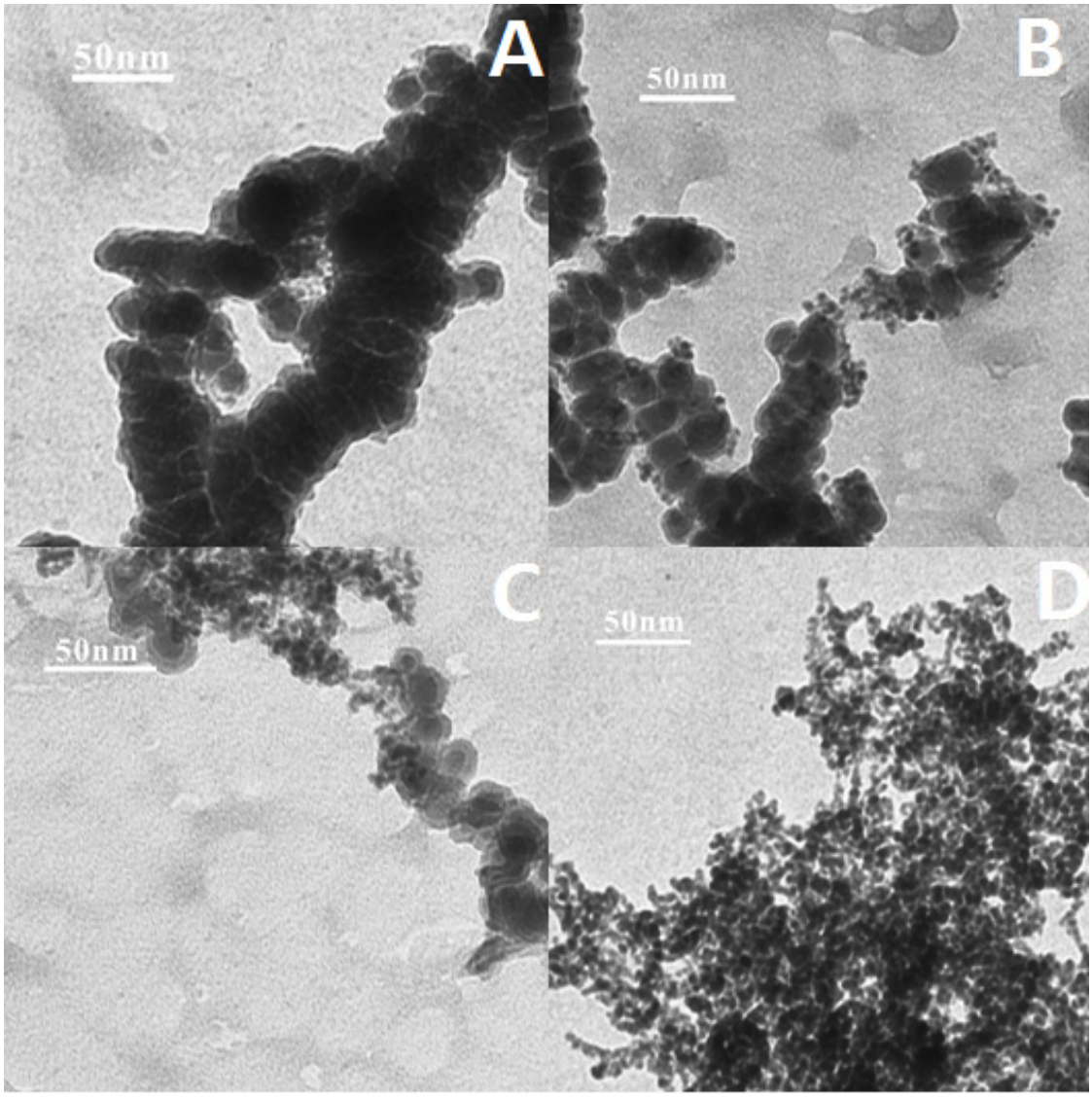

Figure 3.1. (A) TEM image of $Fe@Fe_xO_y$ NPs synthesized in methanol/water (v/v) 1:1 solvents. B-D show TEM images of $Fe@Fe_xO_y$/Pd synthesized with different molar ratios of $Fe@Fe_xO_y$ to Pd^{2+} (B) 50:1; (C) 20:1; (D) 5:1.

STEM/EDX elemental mapping was performed to give more insight into the distribution of each element in the NPs. Figure 3.2 A shows a large area STEM image of Fe@Fe_xO_y/Pd NPs synthesized with a Fe:Pd ratio of 20:1 in high-angle annular dark field mode, and Figure 3.2 B shows a close-up of a small area of this image. In bright field images both Fe@Fe_xO_y NPs and putative Pd NPs on their surface can be seen. As shown in Figure 3.2 C, large scale EDX maps suggest that Pd distribution is associated with the presence of Fe@Fe_xO_y NPs and that the Pd is fairly well-dispersed. High-resolution Fe and oxygen EDX maps in Figure 3.2 D show that the Fe@Fe_xO_y particles do indeed have core@shell structures with Fe oxide shells of *ca*. 3-5 nm. In addition, the Pd distribution suggests the formation of Pd clusters (< 2nm) and/or NPs on the surface of the Fe@Fe_xO_y particles, and not in the core of the NPs. Based on TEM data, we propose a possible growth mechanism as follows: in the synthesis of Fe@Fe_xO_y/Pd NPs, the Pd(II) ions are adsorbed on the surfaces of Fe@Fe_xO_y NPs and reduced by electrons through tunneling between the Fe core and thin oxide layer.[41,42] When high Fe:Pd ratios were used, small Pd NPs formed on the oxide shell and there was little size change of the Fe@Fe_xO_y NPs (Figures 3.1 B and 3.1 C, Figure 3.2 B). As the Fe:Pd ratio was decreased (*i.e.* by increasing the amount of Pd(II) in the synthesis), most of the Fe@Fe_xO_y NPs were completely oxidized and a complete disappearance of Fe@Fe_xO_y NPs was seen, presumably due to penetration of the oxide layer (Figure 3.1 D).

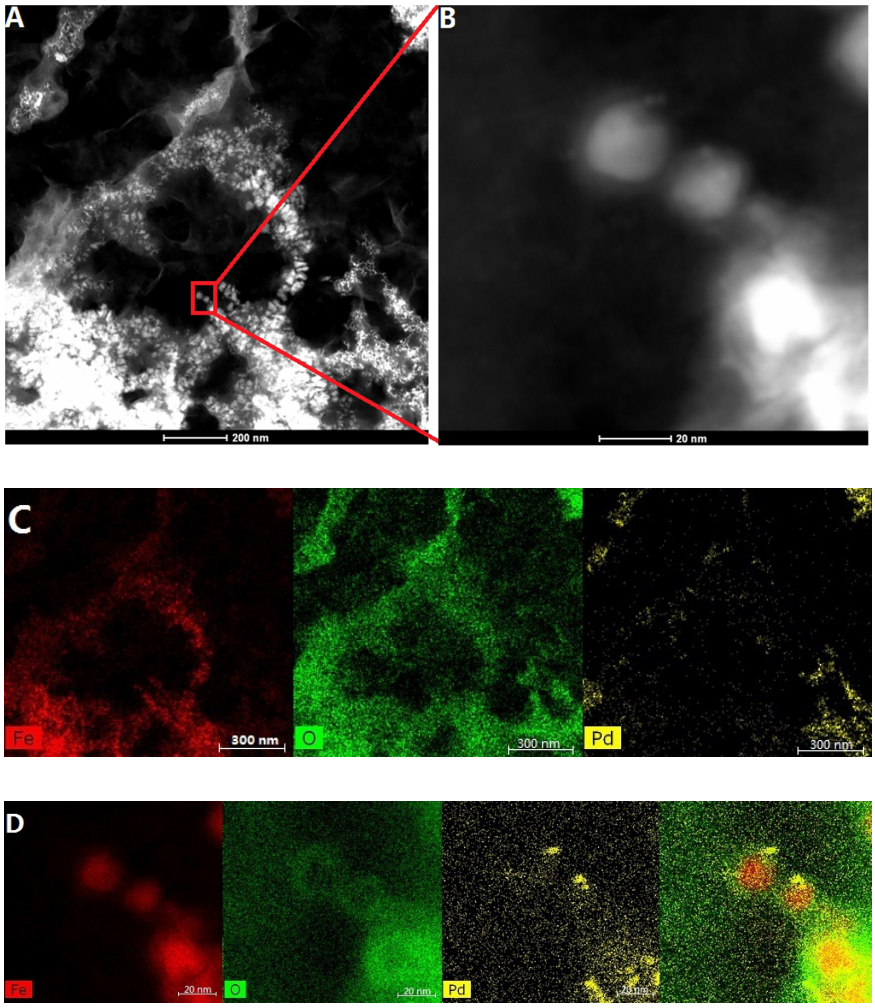

Figure 3.2. (A, B) High-angle annular dark-field STEM images, and (C, D) EDX elemental mapping images of Fe@Fe_xO_y/Pd NPs synthesized with 20:1 molar ratio of Fe@Fe_xO_y NPs to Pd(II).

Similar STEM images/EDX maps were also observed in the synthesis of Fe@Fe_xO_y/Cu NPs with different molar ratios of Fe@Fe_xO_y NPs to Cu(II) (Figure 3.3). However, in this particular system, Cu speciation after reaction is much less homogenous, which suggests breakthrough events of the oxide shell are more common in the Cu case. This is in fair agreement with recent results by Moores and coworkers on a similar system.[43] EXAFS analysis of the Pd and Cu samples, shown below, are in agreement that Cu distribution is much more heterogeneous and much larger NP sizes are seen. One possible explanation for this difference is that a secondary galvanic reaction may be at play in the Pd system; the redox potential for

Pd(II) reduction ($E^{o}_{½}$ = 0.951 V) is quite high, and thus Pd can possibly be reduced both by the Fe(0) core (Fe^{2+}/Fe^{0}, $E^{o}_{½}$ = -0.447 V) and Fe(II) species in the shell (Fe^{3+}/Fe^{2+}, $E^{o}_{½}$ = 0.771 V).[44] However, in the case of Cu(II) reduction ($E^{o}_{½}$ = 0.342 V), the only mechanism that can allow for Cu reduction is oxidation of the Fe(0) core.[44]

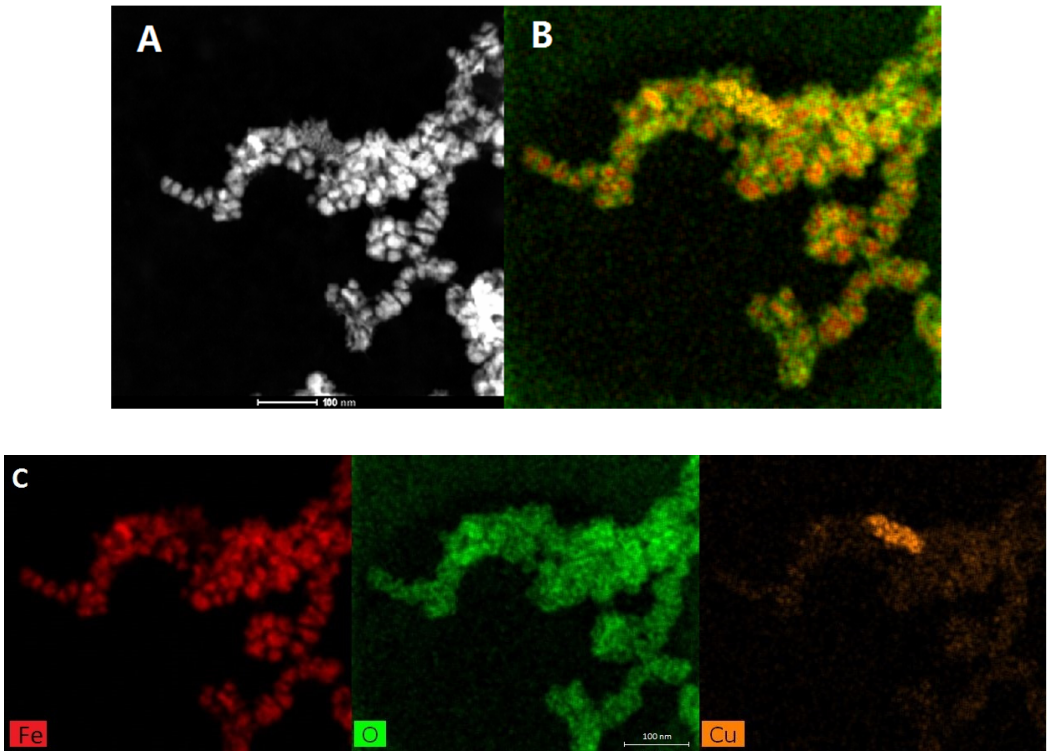

Figure 3.3. (A) High-angle annular dark-field STEM images and (B, C) EDX elemental mapping images of Fe@Fe_xO_y/Cu NPs synthesized with 20:1 molar ratios of Fe@Fe_xO_y NPs to Cu(II).

The powder X-ray diffraction (PXRD) patterns of the Fe@Fe_xO_y NPs and different ratios of Fe@Fe_xO_y/Pd NPs are shown in Figure 3.4. Fe@Fe_xO_y NPs are mainly in α-Fe state (peak at 2θ value of 52.4°), which is in agreement with previous reports.[22,27] As the molar ratio of Fe@Fe_xO_y NPs to Pd^{2+} decreases from 50:1 to 5:1, the peak at 52.4° disappears gradually and two broad {111} and {002} peaks are seen at 47.1° and 54.9° 2θ respectively which correspond well to that expected for fcc Pd. These PXRD patterns reveal the emergence of small Pd nanoparticles in the 5:1 Fe@Fe_xO_y/Pd samples and the disappearance of the underlying broad Fe/Fe oxide peaks, presumably due to the amorphous nature of the final materials.

Fe@Fe_xO_y/Cu NPs synthesized with 5:1 Fe:Cu ratios have a main peak at 2θ value of 50.8° which reveals the existence of Cu fcc metal.

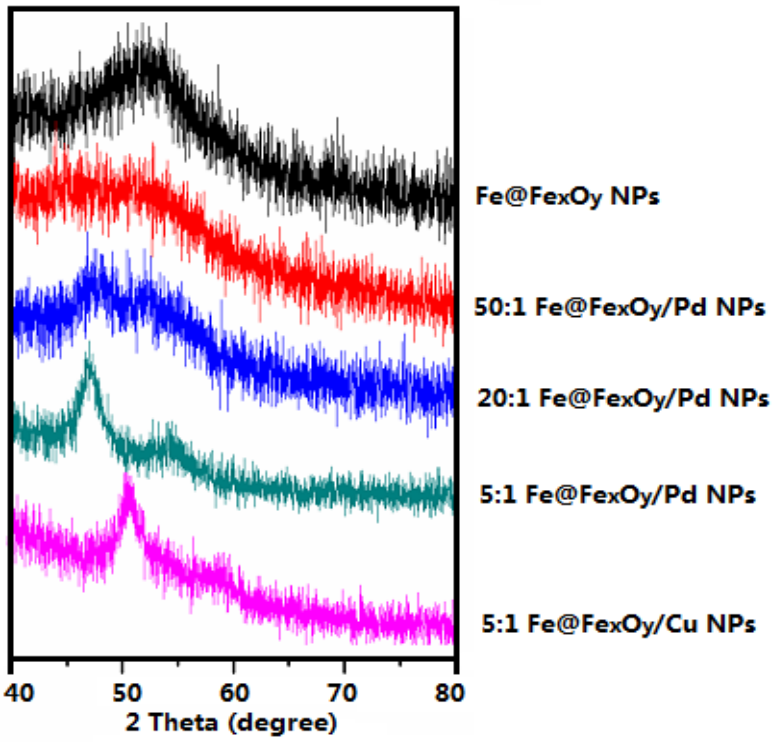

Figure 3.4. PXRD patterns.

XAS studies further support TEM and EDX observations, and provide details on both the formation of the galvanic exchange reactions and speciation of the Pd, Cu and Fe in the resulting NPs. Fe K-edge XANES spectra of Fe@Fe_xO_y/Pd NPs (Figure 3.5) show a decrease of the peak at 7112 eV with an increase in the molar ratios of Fe@Fe_xO_y NPs to Pd(II), which indicates a corresponding decrease in the amount of Fe(0) in the resulting Fe@Fe_xO_y/Pd NPs. Figure 3.6 shows the Pd K-edge k-space EXAFS spectra for the resulting bimetallic NPs with different molar ratios of Fe@Fe_xO_y NPs to Pd(II). The similarity of these plots show that there is no significant shift in the periodicity of the EXAFS wave compared to Pd foil, which suggests that the Pd is all in the zero-valent state and the extent of alloying between Fe and Pd is very low. This is in agreement with STEM/EDX results that Pd(II) was reduced to form small Pd NPs rather than core-shell structures with Fe. The slight dampening of the amplitude of the signals of the resulting NPs compared to Pd foil is due to the presence of under-coordinated

surface Pd atoms on the surface of the particles, and is a sign of small average NP size.[45] EXAFS fitting shows the average N_{Pd-Pd} coordination number is in the 9-10 range for all Pd:Fe ratios examined, which is indicative of Pd NPs with a size in the 2 nm range (Table 3.1 and Figure 3.7). For Fe@Fe_xO_y/Cu NPs, k-space Cu K-edge EXAFS results (Figure 3.8) show that the amplitudes and periodicity of the EXAFS waves of the resulting NPs are nearly identical to that of Cu foil, which indicate that the Cu is all in the zero-valent state after reaction, and have much larger NP sizes such that average coordination numbers approach that of the bulk (*i.e.* 12). The Cu speciation is also confirmed by the Cu K-edge first derivative XANES spectrum of Fe@Fe_xO_y/Cu NPs through comparing it with Cu foil, Cu(I) and Cu(II) standards (Figure 3.9). Moores and coworkers originally reported the final speciation of Cu in the bimetallic NPs was Cu(I) and Cu(II) characterized by XPS,[13] but later showed Cu(0) formation by EELS mapping,[42] which is in agreement with our results which show only Cu(0) from XANES spectra.

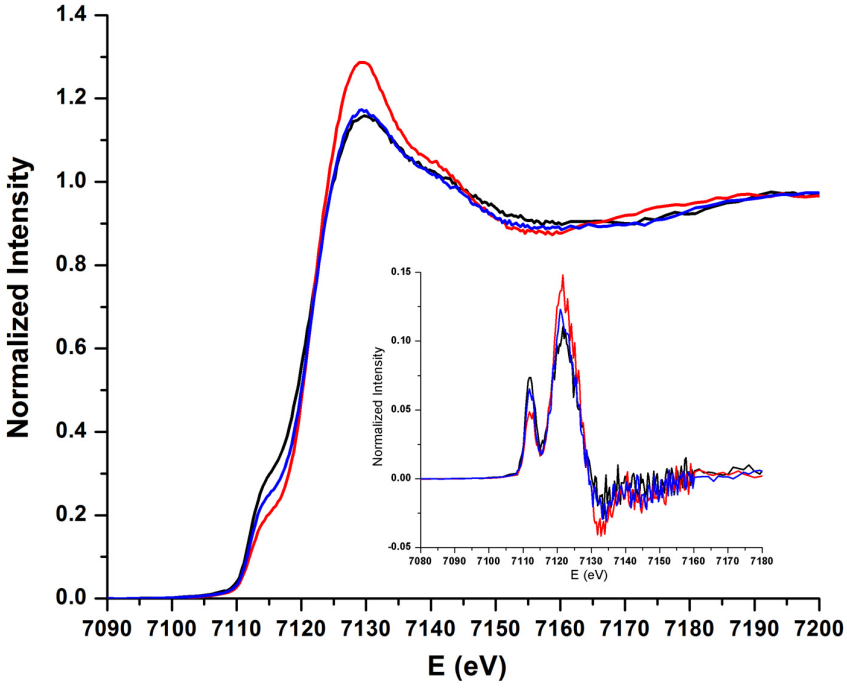

Figure 3.5. Fe K-edge XANES spectra of Fe@Fe_xO_y/Pd NPs synthesized with different molar ratios of Fe@Fe_xO_y NPs to Pd(II) (black) 50:1, (blue) 20:1, (red) 5:1 and their related first derivative XANES spectra (insert).

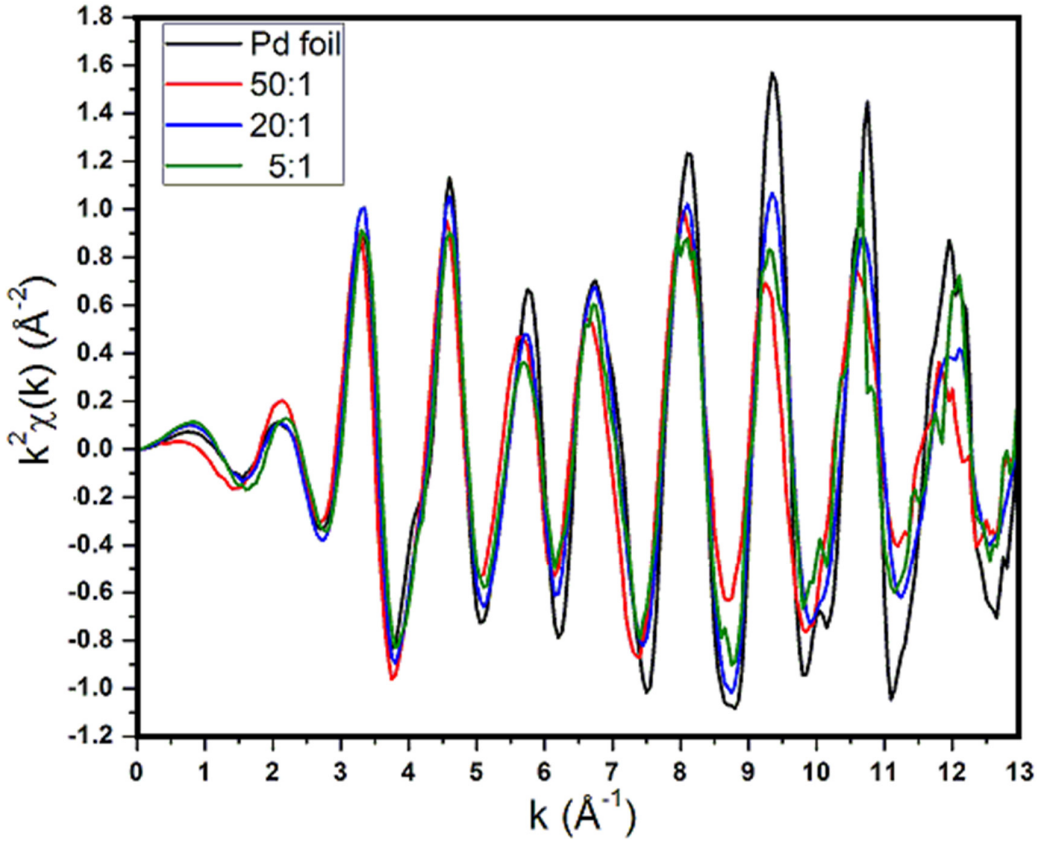

Figure 3.6. Pd K-edge EXAFS spectra in k-space for Fe@Fe_xO_y/Pd NPs with different molar ratios of Fe@Fe_xO_y NPs to Pd(II).

Table 3.1. Values for the Pd K-edge EXAFS fitting of Fe@Fe_xO_y/Pd NPs with different molar ratios of Fe@Fe_xO_y NPs to Pd(II).

Fe:Pd Ratio	Shell	C.N.[1]	R (Å)	σ^2 (Å)	ΔE_0 (eV)
50:1	Pd-Pd	10.3 (9)	2.755 (4)	0.010 (1)	3.3 (6)
20:1	Pd-Pd	10.0 (9)	2.74 (1)	0.008 (1)	3.5 (5)
5:1	Pd-Pd	9.3 (8)	2.752 (1)	0.009 (1)	5.1 (5)

[1] First shell Coordination Number

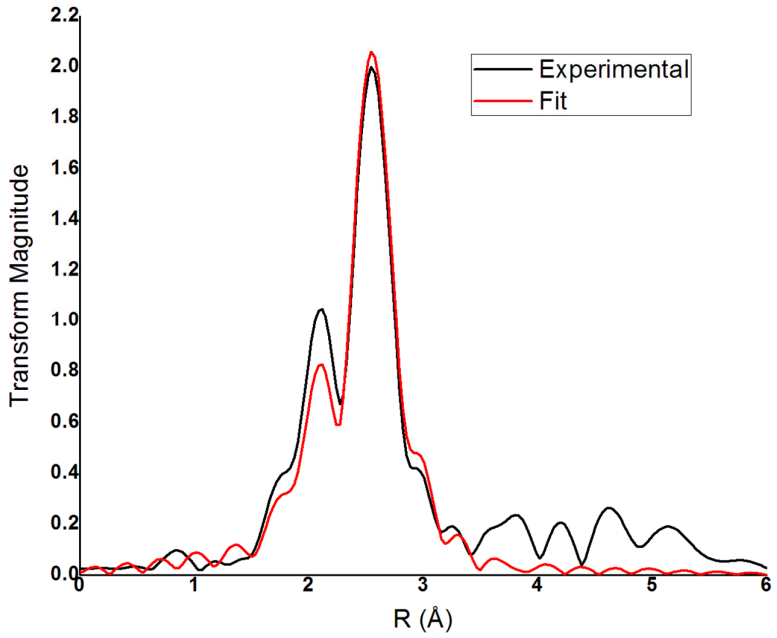

Figure 3.7. Pd K-edge EXAFS fit of Fe@Fe_xO_y/Pd NPs with 20:1 molar ratios of Fe@Fe_xO_y NPs to Pd(II) in R space.

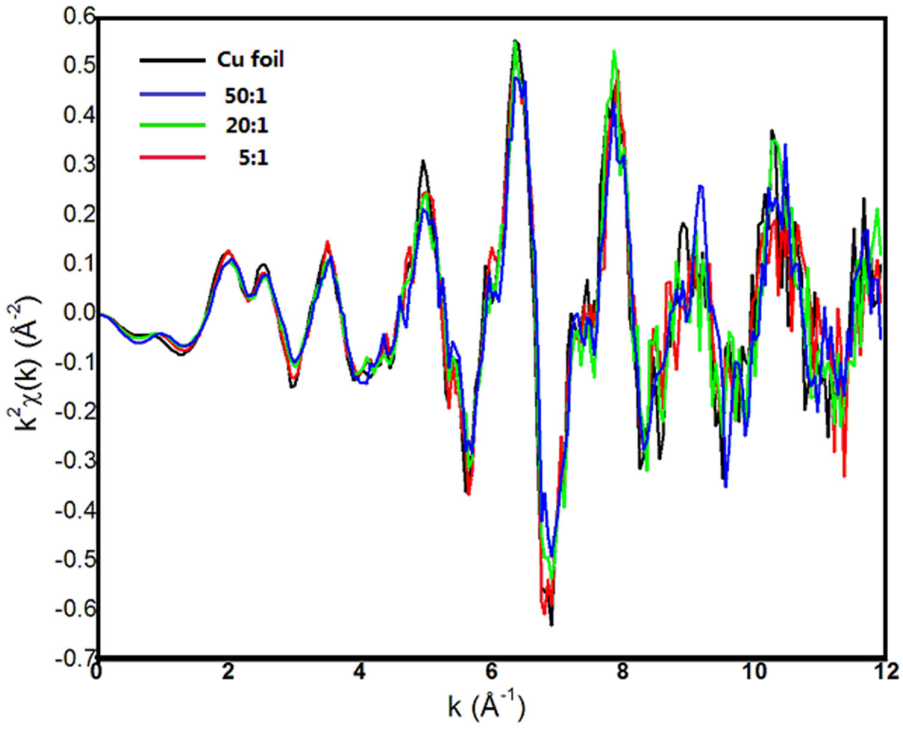

Figure 3.8. Cu K-edge EXAFS spectra in k-space for Fe@Fe_xO_y/Cu NPs with different molar ratios of Fe@Fe_xO_y NPs to Cu(II).

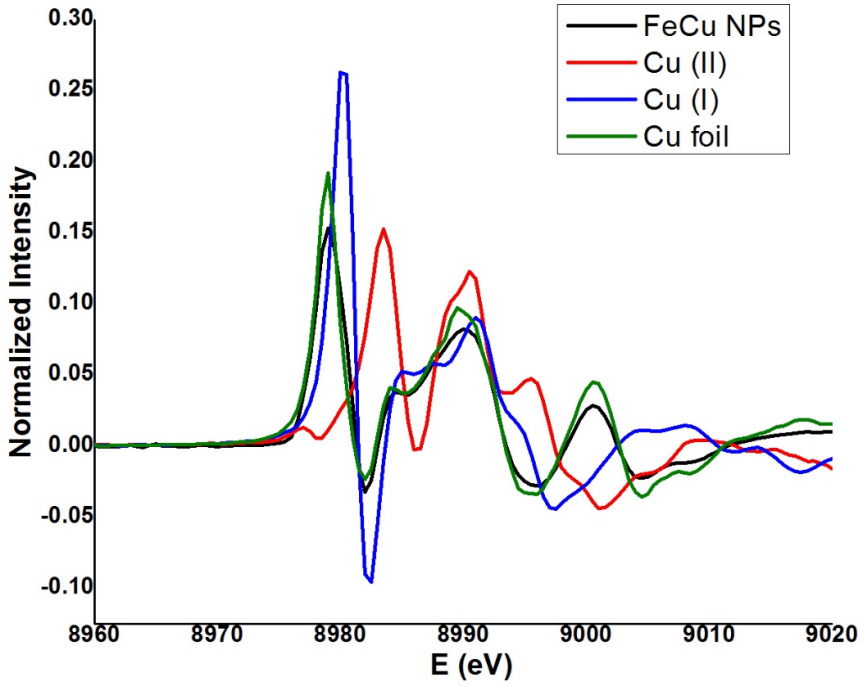

Figure 3.9. Cu K-edge first derivative XANES spectra of Fe@Fe_xO_y/Cu NPs with 20:1 molar ratios of Fe@Fe_xO_y NPs to Cu(II) and standards.

Finally, we wished to monitor the formation processes of these reactions by using an *in situ* liquid cell setup (Figure 3.10) that has been developed for the SXRMB beamline at the Canadian Light Source.[27,46,47] In this work, we further developed the cell to allow for the addition of Pd or Cu salt solutions into the cell to mix with Fe@Fe_xO_y NPs. In the XANES region, the absorption edge energy often increases correspondingly as the oxidation state of the metal increases. In addition, for lower energy L-edge spectra, which probe the occupancy of the valence d band of transition metals, the amplitude of the white line at the absorption edge is directly related to the number of vacancies in the d-band. *In situ* solution Pd L_3-edge, Cu K-edge and Fe K-edge XANES measurements were conducted to study the formation processes of Fe@Fe_xO_y/Pd and Fe@Fe_xO_y/Cu NPs. As shown in Figure 3.11 A, the reduction of Pd(II) by Fe@Fe_xO_y NPs begins nearly instantaneously as they are mixed together, judged by a decrease in white line intensity in the Pd L_3-edge and a left shift in the absorption maximum. These results are indicative of a reduction of Pd(II) to Pd(0). The results of linear combination fitting with Pd foil and $Pd(NO_3)_2$ standards allow for a plot of the fraction of Pd(0) vs. time. The reduction of Pd(II) occurs quickly, and results show that Pd^{2+} is nearly fully reduced after

20 minutes (Figure 3.11 B). Unfortunately, we were not able to collect enough data points for a full kinetic analysis. This reduction was also confirmed by *ex situ* Pd K-edge XANES spectra, which was indicative of zero-valent Pd NPs (Figure 3.12). The slight shift between the XANES edges of reduced Pd NPs and metallic Pd foil may be due to an electronic effect occurring between the Fe@Fe_xO_y NPs and Pd NPs on the surface. *In situ* Fe K-edge XANES spectra were also collected, and show a further oxidation of Fe@Fe_xO_y NPs during the reduction of Pd(II) (Figure 3.13). Linear combination fitting using standards $Fe(NO_3)_3$, $FeSO_4$, and Fe foil shows the relative mole fraction of Fe(0) in the Fe@Fe_xO_y NPs decreases from 74% to 57% after the formation of Fe@Fe_xO_y/Pd bimetallic NPs synthesized with a 20:1 Fe:Pd ratio (Table 3.2). The extent of Fe oxidation is a little higher than expected from a stoichiometric Fe to Pd galvanic reduction, which suggests that a small amount of Fe is further oxidized by air during these reactions. The oxidation of Fe@Fe_xO_y NPs occurs over *ca*. 18 minutes, which is in good agreement with Pd L_3-edge results.

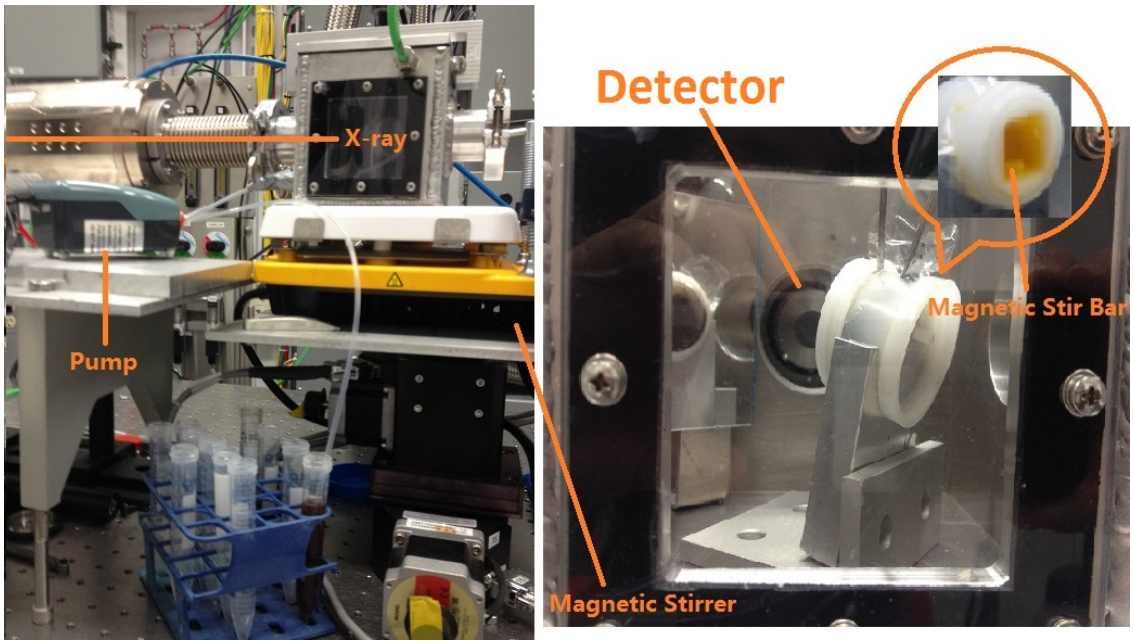

Figure 3.10. Reactor setup for *in situ* fluorescence XAS.

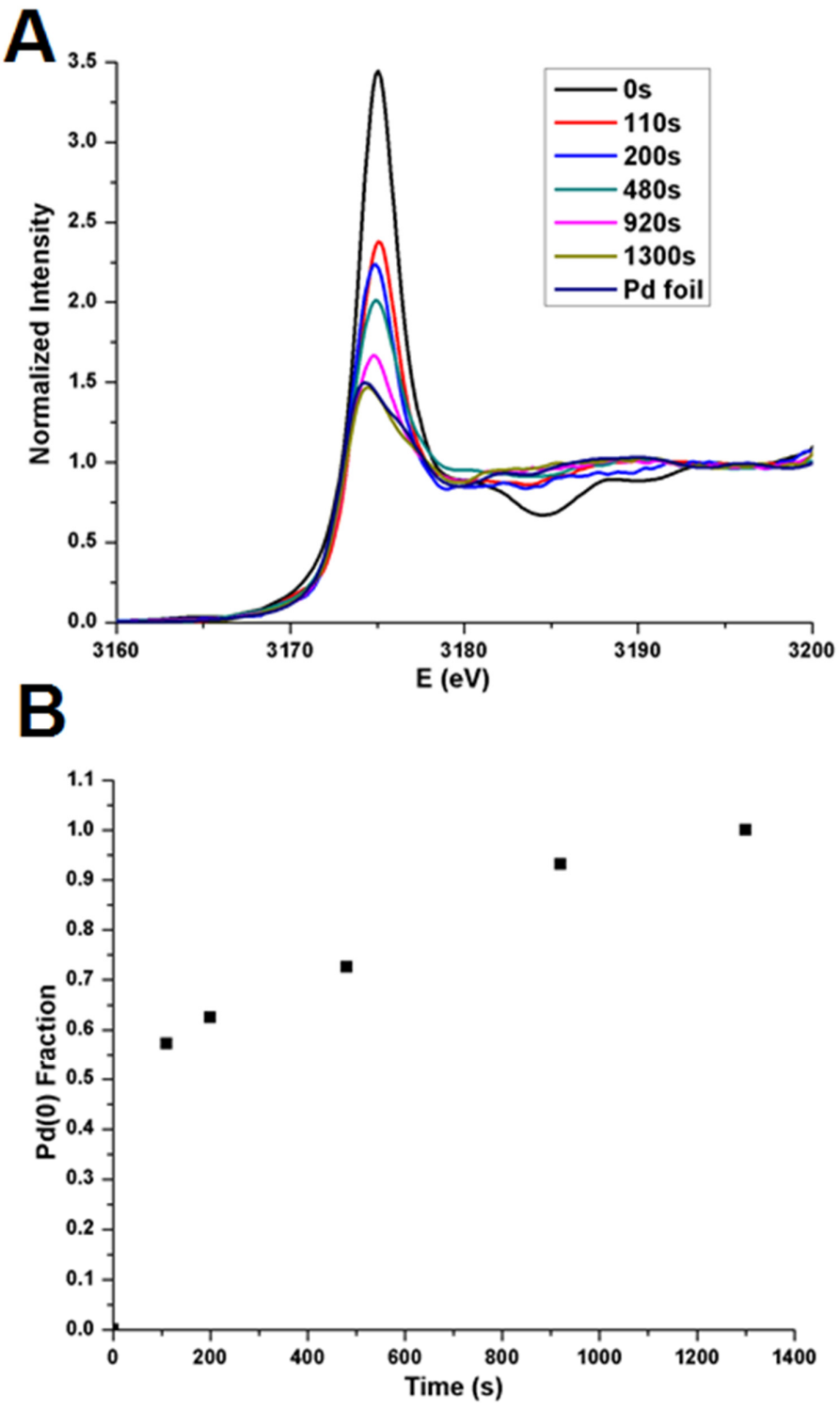

Figure 3.11. (A) Pd L-edge XANES spectra of the reduction process of Pd(II) in the synthesis of Fe@Fe_xO_y/Pd NPs with 20:1 molar ratios of Fe@Fe_xO_y NPs to Pd(II); (B) Pd(0) fraction versus reduction time.

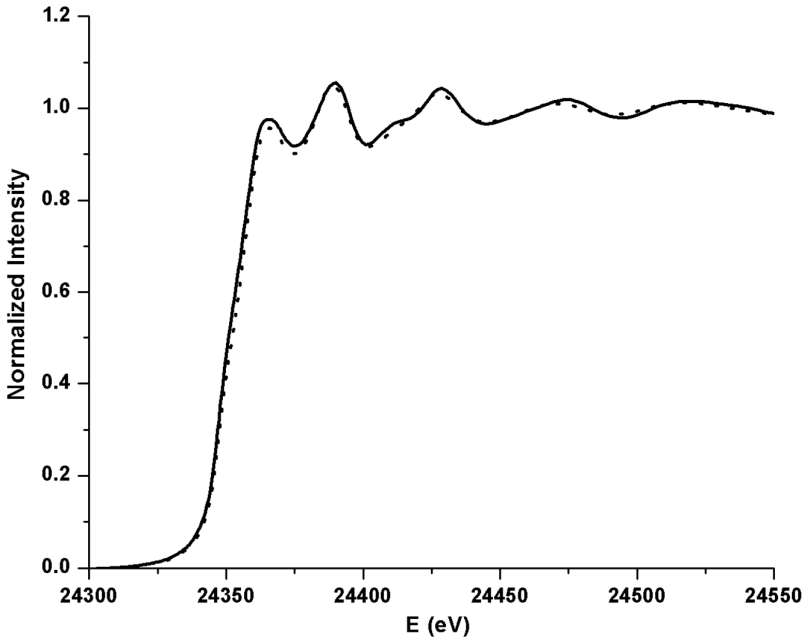

Figure 3.12. Pd K-edge XANES spectra of the resulting Fe@Fe_xO_y/Pd NPs (dot line) and Pd foil (solid line).

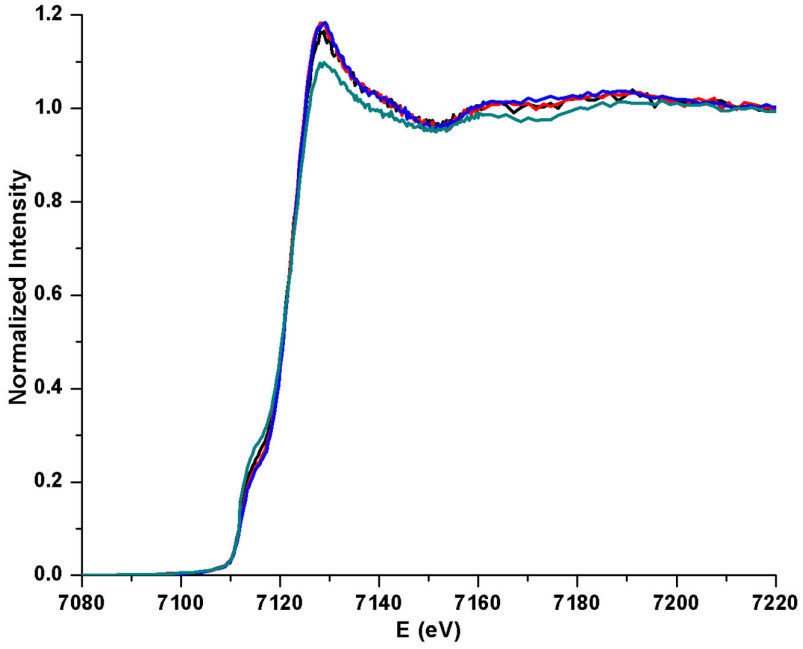

Figure 3.13. Fe K-edge XANES spectra of the oxidation process of Fe@Fe_xO_y NPs in the synthesis of Fe@Fe_xO_y /Pd NPs with 20:1 molar ratios of Fe@Fe_xO_y NPs to Pd(II) (green) 0 min; (black) 3 min; (red) 18 min; (blue) 33 min.

Table 3.2. XANES fitting results of the oxidation of Fe@Fe_xO_y NPs in the formation of Fe@Fe_xO_y/Pd and Fe@Fe_xO_y/Cu NPs with 20:1 molar ratios of Fe@Fe_xO_y NPs to Pd(II)/ Cu(II).

Sample	Reaction Time (min)	Fe (0)%	Fe(II)%	Fe(III)%
Fe@Fe_xO_y/Pd NPs	0	74(1)	14(1)	11(1)
	3	60(1)	26(1)	14(1)
	18	57(1)	24(1)	19(1)
Fe@Fe_xO_y/Cu NPs	0	74(1)	14(1)	11(1)
	3	53(1)	28(1)	19(1)
	18	51(1)	35(1)	14(1)

Similar results were observed in the reduction process of Cu(II) by Fe@Fe_xO_y NPs monitored by Cu K-edge and Fe K-edge XANES spectra (Figure 3.14 A and 3.15). The reaction was completed after 22 minutes, and a plot of the fraction of Cu(0) vs. time could be generated by linear combination fitting of results with Cu foil and $CuSO_4$ standards (Figure 3.14 B). The data shows a rapid reduction of Cu in the first few minutes of the reaction; again, unfortunately we could not obtain enough data for a full kinetic analysis. The oxidation of Fe from the Fe K edge was similarly observed in the meantime (Figure 3.15). Linear combination fitting shows the relative fraction of Fe(0) in the Fe@Fe_xO_y NPs decreases from 74% to 51% in the formation of Fe@Fe_xO_y/Cu bimetallic NPs, and that there was slightly more Fe(II) present at the end of the reaction in the Cu samples than in Pd samples. This may be due to a secondary galvanic mechanism by which Fe(II) centers can reduce Pd(II) but not Cu(II). The results reveal that Fe@Fe_xO_y/Pd NPs and Fe@Fe_xO_y/Cu NPs can be easily synthesized via galvanic reactions between PVP stabilized Fe@Fe_xO_y NPs and Pd(II)/Cu(II) salts.

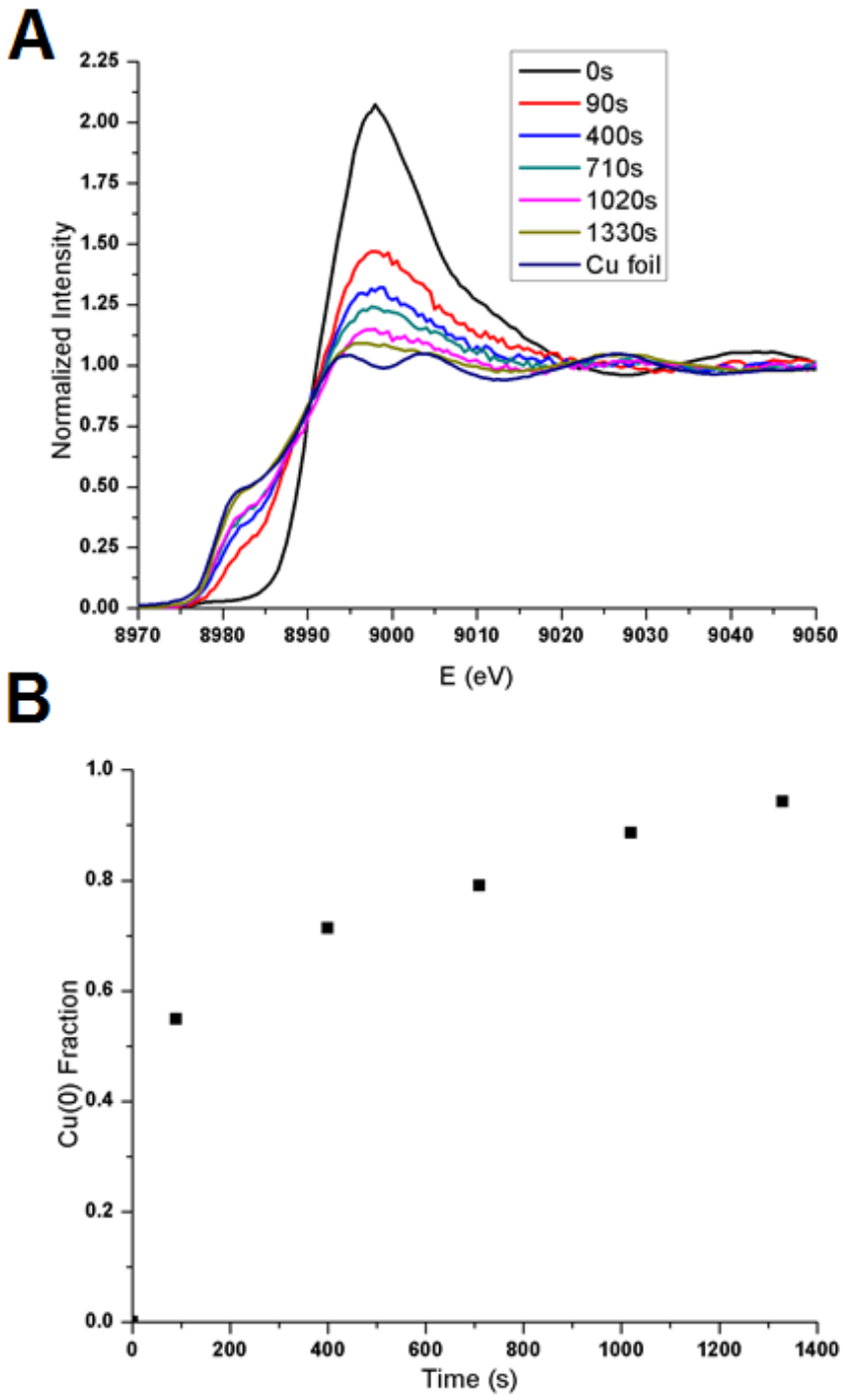

Figure 3.14. (A) Cu K-edge XANES spectra of the reduction process of Cu(II) in the synthesis of Fe@Fe_xO_y/Cu NPs with 20:1 molar ratios of Fe@Fe_xO_y NPs to Cu(II); (B) Cu(0) fraction versus reduction time.

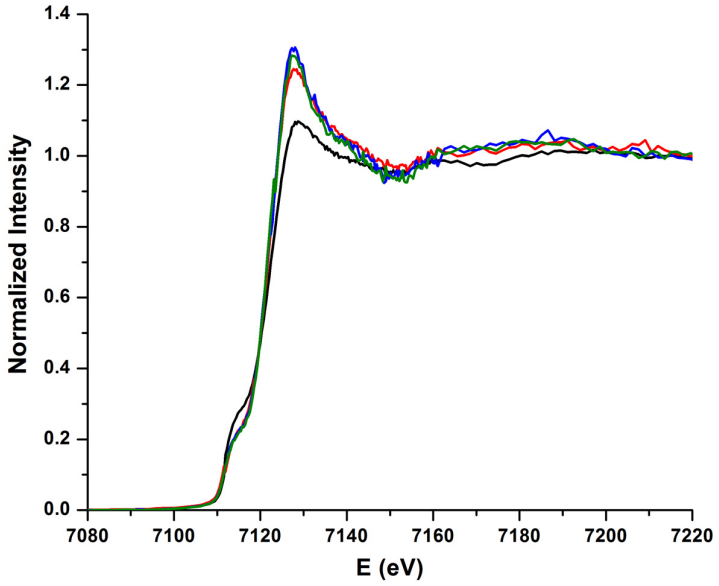

Figure 3.15. Fe K-edge XANES spectra of the oxidation process of Fe@Fe_xO_y NPs in the synthesis of Fe@Fe_xO_y/Cu NPs with 20:1 molar ratios of Fe@Fe_xO_y NPs to Cu(II) (green) 0 min; (red) 3 min; (blue) 18 min; (green) 33 min.

Fe@Fe_xO_y/Pd NPs have been reported to exhibit high catalytic activity toward Suzuki-Miyaura cross-coupling reactions in aqueous solution at room temperature in air, and Fe@Fe_xO_y cores have been suggested to have a possible role in allowing the re-deposition of leached Pd effectively.[12,26] Therefore, we used *in situ* XANES spectra to study the metal speciations of Pd and Fe in Fe@Fe_xO_y/Pd NPs during Suzuki-Miyaura cross-coupling reactions. ^{1}H NMR results show that Fe@Fe_xO_y/Pd NPs can catalyze iodobenzene with benzeneboronic acid to form the biphenyl product in 1 hour at room temperature with a yield of *ca.* 90% (Figure 3.16). Linear combination fitting of Fe K edge XANES data shows the relative fraction of Fe(0) in the Fe@Fe_xO_y/Pd bimetallic NPs decreases with time, with an increase of the mole fraction of Fe(II) and Fe(III) over 40 minutes, which indicates the oxidation of Fe@Fe_xO_y cores when Fe@Fe_xO_y/Pd NPs are used in the cross-coupling reaction (Figure 3.17 A and Table 3.3). Meanwhile, little to no change is seen in the Pd L_3-edge data during this time (Figure 3.17 B). This is strong evidence that the Fe NP cores are being sacrificed to reduce oxidized Pd in the reaction (either still absorbed on the surface or having leached into the solution) back to Pd^0, which is in agreement with previous hypotheses.[10]

Control reactions of Fe@Fe_xO_y NPs used directly in the cross-coupling reaction mixture (with no Pd) were also run, and there was little change in the Fe K-edge spectra in this scenario (Figure 3.18). Similarly, Fe@Fe_xO_y/Pd NPs showed no obvious oxidation in air at the Fe K edge over a similar time-scale (Figure 3.19).

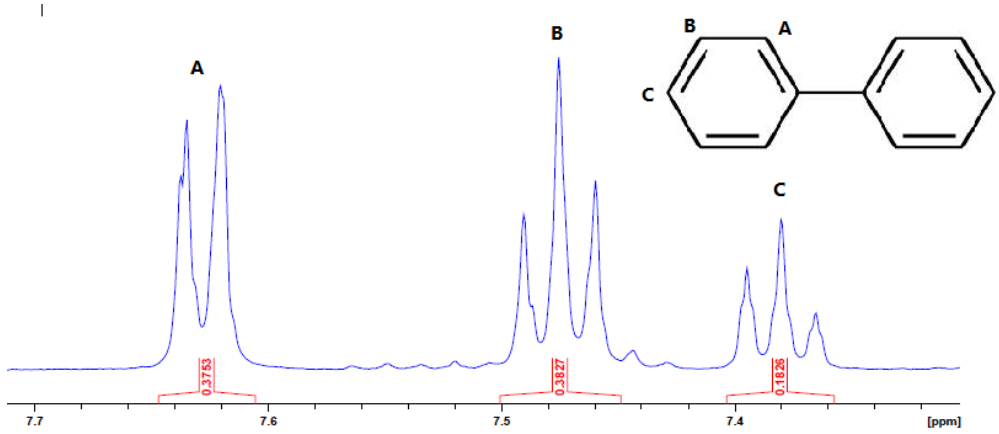

Figure 3.16. ^{1}H NMR spectra of biphenyl in $CDCl_3$.

Table 3.3. XANES fitting results of the oxidation of Fe@Fe_xO_y/Pd NPs in cross-coupling reaction.

Reaction Time (min)	Fe (0)%	Fe(II)%	Fe(III)%
0	72(1)	11(1)	18(1)
20	58(1)	26(1)	16(1)
26	48(1)	32(1)	20(1)
33	44(1)	35(1)	21(1)
39	41(1)	38(1)	21(1)
46	41(1)	39(1)	21(1)

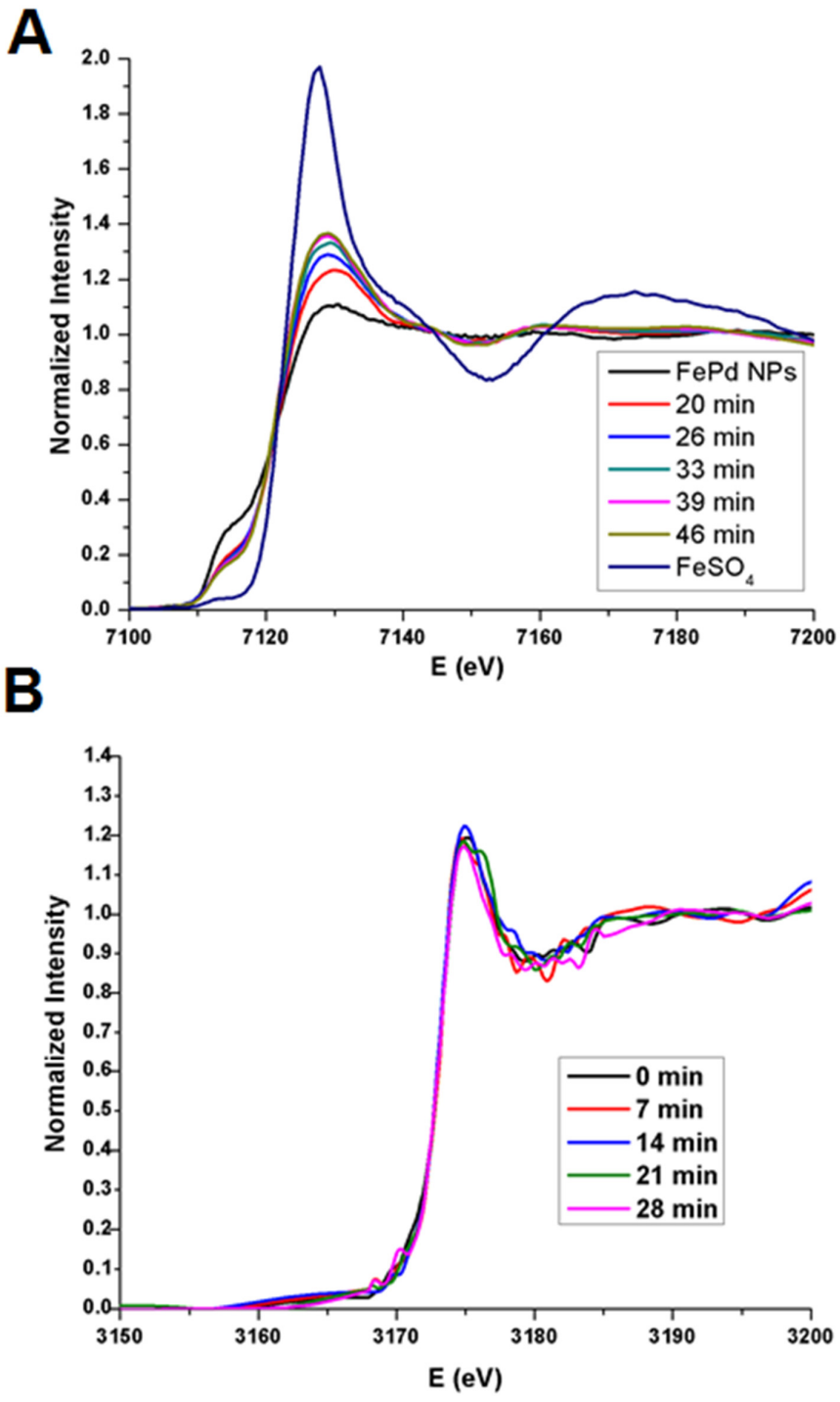

Figure 3.17. (A) Fe K-edge XANES spectra of Fe@Fe_xO_y/Pd NPs and (B) Pd L-edge XANES spectra of Fe@Fe_xO_y/Pd NPs during cross-coupling reaction.

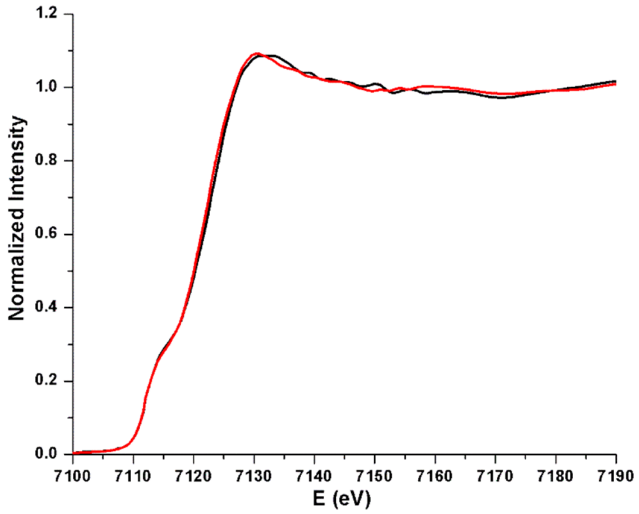

Figure 3.18. Fe K-edge XANES spectra of Fe@Fe_xO_y NPs (black) and them in iodobenzene (red) with benzeneboronic acid cross-coupling mixture (after 20 minutes).

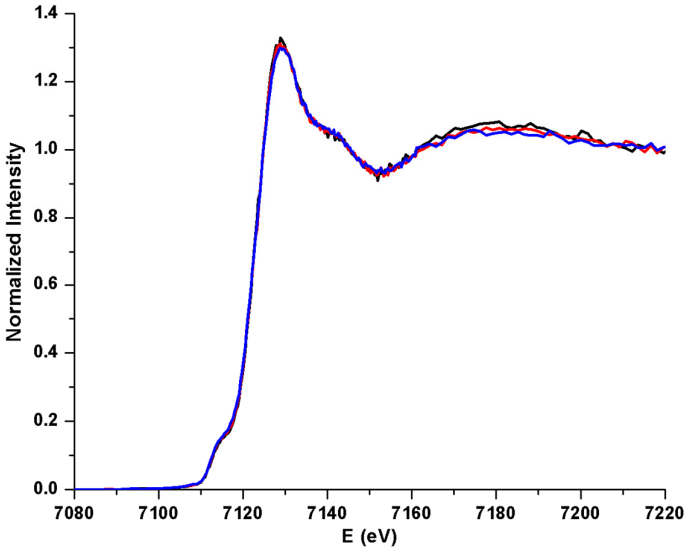

Figure 3.19. Fe K-edge XANES spectra of Fe@Fe_xO_y/Pd NPs exposed in air (blue) 0 min; (red) 15 min; (black) 30 min.

3.5 Conclusion

TEM, XRD, and XAS results show that different molar ratios of Fe@Fe_xO_y NPs to Pd(II) or Cu(II) result in Pd or Cu NPs, respectively, on the surface of Fe@Fe_xO_y NPs, particularly at high Fe:metal ratios. We have successfully monitored the reduction processes of Pd(II) and

Cu(II) toward the formation of Fe@Fe_xO_y/Pd and Fe@Fe_xO_y/Cu NPs through using *in situ* liquid cell Pd L_3-edge and Cu K-edge XANES spectra, and the corresponding oxidation of Fe in the Fe@Fe_xO_y NPs by Fe K-edge XANES spectra. *In situ* XANES results also show that these Fe@Fe_xO_y NPs can re-reduce oxidized Pd in Suzuki-Miyaura cross-coupling reactions. This study shows the power of *in situ* liquid cell XAS measurements in following metal speciation in real time for NP transformations in solution.

Acknowledgments

The authors acknowledge financial assistance from the National Sciences and Engineering Research Council of Canada (NSERC). XAS experiments described in this paper were performed at the Canadian Light Source, which is supported by the Natural Sciences and Engineering Research Council of Canada, the National Research Council Canada, the Canadian Institutes of Health Research, the Province of Saskatchewan, Western Economic Diversification Canada, and the University of Saskatchewan. The STEM/EDX part of his work was supported by means of a DAAD (German Academic Exchange Service) grant, which is gratefully acknowledged.

3.6 References

1. Haruta, M.; Kobayashi, T.; Sano, H.; Yamada, N. Novel Gold Catalysts for the Oxidation of Carbon Monoxide at A Temperature far Below 0 °C. *Chem. Lett.* **1987**, *2*, 405–408.
2. Jagadeesh, R. V.; Surkus, A.; Junge, H.; Pohl, M.; Radnik, J.; Huan, H.; Schünemann, V.; Brückner, A.; Beller, M. Nanoscale Fe_2O_3-Based Catalysts for Selective Hydrogenation of Nitroarenes to Anilines. *Science* **2013**, *342*, 1073–1076.
3. Zhang, H.; Jin, M.; Xia, Y. Enhancing the Catalytic and Electrocatalytic Properties of Pt-Based Catalysts by Forming Bimetallic Nanocrystals with Pd. *Chem. Soc. Rev*. **2012**, *41*, 8035–8049.
4. Sachan, R.; Malasi, A.; Ge, J.; Yadavali, S.; Krishna, H.; Gangopadhyay, A.; Garcia, H.; Duscher, G.; Kalyanaraman, R. Ferroplasmons: Intense Localized Surface Plasmons in Metal-Ferromagnetic Nanoparticles. *ACS Nano* **2014**, *8*, 9790–9798.
5. Zhang, C.; Wang, X.; Sun, J.; Kou, T.; Zhang, Z. Synthesis and Antibacterial Properties of Magnetically Recyclable Nanoporous Silver/Fe_3O_4 Nanocomposites through One-step Dealloying. *CrystEngComm* **2013**, *15*, 3965–3973.
6. Zhang, Z.; Zhang, C.; Sun, J.; Kou, T.; Bai, Q.; Wang, Y.; Ding, Y. Ultra Nanoporous

PdFe/Fe_3O_4 Catalysts with Doubly Enhanced Activities towards Electro-Oxidation of Methanol and Ethanol in Alkaline Media. *J. Mater. Chem. A* **2013**, *1*, 3620–3628.

7. Zhang, H.; Jin, M. S.; Wang, J. G.; Li, W. Y.; Camargo, P. H. C.; Kim, M. J.; Yang, D.; Xie, Z. X.; Xia, Y. N. Synthesis of Pd-Pt Bimetallic Nanoparticles with A Concave Structure through a Bromide-Induced Galvanic Replacement Reaction. *J. Am. Chem. Soc*. **2011**, *133*, 6078–6089.

8. Calver, C. F.; Dash, P.; Scott, R. W. J. Selective Hydrogenations with Ag-Pd Catalysts Prepared by Galvanic Exchange Reactions. *ChemCatChem* **2011**, *3*, 695–697.

9. Zhang, Q.; Xie, J.; Lee, J. Y.; Zhang, J.; Boothroyd, C. Synthesis of Ag@AgAu Metal Core/Alloy Shell Bimetallic Nanoparticles with Tunable Shell Compositions by A Galvanic Replacement Reaction. *Small* **2008**, *8*, 1067–1071.

10. Netzer, N. L.; Qiu, C.; Zhang, Y.; Lin, C.; Zhang, L.; Fong, H.; Jiang, C. Gold-Silver Bimetallic Porous Nanowires for Surface-Enhanced Raman Scattering. *ChemComm* **2011**, *47*, 9606–9608.

11. Sun, Y. Silver Nanowires-Unique Templates for Functional Naostructures. *Nanoscale* **2010**, *2*, 1626–1624.

12. Zhou, S.; Johnson, M.; Veinot, J. G. C. Iron/Iron Oxide Nanoparticles: a Versatile Support for Catalytic Metals and Their Application in Suzuki-Miyaura Cross-Coupling Reactions. *Chem. Comm*. **2010**, *46*, 2411–2413.

13. Hudson, R.; Li, C.-J.; Moores, A. Magnetic Copper-Iron Nanoparticles as Simple Heterogeneous Catalysts for the Azide-Alkyne Click Reaction in Water. *Green Chem*. **2012**, *14*, 622–624.

14. Hudson, R.; Chazelle, V.; Bateman, M.; Roy, R.; Li, C.-J.; Moores, A. Sustainable Synthesis of Magnetic Ruthenium-Coated Iron Nanoparticles and Application in the Catalytic Transfer Hydrogenation of Ketones. *ACS Sustain. Chem. Eng*. **2015**, *3*, 814–820.

15. Zhang, Y.; Su, Y.; Zhou, X.; Dai, C.; Keller, A. A. A New Insight on the Core-Shell Structure of Zerovalent Iron Nanoparticles and Its Application for Pb(II) Sequestration. *J. Hazard. Mater.* **2013**, *263*, 685–693.

16. Yan, W.; Herzing, A. A.; Kiely, C. J.; Zhang, W. Nanoscale Zero-Valent Iron (nZVI): Aspects of the Core-Shell Structure and Reactions with Inorganic Species in Water. *J. Contam. Hydrol.* **2013**, *15*, 2141–2148.

17. Li, X.; Zhang, W. Iron Nanoparticles: the Core-Shell Structure and Unique Properties for Ni(II) Sequestration. *Langmuir* **2006**, *22*, 4638–4642.

18. Yan, W.; Vasic, R.; Frenkel, A. I.; Koel, B. E. Intraparticle Reduction of Arsenite (As(III)) by Nanoscale Zerovalent Iron (nZVI) Investigated with *in Situ* X-ray Absorption Spectroscopy. *Environ. Sci. Technol.* **2012**, *46*, 7018–7026.

19. Zhang, W. *J.* Nanoscale Iron Particles for Environmental Remediation: an Overview. *Nanopart. Res*. **2003**, *5*, 323–332.

20. Hudson, R.; Hamsaka, G.; Osako, T.; Yamada, Y. M. A.; Li, C. J.; Uozumi, Y.; Moores, A. Highly Efficient Iron(0) Nanoparticle-catalyzed Hydrogenation in Water in Flow. *Green Chem.* **2013**, *15*, 2141–2148.

21. Glavee, G. N.; Klabunde, K. J.; Sorensen, C. M.; Hadjipanayis, G. C. Chemistry of Borohydride Reduction of Iron(II) and Iron(III) Ions in Aqueous and Nonaqueous Media. Formation of Nanoscale Fe, FeB, and Fe_2B Powders. *Inorg Chem*. **1995**, *34*, 28–35.

22. Sun, Y. P.; Li, X. Q.; Cao, J. S.; Zhang, W. X.; Wang, H. P. Characterization of Zero-Valent Iron Nanoparticles. *Adv. Colloid Interface Sci*. **2006**, *120*, 47-56.

23. Kovács, S.; Zih-Perényi, K.; Révész, Á.; Novák, Z. Copper on Iron: Catalyst and Scavenger for Azide-Alkyne Cycloaddition. *Synthesis* **2012**, *44*, 3722–3730.

24. Ishikawa, S.; Hudson, R.; Masnadi, M.; Bateman, M.; Castonguay, A.; Braidy, N.; Moores, A.; Li, C. Cyclopropanation of Diazoesters with Styrene Derivatives Catalyzed by Magnetically Recoverable Copper-Plated Iron Nanoparticles. *Tetrahedron* **2014**, *70*, 8952–8958.

25. Kovács, S.; Novák, Z. Oxidoreductive Coupling of Thiols with Aryl Halides Catalyzed by Copper on Iron. *Org. Biomol. Chem.* **2011**, *9*, 711–716.

26. Macdonald, J. E.; Kelly, J. A.; Veinot, J. G. C. Iron/Iron Oxide Nanoparticle Sequestration of Catalytic Metal Impurities from Aqueous Media and Organic Reaction Products. *Langmuir* **2007**, *23*, 9543–9545.

27. Yao, Y.; Hu, Y.; Scott, R. W. J. Watching Iron Nanoparticles Rust: An *in Situ* X-ray Absorption Spectroscopic Study. *J. Phys. Chem. C* **2014**, *118*, 22371–22324.

28. Balcha, T.; Strobl, J. R.; Fowler, C.; Dash, P.; Scott, R. W. J. Selective Aerobic Oxidation of Crotyl Alcohol Using AuPd Core-Shell Nanoparticles. *ACS Catal*. **2011**, *1*, 425–436.

29. Shi, H.; Lercher, J. A.; Yu, X. Sailing into Uncharted Waters: Recent Advances in the *in Situ* Monitoring of Catalytic Processes in Aqueous Environments. *Catal. Sci. Technol*. **2015**, *5*, 3035–3060.

30. Dreher, M.; Johnson, B.; Peterson, A. A.; Nachtegaal. M.; Wambach, J.; Vogel, F. Catalysis in Supercritical Water: Pathway of the Methanation Reaction and Sulfur Poisoning over A Ru/C Catalyst During the Reforming of Biomolecules. *J. Catal.* **2013**, *301*, 38–45.

31. Yao, T.; Liu, S.; Sun, Z.; Li, Y.; He, S.; Cheng, H.; Xie, Y.; Liu, Q.; Jiang, Y.; Wu, Z.; *et al*. Probing Nucleation Pathways for Morphological Manipulation of Platinum Nanocrystals. *J. Am. Chem. Soc*. **2012**, *134*, 9410–9416.

32. Tupy, S. A.; Karim, A. M.; Bagia, C.; Deng, W.; Huang, Y.; Dionisios, G. V.; Chen, J. G. Correlating Ethylene Glycol Reforming Activity with in Situ EXAFS Detection of Ni

Segregation in Supported NiPt Bimetallic Catalysts. *ACS Catal*. **2012**, *2*, 2290–2296.

33. Lee, A. F.; Ellis, P. J.; Fairlamb, I. J. S.; Wilson, K. Surface Catalysed Suzuki-Miyaura Cross-Coupling by Pd Nanoparticles: An Operando XAS Study. *Dalton Trans*. **2010**, *39*, 10473–10482.

34. Nelson, R. C.; Miller, J. T. An Introduction to X-ray Absorption Spectroscopy and Its *in Situ* Application to Organometallic Compounds and Homogeneous Catalysts. *Catal. Sci. Technol*. **2012**, *2*, 461-470.

35. Krishna, K. S.; Navin, C. V.; Biswas, S.; Singh, V; Ham, K.; Bovenkamp, G. L.; Theegala, C. S.; Miller, J. T.; Spivey, J. J; Kumar, C. S. S. R. Microfluidics for Time-resolved Mapping of the Growth of Gold Nanostructures. *J. Am. Chem. Soc.* **2013**, *135*, 5450–5456.

36. Anderson, R. M.; Zhang, L.; Loussaert, J. A.; Frenkel, A. I.; Henkelman, G.; Crooks, R. M. An Experimental and Theoretical Investigation of the Inversion of Pd@Pt Core@Shell Dendrimer-Encapsulated Nanoparticles. *ACS Nano* **2013**, *10*, 9345–9353.

37. Abramoff, M. D.; Magalhães, P. J.; Ram, S. J. Image Processing with ImageJ. *Biophotonics Int*. **2004**, *11*, 36–42.

38. Newville, M. IFEFFIT: Interactive XAFS Analysis and FEFF Fitting. *J. Synchrotron Radiat*. **2001**, *8*, 322–324.

39. Ravel, B.; Newville, M. ATHENA, ARTEMIS, HEPHAESTUS: Data Analysis for X-ray Absorption Spectroscopy Using IFEFFIT. *J. Synchrotron Radiat*. **2005**, *12*, 537–541.

40. Li, X.; Elliott, D. W.; Zhang, W. Zero-Valent Iron Nanoparticles for Abatement of Environmental Pollutants: Materials and Engineering Aspects. *Crit. Rev. Environ. Sci. Technol*. **2006**, *31*, 111–122.

41. Cabot, A.; Puntes, V. F.; Shevchenko, E.; Yin, Y.; Balcells, L.; Marcus, M. A.; Hughes, S. M.; Alivisatos, P. A. Vacancy Coalescence during Oxidation of Iron Nanoparticles. *J. Am. Chem. Soc*. **2007**, *129*, 10358–10360.

42. Huang, J.; Chen, W.; Zhao, W.; Li. Y.; Li, X.; Chen, C. One-Dimensional Chainlike Arrays of Fe_3O_4 Hollow Nanospheres Synthesized by Aging Iron Nanoparticles in Aqueous Solution. *J. Phys. Chem. C* **2009**, *113*, 12067–12071.

43. Masnadi, M.; Yao, N.; Braidy, N.; Moores, A. Cu(II) Galvanic Reduction and Deposition onto Iron Nano- and Microparticles: Resulting Morphologies and Growth Mechanisms. *Langmuir* **2015**, *31*, 789–798.

44. *CRC Handbook of Chemistry and Physics*, CRC Press, Cleveland, OH, 96th edition, **2010**.

45. Shivhare, A.; Chevrier, D. M.; Purves, R. W.; Scott, R. W. J. Following the Thermal Activation of $Au_{25}(SR)_{18}$ Clusters for Catalysis by X-ray Absorption Spectroscopy. *J. Phys. Chem. C* **2013**, *117*, 20007–20016.

46. Maclennan, A.; Banerjee, A.; Hu, Y.; Miller, J. T.; Scott, R. W. J. *In Situ* X-ray Absorption Spectroscopic Analysis of Gold-Palladium Bimetallic Nanoparticle Catalysts. *ACS Catal.* **2013**, *3*, 1411–1419.

47. Liu, L.; Burnyeat, C. A.; Lepsenyi, R. S.; Nwabuko, I. O.; Kelly, T. L. Mechanism of Shape Evolution in Ag Nanoprisms Stabilized by Thiol-Terminated Poly(ethylene glycol): An *in Situ* Kinetic Study. *Chem. Mater.* **2013**, *25*, 4206–4214.

CHAPTER 4

4. *In situ* X-ray absorption spectroscopic studies of magnetic $Fe@Fe_xO_y/Pd$ nanoparticle catalysts for hydrogenation reactions

This is a continuation of work described in Chapter 3 where 50:1, 20:1 and 5:1 $Fe@Fe_xO_y/Pd$ nanoparticles have been synthesized and their structures have been determined well by TEM and X-ray absorption spectroscopy. In this work, I applied these nanoparticles for the hydrogenation of 2-methyl-3-buten-2-ol. The 50:1 and 20:1 $Fe@Fe_xO_y/Pd$ NPs could be magnetically recovered after the catalytic reactions, and also could be agitated in a reaction solution via a magnetic field to improve mass transfer of reagents. The 5:1 $Fe@Fe_xO_y/Pd$ nanocatalysts in ethanol exhibit a high TOF of 3600 h^{-1} for the hydrogenation. Fe K-edge XAS shows that Fe(0) in $Fe@Fe_xO_y/Pd$ NPs can be oxidized by water, while they are stable in ethanol.

This work has been published in Catalysis Today, 2017, doi: org/10.1016/j.cattod.2017.02.049, in press. This work has been co-authored with Stefano Rubino (2rd author) and Byron D. Gates (3th author) who did the EDX mapping. William Barrett is thanked for assistance with some of the hydrogenation reactions. I am the major contributor of the experimental work and wrote the first draft of the manuscript. The final manuscript was submitted for publication after revisions by Dr. Yongfeng Hu and Dr. Robert W. J. Scott.

4.1 Abstract

Core@shell Fe@Fe_xO_y nanoparticles (NPs) have attracted a great deal of interest as potential magnetic supports for catalytic metals via galvanic exchange reactions. In this study Fe@Fe_xO_y/Pd bimetallic NPs were synthesized through galvanic exchange reactions using 50:1, 20:1 and 5:1 molar ratios of Fe@Fe_xO_y NPs to $Pd(NO_3)_2$. The resulting Fe@Fe_xO_y/Pd NPs have Pd NPs on the Fe oxide surfaces, and still retain their response to external magnetic fields. The materials could be recovered after the reaction by an external magnetic field, and agitation of the solution via a magnetic field led to improvements of mass transfer of the substrates to the catalyst surface for hydrogenation reactions. The Fe@Fe_xO_y/Pd NPs derived from the 5:1 molar ratio of their respective salts (Fe:Pd) exhibited a higher catalytic activity than particles synthesized from 20:1 and 50:1 molar ratios for the hydrogenation of 2-methyl-3-buten-2-ol. The highest turnover frequency reached 3600 h^{-1} using ethanol as a solvent. *In situ* XANES spectra show that the Fe@Fe_xO_y NPs in the Fe@Fe_xO_y/Pd system are easily oxidized when dispersed in water, while they are very stable if ethanol is used as a solvent. This oxidative stability has important implications for the sustainable use of such particles in real world applications.

4.2 Introduction

Nanoparticles (NPs) can have dramatically different properties compared to their bulk counterparts due to their large surface-to-volume ratios and size-dependent electronic properties.[1,2] They have broad applications in catalysis, drug delivery, and environmental remediation.[3-6] Because of their small sizes, the separation of NPs from solutions after applications can be particularly problematic. Magnetic Fe or Fe oxide NPs have attracted tremendous attention, because they can be isolated from the liquid medium by simply applying an external magnetic field.[7-9] Moreover, Fe or Fe oxide NPs can respond to common magnetic stirrers, which opens up the possibilities of using them as nanoscale magnetic stir bars for mass transfer acceleration in microfluidic systems. For example, Chen's group assembled Fe_3O_4 NPs to form 1D chains preserved in a shell of silica.[10] The resulting Fe_3O_4 chains remain suspended and stir independently within a small liquid droplet. Song's group grafted Pd NPs on the

surfaces of Fe_3O_4 nanochains using poly(cryclotriphosphazene-*co*-4,4'-sulfonyldiphenol) (PZS), and applied these nanochains as catalysts and nanometer-sized magnetic stir bars for microscopic hydrogenation reactions.[11] Considering that metallic Fe NPs also have interesting magnetic behavior, further studies into their magnetic performance and stability are required for applications in catalysis and microfluidic research.

Both Fe(0) and Fe(II) have relatively low standard electrode potentials (Fe^{2+}/Fe^0, $E^o_{½}$ = -0.447 V, Fe^{3+}/Fe^{2+}, $E^o_{½}$ = 0.771 V), so they can be used to reduce another metal onto their surfaces to form bimetallic NPs through galvanic exchange reactions.[12] Many bimetallic NPs, such as FePd, FeCu, FeRu, have been synthesized successfully by this method.[13-16] Recently, we showed that $Fe@Fe_xO_y$ NPs are very effective reductants for galvanic exchange reactions which can fully reduce Pd or Cu salts onto their surfaces to form Pd or Cu NPs.[17] We also demonstrated that these galvanic reactions can be monitored by *in situ* X-ray absorption spectroscopy (XAS). Depending on the metal deposited on the $Fe@Fe_xO_y$ NPs, the resulting bimetallic NPs can be used to further catalyze a variety of organic reactions. For example, Moores' group has shown that $Fe@Fe_xO_y@Cu$ NPs are active for the heterogeneous azide-alkyne click reactions and the cyclopropanation of diazoesters with styrene derivatives,[14,18] and Zhou and coworkers have reported that $Fe@Fe_xO_y@Pd$ NPs are active catalysts for Suzuki-Miyaura cross-coupling reactions.[13] Pd can catalyze not only C-C coupling reactions, but also a myriad of hydrogenation reactions, and Pd/C is widely used as a catalyst for hydrogenation reactions.[19-21] A variety of supports have also been investigated to further improve the catalytic activity, stability and selectivity of Pd sites in different hydrogenation reactions. He and coworkers reported that covalent triazine (CTF) framework-supported Pd NPs exhibit *ca*. 3.6 times faster reaction rates than Pd/C for the catalytic hydrogenation of N-methylpyrrole; the accelerated rate was attributed to intensified electronic interactions between the Pd NPs and the CTF.[22] The Fe_3O_4-PZS-Pd nanochains show much better stability during cycling tests for the hydrogenation of styrene in comparison with commercial Pd/C, because the interaction between PZS and Pd can efficiently prevent the aggregation of Pd NPs and the magnetic Fe_3O_4 component can assist with recovering these nanomaterials with almost no loss.[11] Studies of Fe-supported Pd NPs for catalytic hydrogenations are rare.[23] For many applications of the

bimetallic NPs based on Fe as mentioned above, it is of great interest to investigate the performance of $Fe@Fe_xO_y@Pd$ NPs for hydrogenation reactions.

The study of the nature of a catalyst and the identity of its active site is important to improve its performance in catalytic reactions. *In situ* and *operando* characterizations of catalysts have been widely practiced by researchers, because they can directly probe catalysts under working conditions. Among various *in situ* techniques, X-ray absorption near edge structure (XANES) spectra are sensitive to the oxidation state and coordination environment of an element and can be used to probe short-range order within materials, and thus it is a useful technique for the characterization of metal NPs in solution.[24-27] We have previously shown that both Fe metal oxidation and galvanic redox reactions of $Fe@Fe_xO_y$ particles with Pd(II) and Cu(II) can be followed by *in situ* XANES.[17,28] Coordination environment changes can also be followed; for example, recently we monitored the reaction of Pd(II) acetate with $Au_{25}(SC_8H_9)_{18}^-$ clusters, and found that Pd(II) acetate was converted to Pd(II) thiolate species through the reaction with S atoms in the staple motifs (-S-Au-S-Au-S-) of the $Au_{25}(SC_8H_9)_{18}^-$ clusters as determined from the changes in the XANES spectra.[29] Based on the results of *in situ* Au L_3-edge XANES spectra on supported-partially oxidized Au NPs, Haider *et al*. proposed that metallic Au is the active species in the aerobic liquid-phase oxidation of alcohols. The conversion of 1-phenylethanol in the oxidation reaction increased with the concomitant reduction of Au species and did not decrease even after the disappearance of oxidized Au species.[30]

Herein, we have synthesized $Fe@Fe_xO_y$/Pd NPs with different molar ratios of Fe to Pd (50:1, 20:1 and 5:1) through galvanic exchange reactions. We also applied the resulting $Fe@Fe_xO_y$/Pd NPs for the hydrogenation of 2-methyl-3-buten-2-ol in a solution of either water or ethanol, and showed they could be magnetically recovered and/or agitated during the reaction. Additionally, we carried out *in situ* XANES experiments to study catalytic speciation in different solvents during the hydrogenation reaction, to better understand differences in catalytic behavior in the different solvents. The magnetic response of 50:1 and 20:1 $Fe@Fe_xO_y$/Pd NPs shows that they hold promise for the design of real nanometer-sized magnetic stir bars for microscopic reactions. The results of the studies indicated that

$Fe@Fe_xO_y$/Pd NPs have a higher catalytic activity in ethanol compared to water for hydrogenation reactions, and *in situ* XANES experiments reveal that these NPs are more stable in ethanol solution, whereas further oxidation of the Fe cores occurs in the presence of water

4.3 Experimental Section

4.3.1 Materials

All chemicals were used as received without further purification. Fe(II) sulfate heptahydrate, methylene blue and 2-methyl-2-butanol were purchased from Sigma-Aldrich. Poly(vinylpyrrolidone) (M. W. 58,000 g/mol), 2-methyl-3-buten-2-ol and Pd(II) nitrate hydrate were purchased from Alfa Aesar. Sodium borohydride, ethanol and methanol (HPLC grade) were purchased from Fisher Scientific. Sulfuric acid was purchased from EMD Millipore. Eighteen MΩ·cm Milli-Q water (Millipore, Bedford, MA) was used for all syntheses.

4.3.2 Synthesis

$Fe@Fe_xO_y$ NPs were synthesized by reducing $FeSO_4 \cdot 7H_2O$ (5.0 mmol) by $NaBH_4$ (25 mmol) in a 1:1 water/methanol (v/v) mixture (20 mL) in the presence of PVP (10 mmol based on monomer unit) under nitrogen gas as previously reported.[28] First a 100 mL round bottom flask with an $FeSO_4 \cdot 7H_2O$ solution (8 mL in water) was purged by nitrogen gas, then a PVP solution (10 mL in methanol) was added to the flask and the mixture was stirred for 10 min. Finally, a solution of $NaBH_4$ (2 mL in water) was added dropwise. After 30 min stirring, 5.0 mL of 1 M H_2SO_4 was added to remove any excess $NaBH_4$ before injecting a Pd(II) nitrate solution (20 mM) to react with the $Fe@Fe_xO_y$ NPs by galvanic exchange reactions, following our previous method.[17]

4.3.3 Catalytic Reactions

4.3.3.1 Hydrogenation of Methylene Blue

A solution of $NaBH_4$ with $Fe@Fe_xO_y$/Pd NPs was prepared by dispersing 0.50 mL of the above solution of $Fe@Fe_xO_y$/Pd NPs and 0.038g sodium borohydride in 10 mL water. A 25 μL

aliquot of this mixture was injected into a 25 μL methylene blue solution (0.050 mM), which was dropped onto a hydrophobic Teflon plate located on top of a magnetic stirrer.

4.3.3.2 Hydrogenation of 2-methyl-3-buten-2-ol

A solution of 0.010 mmol Fe@Fe_xO_y/Pd NPs (molar concentration determined based on Pd content) in 5.0 mL water was added to a round bottom flask filled with 1.1 atm hydrogen gas. To this solution, a 0.20 mL 2-methyl-3-buten-2-ol (1.9 mmol) solution was added to obtain a 190:1 substrate to catalyst molar ratio. The pressure was monitored by a differential pressure manometer (407910, Extech Instrument), and the reaction progress was also followed by ^1H NMR by extracting products from the reaction solutions with 2 mL aliquots of $CDCl_3$. Turnover frequencies (TOFs) were measured by plotting either product conversion or H_2 consumption (as a proxy for product conversion, a direct correspondence between NMR results and H_2 pressure decay was always observed) over reaction time. These results are reported in either (moles product formed/ moles Pd)/time or (moles H_2 consumed/moles Pd)/time.

4.3.4 Characterization

Transmission electron microscopy (TEM) analyses of the NPs were initially conducted using a HT7700 microscope (Hitachi High-Technologies) operating at 100 kV. The samples were prepared by drop-casting one drop of dilute, aqueous sample onto a carbon-coated 200 mesh copper grid (Electron Microscopy Sciences, Hatfield, PA).

Elemental maps were obtained using an FEI Osiris STEM equipped with ChemiSTEM Technology integrating the signal from four Energy Dispersive X-ray (EDX) spectrometers. A 200 kV electron beam was focused to a nanometer-sized spot and scanned across the sample to excite electrons from the core shells. As the electron beam is raster scanned across the sample, a full X-ray spectrum is collected for each pixel. By selecting the appropriate energy window, a specific element is selected and its distribution in the sample can be displayed as an elemental map. By selecting several windows, different elemental maps can be obtained simultaneously from a single scan, provided that the ionization energies do not significantly overlap. False color maps can be also superimposed to determine where two or more elements

coexist and in what relative amount. Scanning time and beam intensity were chosen as a compromise between signal-to-noise ratio and radiation damage to the sample.

Fe K-edge and Pd L-edge XANES spectra were collected at the Soft X-ray Microcharacterization Beamline (SXRMB) at the Canadian Light Source (CLS). The measurements were conducted under an ambient atmosphere for observing the Fe K-edge and under helium for obtaining the Pd L_3-edge spectra. Decreasing the beam flux by defocusing and/or filtering the beam with Kapton filters and stirring the sample via magnetic stirring were used to avoid sample damage due to photoreduction. Liquid cells (SPEX CertiPrep Disposable XRF X-Cell sample cups) were covered with a 4 μm ultralene film (purchased from Fisher Scientific, Ottawa, ON) and used for XANES analysis. The data were analyzed using the Athena software.[31,32] Fe foil transmission spectrum and fluorescence spectra of $FeSO_4 \cdot 7H_2O$ and $Fe(NO_3)_3 \cdot 9H_2O$ aqueous solutions (50 mM) were measured under the same conditions and used as standards for linear combination analysis XANES fitting in the range of 7100 to 7150 eV. The R-factors on the mismatch between data and fit are all lower than 0.001.

The ^1H NMR spectra were recorded in $CDCl_3$ on a Bruker 500 MHz Advance NMR spectrometer. Chemical shifts were recorded in parts per million (ppm), using the residual solvent peak for calibration. The composition of the reaction mixture was analyzed by a gas chromatography (GC, Agilent Technologies 7890A) with a flame ionization detector and a HP-5 capillary column (30 m × 0.32 mm × 0.25 μm, J&W Scientific).

4.4 Results and Discussion

The Fe@Fe_xO_y NPs (16.0 ± 6.0 nm) were synthesized by reducing $FeSO_4 \cdot 7H_2O$ with $NaBH_4$ in a mixture of ethanol and water (1:1 volume ratio) containing PVP as a stabilizer.[28] Different molar ratios of Fe@Fe_xO_y/Pd (prepared as 50:1, 20:1, and 5:1 based on Fe:Pd molar ratios) NPs were synthesized by mixing the solution of Fe@Fe_xO_y NPs with a Pd(II) nitrate solution under nitrogen gas purging as described previously.[17] Figure 4.1 A and 4.1 C show dark field STEM images of the particles synthesized at the 20:1 and 5:1 Fe:Pd molar ratios, respectively. As seen previously, the Fe@Fe_xO_y particles self-assemble into larger chain-like nanostructures, presumably due to magnetic interactions between particles in solution.[28] As

shown in the STEM elemental maps (Figure 4.1 B), the 20:1 $Fe@Fe_xO_y$/Pd NPs have isolated small Pd NPs (3 ± 2 nm) deposited on the surfaces of the $Fe@Fe_xO_y$ NPs. In the system of 5:1 $Fe@Fe_xO_y$/Pd NPs most of the $Fe@Fe_xO_y$ NPs have been consumed in the galvanic exchange formation, leaving a hybrid material that contains a fairly well-dispersed Pd on the surfaces of these Fe oxide supports (Figure 4.1 D). It was very difficult to resolve individual Pd NPs in the samples containing a higher Pd loading.

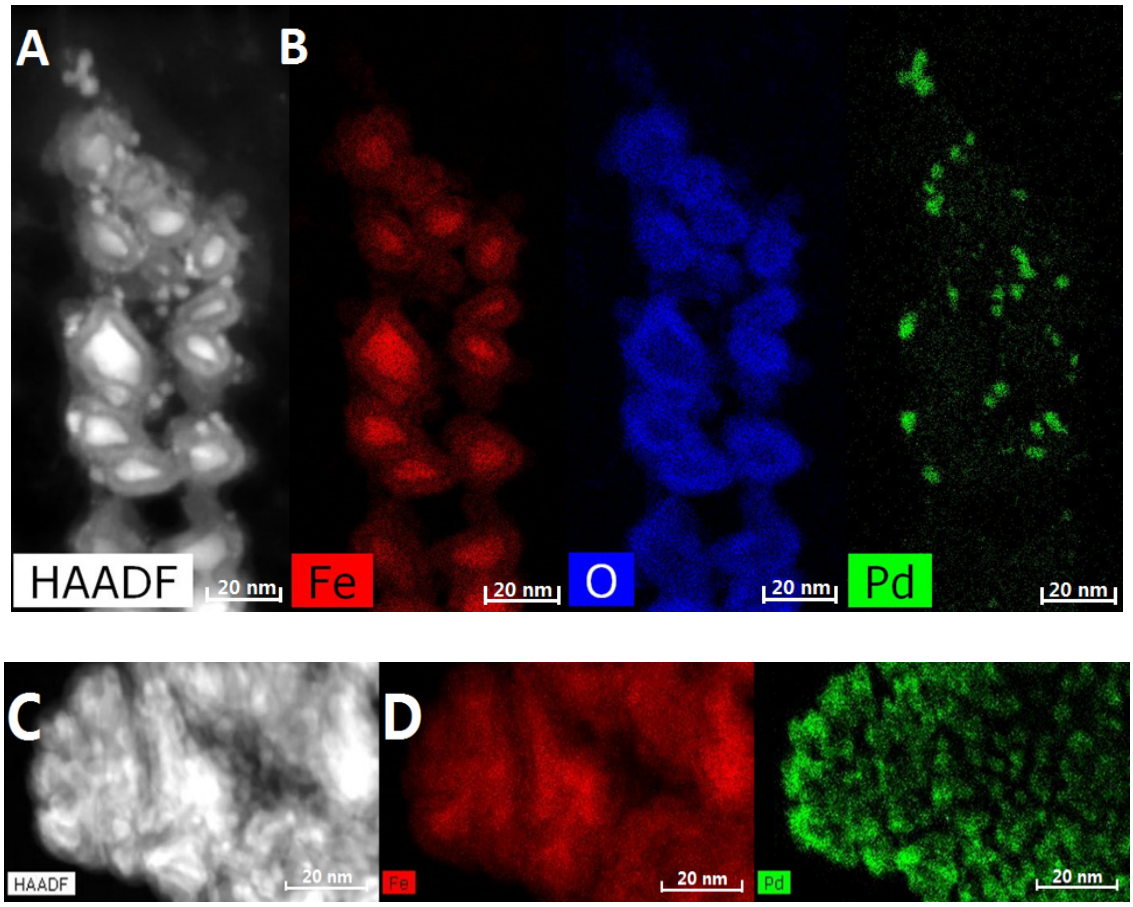

Figure 4.1. High-angle annular dark-field STEM images and EDX elemental maps of the $Fe@Fe_xO_y$/Pd NPs prepared from 20:1 (A and B) and 5:1 (C and D) molar ratios of $Fe@Fe_xO_y$ NPs to Pd(II).

Fe supported bimetallic NPs have been applied in a variety of catalytic reactions.[13-16,33,34] The presence of Fe in these bimetallic NPs not only allows them to be easily separated from reaction solutions by an external magnet, but they can also act as a redox scavenger to redeposit

the leached metal and avoid the contamination of the organic product. Fe atoms have a strong magnetic moment due to their high number of unpaired 3d electrons, thus Fe and Fe oxide materials exhibit strong magnetic properties.[35] The large surface area to volume ratio of Fe and Fe oxide NPs can result in increased remanence and coercivity and can give these NPs improved magnetic properties in comparison to their bulk counterparts.[36,37] The fact that the original Fe@Fe_xO_y NPs self-assemble into larger domains may allow them to be used for stirring at the microscopic scale. Indeed this is the case for the Fe@Fe_xO_y/Pd NPs synthesized with 50:1 and 20:1 molar ratios of Fe@Fe_xO_y NPs to Pd(II). The resulting NPs have strong responses to the magnetic field of a common stir plate, and allow for a solution to be stirred in the absence of a macroscopic stir bar (Figure 4.2). However, the Fe@Fe_xO_y/Pd NPs synthesized with a 5:1 molar ratio of Fe@Fe_xO_y NPs to Pd(II) do not agitate a solution upon magnetic stirring. In addition, we examined the relative ease of magnetically separating each of the NP systems from solution. The 50:1 and 20:1 Fe@Fe_xO_y/Pd NPs could be separated by an external magnet from the reaction solutions after 9 s (Figure 4.3), while the separation of the 5:1 Fe@Fe_xO_y/Pd NPs from solution takes a much longer time (more than 30 s). These results indicate the possibility of using these bimetallic catalysts as magnetically recoverable catalysts and magnetic stirrers, provided that the Pd loading is not too high.

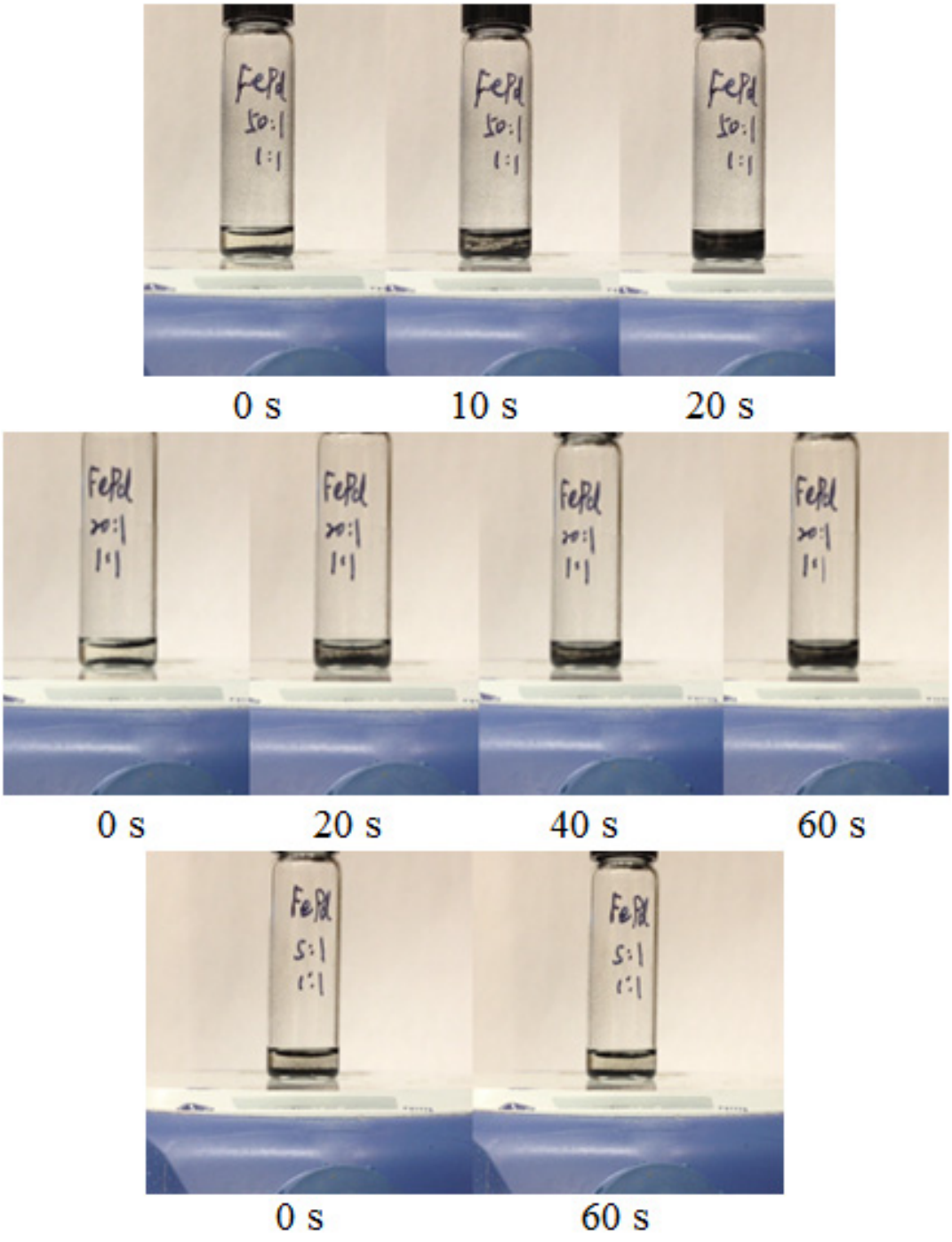

Figure 4.2. The comparison of stirring ability of different molar ratios of Fe@Fe_xO_y/Pd NPs on a magnetic stirrer at a speed of 1600 rpm.

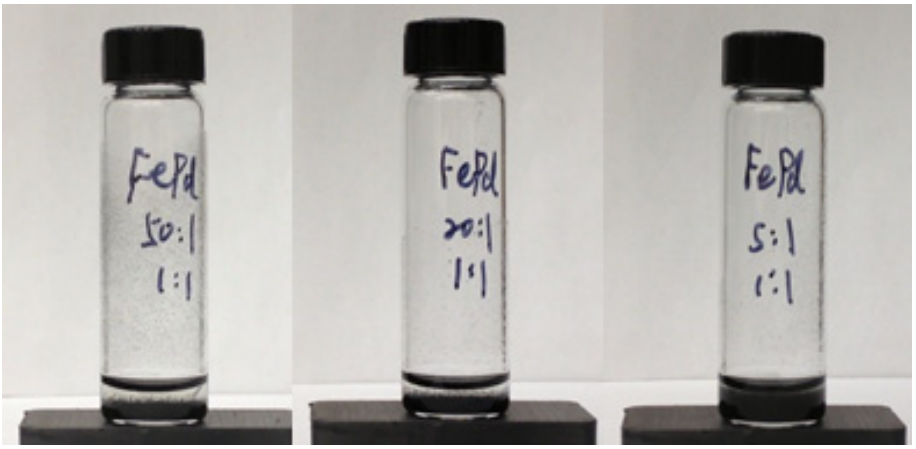

Figure 4.3. The comparison of magnetic recycling ability of different molar ratios of Fe@Fe_xO_y/Pd NPs on a magnet after 9s.

To further test whether Fe@Fe_xO_y/Pd NPs can improve the reaction rate for catalytic reactions by alleviating mass transfer issues, we applied the Fe@Fe_xO_y/Pd NPs as catalysts and microscopic stirrers for the hydrogenation of 2-methyl-3-buten-2-ol in water under a 1.1 atm H_2 gas and 25 °C (Scheme 4.1). The addition of the 50:1 Fe@Fe_xO_y/Pd NPs as catalysts yielded a TOF of 21 h^{-1} for the hydrogenation of 2-methyl-3-buten-2-ol to 2-methyl-2-butanol as determined by NMR in the absence of stirring, whereas the TOF was improved to 34 h^{-1} by stirring the solution using the 50:1 Fe@Fe_xO_y/Pd NPs (Figure 4.4). This result confirms that the NPs can improve mass-transfer of the substrates to the catalyst surface. As this test was performed on a 5 mL sample and not a droplet with a small volume, the difference between the stirred and non-stirred states is not significant. A microscopic model test system was also carried out using Fe@Fe_xO_y/Pd NPs to catalyze the hydrogenation of methylene blue (MB) within small liquid droplets. Solutions containing either 50:1 or 20:1 Fe@Fe_xO_y/Pd NPs and $NaBH_4$ were injected into the MB droplet. MB could be reduced by the $NaBH_4$ and converted to a colorless leucomethylene blue solution in 30 seconds when agitated by the 50:1 or 20:1 Fe@Fe_xO_y/Pd NPs (Figure 4.5). In comparison, it was difficult to reduce MB by the addition of $NaBH_4$ without the stirring of NPs. This study reveals that the agitation of the 50:1 and 20:1 Fe@Fe_xO_y/Pd NPs using an external magnetic field can effectively mix the reactants and improve the reaction rate.

Scheme 4.1. The hydrogenation of 2-methyl-3-buten-2-ol.

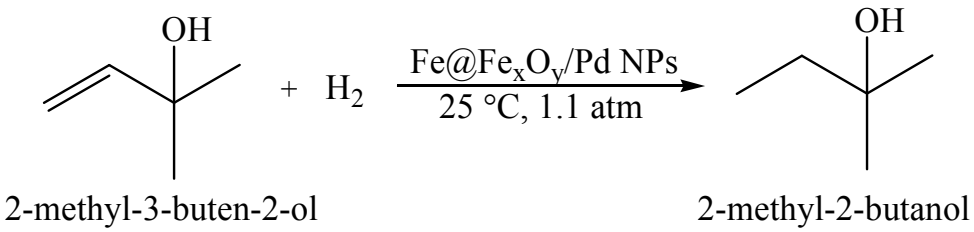

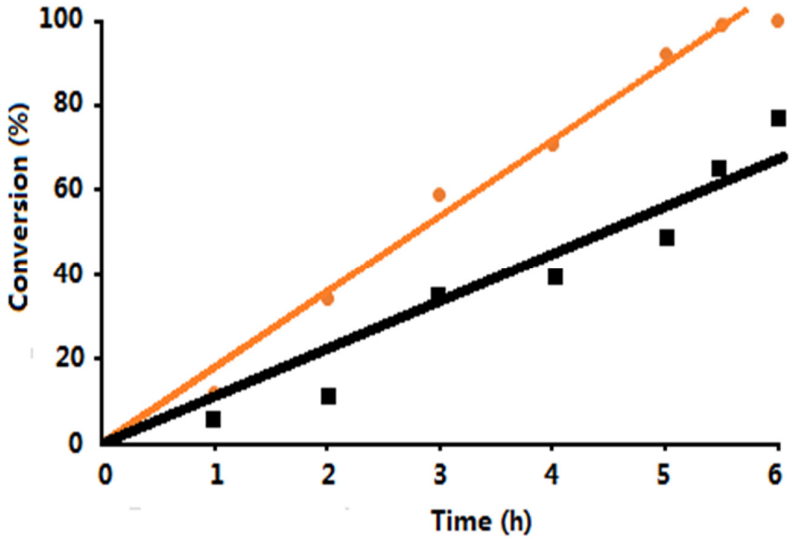

Figure 4.4. The conversion of 2-methyl-3-buten-2-ol to 2-methyl-2-butanol in the hydrogenation reaction (black square) using the 50:1 $Fe@Fe_xO_y$/Pd NPs as catalysts without stirring, and (orange dot) using 50:1 $Fe@Fe_xO_y$/Pd NPs as both catalysts and magnetic stirrers in a 5 mL solution.

50:1 Fe@Fe_xO_y/Pd NPs

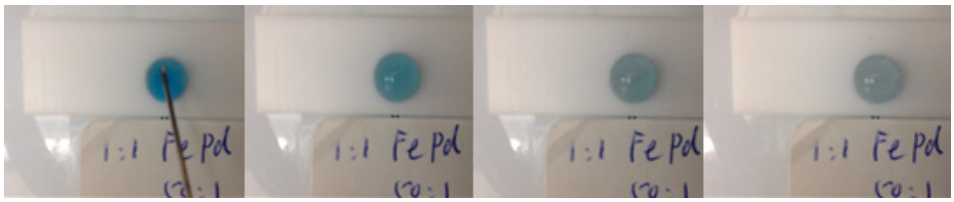

0s 10s 20s 25s

20:1 Fe@Fe_xO_y/Pd NPs

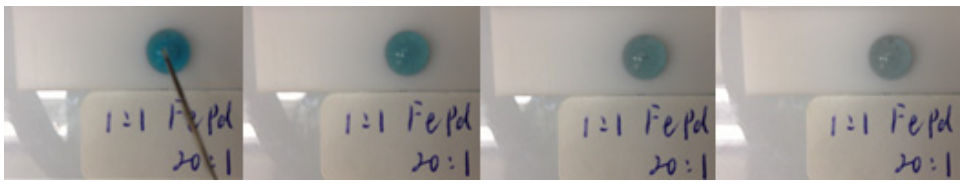

0s 10s 20s 25s

Without Fe@Fe_xO_y/Pd NPs

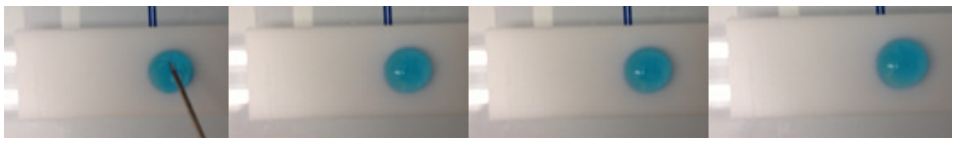

0s 10s 20s 25s

Figure 4.5. The comparison of the hydrogenation of methylene blue by $NaBH_4$ in smaller volume liquid droplet with and without the stirring of Fe@Fe_xO_y/Pd NPs.

Having established that the Fe@Fe_xO_y/Pd NPs can be effective catalysts, we sought to optimize the catalyst system in terms of the Pd loading, solvent composition, and long-term stability of the catalyst. For these studies larger volumes of solutions were used along with a macroscopic magnetic stir bar (egg shaped, 7/8 inch × 3/8 inch) rotated at 1600 rpm to minimize mass transfer effects for the hydrogenation reactions and thus better compare actual catalytic activities. The progress of the reaction was monitored by measuring the decrease in pressure of H_2 filled in a round bottom flask as a function of reaction time. When Fe@Fe_xO_y NPs (in the absence of Pd) were used as the catalyst for the hydrogenation of 2-methyl-3-buten-

2-ol in water at 1.1 atm H_2 (g) and 25 °C, there was no decrease in the pressure of H_2. However, Fe@Fe_xO_y/Pd NP catalysts (50:1, 20:1 and 5:1 Fe:Pd molar ratios) exhibit high TOFs. As shown in Figure 4.6, the reaction follows a zero order rate law, and reaches completion once all the substrate is consumed. The decrease of the moles of the H_2 gas in the reaction from 0.0482 mol to 0.0463 mol reveals that the consumption of H_2 is 1:1 with respect to the substrate 2-methyl-3-buten-2-ol (1.9 mmol used for the reaction). The 5:1 Fe@Fe_xO_y/Pd NPs showed the highest TOF (*ca.* 1300 h^{-1}) in comparison to the 50:1 and 20:1 Fe@Fe_xO_y/Pd NPs (TOF of 385 h^{-1} and 785 h^{-1}, respectively). As noted earlier, Fe@Fe_xO_y NP controls showed no activity for hydrogenations, confirming that Pd is the active catalyst for this reaction. The higher TOF of 5:1 Fe@Fe_xO_y/Pd NPs compared to 50:1 and 20:1 Fe@Fe_xO_y/Pd NPs suggests that the Pd is more dispersed and has a higher surface area for the 5:1 Fe@Fe_xO_y/Pd NPs, which is in agreement with the results of elemental EDX maps shown earlier.

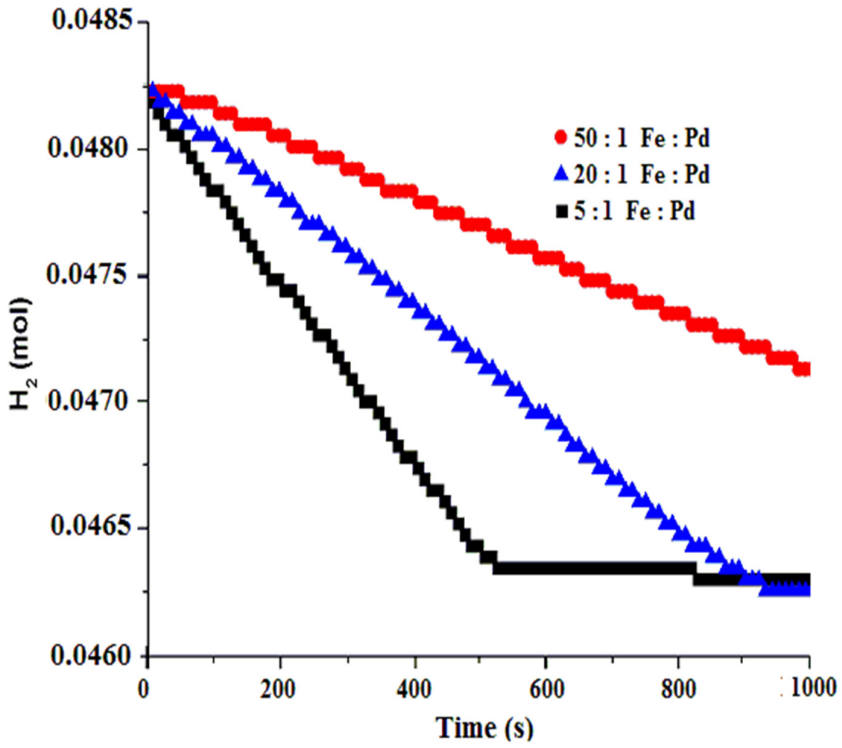

Figure 4.6. The rate of hydrogen consumption in the hydrogenation of 2-methyl-3-buten-2-ol in water using the 50:1 (red circle), 20:1 (blue triangle) and 5:1 (black square) Fe@Fe_xO_y/Pd NPs as catalysts.

The reusability of the Fe@Fe_xO_y/Pd NPs was also examined by using 20:1 Fe@Fe_xO_y/Pd NPs as an example. These NPs were recycled by isolating the NPs from solution using centrifugation. The results of this evaluation are summarized in Figure 4.7. Surprisingly, the Fe@Fe_xO_y/Pd NPs exhibited a higher catalytic activity upon recycling. However, it also became successively more difficult to fully recover the material with an external magnet. The TEM images show that there are fewer and/or significantly smaller Fe@Fe_xO_y NPs remaining in the bimetallic NPs system as the number of cycles increased (Figure 4.8). The result suggests that the Fe@Fe_xO_y NPs are degrading over time. This conclusion is also supported by *ex situ* XANES measurements, as shown in Figure 4.9. There is almost no change in the speciation of the zero-valent Pd NPs as judged by comparing the Pd L_3-edge XANES spectra after different recycling tests (Figure 4.9 A), while the Fe K-edge XANES spectra show a significant shift to higher energies upon using the catalysts over 6 cycles (Figure 4.9 B). These results are consistent with the progressive oxidation of the Fe@Fe_xO_y NPs to Fe(II) and Fe(III) oxides.[28]

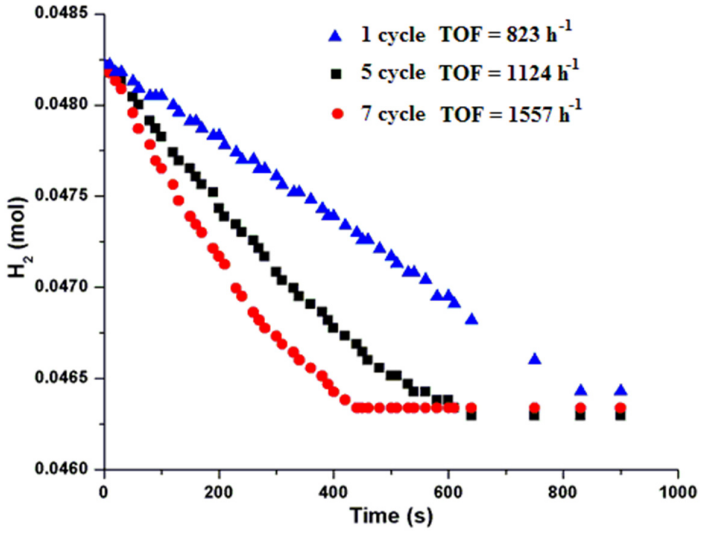

Figure 4.7. The rates of hydrogen consumption in the hydrogenation of 2-methyl-3-buten-2-ol in water using the 20:1 Fe@Fe_xO_y/Pd NPs recycled for the use in sequential catalytic cycles.

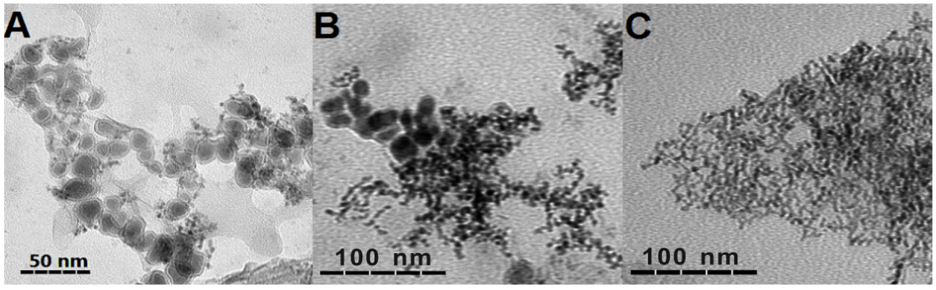

Figure 4.8. TEM images of the 20:1 Fe@Fe_xO_y/Pd NPs: (A) before hydrogenation reaction; (B) after 4 cycles; and (C) after 6 cycles.

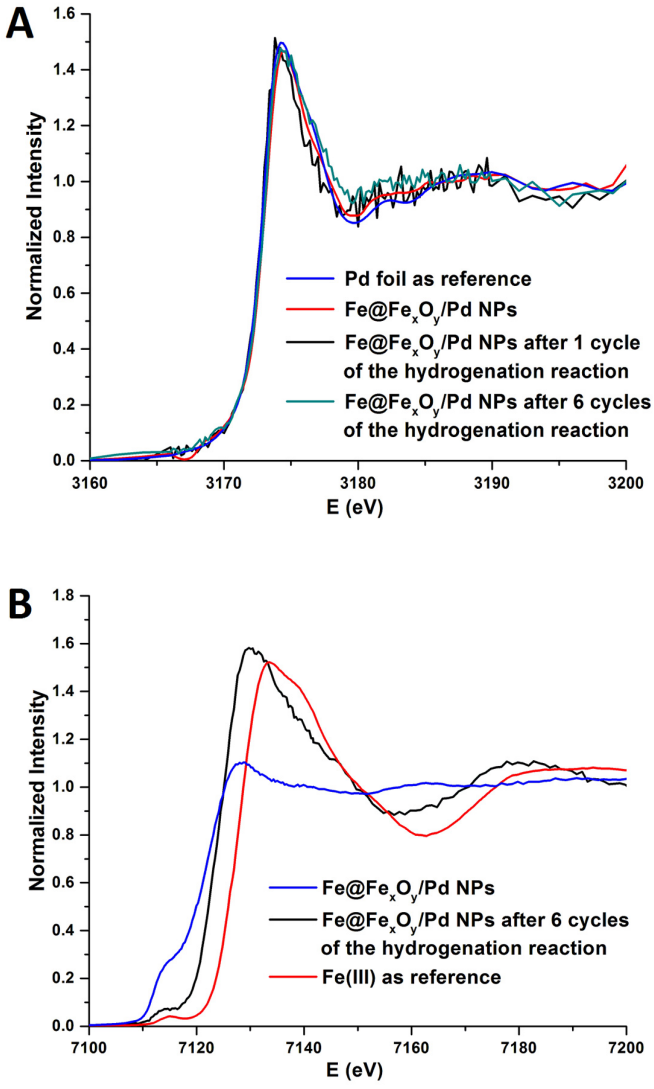

Figure 4.9. The Pd L-edge (A) and Fe K-edge (B) XANES spectra of the 20:1 molar ratio Fe@Fe_xO_y/Pd NPs.

To determine whether the oxidation of Fe@Fe_xO_y NPs takes place during the hydrogenation reaction or during the recycling process, *in situ* XANES studies were carried out. The *in situ* setup is shown in Figure 4.10, and consisted of a liquid cell loaded with Fe@Fe_xO_y NPs and 2-methyl-3-buten-2-ol in water, and placed inside an aluminum box which was located on top of a magnetic stirrer (not shown) to ensure the constant mixing of the reaction mixture. Hydrogen gas was bubbled into the liquid cell to start the reaction and the reaction was monitored at the Pd L_3-edge and Fe K-edge, as shown in Figure 4.11. No significant change of the *in situ* Pd L_3-edge XANES spectra was observed (Figure 4.11 A), which is not overly surprising as Pd typically remains in the zero-valent state during hydrogenation reactions.[38] However, slight oxidation of the Fe@Fe_xO_y NPs could be observed from *in situ* Fe K-edge XANES spectra (Figure 4.11 B). Through fitting the Fe K-edge XANES spectra using a linear combination fitting with standards (Fe foil, $FeSO_4$ and $Fe(NO_3)_3$) as we did in our previous work,[28] it is revealed that the Fe@Fe_xO_y NPs in the Fe@Fe_xO_y/Pd NP systems contain 56% Fe(0) (Table 4.1). These standards were chosen as they led to the best fits of the experimental data; we were not able to fit the data using standards involving different oxide and hydroxide phases of Fe. This Fe(0) content decreases to 49% after 30 min of the hydrogenation reaction in water, and all the Fe(0) was oxidized after 6 cycles (to 60% Fe(II) and 40% Fe(III), the fitted data from Figure 4.9 B, Table 4.2). This result indicates that the oxidation of Fe@Fe_xO_y NPs happens during the reaction. We note that water is the solvent for this reaction; water can react with exposed Fe in Fe@Fe_xO_y NPs and oxidize Fe(0) to Fe(II), which is likely the reason for oxidation of the Fe@Fe_xO_y NPs in the reaction.[39] The Fe(II) is then further oxidized to Fe(III) during the recycling process when the samples are exposed to air.

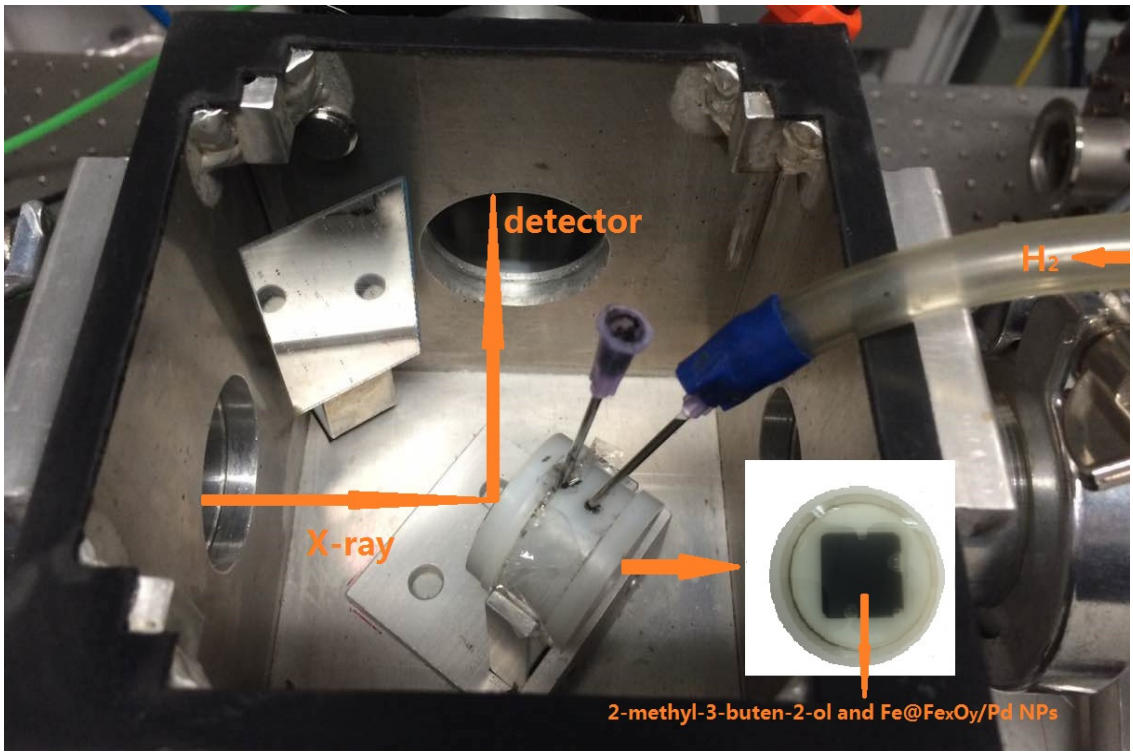

Figure 4.10. The hydrogenation setup for *in situ* fluorescence XANES studies.

Table 4.1. XANES fitting results showing mole fractions of each Fe standard depicting the changes of Fe@Fe_xO_y NPs in the Fe@Fe_xO_y/Pd NPs during the hydrogenation reaction.

Sample	Reaction Time (min)	Fe (0)%	Fe(II)%	Fe(III)%
Fe@Fe_xO_y/Pd NPs	0	56(0)	31(0)	14(1)
	15	51(0)	31(0)	18(1)
	30	49(0)	34(0)	17(1)

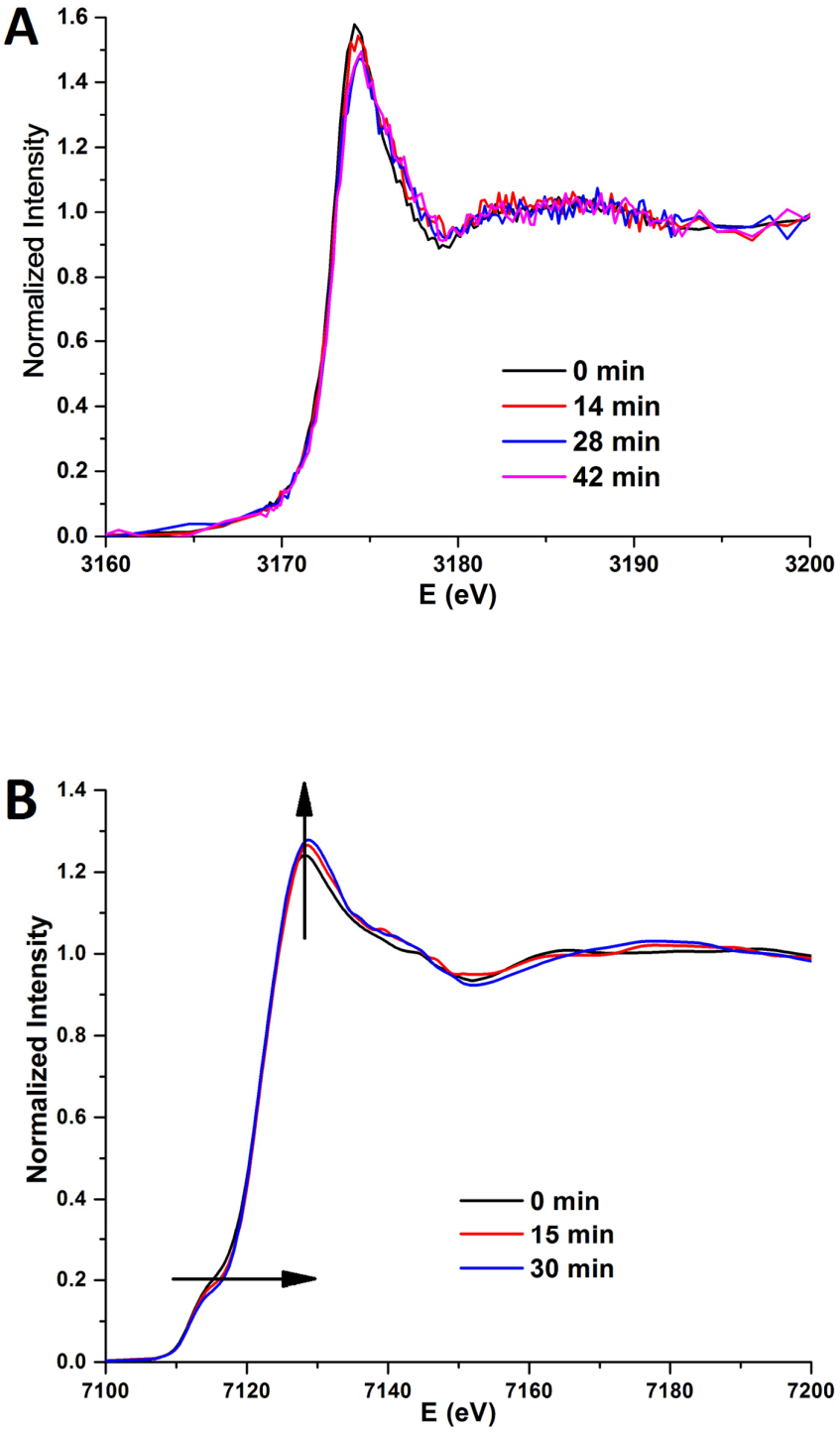

Figure 4.11. The Pd L_3-edge (A) and Fe K-edge (B) XANES spectra of the 20:1 molar ratio Fe@Fe_xO_y/Pd NPs in the hydrogenation reaction using water as a solvent.

Table 4.2. XANES fitting results showing mole fractions of each Fe standard depicting the changes to Fe@Fe_xO_y NPs in the Fe@Fe_xO_y/Pd NPs before and after 6 cycles of hydrogenation reactions.

Sample	Cycle	Fe (0)%	Fe(II)%	Fe(III)%
Fe@Fe_xO_y/Pd NPs	0	56(0)	31(0)	14(1)
	6	0(0)	60(0)	40(0)

In order to address this oxidation damage to the NPs, we switched the solvent from water to ethanol for the hydrogenation reactions, as ethanol should not react with Fe(0). The Pd L_3-edge XANES spectra indicate that the Pd NPs have no change before and after the hydrogenation reaction in ethanol (Figure 4.12). There is also no change observed in the *in situ* Fe K-edge XANES spectra (Figure 4.13). These results confirm that the Fe@Fe_xO_y NPs are quite stable in ethanol. The Fe@Fe_xO_y/Pd NPs also showed a much higher catalytic activity in ethanol than in water, as shown in Figure 4.14. The 5:1 Fe@Fe_xO_y/Pd NPs showed improvements in TOF from *ca*. 1300 h^{-1} in water to 3600 h^{-1} in ethanol, an increase of 2.8 times in magnitude. The NMR and GC results confirmed that the conversion of 2-methyl-3-buten-2-ol to 2-methylbutan-2-ol is completed in 4 min when catalyzed by 5:1 Fe@Fe_xO_y/Pd NPs with a 190:1 substrate to catalyst ratio in ethanol. No change was seen in the TOF for the hydrogenation reaction upon recycling the catalysts for three cycles in ethanol, and no significant changes were seen by TEM (Figure 4.15). This catalytic result is a very high TOF for the hydrogenation of 2-methyl-3-buten-2-ol under ambient conditions, and compares favourably with many excellent hydrogenation catalysts in the literature.[40-43] The factors determining solvent influence in the hydrogenation reactions have been studied by many groups.[38,44-48] The solubility of H_2 (g) seems to be the most significant factor influencing the rate of this reaction along with the high stability of the support in ethanol. The solubility of H_2 (2.98×10^{-3} mol/L) in ethanol is significantly higher than that in water (0.81×10^{-3} mol/L).[49] These results are also consistent with Nikoshvili group's studies on the selective and solvent

dependent hydrogenation of 2-methyl-3-butyn-2-ol to 2-methyl-3-buten-2-ol over Pd NPs stabilized in hypercrosslinked polystyrene.[38]

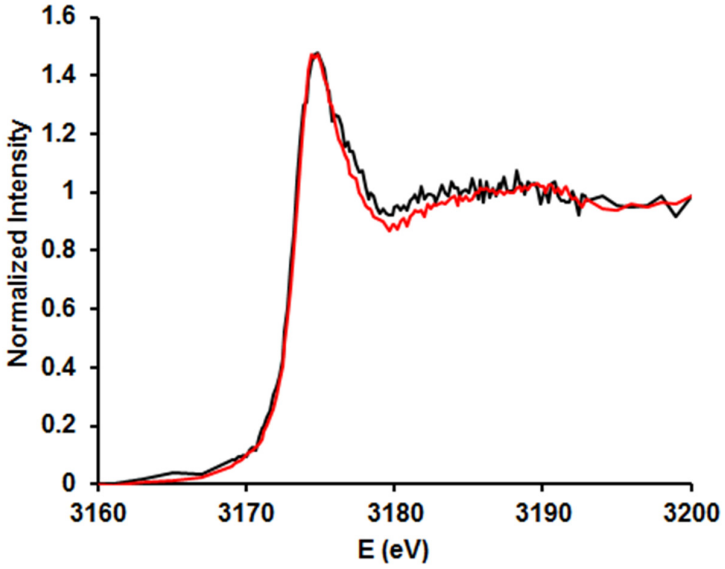

Figure 4.12. The Pd L_3-edge XANES spectra of the 20:1 Fe@Fe_xO_y/Pd NPs before (black) and after (red) a hydrogenation reaction using ethanol as a solvent.

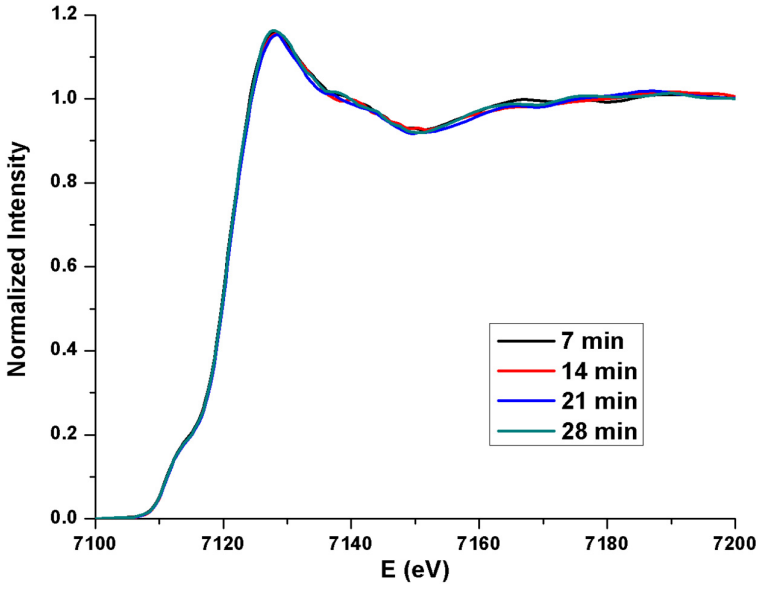

Figure 4.13. The Fe K-edge XANES spectra of the 20:1 Fe@Fe_xO_y/Pd NPs in the hydrogenation reaction using ethanol as a solvent.

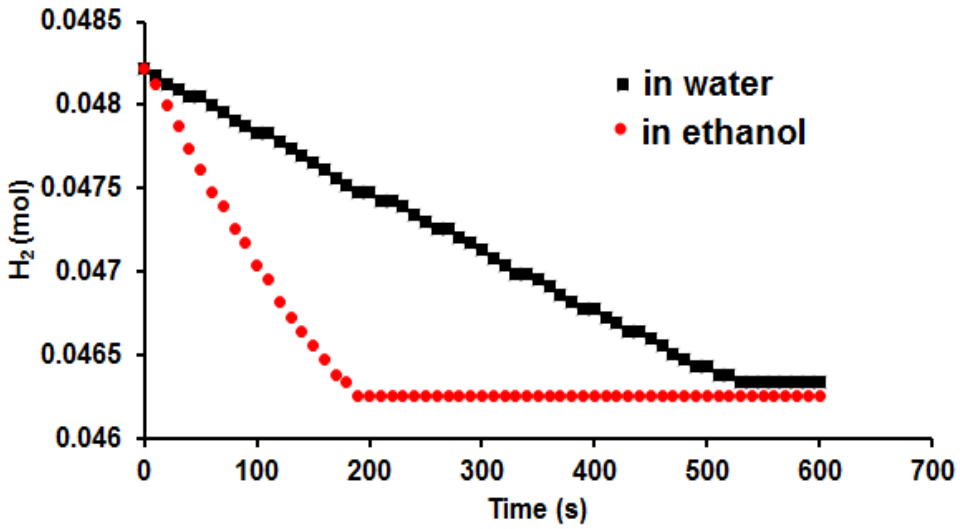

Figure 4.14. The rates of hydrogen consumption for the hydrogenation of 2-methyl-3-buten-2-ol using the 5:1 Fe@Fe_xO_y/Pd NPs as catalysts in either water or ethanol.

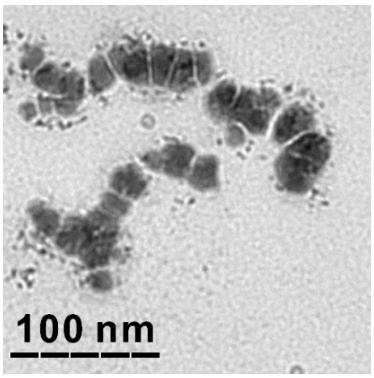

Figure 4.15. TEM images of the 20:1 Fe@Fe_xO_y/Pd NPs after 3 cycles of hydrogenation reactions in ethanol.

4.5 Conclusion

A suspension of either 50:1 or 20:1 Fe@Fe_xO_y/Pd NPs can act as both magnetically recoverable catalysts and magnetic stirrers to improve the mixing of reactants in catalytic hydrogenation reactions. For studies on the catalytic activity of the Fe@Fe_xO_y/Pd NPs for the hydrogenation of 2-methyl-3-buten-2-ol, the 5:1 molar ratio Fe@Fe_xO_y/Pd NPs exhibit a high TOF of 3600 h^{-1} using ethanol as the solvent. *In situ* XANES spectra show that water as a solvent in the hydrogenation reaction can oxidize the Fe(0) core in Fe@Fe_xO_y/Pd NPs, while

the same Fe@Fe_xO_y/Pd NPs are very stable when dispersed in ethanol. This result shows that while these composite materials have viability as low cost, magnetically recoverable catalysts, they do not have long-term stability in water which may limit their possible applications.

Acknowledgments

The authors acknowledge financial assistance from the National Sciences and Engineering Research Council of Canada (NSERC) and the Canada Research Chairs Program (B. D. Gates). XANES experiments described in this paper were performed at the Canadian Light Source, which is supported by NSERC, the National Research Council Canada, the Canadian Institutes of Health Research, the Province of Saskatchewan, Western Economic Diversification Canada, and the University of Saskatchewan. This work also made use of 4D LABS (www.4dlabs.ca) shared facilities supported by the Canada Foundation for Innovation (CFI), British Columbia Knowledge Development Fund (BCKDF), Western Economic Diversification Canada, and Simon Fraser University.

4.6 References

1. Haruta, M.; Kobayashi, T.; Sano, H.; Yamada, N. Novel Gold Catalysts for the Oxidation of Carbon Monoxide at A Temperature far Below 0 °C. *Chem. Lett.* **1987**, *2*, 405–408.
2. Jagadeesh, R. V.; Surkus, A.; Junge, H.; Pohl, M.; Radnik, J.; Huan, H.; Schünemann, V.; Brückner, A.; Beller, M. Nanoscale Fe_2O_3-Based Catalysts for Selective Hydrogenation of Nitroarenes to Anilines. *Science* **2013**, *342*, 1073–1076.
3. Zhang, H.; Jin, M.; Xia, Y. Enhancing the Catalytic and Electrocatalytic Properties of Pt-Based Catalysts by Forming Bimetallic Nanocrystals with Pd. *Chem. Soc. Rev*. **2012**, *41*, 8035–8049.
4. Sun, T.; Zhang, Y. S.; Pang, B.; Hyun, D. C.; Yang, M.; Xia, Y. Engineered Nanoparticles for Drug Delivery in Cancer Therapy. *Angew. Chem. Int. Ed*. **2014**, *53*, 12320–12364.
5. Kaur, A.; Gupta, U. A Review on Applications of Nanoparticles for the Preconcentration of Environmental Pollutants. *J. Mater. Chem.* **2009**, *19*, 8279–8289.
6. Sachan, R.; Malasi, A.; Ge, J.; Yadavali, S.; Krishna, H.; Gangopadhyay, A.; Garcia, H.; Duscher, G.; Kalyanaraman, R. Ferroplasmons: Intense Localized Surface Plasmons in Metal-Ferromagnetic Nanoparticles. *ACS Nano* **2014**, *8*, 9790–9798.
7. Schejn, A.; Mazet, T.; Falk, V.; Balan, L.; Aranda, L.; Medjahdi, G.; Schneider, R. Fe_3O_4@ZIF-8: Magnetically Recoverable Catalysts by Loading Fe_3O_4 Nanoparticles inside

a Zinc Imidazolate Framework. *Dalton Trans*. **2015**, *44*, 10136–10140.

8. Hudson, R.; Feng, Y.; Varma, R. S.; Moores, A. Bare Magnetic Nanoparticles: Sustainable Synthesis and Applications in Catalytic Organic Transformations. *Green Chem*. **2014**, *16*, 4493–4505.

9. Li, A. Y.; Kaushik, M.; Li, C.-J.; Moores, A. Microwave-Assisted Synthesis of Magnetic Carboxymethyl Cellulose-Embedded Ag-Fe_3O_4 Nanocatalysts for Selective Carbonyl Hydrogenation. *ACS Sustainable Chem. Eng*. **2016**, *4*, 965–973.

10. Chong, W. H.; Chin, L. K.; Tan, R. L. S.; Wang, H.; Liu, A. Q.; Chen, H. Stirring in Suspension: Nanometer-Sized Magnetic Stir Bars. *Angew. Chem. Int. Ed*. **2013**, *52*, 8570–8573.

11. Yang, S.; Cao, C.; Sun, Y.; Huang, P.; Wei, F.; Song, W. Nanoscale Magnetic Stirring Bars for Heterogeneous Catalysis in Microscopic Systems. *Angew. Chem. Int. Ed*. **2015**, *54*, 2661–2664.

12. *CRC Handbook of Chemistry and Physics*, 96th ed.; CRC Press: Cleveland, OH, **2010**.

13. Zhou, S.; Johnson, M.; Veinot, J. G. C. Iron/Iron Oxide Nanoparticles: a Versatile Support for Catalytic Metals and Their Application in Suzuki-Miyaura Cross-Coupling Reactions. *Chem. Commun*. **2010**, *46*, 2411–2413.

14. Hudson, R.; Li, C.-J.; Moores, A. Magnetic Copper-Iron Nanoparticles as Simple Heterogeneous Catalysts for the Azide-Alkyne Click Reaction in Water. *Green Chem*. **2012**, *14*, 622–624.

15. Hudson, R.; Chazelle, V.; Bateman, M.; Roy, R.; Li, C.-J.; Moores, A. Sustainable Synthesis of Magnetic Ruthenium-Coated Iron Nanoparticles and Application in the Catalytic Transfer Hydrogenation of Ketones. *ACS Sustain. Chem. Eng*. **2015**, *3*, 814–820.

16. Zhang, Y.; Su, Y.; Zhou, X.; Dai, C.; Keller, A. A. A New Insight on the Core-Shell Structure of Zerovalent Iron Nanoparticles and Its Application for Pb(II) Sequestration. *J. Hazard. Mater.* **2013**, *263*, 685–693.

17. Yao, Y.; Patzig, C.; Hu, Y.; Scott, R. W. J. *In Situ* X-ray Absorption Spectroscopic Study of Fe@Fe_xO_y/Pd and Fe@Fe_xO_y/Cu Nanoparticle Catalysts Prepared by Galvanic Exchange Reactions. *J. Phys. Chem. C* **2015**, *119*, 21209–21218.

18. Ishikawa, S.; Hudson, R.; Masnadi, M.; Bateman, M.; Castonguay, A.; Moores, A.; Li, C.-J. Cyclopropanation of Diazoesters with Styrene Derivatives Catalyzed by Magnetically Recoverable Copper-Plated Iron Nanoparticles. *Tetrahedron* **2014**, *70*, 6162–6168.

19. Nishimura, S. *Handbook of Heterogeneous Catalytic Hydrogenation for Organic Synthesis*; John Wiley & Sons: New York, **2001**.

20. Rylander, P. N. *Hydrogenation Methods*; Academic Press: New York, **1985**.

21. Sajiki, H.; Ikaea, T.; Hirota, K. Cleavage of the THP Protecting Group under Pd/C-Catalyzed Hydrogenation Conditions. *Tetrahedron Lett*. **2001**, *42*, 7699–7701.

22. He, T.; Liu, L.; Wu, G.; Chen, P. Covalent Triazine Framework-Supported Palladium Nanoparticles for Catalytic Hydrogenation of N-Heterocycles. *J. Mater. Chem. A* **2015**, *3*, 16235–16241.

23. Yuan, J. Preparation of 2,4-difluoroaniline by Catalytic Hydrogenation in the Presence of Pd-Fe/TiO_2 Catalyst at Normal Pressure. *Pesticides* **2007**, *46*, 827–829.

24. Anderson, R. M.; Zhang, L.; Loussaert, J. A.; Frenkel, A. I.; Henkelman, G.; Crooks, R. M. An Experimental and Theoretical Investigation of the Inversion of Pd@Pt Core@Shell Dendrimer-Encapsulated Nanoparticles. *ACS Nano* **2013**, *10*, 9345–9353.

25. Wang. L.; Zhang, S.; Zhu, Y.; Patlolla, A.; Shan, J.; Yoshida, H.; Takeda, S.; Frenkel, A. I.; Tao, F. Catalysis and *in Situ* Studies of Rh_1/Co_3O_4 Nanorods in Reduction of NO with H_2. *ACS Catal*. **2013**, *3*, 1011–1019.

26. Ohyama, J.; Teramura, K.; Shishido, T.; Hitomi, Y.; Kato, K.; Tanida, H.; Uruga, T.; Tanaka, T. *In Situ* Au L_3 and L_2 Edge XANES Spectral Analysis during Growth of Thiol Protected Gold Nanoparticles for the Study on Particle Size Dependent Electronic Properties. *Chem. Phys. Lett*. **2011**, *507*, 105–110.

27. Maclennan, A.; Banerjee, A.; Hu, Y.; Miller, J. T.; Scott, R. W. J. *In Situ* X-ray Absorption Spectroscopic Analysis of Gold-Palladium Bimetallic Nanoparticle Catalysts. *ACS Catal.* **2013**, *3*, 1411–1419.

28. Yao, Y.; Hu, Y.; Scott, R. W. J. Watching Iron Nanoparticles Rust: An *in Situ* X-ray Absorption Spectroscopic Study. *J. Phys. Chem. C* **2014**, *118*, 22317–22324.

29. Shivhare, A.; Lee, K. E.; Hu, Y.; Scott, R. W. J. Following the Reactivity of $Au_{25}(SC_8H_9)_{18}^-$ Clusters with Pd^{2+} and Ag^+ Ions Using *in Situ* X-ray Absorption Spectroscopy: A Tale of Two Metals. *J. Phys. Chem. C* **2015**, *119*, 23279–23284.

30. Haider, P.; Grunwaldt, J.-D.; Seidel, R.; Baiker, A. Gold Supported on Cu-Mg-Al and Cu-Ce Mixed Oxides: An *in Situ* XANES Study on the State of Au during Aerobic Alcohol Oxidation. *J. Catal.* **2007**, *250*, 313–323.

31. Newville, M. IFEFFIT: Interactive XAFS Analysis and FEFF Fitting. *J. Synchrotron Radiat*. **2001**, *8*, 322–324.

32. Ravel, B.; Newville, M. ATHENA, ARTEMIS, HEPHAESTUS: Data Analysis for X-ray Absorption Spectroscopy Using IFEFFIT. *J. Synchrotron Radiat*. **2005**, *12*, 537–541.

33. Kovács, S.; Zih-Perényi, K.; Révész, Á.; Novák, Z. Copper on Iron: Catalyst and Scavenger for Azide-Alkyne Cycloaddition. *Synthesis* **2012**, *44*, 3722–3730.

34. Kovács, S.; Novák, Z. Oxidoreductive Coupling of Thiols with Aryl Halides Catalyzed by Copper on Iron. *Org. Biomol. Chem.* **2011**, *9*, 711–716.

35. Wasilewshi, P.; Kletetschka, G. Lodestone: Natures Only Permanent Magnet-What It Is and How It Gets Charged. *Geophys. Res. Let.* **1999**, *26*, 2275–2278.

36. Issa, B.; Obaidat, I. M.; Albiss, B. A. Haik, Y. Magnetic Nanoparticles: Surface Effects and Properties Related to Biomedicine Applications. *Int. J. Mol. Sci.* **2013**, *14*, 21266–21305.

37. Kim, D. K.; Zhang, Y.; Voit, W.; Rao, K. V.; Muhammed, M. Synthesis and Characterization of Surfactant-Coated Superparamagnetic Monodispersed Iron Oxide Nanoparticles. *J. Magn. Magn. Mater.* **2001**, *225*, 30–36.

38. Nikoshvili, L.; Shimanskaya, E.; Bykov, A.; Yuranov, I.; Kiwi-Minsker, L.; Sulman, E. Selective Hydrogenation of 2-methyl-3-butyn-2-ol over Pd-nanoparticles Stabilized in Hypercrosslinked Polystyrene: Solvent Effect. *Catal. Today* **2015**, *241*, 179–188.

39. Li, X.; Elliott, D. W.; Zhang, W. Zero-Valent Iron Nanoparticles for Abatement of Environmental Pollutants: Materials and Engineering Aspects. *Crit. Rev. Environ. Sci. Technol*. **2006**, *31*, 111–122.

40. Ma. R.; Semagina, N. Nanoparticle Shape Effect Study as An Efficient Tool to Reveal the Structure Sensitivity of Olefinic Alcohol Hydrogenation. *J. Phys. Chem. C* **2010**, *114*, 15417–15423.

41. Shen. J.; Semagina, N. Iridium- and Platinum-Free Ring Opening of Indan. *ACS Catal.* **2014**, *4*, 268–279.

42. Banerjee, A.; Scott, R. W. J. Optimization of Transition Metal Nanoparticle-Phosphonium Ionic Liquid Composite Catalytic Systems for Deep Hydrogenation and Hydrodeoxygenation Reactions. *Green Chem*. **2015**, *17*, 1597–1604.

43. Niu, Y.; Yeung, L. K.; Crooks, R. M. Size-Selective Hydrogenation of Olefins by Dendrimer-Encapsulated Palladium Nanoparticles. *J. Am. Chem. Soc*. **2001**, *123*, 6840–6846.

44. Sadeghmoghaddam, E.; Gu, H.; Shon, Y.–S. Pd Nanoparticle-Catalyzed Isomerization vs Hydrogenation of Allyl Alcohol: Solvent-Dependent Regioselectivity. *ACS Catal.* **2012**, *2*, 1838–1845.

45. Bertero, N. M.; Trasarti, A. F.; Apesteguia, C. R.; Marchi, A. J. Catalytic and Kinetic Study of the Liquid-Phase Hydrogenation of Acetophenone over Cu/SiO_2 Catalyst. *Appl. Catal. A: Gen.* **2011**, *394*, 228–238.

46. Rajadhyskasha, R. A.; Karwa, S. I. Solvent Effects in Catalytic Hydrogenation. *Chem. Eng. Sci.* **1986**, *41*, 1765–1770.

47. Augustine, R. L.; Warner, R. W.; Melnick, M. J. Heterogeneous Catalysis in Organic Chemistry. 3. Competitive Adsorption of Solvents during Alkene Hydrogenations. *J. Org. Chem.* **1984**, *49*, 4853–4856.

48. Toukoniitty, E.; Mäki-Arvela, P.; Kuusisto, J.; Nieminen, V.; Päivärinta, J.; Hotokka, M.; Salmi, T.; Yu Murzin, D. Solvent Effects in Enantioselective Hydrogenation of 1-phenyl-1,2-propanedione. *J. Mol. Catal*. **2002**, *192*, 135–151.

49. Ghavre, M.; Morrissey, S.; Gathergood, N. in: Kokorin A. (Ed.) Hydrogenation in Ionic Liquids, Ionic Liquids: Applications and Perspectives. **2011**, 331–392.

CHAPTER 5

5. X-ray Absorption Spectroscopic Studies on the Penetrability of Hollow Iron Oxide Nanoparticles by Galvanic Exchange Reactions

In this work, through capturing the core-void-shell Fe-Fe_xO_y intermediates during the formation of hollow Fe oxide NPs and utilizing the remaining Fe core in the core-void-shell structure to reduce Pd(II) to Pd(0), the penetrability of hollow Fe oxide NPs was studied. *Ex situ* TEM and *in situ* high-temperature X-ray absorption spectroscopy were used to follow the speciation of the Fe and Pd in the system.

This chapter is a manuscript in preparation. This work has been co-authored with Christian Patzig (2rd author) who did EDX mapping. Syed Naqvi is thanked for assistance with some of the catalytic reactions. Aimee Maclennan is thanked for the design of high temperature liquid cell. I did all the experimental work along with the writing of the first draft of the manuscript. The manuscript has been revised by Dr. Yongfeng Hu and Dr. Robert W. J. Scott.

5.1 Abstract

Hollow Fe oxide nanoparticles have many applications in catalysis, drug delivery and energy storage. Hollow Fe oxide shells can also be used for preventing the sintering of catalytically active cores and for magnetic recovery of bimetallic nanoparticles. However, more studies are required under real reaction conditions on the availability of the interior surface or active cores in hollow nanoparticles. Herein, we introduce a simple approach to study the penetrability of hollow Fe oxide shells by attempting galvanic exchange reactions between the remaining Fe(0) core within the hollow Fe oxide shell and Pd(II) salts. First, *in situ* high temperature Fe K-edge XANES was used to monitor the formation of hollow Fe oxide nanoparticles from Fe nanoparticles. Core-void-shell Fe-Fe oxide nanoparticle intermediates were captured at different time intervals and then reacted with Pd(II). The reduction of Pd(II) was characterized by *in situ* Pd L_3-edge XANES spectra. The results show that the core-void-shell nanoparticles had Fe_3O_4 shells, which were found to be impenetrable to Pd(II) salts when the thickness of the shell was more than 2 nm. However, the core could be accessed using a high-temperature etching strategy for the shell, which then allowed for galvanic reactions with Pd.

5.2 Introduction

With large surface areas and low material density, studies of hollow nanoparticles (NPs) are promising.[1-6] A versatile method to fabricate hollow nanostructures relies on the Kirkendall effect, with the formation of a void inside a nanostructure as a consequence of the difference in diffusion rates of the atoms moving into the core of the NP compared to atoms moving to the surface.[7-10] For example, Alivisatos' group successfully synthesized hollow CoO NPs by the faster outward diffusion of Co atoms from Co NPs than the inward diffusion of O_2 at 455 K.[11] They further encapsulated Pt NPs in the CoO shell by depositing Co shells on Pt NPs and transforming the Co shell into a hollow CoO shell, and the Pt core in the resulting core-void-shell Pt-CoO NPs was an accessible catalysts for ethylene hydrogenation. Many groups have shown that Fe NPs synthesized by the thermal decomposition of $Fe(CO)_5$ in octadecene with oleylamine as the stabilizer can also be oxidized by O_2 at high temperature to form hollow Fe

oxide NPs.[12-14] Similarly, core-void-shell Au-Fe_3O_4 NPs have also been synthesized by oxidizing Au-Fe core-shell NPs.[15] Podsiadlo *et al*. revealed that such Fe oxide shells seem to be non-porous and impenetrable by gases and liquids.[16] Cheng *et al*. revealed that they needed to etch the hollow Fe_3O_4 NPs to achieve cisplatin storage and release.[17] Rak *et al*. found that etched hollow Fe_3O_4 NPs have higher catalytic selectivity and activity for the selective oxidation of styrene than non-etched hollow Fe_3O_4 NPs due to the higher exposure of the interior surface.[18] As hollow Fe oxide shells could be useful for preventing the sintering of the catalytically active cores and allow for magnetic recovery of catalysts, more studies on the penetrability of Fe oxide shells are required under real reaction conditions.

Galvanic exchange reactions occur when the metals in a NP are displaced by the reduction of other metal ions with a higher electrochemical potential than the displaced metal, which have been widely used for the synthesis of bimetallic NPs.[19-21] Fe(0) has a relatively low standard electrode potential (Fe^{2+}/Fe^0, $E^o_{½}$ = -0.447 V), thus zero-valent Fe NPs have been used as precursors to seed, reduce and support other metals in the synthesis of bimetallic NPs by galvanic exchange reactions.[22-27] Various bimetallic NPs based on Fe NPs, such as FePd,[23] FeCu,[24,25] FeRu[26] and FePt,[27] have been synthesized by galvanic exchange reactions and applied as catalysts for different catalytic reactions ranging from carbon-coupling chemistry to alkene and alkyne hydrogenations. Our group recently studied the formation of Fe@Fe_xO_y/Pd NPs from Fe@Fe_xO_y NPs and Pd(II) salts in aqueous solutions by galvanic exchange reactions, and showed that reduction of Pd(II) is nearly complete after 20 min.[28] Therefore, we sought to utilize galvanic exchange reactions between Fe and Pd(II) to study the penetrability of Fe oxide shells in partially oxidized core-void-shell Fe(0)-Fe oxide NPs. If the Fe(0) core in the Fe oxide shell is still accessible for reaction, then exchange with Pd should occur.

X-ray absorption spectroscopy (XAS) is a powerful tool to probe the oxidation states and coordination environments of elements in materials with short-range order such as nanostructures. With recent advances in developing *in situ* cells, it has now become possible to study materials under a variety of different *in situ* and operando conditions.[28-35] Recently, our group studied the oxidation mechanism of Fe NPs in aqueous solutions via *in situ* Fe K-edge XAS at room temperature using a liquid cell with an X-ray permeable window.[32] With

the same liquid cell, we also studied the formation of Fe@Fe_xO_y/Pd and Fe@Fe_xO_y/Cu bimetallic NPs at room temperature by *in situ* Pd L_3-edge and Cu K-edge X-ray absorption near-edge structure spectroscopy (XANES).[28] As many reactions are carried out at high temperature and/or high pressure, different high pressure/high temperature liquid cells have been developed to collect *in situ* XAS data. For example, Testemale and coworkers have designed a cell which consists of an internally heated helium-pressurized autoclave with cold walls and can vary the temperature and the pressure independently over ranges of 30-1700 °C and 1-1200 bar.[33,34] Nelson and Miller previously developed a general-purpose liquid cell which can be operated up to 250 °C. It is composed of a small sample cell fabricated from a chemically resistant polymer housed inside a heated aluminum block which has machined paths for both incoming X-rays and outgoing X-ray fluorescence from the sample.[35]

In this work, we used a similar high temperature liquid cell to monitor the formation of hollow Fe oxide NPs and intermediate core-void-shell Fe-Fe_3O_4 NPs from as-synthesized Fe NPs via *in situ* Fe K-edge XAS at 180 °C. *Ex situ* TEM measurements showed the core-void-shell structures forming at intermediate times, followed by the formation of hollow Fe oxide NPs after 45 minutes. Core-void-shell Fe-Fe oxide NP intermediates were captured during the formation of hollow Fe oxide NPs from Fe NPs at different time intervals and reacted with Pd(II). Pd L_3-edge XAS was used to characterize the reduction of Pd(II) to study the penetrability of Fe oxide shells in the formation of hollow Fe oxide NPs. Results show that the Fe_3O_4 shells that result in such NPs are impenetrable beyond 2 nm thicknesses, and must be etched to take advantage of the reactivity of the leftover Fe(0) core.

5.3 Experimental Section

5.3.1 Materials

All chemicals were used as received without further purification. Oleylamine, Fe(0) pentacarbonyl and benzyl ether were purchased from Sigma-Aldrich. 1-Octadecene, oleic acid, 2-methyl-3-buten-2-ol, 2-methylbutan-2-ol and palladium (II) acetate were purchased from Alfa Aesar. Hexane, toluene and ethanol (HPLC grade) were purchased from Fisher Scientific.

5.3.2 Synthesis

5.3.2.1 Synthesis of Fe Nanoparticles and Core-void-shell Fe-Fe_3O_4 Nanoparticles

Fe NPs were obtained by thermal decomposition of Fe(0) pentacarbonyl (0.70 mL) in 20 mL air-free 1-octadecene (90%) with 0.60 mL oleylamine (70%) at 180 °C for 30 min. To make core-void-shell Fe-Fe_3O_4 NPs, air was introduced into the resulting solution at a rate of 80 mL/min, and the system was heated at 180 °C at successive intervals between 15 min and 45 min. Core-void-shell Fe-Fe_3O_4 NPs were also made by heating at 220 °C or 260 °C for 15 min or 10 min respectively. After heating, the sample was cooled down to room temperature. The core-void-shell Fe-Fe_3O_4 NPs were precipitated out by adding 10 mL of hexane and 150 mL of ethanol and washed 3 times with hexane and ethanol.

5.3.2.2 Preparation of Etched Core-void-shell Fe-Fe_3O_4 Nanoparticles

The purified core-void-shell Fe-Fe_3O_4 NPs were redispersed into 5mL of hexane, and followed by adding 20 mL of benzyl ether mixed with 0.17 mL of oleylamine and 0.16 mL of oleic acid. Then the mixture was kept at 130 °C under N_2 for 20 min to remove hexane. Subsequently, the solution was heated to 260 °C to etch the core-void-shell Fe-Fe_3O_4 NPs for 45 min followed a process developed by Sun's group.[17]

5.3.2.3 Galvanic exchange reactions

The galvanic exchange reactions were carried out by mixing as-synthesized Fe NPs or core-void-shell Fe-Fe_3O_4 NPs or etched core-void-shell Fe-Fe_3O_4 NPs with a 20 mM toluene solution of Pd acetate (50:1 Fe:Pd molar ratio) stirred at either 22 °C or 50 °C for 12 h.

5.3.3 Catalytic Reactions

5.0 mg etched core-void-shell Fe-Fe_3O_4/Pd NPs in 5.0 mL toluene were added to a 2.0 L round bottom flask filled with 1.2 atm hydrogen gas at 22 °C. To this solution, a 0.10 mL (0.94 mmol) of 2-methyl-3-buten-2-ol was added to start the reaction. The reaction was stirred with a magnetic stir bar (egg shaped, 7/8 inch × 3/8 inch) at 1600 rpm. The products were analyzed by GC with ethanol as solvent.

5.3.4 Characterization

Transmission electron microscopy (TEM) analyses of the NPs were conducted using a HT7700 microscope operating at 100 kV. The samples were prepared by drop-casting a small amount of diluted NPs in ethanol onto a carbon-coated copper grid (Electron Microscopy Sciences, Hatfield, PA). Average particle diameters were determined by manually measuring more than 100 NPs from each sample using the ImageJ program.[36] An FEI Titan 80-300 transmission electron microscope (FEI company), equipped with a high-angle annular dark field (HAADF) detector (Fischione Model 3000, Fischione company) and an energy dispersive X-ray (EDX) spectrometer with a Super-X EDX (FEI Company) detector consisting of four silicon drift detectors was used to perform scanning transmission electron microscopy analyses (STEM) in combination with EDX element distribution maps. The STEM-EDX experiments were performed at an acceleration voltage of 300 kV and at a camera length of 115 mm. As the electron beam is raster scanned across the sample, a full X-ray spectrum of each chosen element is collected for each pixel. Element distribution maps of Fe and Pd were derived by evaluating the peak intensities of the Fe K_α and Pd L_α X-ray signals with commercially available software Esprit v1.9 (Bruker Company) by means of spectral imaging.

Fe K-edge and Pd L-edge XANES spectra were collected at the Soft X-Ray Microcharacterization Beamline (SXRMB) at the CLS. The measurements were conducted under ambient atmosphere for Fe K-edge measurements and under helium for Pd L_3-edge measurements. To prevent photoreduction of Pd salts, we lowered the beam flux by defocusing and/or filtering the beam with Kapton filters. For Pd L-edge XANES, room temperature liquid cells (SPEX CertiPrep Disposable XRF X-Cell sample cups) were covered with a 4 μm Ultralene film (purchased from Fisher Scientific, Ottawa, ON). The *in situ* high temperature liquid cell was fabricated out of a Vespel^R SP-1 rod (DuPont). The cell has a Swagelok VCO cap which is connected to a gas flow manifold. The liquid cell is mounted in an aluminum mounting block wrapped with heating tape to control the temperature (Figure 5.1). The temperature was measure by a digital thermometer by inserting a thermocouple connector into the aluminum block. The XANES data was analyzed using the Athena software.[37,38] Linear combination fitting in the range of 7100 to 7180 eV was used with Fe foil, FeO, and Fe_3O_4

standards to measure the relative fraction of each species in the NPs at different oxidation time. The R-factors on the mismatch between data and fit are all lower than 0.001, which indicats the fits are good.[39]

The composition of the reaction mixture for the hydrogenation of 2-methyl-3-buten-2-ol was analyzed by a gas chromatograph (GC) using a flame ionization detector (FID, Agilent Technologies 7890A).

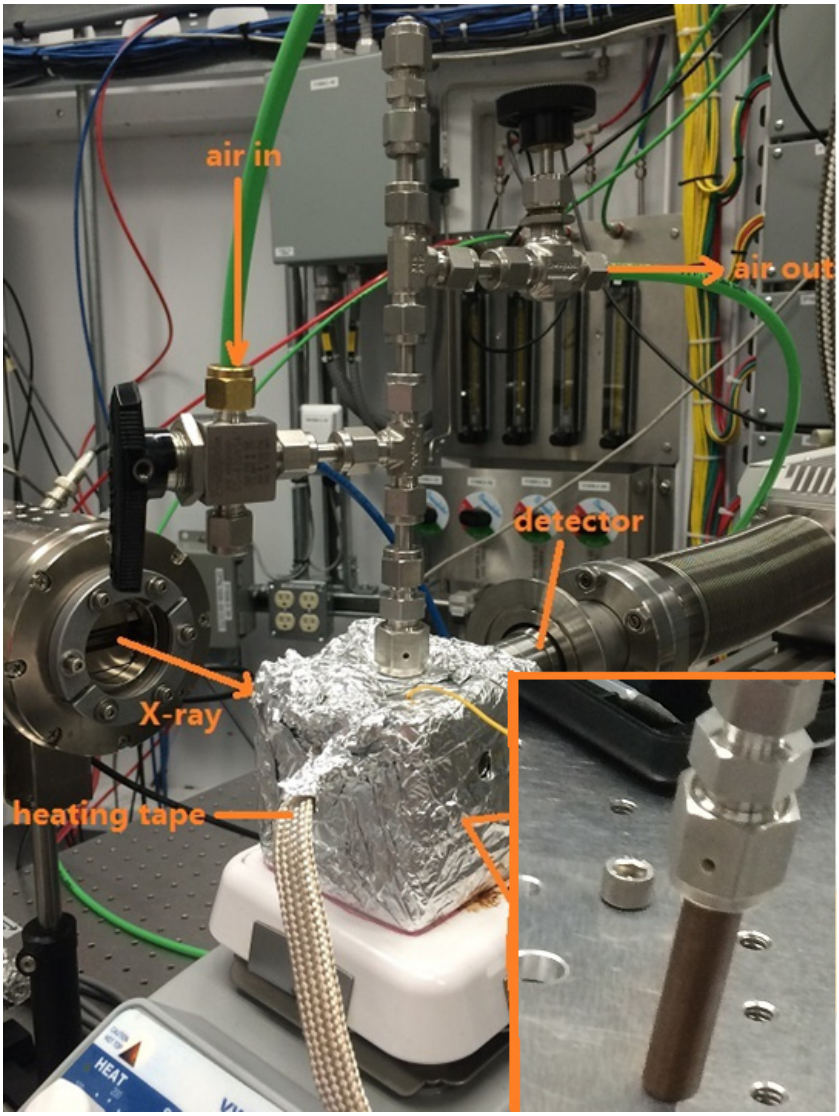

Figure 5.1. The high temperature oxidation setup for *in situ* fluorescence XANES studies.

5.4 Results and Discussion

Fe NPs were synthesized by a conventional decomposition reaction of $Fe(CO)_5$ in an oleylamine/octadecene solution at 180 °C for 30 min.[13,14] As shown in Figure 5.2 A, the average sizes of these Fe NPs are 8.7 ± 1.1 nm. Core-void-shell Fe-Fe oxide and finally hollow Fe oxide NPs were synthesized via the Kirkendall effect upon oxidation of Fe NPs in an octadecene solution by air flow at 180 °C.[14,18] Figure 5.2 shows the TEM images at different times for the oxidation of Fe NPs at 180 °C and the formation of intermediate core-void-shell Fe-Fe oxide NPs, followed by the final formation of hollow Fe oxide NPs. After 15 min oxidation (Figure 5.2 B), a thin layer of Fe oxide (1.9 ± 0.3 nm) formed on the surface of Fe core (6.4 ± 1.2 nm). As the oxidation time increases, the oxide layer grows from 2.2 ± 0.4 nm in Figures 5.2 C and 5.2 D to 3.1 ± 0.5 nm in Figure 5.2 F (45 min). At the same time, the size of the Fe cores in the center of the intermediate core-void-shell particles continues to shrink; after 20 min Fe core sizes are 5.6 ± 0.7 nm in Figures 5.2 C and 5.2 D, while after 30 min they are only 3.6 ± 0.7 nm in Figure 5.2 E. After 45 min, there are no apparent Fe cores left in the NPs.

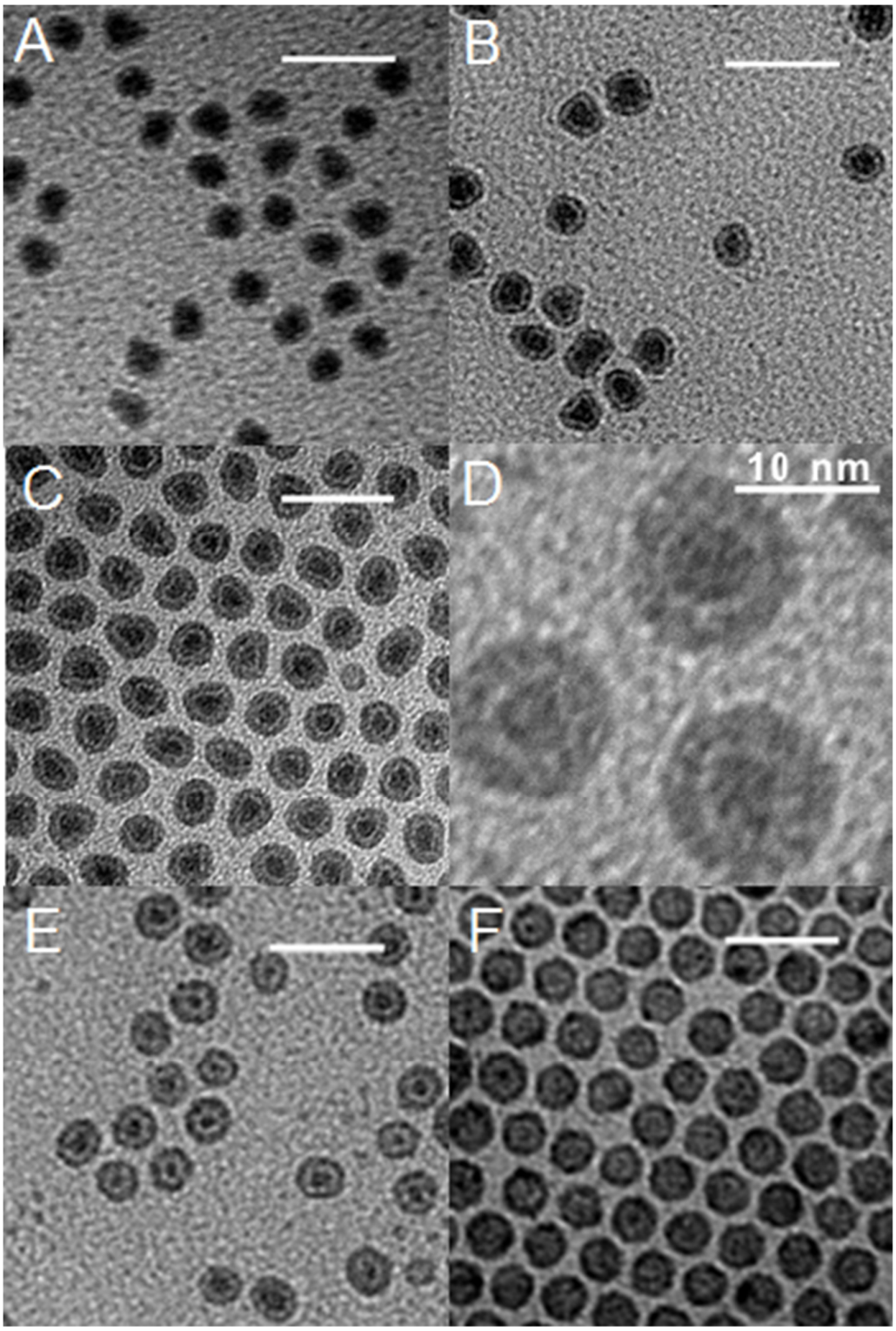

Figure 5.2. TEM images of the oxidation of as-synthesized Fe NPs at 180 °C upon an increase in the oxidation time (A) 0 min; (B) 15 min; (C) 20 min; (D) magnified view after 20 min oxidation; (E) 30 min; (F) 45 min. Scale bar corresponds to 30 nm.

To follow the formation of hollow Fe oxide NPs and determine the relative speciation of the particles before and after oxidation, Fe K-edge XANES spectra were collected by using an *in situ* high temperature liquid cell (Figure 5.1). 2.0 mL of an as-synthesized Fe NP solution was injected into the high-temperature liquid XAS cell, followed by *in situ* heating to 180 °C under a flow of air. The results show that upon an increase in the oxidation time, the Fe K-edge absorption edge shifts to higher energy, which indicates that the Fe NPs become oxidized (Figure 5.3 A). The XAS spectra show no further changes after 47 min, and the spectrum of the hollow Fe oxide is similar to that of the Fe_3O_4 reference (Figure 5.3 B). This shows that the hollow Fe oxide shell is likely comprised of magnetite, which agrees with results from other groups.[16,18] To ensure that oxidation was indeed complete, we also synthesized hollow Fe oxide NPs at 220 and 260 °C, respectively, and their Fe K-edge XANES spectra were also similar to the magnetite reference. Linear combination fitting was used with Fe foil, FeO, and Fe_3O_4 standards to measure their relative fraction in the NPs at different oxidation time (Table 5.1). The first spectrum was considered to be after 5 min oxidation time taking into account the time consumed to load the as-synthesized Fe NPs to the *in situ* setup and to scan the pre-edge. After 47 min oxidation, the Fe K-edge spectrum fits best to only a Fe_3O_4 standard, which is in agreement with the observation from TEM that these particles seemed to be nearly completely hollow.

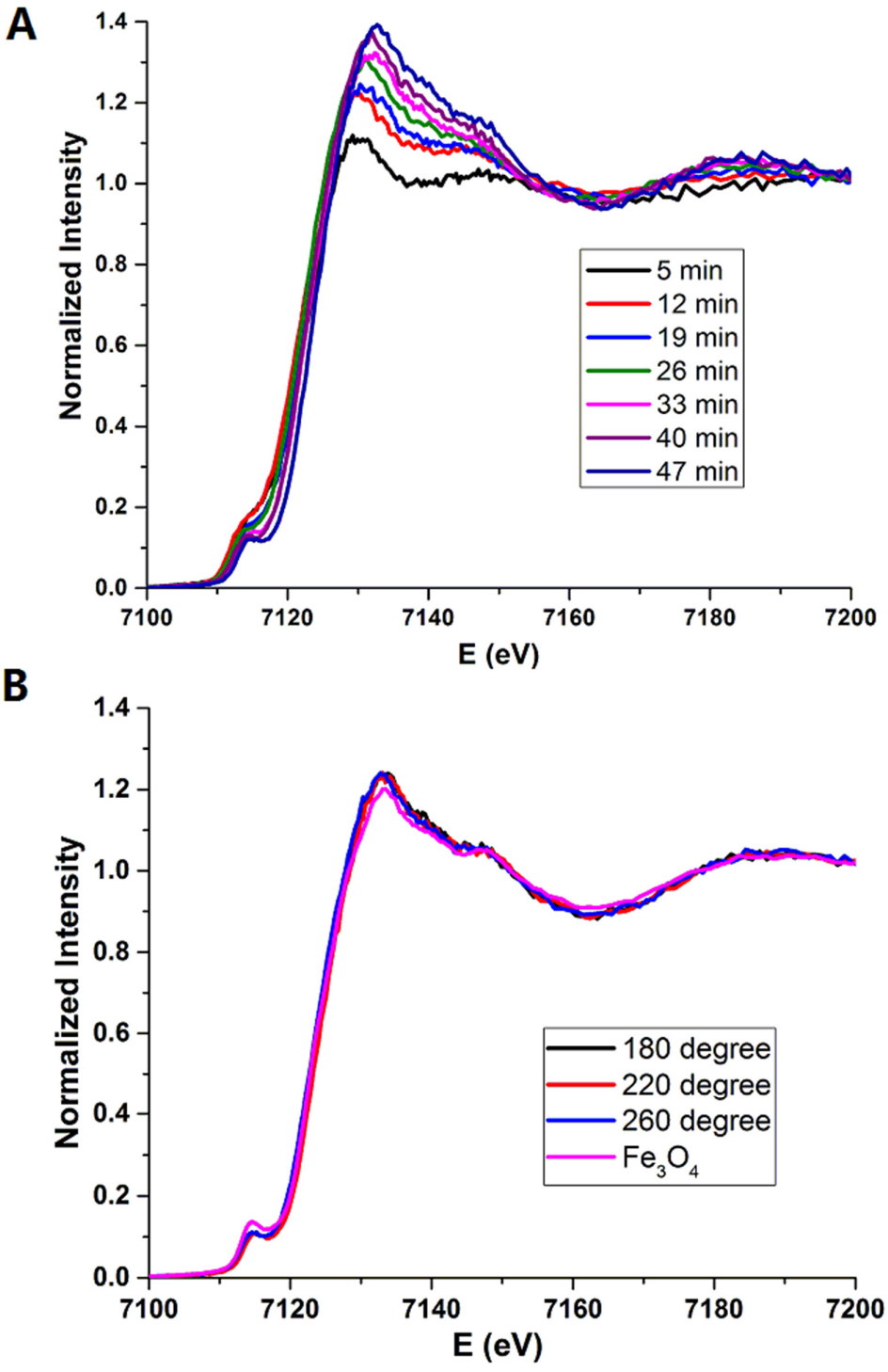

Figure 5.3. (A) *In situ* Fe K-edge XANES spectra of the oxidation process of Fe@Fe_xO_y NPs at 180 °C and (B) Fe K-edge XANES spectra of hollow Fe oxide NPs synthesized at different temperature compared with a Fe_3O_4 standard.

Table 5.1. XANES fitting results showing mole fractions of each Fe standard.

Oxidation Time (min)	Fe(0)	FeO	Fe_3O_4
5	0.553(9)	0.224(19)	0.223(16)
12	0.297(7)	0.187(15)	0.516(13)
19	0.242(5)	0.197(12)	0.561(11)
26	0.122(5)	0.164(11)	0.714(10)
33	0.079(5)	0.139(11)	0.782(10)
40	0.002(5)	0.088(12)	0.911(11)
47	0(0)	0(0)	1(0)

In order to better study the shrinkage of the Fe core sizes in the oxidation, the values of Fe(0)% from the fitting results were converted to the relative size of Fe cores by using Equation 5.1:

$$n = 4\pi R^3/3V_g \quad \textbf{(5.1)}$$

Where V_g is the molar volume of Fe (7.09 cm^3/mol) and R is the radius of a spherical particle, assuming an average starting diameter of 8.7 nm as seen from TEM. As shown in Figure 5.4, the calculated size of the Fe(0) core from XAS decreases linearly upon oxidation with a rate of *ca*. 0.17 nm/min, which is much faster than the rate of oxidation of polymer-stabilized Fe NPs in water observed by our group at room temperature previously (0.022 nm/min).[32] Most importantly, there is general agreement between Fe core sizes calculated from XAS data and *ex situ* core sizes determined by TEM, which shows that *in situ* XAS is a viable method to follow changes Fe NP oxidation in real time.

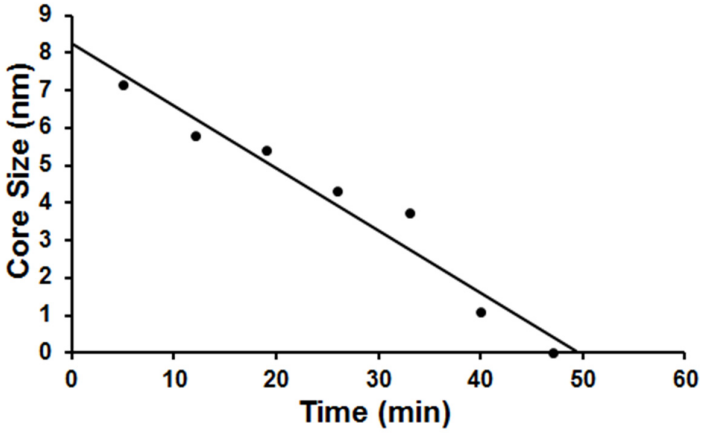

Figure 5.4. Calculated core size of Fe(0) as a function of time.

To study the penetrability of Fe_3O_4 shells, as-synthesized Fe NPs and the core-void-shell Fe-Fe_3O_4 intermediates oxidized at different time intervals were mixed with Pd acetate in toluene to determine whether the remaining Fe core in the core-void-shell structure can reduce Pd(II) to Pd(0) by a galvanic exchange reaction. Due to the lack of contrast between the resulting Fe-Fe_3O_4 NPs and Pd NPs, it was not possible to monitor the reduction of Pd by conventional bright-field TEM. XANES spectra are very sensitive to the oxidation states of an element, thus we used Pd L_3-edge XANES spectra to study the reduction of Pd(II). First, we mixed the as-synthesized Fe NPs in octadecene with Pd(II) in toluene at room temperature. As shown in Figure 5.5 A, the Pd(II) ions can be reduced to Pd(0) after 12 h reaction, which is similar to previous results in our lab for the synthesis of Fe@Fe_xO_y/Pd NPs in aqueous solutions by galvanic exchange reactions.[28] However, as the Fe_3O_4 shell thickness increases upon the oxidation of Fe NPs, it appears that the Fe_3O_4 shell gradually becomes impenetrable. After mixing Fe-Fe_3O_4 core-void-shell intermediates which have thin shells (Fe NPs oxidized at 180 °C for 15 min, Figure 5.5 B) with Pd acetate for 12 h at room temperature, there was no obvious reduction of Pd acetate in the Pd L_3-edge XANES spectrum (pink line in Figure 5.5 B). When we heated the mixture to 50 °C to accelerate the reaction, the Pd acetate could be reduced by the Fe cores (red line in Figure 5.5 B). However, upon increasing the thickness of the Fe_3O_4 shells to *ca*. 2.5 nm (Fe NPs oxidized at 180 °C for 20 min, Figure 5.2 C and 5.2 D) with Pd(II), even after heating at 50 °C, the Pd acetate was no longer reduced (Figure 5.5 C). To confirm these results, reactions between other core-void-shell Fe-Fe_3O_4 intermediates

(Fe@Fe_xO_y NPs oxidized at 220 °C for 15 min and at 260 °C for 10 min, Figure 5.6) with Pd acetate were also attempted at 50 °C. In both cases, the Fe_3O_4 shells also were impenetrable to Pd acetate (Figure 5.5 C).

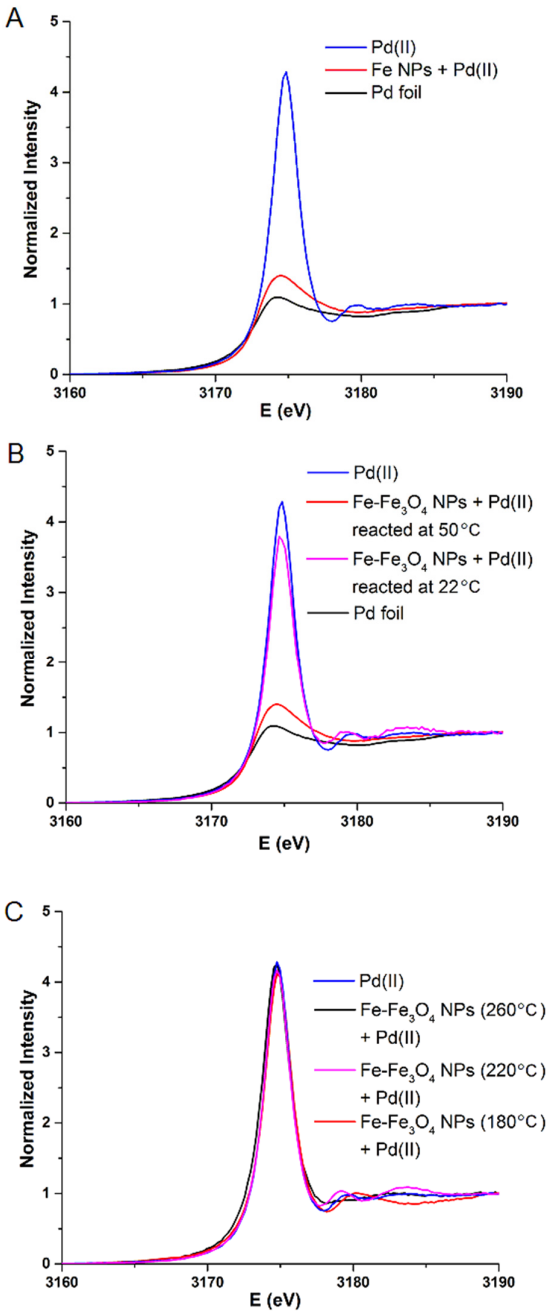

Figure 5.5. Pd L_3-edge XANES spectra. (A) After a reaction between as-synthesized Fe NPs with Pd(II) at 22 °C. (B) After a reaction between Fe-Fe_3O_4 NPs synthesized after 15 min oxidation at 180 °C with Pd(II) at 22 °C and 50 °C, respectively. (C) After a reaction between Fe-Fe_3O_4 NPs synthesized after 20 min oxidation at 180 °C or Fe-Fe_3O_4 NPs synthesized after 15 min oxidation at 220 °C or Fe-Fe_3O_4 NPs synthesized after 10 min oxidation at 260 °C with Pd(II) at 50 °C, respectively.

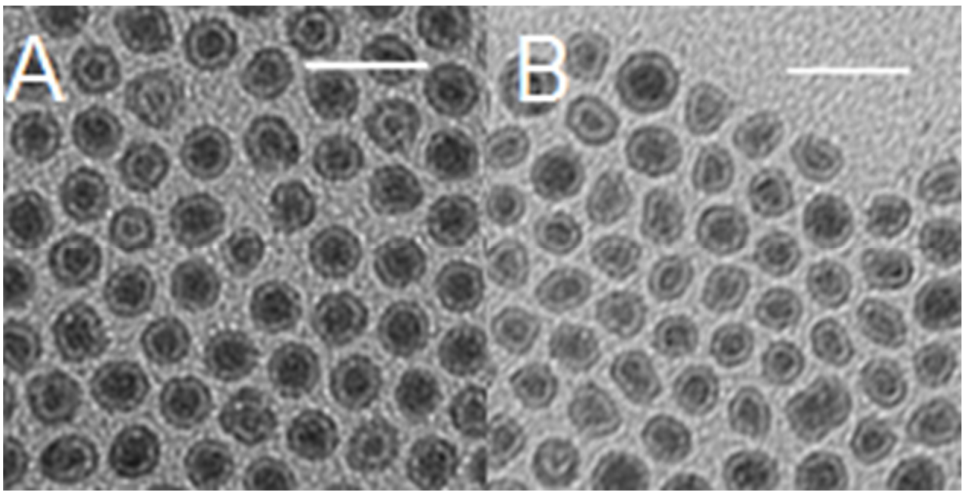

Figure 5.6. TEM images of Fe@Fe_xO_y NPs oxidized at 220 °C for 15 min (A) and Fe@Fe_xO_y NPs oxidized at 260 °C for 10 min (B). Scale bar corresponds to 30 nm.

To further demonstrate that the Fe_3O_4 shells block the reactions between the Fe core and Pd acetate, we followed a strategy documented by Cheng *et al.* to etch the core-void-shell Fe-Fe_3O_4 intermediates under nitrogen at 260 °C in benzyl ether mixed with oleylamine and oleic acid for 45 min to create cracks in many of the Fe_3O_4 shells.[17] As shown in Figure 5.7 A, there are large pores created in the Fe_3O_4 shells after etching. Pd L_3-edge XANES spectra show that the etched core-void-shell Fe-Fe_3O_4 NPs can reduce Pd(II) by galvanic exchange reactions at 50 °C (blue line in Figure 5.7 B). Even at 22 °C, a lower intensity of the Pd L_3-edge spectrum compared to that of Pd(II) indicates the partial reduction of the Pd(II) by etched core-void-shell Fe-Fe_3O_4 NPs (black line in Figure 5.7 B). Figure 5.8 shows a STEM image of the final composites along with EDX maps showing the Pd and Fe domains. These images show that the reduced Pd NPs grew from a fraction of the etched core-void-shell Fe-Fe_3O_4 NPs rather than uniformly within each NP, suggesting that only a fraction of the Fe NPs are sufficiently etched to allow for galvanic exchange reactions between Pd(II) and the Fe cores. This suggests that there are a low number of nucleation sites (Fe cores), available for reaction, and thus Pd deposition occurs only in isolated regions, followed by complete consumption of the Fe cores in these regions and dendritic growth of the resulting Pd NPs. The resulting structure resemble the non-homogeneous deposition of Cu on Fe@Fe_xO_y NPs, which relied on the Cu(II) salts being able to reach the Fe cores.[21,28]

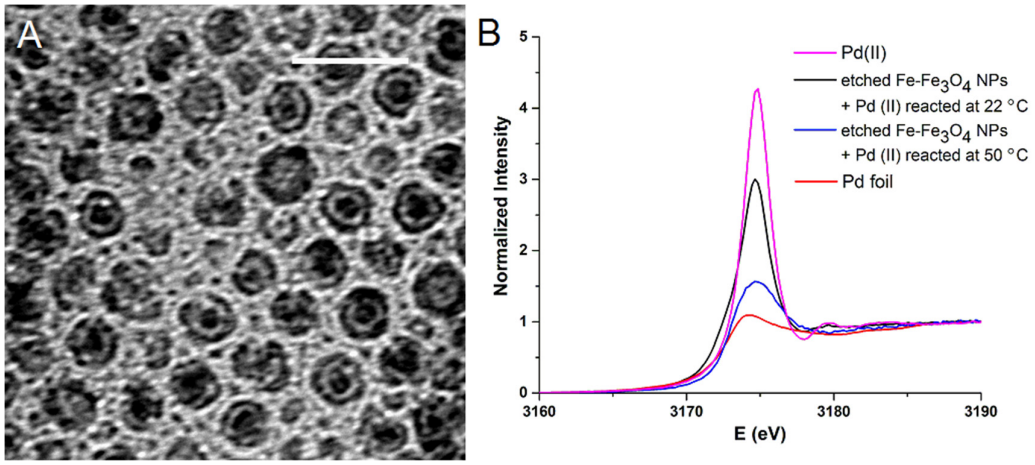

Figure 5.7. (A) TEM images of etched Fe-Fe_3O_4 NPs. Scale bar corresponds to 30 nm. (B) Pd L_3-edge XANES spectra.

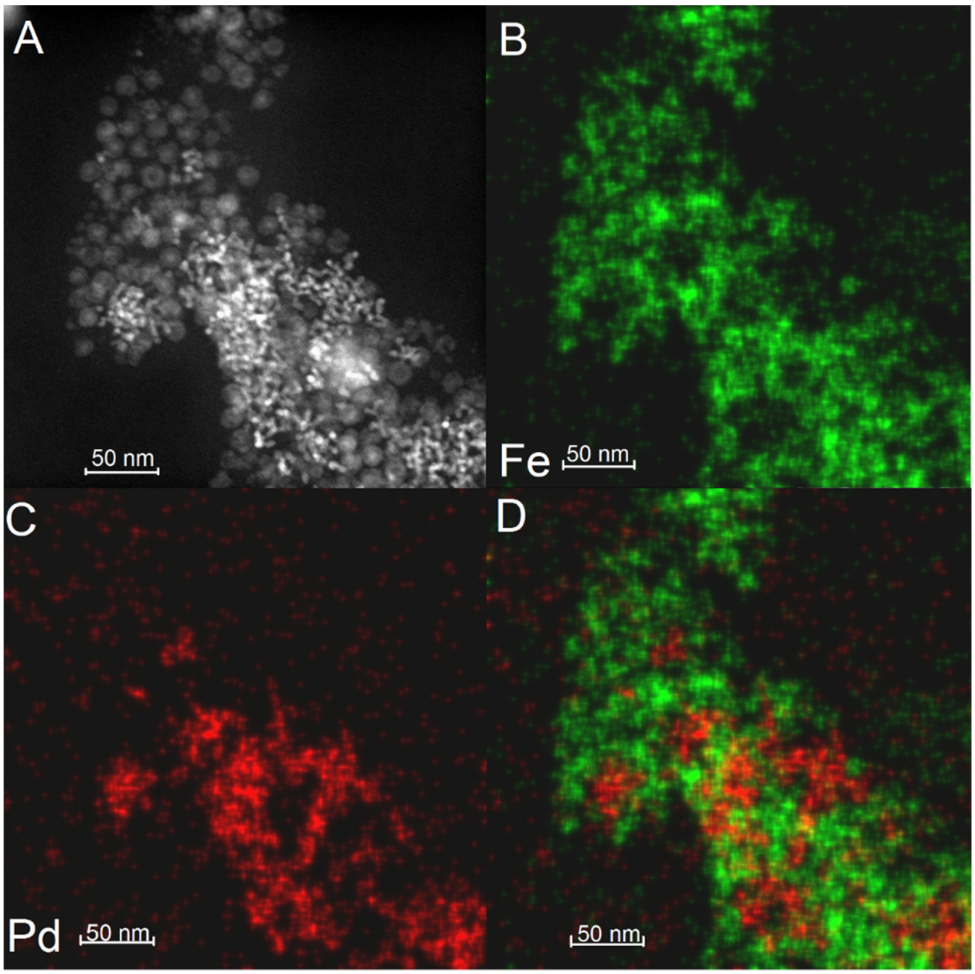

Figure 5.8. (A) High-angle annular dark-field STEM images, and (B, C, D) EDX elemental mapping images of core-void-shell Fe-Fe_3O_4/Pd NPs.

Finally, we applied the etched core-void-shell Fe-Fe_3O_4/Pd NPs as catalysts for the hydrogenation of 2-methyl-3-buten-2-ol to confirm the formation of Pd NPs on the etched core-void-shell Fe-Fe_3O_4 NPs. The hydrogenation reactions were carried out in toluene at 1.2 atm H_2 (g) and 22 °C (Scheme 5.1). Etched core-void-shell Fe-Fe_3O_4 NPs showed no activity for this reaction, so Pd is the only catalyst for this reaction.[40] When the etched core-void-shell Fe-Fe_3O_4/Pd NPs were used as catalysts for the hydrogenation reaction, 98% conversion was seen for 2-methyl-3-buten-2-ol hydrogenation in 30 min with 2-methyl-2-butanol as the only product (Table 5.2). The core-void-shell Fe-Fe_3O_4/Pd could be recycled with only a small drop in conversion, likely due to small loss of material upon recycling. These studies reveal that Pd(II) was reduced to Pd(0) by etched core-void-shell Fe-Fe_3O_4 NPs, and the resulting Pd NPs are available for catalytic reactions.

Scheme 5.1. The hydrogenation of 2-methyl-3-buten-2-ol.

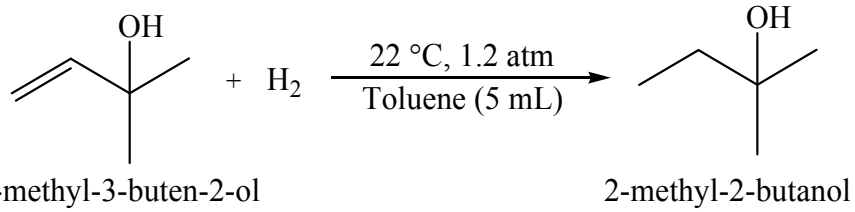

Table 5.2. Data for the hydrogenation of 2-methyl-3-buten-2-ol.

Entry	Catalyst	Conversion
1	Etched Fe-Fe_3O_4 NPs	0%
2	Etched Fe-Fe_3O_4/Pd NPs	98%
3	Etched Fe-Fe_3O_4/Pd NPs (recycled 1 time)	92%

Reaction conditions: All reactions are carried at 25 °C, the substrate/catalyst ratio is 15:1, and conversion is calculated after 30 min reaction.

5.5 Conclusion

TEM and *in situ* high temperature Fe K-edge XANES spectra have been used to monitor the formation of hollow Fe_3O_4 NPs. The core-void-shell Fe-Fe_3O_4 intermediates in the formation of hollow Fe_3O_4 NPs have been captured and reacted with Pd(II) to study the

penetrability of the Fe_3O_4 shells. Pd L_3-edge XANES spectra show that the Fe_3O_4 shells were impenetrable to Pd(II) salts when the thickness of the shell is more than 2 nm. However, the core could be accessed using a high-temperature etching strategy for the shell.

Acknowledgments

The authors acknowledge financial assistance from the National Sciences and Engineering Research Council of Canada (NSERC). The authors acknowledge Syed Naqvi for assistance with catalytic studies. We thank Aimee Maclennan for the design of high temperature liquid cell. XANES experiments described in this paper were performed at the Canadian Light Source, which is supported by NSERC, the National Research Council Canada, the Canadian Institutes of Health Research, the Province of Saskatchewan, Western Economic Diversification Canada, and the University of Saskatchewan.

5.6 References

1. Koo, B.; Xiong, H.; Slater, M. D.; Prakapenka, V. B.; Balasubramanian, M.; Podsiadlo, P.; Johnson, C. S.; Rajh, T.; Shevchenko, E. V. Hollow Iron Oxide Nanoparticles for Application in Lithium Ion Batteries. *Nano Lett.* **2012**, *12*, 2429–2435.

2. Koo, B.; Chattopadhyay, S.; Shibata, T.; Prkapenka, V. B.; Johnson, C. S.; Rajh, T.; Shevchenko, E. V. Intercalation of Sodium Ions into Hollow Iron Oxide Nanoparticles. *Chem. Mater.* **2013**, *25*, 245–252.

3. Shin, J.; Anisur, R. M.; Ko, M. K.; Im, G. H.; Lee, J. H.; Lee, I. S. Hollow Manganese Oxide Nanoparticles as Multifunctional Agents for Magnetic Resonance Imaging and Drug Delivery. *Angew. Chem. Int. Ed*. **2011**, *50*, 3158–3163.

4. Cao, S.-W.; Zhu, Y.-J.; Ma, M.-Y.; Li, L.; Zhang, L. Hierarchically Nanostructured Magnetic Hollow Spheres of Fe_3O_4 and γ-Fe_2O_3: Preparation and Potential Application in Drug Delivery. *J. Phys. Chem.* C **2008**, *112*, 1851–1856.

5. Bai, Z.; Yang, L.; Li, L.; Lv, J.; Wang, K.; Zhang, J. A Facile Preparation of Hollow Palladium Nanosphere Catalysts for Direct Formic Acid Fuel Cell. *J. Phys. Chem.* C **2009**, *113*, 10568–10573.

6. Lai, X,; Li, J.; Korgel, B. A.; Dong, Z.; Li, Z.; Su, F.; Su, J.; Wang, D. General Synthesis and Gas-Sensing Properties of Multiple-Shell Metal Oxide Hollow Microshperes. *Angew. Chem. Int. Ed*. **2011**, *50*, 2738–2741.

7. Fan, H. J.; Gösele, U.; Zacharias, M. Formation of Nanotubes and Hollow Nanoparticles Based on Kirkendall and Diffusion Processes: A Review. *Small* **2007**, *30*, 1660–1671.

8. Wang, W.; Dahi, M.; Yin, Y. Hollow Nanocrystals through the Nanoscale Kirkendall Effect. *Chem. Mater*. **2013**, *25*, 1179–1189.

9. Chen, X.; Zhang, Z.; Qiu, Z.; Shi, C.; Li, X. Hydrothermal Fabrication and Characterization of Polycrystalline Linneite (Co_3S_4) Nanotubes Based on the Kirkendall Effects. *J. Colloid Interface Sci*. **2007**, *308*, 271–275.

10. Wang, Q.; Geng, B.; Wang, S.; Ye, Y.; Tao, B. Modified Kirdendall Effect for Fabrication of Magnetic Nanotubes. *Chem. Commun*. **2010**, *46*, 1899–1901.

11. Yin, Y.; Rioux, R. M.; Erdonmez, C. K.; Hughes, S.; Somorjai, G. A.; Alivisatos, A. P. Formation of Hollow Nanocrystals through the Nanoscale Kirkendall Effect. *Science* **2004**, *304*, 711–714.

12. Peng, S.; Wang, C.; Xie, J.; Sun, S. Synthesis and Stabilization of Monodisperse Fe Nanoparticles. *J. Am. Chem. Soc*. **2006**, *128*, 10676–10677.

13. Peng, S.; Sun, S. H. Synthesis and Characterization of Monodisperse Hollow Fe_3O_4 Nanoparticles. *Angew. Chem. Int. Ed*. **2007**, *46*, 4155-4158.

14. Cabot, A.; Puntes, V. F.; Shevchenko, E.; Yin, Y.; Balcells, L.; Marcus, M. A.; Hughes, S. M.; Alivisatos, A. P. Vancancy Coalescence during Oxidation of Iron Nanoparticles. *J. Am. Chem. Soc*. **2007**, *129*, 10358–10360.

15. Shevchenko, E. V.; Bodnarchuk, M. O.; Kovalenko, M. V.; Talapin, D. V.; Smith, R. K.; Aloni, S.; Heiss, W.; Alivisatos, A. P. Gold/Iron Oxide Core/Hollow-Shell Nanoparticles. *Adv. Mater*. **2008**, *20*, 4323–4329.

16. Podsiadlo, P.; Kwon, S. G.; Koo, B.; Lee, B.; Prakapenka, V. B.; Dera, P.; Zhuravlev, K. K.; Krylova, G.; Shevchenko, E. V. How "Hollow" Are Hollow Nanoparticles? *J. Am. Chem. Soc*. **2013**, *135*, 2435–2438.

17. Cheng, K.; Peng, S.; Xu, C.; Sun, S. Porous Hollow Fe_3O_4 Nanoparticles for Targeted Delivery and Controlled Release of Cisplatin. *J. Am. Chem. Soc*. **2009**, *131*, 10637–10644.

18. Rak, M. J.; Lerro, M.; Moores, A. Hollow Iron Oxide Nanoshells are Active and Selective Catalysts for the Partial Oxidation of Styrene with Molecular Oxygen. *Chem. Commun*. **2014**, *50*, 12482–12485.

19. Zhang, Y.; Diao, W.; Monnier, J. R.; Williams, C. T. Pd-Ag/SiO_2 Bimetallic Catalysts Prepared by Galvanic Displacement for Selective Hydrogenation of Acetylene in Excess Ethylene. *Catal. Sci. Technol*. **2015**, *5*, 4123–4132.

20. Calver, C. F.; Dash, P.; Scott, R. W. J. Selective Hydrogenations with Ag-Pd Catalysts Prepared by Galvanic Exchange Reactions. *ChemCatChem* **2011**, *3*, 695–697.

21. Masnadi, M.; Yao, N.; Bradiy, N.; Moores, A. Cu(II) Galvanic Reduction and Deposition onto Iron Nano- and Microparticles: Resulting Morphologies and Growth Mechanisms. *Langmuir* **2015**, *31*, 789–798.

22. CRC Handbook of Chemistry and Physics, 96th ed.; CRC Press: Cleveland, OH, 2010.

23. Zhou, S.; Johnson, M.; Veinot, J. G. C. Iron/Iron Oxide Nanoparticles: A Versatile Support for Catalytic Metals and Their Application in Suzuki-Miyaura Cross-Coupling Reactions. *Chem. Commun*. **2010**, *46*, 2411–2413.

24. Hudson, R.; Li, C.-J.; Moores, A. Magnetic Copper-iron Nanoparticles as Simple Heterogeneous Catalysts for the Azide-alkyne Click Reaction in Water. *Green Chem*. **2012**, *14*, 622–624.

25. Ishikawa, S.; Hudson, R.; Masnadi, M.; Bateman, M.; Castonguay, A.; Moores, A.; Li, C.-J. Cyclopropanation of Diazoesters with Styrene Derivatives Catalyzed by Magnetically Recoverable Copper-Plated Iron Nanoparticles. *Tetrahedron* **2014**, *70*, 6162–6168.

26. Hudson, R.; Chazelle, V.; Bateman, M.; Roy, R.; Li, C.-J.; Moores, A. Sustainable Synthesis of Magnetic Ruthenium-Coated Iron Nanoparticles and Application in the Catalytic Transfer Hydrogenation of Ketones. *ACS Sustain. Chem. Eng*. **2015**, *3*, 814–820.

27. Shi, Y.; Yuan, Z.; Wei, Q.; Sun, K.; Xu, B. Pt-FeO_x/SiO_2 Catalysts Prepared by Galvanic Displacement Show High Selectivity for Cinnamyl Alcohol Production in the Chemoselective Hydrogenation of Cinnamaldehyde. *Catal. Sci. Technol*. **2016**, *6*, 7033–7037.

28. Yao, Y.; Patzig, C.; Hu, Y.; Scott, R. W. J. In Situ X-ray Absorption Spectroscopic Study of Fe@Fe_xO_y/Pd and Fe@Fe_xO_y/Cu Nanoparticle Catalysts Prepared by Galvanic Exchange Reactions. *J. Phys. Chem. C* **2015**, *119*, 21209–21218.

29. Li, Y.; Zakharov, D.; Zhao, S.; Tappero, R.; Jung, U.; Elsen, A.; Baumann, Ph.; Nuzzo, R. G.; Stach, E. A.; Frenkel, A. I. Complex Structural Dynamics of Nanocatalysts Revealed in Operando Conditions by Correlated Imaging and Spectroscopy Probes. *Nat. Commun.* **2015**, *6*, 7583.

30. Fontaine, C. L.; Barthe, L.; Rochet, A.; Briois, V. X-ray Absorption Spectroscopy and Heterogeneous Catalysis: Performances at the SOLEIL's SAMBA Beamline. *Catal. Today* **2013**, *205*, 148–158.

31. Hong, J.; Marceau, E.; Khodakov, A. Y.; Gaberová, L.; Griboval-Constant, A.; Girardon, J.-S.; Fontaine, C. L.; Briois, V. Speciation of Ruthenium as a Reduction Promoter of Silica-Supported Co Catalysts: A Time-Resolved in Situ XAS Investigation. *ACS. Catal.* **2015**, *5*, 1273–1282.

32. Yao, Y.; Hu, Y.; Scott, R. W. J. Watching Iron Nanoparticles Rust: An in situ X-ray Absorption Spectroscopic Study. *J. Phys. Chem. C* **2014**, *118*, 22371–22324.

33. Testemale, D.; Argoud, R.; Geaymond, O.; Hazemann, J. High Pressure/High Temperature Cell for X-ray Absorption and Scattering Techniques. *Rev. Sci. Instrum*. **2005**, *76*, 043905.

34. Pokrovski, G. S.; Roux, J.; Hazemann, J.; Testemale, D. An X-ay Absorption Spectroscopy Study of Argutite Solubility and Aqueous Ge(IV) Speciation in Hydrothermal Fluids to

500 °C and 400 bar. *Chem. Geol.* **2005**, *217*, 127–145.

35. Nelson, R. C.; Miller, J. T. An Introduction to X-ray Absorption Spectroscopy and Its in situ Application to Organometallic Compounds and Homogeneous Catalysts. *Catal. Sci. Technol*. **2012**, *2*, 461–470.

36. Abramoff, M. D.; Magalhäes, P. J.; Ram, S, J. Image Processing with ImageJ. *Biophotonics Int*. **2004**, *11*, 36–42.

37. Newville, M. IFEFFIT: Interactive XAFS Analysis and FEFF Fitting. *J. Synchrotron Radiat*. **2001**, *8*, 322–324.

38. Ravel, B.; Newville, M. ATHENA, ARTEMIS, HEPHAESTUS: Data Analysis for X-ray Absorption Spectroscopy Using IFEFFIT. *J. Synchrotron Radiat*. **2005**, *12*, 537–541.

39. Calvin, S. XAFS for Everyone. CRC Press, **2013**.

40. Shen. J.; Semagina, N. Iridium- and Platinum-Free Ring Opening of Indan. *ACS Catal.* **2014**, *4*, 268–279.

CHAPTER 6

6. Hydrogenation of Alkenes Catalyzed by Fe Nanoparticles in Ethanol and Tetraalkylphosphonium Ionic Liquids

In this work, we synthesized different sizes of Fe@Fe_xO_y nanoparticles following the synthetic method described in Chapter 2. We applied these different sizes of Fe@Fe_xO_y nanoparticles to catalyze the hydrogenation of alkenes in order to determine the importance of the size of Fe NPs for hydrogenation reactions. We also synthesized Fe nanoparticles in a P[6,6,6,14]Cl ionic liquid and applied them for the hydrogenation reactions, and compared their catalytic abilities with Fe NPs in ethanol. Fe K-edge XANES spectra were applied to study the changes of Fe nanoparticles in the catalysis.

This chapter is a manuscript in preparation. In this work, I led the project and collected all the XANES spectra and analyzed the data. William Barrett and Michael-Roy Durr assisted with the synthesis of Fe nanoparticles in ethanol, methanol/water and tetraalkylphosphonium ionic liquids and carried out many of the hydrogenation reactions and the analysis of the products by GC under my supervision. Abhinandan Banerjee developed the methodology to synthesize Fe nanoparticles in ionic liquids. The first draft of the manuscript is written by myself. The final manuscript will be submitted for publication after revisions by Dr. Yongfeng Hu and Dr. Robert W. J. Scott.

6.1 Abstract

Fe NPs have been shown to be effective catalysts for the hydrogenation of alkenes and alkynes under high H_2 pressures. However, there are no comprehensive studies on the effect of Fe NP size on catalytic activity, and the application of Fe NPs synthesized in non-volatile solvents such as ionic liquids for such reactions are rare. Herein, we synthesized different sizes of Fe NPs in protic solvents and studied the effect of NP size for the hydrogenation of 2-norbornene and 1-octene in ethanol under moderately high hydrogen pressures. We also compared their catalytic ability and stability with Fe NPs synthesized in tetraalkylphosphonium P[6,6,6,14]Cl ionic liquids. TEM and Fe K-edge XANES spectra were used to characterize these Fe NPs before and after catalysis. Results show that Fe NPs synthesized in protic solvents with large sizes have more prolonged catalytic activity and stability compared to those with small sizes, because small Fe NPs are oxidized quickly when exposed to water and/or air. Small Fe NPs synthesized in the ionic liquid solvent had a higher catalytic activity than the NPs synthesized in protic solvents, but they degrade quickly over time after exposure to air.

6.2 Introduction

Hydrogenation of alkenes and alkynes is one class of chemical reactions with great importance to the food, pharmaceutical, petrochemical and fine chemical industries.[1-5] Precious metals such as Pd, Pt, Ru, and Rh are commonly used to catalyze such reactions,[2,6,7] but they are typically quite expensive. Fe based catalysts have attracted a great deal of interest because of their high natural abundance and low toxicity. A number of groups have developed various homogeneous Fe complexes to catalyze hydrogenation reactions.[8-10] Compared to homogeneous catalysts, heterogeneous catalysts are more amenable to recycling and scalability, and several groups have looked to develop Fe nanoparticles (NPs) to catalyze this reaction.[11-15] For example, the de Vries group and Chaudret group have shown that small Fe NPs with sizes of *ca.* 2 nm have high activity for the hydrogenation of olefins and alkynes at room temperature with 10 bar H_2.[12-14] Moores' group synthesized much larger Fe@Fe_xO_y (core@shell) NPs with an average Fe NP core diameter of 44 ± 8.3 nm and an Fe oxide shell thickness of 6 ± 2 nm though using $NaBH_4$ to reduce $FeSO_4$ in a water/methanol mixture, and

applied them to catalyze the hydrogenation of olefins and alkynes at 80 °C under 40 bar H_2 in ethanol.[15] These NPs could be magnetically recovered from the reaction solution and reused up to 10 times. Recently, our group showed one can control the sizes of the resulting Fe@Fe_xO_y NPs through using different molar ratios of methanol to water with poly(vinylpyrrolidone) (PVP) as a stabilizer.[16] The size of a NP can impact its surface area and the bonding strength with the reactants,[17] and further influence its activity and selectivity in a catalytic reaction.[18] Therefore, we sought to optimize the size of Fe NPs and explore different solvent systems for the use of Fe NPs to catalyze hydrogenation reactions.

Ionic liquids (ILs) have been widely used as solvents and stabilizers in the synthesis of NPs due to their unique properties, such as high polarity, negligible vapor pressure and thermal stability.[19,20] Several groups have synthesized NPs in ILs and applied them as catalysts for the hydrogenation of alkenes or alkynes.[21-23] For example, our group showed that Pd NPs embedded in tetraalkylphosphonium halide ILs are active and recyclable catalysts for the reduction of a variety of olefins.[21] Moores' group synthesized Ru NPs in tetraalkylphosphonium and imidazolium ILs,[22] and showed that the Ru NPs synthesized in tetraalkylphosphonium-based ILs have higher catalytic activities for the hydrogenation of cyclohexene compared to the NPs synthesized in imidazolium ILs due to the higher ionicity of tetraalkylphosphonium ILs. To the best of our knowledge, there is only one study in the literature using Fe NPs synthesized in imidazolium ILs for the semi-hydrogenation of alkynes at 80 °C with 60 bar H_2.[23] Thus we wanted to examine the use of Fe NPs in tetraalkylphosphonium ILs for hydrogenation reactions.

X-ray absorption spectroscopy (XAS) is a powerful tool to probe the oxidation states and coordination environments of elements in materials with short-range order such as nanostructures. XAS places few experimental constraints on the samples; for example, it is possible to follow speciation and oxidation state changes in liquid solutions using XAS. By using liquid cells with X-ray permeable windows, our group has shown that *in situ* XAS studies can be done to follow catalyst speciation in their reaction solutions.[16,24-26] For example, Maclennan *et al*. showed that Pd(II) becomes reduced to Pd(0) on the surfaces of Au NPs upon exposure to crotyl alcohol and the resulting Pd atoms are very stable toward oxygen gas by *in*

situ Pd L_3-edge and K-edge XAS.[25] We recently showed that one can follow the oxidation of Fe NPs via *in situ* Fe K-edge XAS, follow galvanic reactions of Fe@Fe_xO_y NPs with Pd(II) and Cu(II) species, and also showed that Fe@Fe_xO_y NPs can re-reduce oxidized Pd in Suzuki-Miyaura cross-coupling reactions.[26] In this work, we used similar liquid cells and studied the changes of Fe NPs before and after hydrogenation reactions by Fe K-edge XANES spectra.

In this study, we synthesized two different sizes of PVP-stabilized Fe@Fe_xO_y NPs by the reduction of Fe salts with $NaBH_4$, and compared their catalytic ability in ethanol for the hydrogenation of alkenes with Fe NPs synthesized in P[6,6,6,14]Cl ILs. TEM and Fe K-edge XANES were used to study the stability of Fe NPs for hydrogenation reactions. Results show that Fe NPs synthesized in P[6,6,6,14]Cl ILs have small sizes and they are more active for the hydrogenation reactions than the Fe NPs synthesized in protic solvents. However, they are quite sensitive to oxygen and have less recyclability than Fe NPs with large sizes.

6.3 Experimental Section

6.3.1 Materials

All chemicals were used as received. Fe(II) sulfate heptahydrate, 1-octene, octane, 2-norbornene and norbornane were purchased from Sigma-Aldrich. Poly(vinylpyrrolidone) (M. W. 58,000 g/mol) was purchased from Alfa Aesar. Sodium borohydride, Fe(III) acetylacetonate ($Fe(acac)_3$), methanol and ethanol (HPLC grade) were purchased from Fisher Scientific. Eighteen MΩ·cm Milli-Q water (Millipore, Bedford, MA) was used for the synthesis of Fe@Fe_xO_y NPs in the mixture of methanol and water. The tri(hexyl)tetradecylphosphonium chloride (P[6,6,6,14]Cl) ILs were purchased from Cytec Industries Ltd.

6.3.2 Synthesis

6.3.2.1 Synthesis of Fe@Fe_xO_y NPs in Protic Solvents

Fe@Fe_xO_y NPs were synthesized by reducing $FeSO_4 \cdot 7H_2O$ (5.0 mmol) by $NaBH_4$ (25 mmol) in a 1:1 water/methanol (v/v) mixture or pure ethanol solution (20 mL) in the presence of PVP (10 mmol based on monomer unit) under nitrogen gas as reported in Chapter 2.[16] The

resulting NPs were magnetically separated from the reaction solutions and dried under vacuum, and then redispersed in ethanol.

6.3.2.2 Synthesis of Fe NPs in Ionic Liquids

P[6,6,6,14]Cl IL was dried under vaccum at 70 °C for 2 hours with stirring before synthesis of Fe NPs. Then 0.090 g of $Fe(acac)_3$ (0.25 mmol) was added under nitrogen to a 17 mL of P[6,6,6,14]Cl IL at 80 °C in a 50 mL round bottom flask, and vigorously stirred. The solution was cooled to 50 °C, and 1.3 mmol of $LiAlH_4$ (0.65 mL, 2.0 M in THF) was injected drop-wise. The deep red solution gradually turned to black, which indicated the formation of Fe NPs. After 10 min, volatile species (THF, byproducts) were removed by vacuum-stripping the system at 80 °C for 30 min. The Fe NPs-IL composites thus obtained were directly transferred to the glass reactor vessel for hydrogenation reactions.

6.3.3 Catalytic Reactions

Hydrogenation reactions were carried out in a dynamic Parr reactor equipped with a temperature control system, a mechanical stirrer, and a pressure meter (Parr 4560). 0.25 mmol of Fe NPs mixed with 5.0 mmol of substrate in 17 mL ethanol or IL were transferred to the glass vessel inside the reactor and flushed with hydrogen gas at 100 psi for 2 min. Then the reactor was filled with hydrogen gas to a pressure of 33 bar, and heated to 80 °C. After 20 h, the mixture was allowed to cool to ambient temperature, and the pressure was released. When the reaction solvent was ethanol, the product was analyzed by GC by diluting the reaction solution with ethanol after removing the catalysts by centrifuging. When the IL was used as the solvent, the reaction mixture was transferred to a round bottom flask and vacuum stripped to extract the product and/or unreacted substrate, followed by analysis of the extracted mixture by GC.

6.3.4 Characterization

Transmission electron microscopy (TEM) analyses of the NPs were initially conducted using a HT7700 microscope (Hitachi High-Technologies) operating at 100 kV. The samples were prepared by drop-casting one drop of dilute, aqueous sample onto a carbon-coated 200

mesh copper grid (Electron Microscopy Sciences, Hatfield, PA). Average particle diameters were determined by manually measuring 50 NPs from each sample using the ImageJ program.[27]

Fe K-edge XANES spectra were collected at the Soft X-ray Microcharacterization Beamline (SXRMB) at the Canadian Light Source (CLS). The Fe K-edge measurements were conducted under an ambient atmosphere. Decreasing the beam flux by defocusing and/or filtering the beam with Kapton filters and stirring the sample via magnetic stirring were used to avoid sample damage due to photoreduction. Liquid cells (SPEX CertiPrep Disposable XRF X-Cell sample cups) were covered with a 4 μm ultralene film (purchased from Fisher Scientific, Ottawa, ON) and used for XANES analysis. The data were analyzed using the Athena software.[28,29] Fe foil transmission spectrum and fluorescence spectra of $FeSO_4 \cdot 7H_2O$ and $Fe(NO_3)_3 \cdot 9H_2O$ aqueous solutions (50 mM) were measured under the same conditions and used as standards for linear combination analysis XANES fitting in the range of 7100 to 7180 eV. The R-factors on the mismatch between data and fit are all lower than 0.01.

The composition of the reaction mixture was analyzed by a gas chromatograph (GC, Agilent Technologies 7890A) with a flame ionization detector and a HP-5 capillary column (30 m × 0.32 mm × 0.25 μm, J&W Scientific).

6.4 Results and Discussion

Two sizes of Fe NPs were synthesized in 9:1 methanol/water (v/v) mixtures and ethanol, respectively, by using $NaBH_4$ to reduce $FeSO_4 \cdot 7H_2O$ with PVP as a stabilizer at room temperature (23 ± 2 °C) under N_2 following previous literature protocols.[16] As shown in Figure 6.1 A and C, the water and trace oxygen in the synthetic system oxidized the surfaces of Fe NPs and the resulting NPs had a Fe core and Fe oxide shell ($Fe@Fe_xO_y$) structure. The average sizes of as-synthesized $Fe@Fe_xO_y$ NPs in the 9:1 methanol/water (v/v) mixture were 7.5 ± 1.0 nm, while those synthesized in ethanol had an average size of 2.7 ± 1.8 nm. Their sizes are in general agreement with our previous work.[16] The synthesis of Fe NPs in IL was achieved by the reduction of $Fe(acac)_3$ with $LiAlH_4$ in P[6,6,6,14]Cl IL at 50 °C under N_2. As shown in Figure 6.1 E, the resulting Fe NPs have very small sizes (1.9 ± 0.5 nm) which is likely due to

the high dispersion of Fe NPs by IL via strong stabilizing interactions with the chloride anion of the IL, along with steric protection by the charge balancing bulky tetraalkylphosphonium cations.[22] The IL was dried before synthesis, therefore, there was no obvious oxidation shell formed on the surfaces of Fe NPs seen in TEM, albeit this is hardly conclusive given their small size.

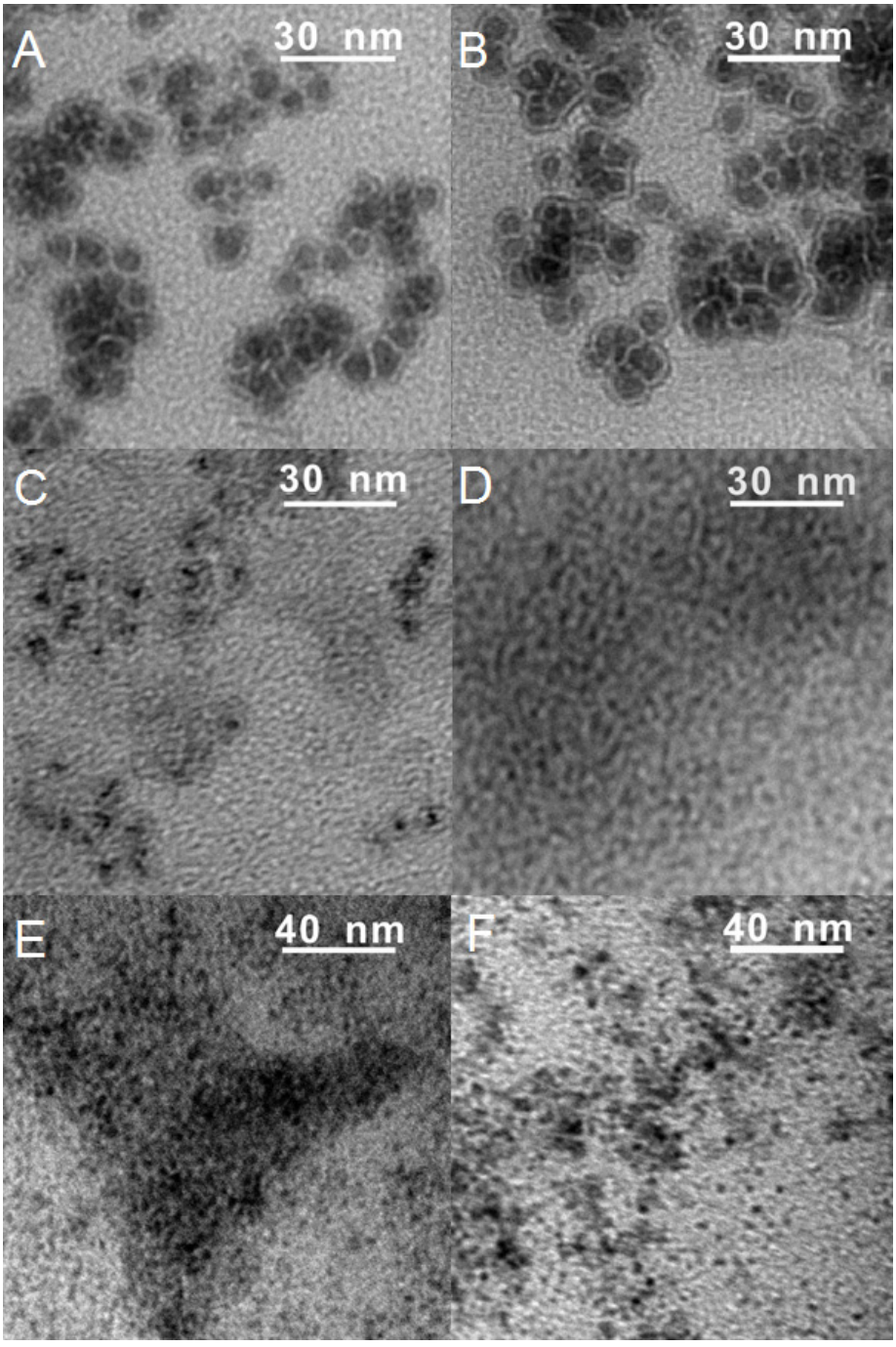

Figure 6.1. TEM image of Fe@Fe_xO_y NPs synthesized in 9:1 methanol/water (v/v) solvents with PVP as a stabilizer before (A) and after (B) hydrogenation reaction; TEM image of Fe@Fe_xO_y NPs synthesized in ethanol with PVP as a stabilizer before (C) and after (D) hydrogenation reaction; and TEM image of Fe NPs synthesized in P[6,6,6,14]Cl IL before (E) and after (F) hydrogenation reaction.

Two separate hydrogenation substrates that were soluble in both ethanol and the P[6,6,6,14]Cl IL were examined as substrates, 2-norbornene and 1-octene, as shown in Scheme 6.1. Reactions were catalyzed by 5 mol% Fe NPs under 33 bar H_2 at 80 °C in 20 h, and the catalytic results are listed in Table 6.1. Fe@Fe_xO_y NPs synthesized in 9:1 methanol/water (v/v) solvents with average sizes of 7.5 ± 1.0 nm are active for the hydrogenation of 2-norbornene with a conversion of 92% (entry 1). No obvious decrease in conversion was seen after 4 cycles (entries 1-4). We also applied Fe NPs synthesized in ethanol with average size of 2.7 ± 1.8 nm for the hydrogenation of 2-norbornene (entry 6). However, these Fe NPs only show 40% conversion which is much lower than that of larger Fe@Fe_xO_y NPs synthesized in the 9:1 methanol/water mixture. Similar results were observed for the hydrogenation of 1-octene. Smaller Fe NPs synthesized in ethanol also show lower conversion (33%, entry 7) than that of the lareger Fe@Fe_xO_y NPs synthesized in methanol/water mixutures (42%, entry 5). To further study the catalytic ability of Fe NPs with small sizes, we applied Fe NPs synthesized in a P[6,6,6,14]Cl IL with average NP sizes of 1.9 ± 0.5 nm for the hydrogenation reactions. These Fe NPs have high catalytic ability for both of the hydrogenation of 2-norbornene (98% conversion, entry 9) and 1-octene (87% conversion, entry 11). Control studies showed the P[6,6,6,14]Cl IL itself cannot catalyze this reaction (1% conversion, entry 8). However, these Fe NPs have poor recyclability (entry 10 and 12), and quickly lose activity after multiple cycles.

Scheme 6.1. The hydrogenation of 2-norbornene and 1-octene.

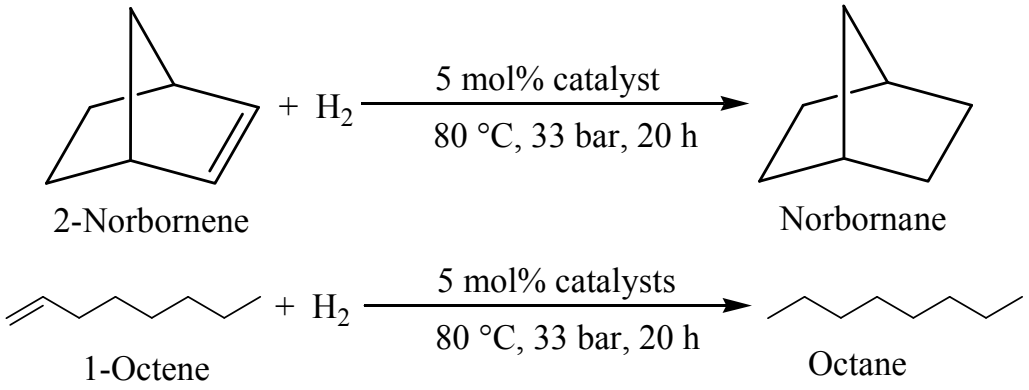

Table 6.1. Summary of the catalytic results for the hydrogenation of 2-norbornene and 1-octene.

Entry	Substrate	Fe NP Catalyst	Solvent	Cycle	Conversion
1	2-Norbornene	7.5 ± 1.0 nm	Ethanol	1	92%
2	2-Norbornene	7.5 ± 1.0 nm	Ethanol	2	92%
3	2-Norbornene	7.5 ± 1.0 nm	Ethanol	3	92%
4	2-Norbornene	7.5 ± 1.0 nm	Ethanol	4	92%
5	1-Octene	7.5 ± 1.0 nm	Ethanol	1	42%
6	2-Norbornene	2.7 ± 1.8 nm	Ethanol	1	40%
7	1-Octene	2.7 ± 1.8 nm	Ethanol	1	33%
8	2-Norbornene	None	P[6,6,6,14]Cl	1	1%
9	2-Norbornene	1.9 ± 0.5 nm	P[6,6,6,14]Cl	1	98%
10	2-Norbornene	1.9 ± 0.5 nm	P[6,6,6,14]Cl	2	7%
11	1-Octene	1.9 ± 0.5 nm	P[6,6,6,14]Cl	1	87%
12	1-Octene	1.9 ± 0.5 nm	P[6,6,6,14]Cl	2	16%

To reveal the reasons for the different catalytic ability and stability of these Fe NPs, the NP catalysts were examined by TEM and Fe K-edge XANES spectra after catalytic reactions. As shown in Figure 6.1 B, there is no very obvious change in average sizes of Fe@Fe_xO_y NPs synthesized in 9:1 methanol/water (v/v) solvents before and after hydrogenation reactions. XANES is very sensitive to the oxidation states of the elements in a material with short-range order. Fe K-edge XANES spectra show these Fe@Fe_xO_y NPs did become very slightly more oxidized after 1 cycle of hydrogenation judged by the right shift of their absorption edge (Figure 6.2 A). Linear combination fitting of the Fe K-edge XANES spectra with standards, Fe foil, $FeSO_4$ and $Fe(NO_3)_3$ were used as standards as reported in our previous work,[16] reveal that the relative Fe(0), Fe(II) and Fe(III) levels showed no significant changes after 1 cycle of

reaction (Table 6.2). Thus, the large sizes of these Fe@Fe_xO_y NPs and initial oxidation of their surfaces by H_2O and trace O_2 allow them have good resistance to further oxidation, while still being fairly good hydrogenation catalysts. Thus these NPs also have good recyclability for catalysis. However, in the case of the 2.7 ± 1.8 nm Fe NPs synthesized in ethanol, the NPs are much more sensitive to oxidation. The XANES spectra after 1 cycle of hydrogenation shows a pronounced energy shift, thus suggesting significantly additional Fe oxidation is occurring (Figure 6.2 B). Linear combination analyses show that the amount of Fe(0) in the system goes from 45% to 33% after 1 cycle of hydrogenation reaction. TEM images after hydrogenation reaction also suggest the final NPs have much smaller sizes (Figure 6.1 D), though we are not certain what is leading to the change in NP size. The drop in catalytic activity upon multiple cycles is attributed to further oxidation of Fe, presumably due to O_2 and water exposure between cycles. The lower initial activity of these smaller NPs is likely due to the much larger fraction of Fe that is oxidized in the system before any catalysis has taken place (*i.e.* only 45% Fe(0) vs. 67% for the 9:1 methanol/water system).

Table 6.2. XANES Fitting Results showing mole fractions of each Fe standard.

Sample	**Fe(0)%**	**Fe(II)%**	**Fe(III)%**
Fe@Fe_xO_y NPs synthesized in 9:1 methanol/water	67(3)	10(2)	23(3)
Fe@Fe_xO_y NPs synthesized in 9:1 methanol/water after hydrogenation reaction	66(2)	11(1)	23(3)
Fe@Fe_xO_y NPs synthesized in ethanol	45(2)	28(1)	28(3)
Fe@Fe_xO_y NPs synthesized in ethanol after hydrogenation reaction	33(1)	18(2)	49(4)

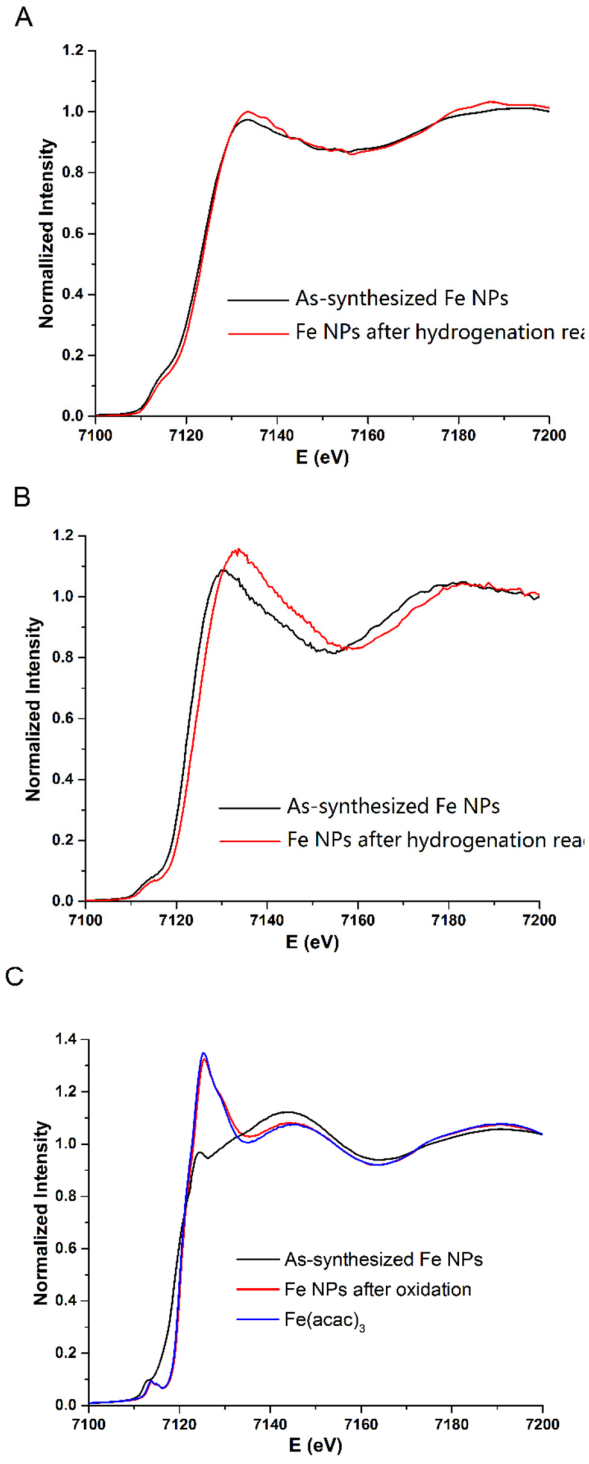

Figure 6.2. Fe K-edge XANES spectra of (A) Fe@Fe_xO_y NPs synthesized in 9:1 methanol/water (v/v) solvents with PVP as a stabilizer; (B) Fe@Fe_xO_y NPs synthesized in ethanol with PVP as a stabilizer and (C) Fe NPs synthesized in P[6,6,6,14]Cl IL.

For the IL system, there were also significant differences in the XANES spectroscopy before and after catalytic reactions. These Fe NPs are very prone to oxidative degradation upon exposure to air and/or moisture; their corrosion is enhanced by chloride anion in the system.[30] The extraction of reactants and products under ambient conditions led to the initially black Fe NP solution turning to a pale yellow colour. Fe K-edge XANES spectra reveal that these Fe NPs after oxidation have similar spectroscopic signature as the original $Fe(acac)_3$ salt in the IL before reduction (Figure 6.2 C). It should be noted that the spectra do not resemble those collected in the ethanol solvent, likely because the Fe coordination environment involves chloride ligands in the IL. There is also a small increase in the average sizes of the NPs to 2.2 ± 0.4 nm (Figure 6.1 F), this might be due to Ostwald ripening observed in many IL studies,[22,31] or perhaps the growth of the particles during oxidation. Thus while the ILs allow for the initial formation of very small, catalytically active species, it is incredibly difficult to reuse these systems for multiple cycles given the extreme sensitivity of this system to oxidation.

6.5 Conclusion

$Fe@Fe_xO_y$ NPs synthesized in 9:1 methanol/water (v/v) solvents with average sizes of 7.5 ± 1.0 nm have better recyclability for hydrogenation reactions than smaller NPs synthesized in ethanol or a tetraalkylphosphonium chloride IL. Liquid phase Fe K-edge XAS results show this is because small Fe NPs are much more easily oxidized in the presence of oxygen and water than the larger systems. Small Fe NPs synthesized in the IL have much higher catalytic ability for both of the hydrogenation of 2-norbornene and 1-octene. This may be because Fe NPs synthesized in IL do not have Fe oxide shells on the surface of Fe NPs, and thus have a more catalytically accessible surface.

Acknowledgments

The authors acknowledge financial assistance from the National Sciences and Engineering Research Council of Canada (NSERC). XANES experiments described in this paper were performed at the Canadian Light Source, which is supported by the Natural Sciences and Engineering Research Council of Canada, the National Research Council Canada, the Canadian

Institutes of Health Research, the Province of Saskatchewan, Western Economic Diversification Canada, and the University of Saskatchewan.

6.6 References

1. Cerveny, L. Catalytic Hydrogenation. Elsevier, **1986**.
2. de Vries, J. G.; Elsevier, C. J. The Handbook of Homogeneous Hydrogenation. Wiley-VCH. **2007**.
3. Arpe, H. J. Industrial Organic Chemistry. Wiley-VCH. **2010**.
4. Welther, A.; Bauer, M.; Mayer, M.; von Wangelin, A. J. Iron(0) Particles: Catalytic Hydrogenations and Spectroscopic Studies. *ChemCatChem.* **2012**, *4*, 1088–1093.
5. Hudson, R.; Hamaska, G.; Osako, T.; Yamada, Y. M. A.; Li, C.-J.; Uozumi, Y.; Moores, A. Highly Efficient Iron(0) Nanoparticle-Catalyzed Hydrogenation in Water in Flow. *Green Chem.* **2013**, *15*, 2141–2148.
6. Niu, Y.; Yeung, L. K.; Crooks, R. M. Size-Selective Hydrogenation of Olefins by Dendrimer-Encapsulated Palladium Nanoparticles. *J. Am. Chem. Soc.* **2001**, *123*, 6840–6846.
7. Lough, A. J.; Morries, R. H.; Ricciuto, L.; Schleis, T. Solution and Crystal Structure of the Dihydrogen Complex $[Ru(H_2)(H)(PMe_2Ph)_4]PF_6$, An Acitive Alkyne Hydrogenation Catalyst. *Inorg. Chim. Acta.* **1998**, *270*, 238–246.
8. Bart, S. C.; Hawrelak, E. J.; Lobkovsky, E.; Chirik, P. J. Low-Valent α-Diimine Iron Complexes for Catlaytic Olefin Hydrogenation. *Organometallics* **2005**, *24*, 5518–5527.
9. Bart, S. C.; Lobkovsky, E.; Chirik, P. J. Preparation and Molecular and Electronic Structures of Iron(0) Dinitrogen and Silane Complexes and Their Application to Catalytic Hydrogenation and Hydrosilation. *J. Am. Chem. Soc.* **2004**, *126*, 13794–13807.
10. Enthaler, S.; Haberberger, M.; Irran, E. Highly Selective Iron-Catalyzed Synthesis of Alkenes by the Reduction of Alkynes. *Chem. Asian J.* **2011**, *6*, 1613–1623.
11. Carter, T. S.; Guiet, L.; Frank, D. J.; West, J.; Thomas, S. P. Iron-Catalysed Reduction of Olefins using a Borohydride Reagent. *Adv. Synth. Catal.* **2013**, *355*, 880–884.
12. Phua, P.-H.; Lefort, L.; Boogers, J. A. F.; Tristany, M.; de Vries, J. G. Soluble Iron Nanoparticles as Cheap and Environmentally Benign Alkene and Alkyne Hydrogenation Catalysts. *Chem. Commun* **2009**, *45*, 3747–3749.
13. Rangheard, C.; Fernández, C. de J.; Phua, P.-H.; Hoorn, J.; Lefort, L.; de Vries, J. G. At the Frontier between Heterogeneous and Homogeneous Catalysts: Hydrogenation of Olefins and Alkynes with Soluble Iron Nanoparticles. *Dalton Trans.* **2010**, *39*, 8464–8471.
14. Kelsen, V.; Wendt, B.; Werkmeister, S.; Junge, K.; Beller, M.; Chaudret, B. The Use of

Ultrasmall Iron(0) Nanoparticles as Catalysts for the Selective Hydrogenation of Unsaturated C-C bonds. *Chem. Commun* **2013**, *49*, 3416–3418.

15. Hudson, R.; Rivière, A.; Cirtiu, C. M.; Luska, K. L.; Moores, A. Iron-Iron Oxides Core-Shell Nanoparticles are active and Magetically Recyclable Olefin and Alkyne Hydrogenation Catalysts in Protic and Aqueous Media. *Chem. Commun* **2012**, *48*, 3360–3362.

16. Yao, Y.; Hu, Y.; Scott, R. W. J. Watching Iron Nanoparticles Rust: An *in Situ* X-ray Absorption Spectroscopic Study. *J. Phys. Chem. C* **2014**, *118*, 22371–22324.

17. Cuenya, B. R.; Behafarid, F. Nanocatalysis: Size- and Shape-dependent Chemisorption and Catalytic Acitivity. *Surf. Sci. Rep.* **2008**, *63*, 169–199.

18. Bai, L.; Wang, X.; Chen, Q.; Ye, Y.; Zheng, H.; Guo, J.; Yin, Y.; Gao, C. Explaining the Size Dependence in Platinum-Nanoparticle-Catalyzed Hydrogenation Reactions. *Angew. Chem. Int. Ed.* **2016**, *55*, 15656–15661.

19. Dash, P.; Dehm, N. A.; Scott, R. Bimetallic PdAu Nanoparticles as Hydrogenation Catalysts in Imidazolium Ionic Liquids. *J. Mol. Catal. A: Chem.* **2008**, *286*, 114–119.

20. Gual, A.; Godard, C.; Castillón, S.; Curulla-Ferré, D.; Claver, C. Colloidal Ru, Co and Fe-Nanoparticles. Synthesis and Application as Nanocatalysts in the Fischer-Tropsch Process. *Catal. Today* **2012**, *183*, 154–171.

21. Banerjee, A.; Theron, R.; Scott, R. W. J. Highly Stable Noble-Metal Nanoparticles in Tetraalkylphosphonium Ionic Liquids for *in Situ* Catalysis. *ChemSusChem* **2012**, *5*, 109–116.

22. Luska, K. L.; Moores, A. Ruthenium Nanoparticle Catalysts Stabilized in Phosphonium and Imidazolium Ionic Liquids: Dependence of Catalyst Stability and Activity on the Ionicity of the Ionic Liquid. *Green Chem.* **2012**, *14*, 1736–1742.

23. Gieshoff, T. N.; Welther, A.; Kessler, M. T.; Prechtl, M. H. G.; von Wangelin A. J. Stereoselective Iron-Catalyzed Alkyne Hydrogenation in Iron Liquids. *Chem. Commun.* **2014**, *50*, 2261–2264.

24. Liu, L.; Burnyeat, C. A.; Lepsenyi, R. S.; Nwabuko, I. O.; Kelly, T. L. Mechanism of Shape Evolution in Ag Nanoprisms Stabilized by Thiol-Terminated Poly(ethylene glycol): an in Situ Kinetic Study. *Chem. Mater.* **2013**, *25*, 4206–4214.

25. Maclennan, A.; Banerjee, A.; Hu, Y.; Miller, J. T.; Scott, R. W. J. *In Situ* X-ray Absorption Spectroscopic Analysis of Gold-Palladium Bimetallic Nanoparticle Catalysts. *ACS Catal.* **2013**, *3*, 1411–1419.

26. Yao, Y.; Patzig, C.; Hu, Y.; Scott, R. W. J. *In Situ* X-ray Absorption Spectroscopic Study of Fe@Fe_xO_y/Pd and Fe@Fe_xO_y/Cu Nanoparticle Catalysts Prepared by Galvanic Exchange Reactions. *J. Phys. Chem. C* **2015**, *119*, 21209–21218.

27. Abramoff, M. D.; Magalhäes, P. J.; Ram, S. J. Image Processing with ImageJ. *Biophotonics Int*. **2004**, *11*, 36-42.

28. Newville, M. IFEFFIT: Interactive XAFS Analysis and FEFF Fitting. *J. Synchrotron Radiat*. **2001**, *8*, 322–324.

29. Ravel, B.; Newville, M. ATHENA, ARTEMIS, HEPHAESTUS: Data Analysis for X-ray Absorption Spectroscopy Using IFEFFIT. *J. Synchrotron Radiat*. **2005**, *12*, 537–541.

30. Banerjee, A.; Theron, R.; Scott, R. W. J. Redispersion of Transition Metal Nanoparticle Catalysts in Tetraalkylphosphonium Ionic Liquids. *Chem. Comm*. **2013**, *49*, 276–278.

31. Maclennan, A.; Banerjee, A.; Scott, R. W. J. Aerobic Oxidation of α,β-Unsaturated Alcohols Using Sequentially-Grown AuPd Nanoparticles in Water and Tetraalkylphosphonium Ionic Liquids. *Catal. Today* **2013**, *207*, 170–179.

CHAPTER 7

7.1 Summary and Conclusion

My PhD studies focused on the synthesis and characterization of Fe@Fe_xO_y NPs and bimetallic NPs based on Fe@Fe_xO_y NPs, and used *in situ* X-ray absorption spectroscopy as a powerful tool to characterize the structures of these NPs, follow their formation processes and study changes in their speciation during catalytic reactions. Therefore, in this thesis, I introduced different methods to synthesize Fe and Fe@Fe_xO_y NPs and bimetallic NPs based on Fe@Fe_xO_y NPs and used different *in situ* XAS setups to characterize them.

First, in Chapter 2, Fe@Fe_xO_y NPs were synthesized by the reduction of Fe salts in methanol or water/methanol mixtures using a $NaBH_4$ reducing agent under nitrogen gas. PVP and different volume ratios of methanol to water were used to control the sizes of the resulting Fe@Fe_xO_y NPs. The relative oxidation kinetics of each NP size were monitored by *in situ* Fe K-edge XANES spectra using an *in situ* liquid cell setup. Linear combination fitting of these *in situ* Fe K-edge XANES spectra by the standards $Fe(NO_3)_3$, $FeSO_4$ and zero-valent Fe foil revealed that these Fe@Fe_xO_y NPs have similar initial Fe(0) contents. While it appears that the rate of Fe(0) oxidation increases with a decrease in average NP size, this is due only to differences in the relative surface areas of the NPs, and in fact similar oxidation mechanisms are at work for all the particle sizes studied. Fe K-edge and L-edge XANES spectra indicated that these NPs with different sizes finally reached the same octahedral-coordinated Fe(III) oxidation state. XRD results further confirmed that these Fe@Fe_xO_y NPs have an α-Fe core before oxidation and have a γ-FeOOH shell after oxidation.

In Chapter 3, Fe@Fe_xO_y NPs were reacted with different molar ratios of Pd(II) and Cu(II) by galvanic exchange reactions to form Fe@Fe_xO_y/Pd and Fe@Fe_xO_y/Cu bimetallic NPs with different morphologies. We further developed the *in situ* liquid cell setup used in Chapter 2 to allow for the addition of Pd or Cu salt solutions into the cell to mix with Fe@Fe_xO_y NPs. Through using this *in situ* liquid cell setup, *in situ* Pd L_3-edge, Cu K-edge and Fe K-edge XANES spectra were collected to follow the formation processes of Fe@Fe_xO_y/Pd and Fe@Fe_xO_y/Cu bimetallic NPs. Linear combination fitting results show that the reduction of

Pd(II) or Cu(II) occurs quickly, and the reduction was completed within 20 min. TEM and STEM results show the resulting PdFe bimetallic systems have finally dispersed Pd NPs on the Fe oxide surface, whereas for the Cu system the deposition of Cu is much more heterogeneous. This was speculated to be due to the fact that the Cu salts have to penetrate the Fe oxide shell to react with the Fe(0) core, whereas Pd salts can react with Fe(II) sites in the Fe oxide shell. *In situ* Pd L_3-edge and Fe K-edge XANES results also show that these Fe@Fe_xO_y NPs can re-reduce oxidized Pd in Suzuki-Miyaura cross-coupling reactions.

In Chapter 4, Fe@Fe_xO_y/Pd NPs are shown to have a high catalytic activity and stability in ethanol compared to water for the hydrogenation of 2-methyl-3-buten-2-ol. TEM images show that Fe@Fe_xO_y NPs are degrading over time in water and *in situ* XANES experiments were carried out. To mimic the reaction conditions, hydrogen gas was bubbled into the liquid cell to start the hydrogenation reaction, and the reaction was monitored at the Pd L_3-edge and Fe K-edge. The results show that these NPs are more stable in ethanol solutions, whereas further oxidation of the Fe cores occurs in the presence of water. In the hydrogenation of 2-methyl-3-buten-2-ol, 5:1 Fe@Fe_xO_y/Pd NPs have the highest turnover frequency around 3600 h^{-1} using ethanol as a solvent, whereas 50:1 or 20:1 Fe@Fe_xO_y/Pd NPs could also be used as magnetically recoverable catalysts.

In Chapter 5, Fe NPs were obtained by the thermal decomposition of Fe pentacarbonyl in the presence of air-free 1-octadecene and oleylamine at 180 °C. Starting with these Fe NPs, the formation of hollow Fe oxide NPs was followed, and the core-void-shell Fe-Fe_xO_y intermediates were captured. Fe K-edge XANES spectra were collected by using an *in situ* high temperature liquid cell, such that the Fe NP speciation during the oxidation reaction to form hollow Fe oxide NPs could be followed. Through capturing the core-void-shell Fe-Fe_xO_y intermediates during the formation of hollow Fe oxide NPs process and utilizing the incompletely oxidized Fe core in the core-void-shell structure to reduce Pd(II) to Pd(0), we studied the penetrability of hollow Fe oxide shells by Pd L_3-edge spectroscopy. Results showed that the Fe oxide shells in the core-void-shell NPs were impenetrable to Pd(II) salts when the thickness of the shell was more than 2 nm, but could be activated by further chemical etching of the structures.

In Chapter 6, $Fe@Fe_xO_y$ NPs synthesized in 9:1 methanol/water (v/v) mixtures and ethanol were applied to catalyze the hydrogenation of 2-norbornene and 1-octene, and their catalytic abilities were compared with Fe NPs synthesized in tetraalkylphosphonium chloride ionic liquids. The results show that 7.5 ± 1.0 nm $Fe@Fe_xO_y$ NPs synthesized in the mixture of methanol and water have higher catalytic activities and stability than smaller 2.7 ± 1.8 nm $Fe@Fe_xO_y$ NPs synthesized in ethanol, and Fe K-edge XANES spectra show that this is because the smaller NPs are much more easily oxidized. 1.9 ± 0.5 nm Fe NPs synthesized in P[6,6,6,14]Cl IL have the highest catalytic activity for the hydrogenation reactions. However, their small sizes and the presence of chloride anions in the IL leads to them getting readily oxidized, and thus their activity drops dramatically upon recycling.

In this thesis, *in situ* XAS has been used to investigate into the oxidation mechanisms of $Fe@Fe_xO_y$ NPs, the formation of $Fe@Fe_xO_y$/Pd and $Fe@Fe_xO_y$/Cu NPs, the penetrability of hollow Fe oxide shells via galvanic exchange reactions between the Fe(0) core within the hollow Fe oxide shell and Pd(II) salts, and the metal speciation in these NPs during catalytic reactions. Thus, I have shown that *in situ* XAS is a very powerful tool for following NP chemistry and catalysis under *in situ* and operando conditions

7.2 Outlook and Future Work

Many groups have shown that the interactions of Au with Pd can significantly improve the activity and selectivity of the resulting AuPd bimetallic NP catalysts for various reactions such as oxidation reactions, acetylene trimerization and hydrodesulphurization reactions compared to their monometallic counterparts.[1] However, the separation of such NPs from solutions after catalytic reactions is still not very efficient, and is often done through sedimentation or filtration in industry. As shown the studies in Chapter 4, introducing magnetic Fe or Fe oxide NPs as supports to realize possible magnetic recovery is a quite promising method. To date, only a few examples have shown the successful synthesis of bimetallic Fe_3O_4 hybrid NPs with high catalytic ability for reactions and magnetic recylability.[2,3] My suggested future work aims at using the following two methods to synthesize AuPd@Fe and $AuPd@Fe_3O_4$ NPs and apply them for catalytic reactions.

7.2.1 Synthesis of AuPd@Fe Core@shell Nanoparticles and Their Catalytic Applications

Xu and co-workers have successfully synthesized Au/Co/Fe triple-layered core-shell NPs through using ammonia borane to reduce a mixture of Au(III), Co(II) and Fe(III) precursors.[6] In the presence of water, ammonia borane can release hydrogen gas at room temperature under ambient atmosphere, following Equation 7.1:

$$NH_3BH_3 + 2\ H_2O \rightarrow NH_4^+ + BO_2^- + 3\ H_2 \quad \textbf{(7.1)}$$

The reduction potentials of the metal precursors are as follows: $E°_{Fe(III)/Fe(II)}$ = +0.77 V *vs*. the standard hydrogen electrode (SHE); $E°_{Fe(II)/Fe(0)}$ = -0.45 V *vs*. SHE; $E°_{Co(II)/Co(0)}$ = -0.28 V *vs*. SHE; $E°_{Au(III)/Au(0)}$ = +0.93 V *vs*. SHE. As Au has the highest reduction potential, it is reduced first by NH_3BH_3, followed by sequential reduction of Co and Fe with H_2 over the Au surface to give Au/Co/Fe triple-layered core-shell NPs with Au-rich cores, Co-rich inter-layers and Fe-rich outer shells. The resulting Au/Co/Fe NPs exhibit much higher catalytic activity for the hydrolytic dehydrogenation of ammonia borane than the corresponding monometallic NPs. They can also be magnetically separated from the reaction solutions by an external magnet.

Inspired by this work, I have laid out a method below to make AuPd@Fe core-shell NPs which should give catalysts with similar acitivities and magnetic properties.

5.0 mg of $HAuCl_4 \cdot 4H_2O$ (0.012 mmol), 3.9 mg of H_2PdCl_4 (0.012 mmol), and 48 mg of $FeCl_3 \cdot 4H_2O$ (0.18 mmol) are dissolved along with PVP (100 mg) in a 100 mL round bottom flask with 10 mL of water. The solution would be stirred at 1600 rpm under room temperature for several minutes, followed by the addition of NH_3BH_3. Due to the high relative reduction potentials of Au and Pd precursors ($E°_{Au(III)/Au(0)}$ = +0.93 V *vs*. SHE; $E°_{Pd(II)/Pd(0)}$ = +0.95 V *vs*. SHE), it is anticipated that a AuPd bimetallic core will be formed first, likely with a Au rich core. The formation of the AuPd bimetallic core can further catalyze the release of H_2 from NH_3BH_3 and the subsequent reduction of Fe(III) to form Fe-rich outer shell by H_2.[4,5] To allow AuPd cores to be accessible to catalytic substrates, mild etching of Fe shells could be achieved by using acetic aicd.[6]

In situ Au L_3-edge, Pd L_3-edge and Fe K-edge XANES can be used to follow the formation process of AuPd@Fe NPs to study the formation kinetics and optimize the formation time. Au L_3-edge and Pd K-edge EXAFS spectra can be used to study the structure of the AuPd cores, and give valuable information about the architecture of the final trimetallic NPs. TEM and EDX maps would give visual confirmation of the structure of the resulting AuPd@Fe NPs.

Our group and others have shown that AuPd bimetallic NPs have higher activity and selectivity for hydrogenation reactions compared to their corresponding monometallic NPs.[7-10] I would apply the resulting AuPd@Fe NPs to catalyze olefin and alkyne hydrogenations. I would also tune the Pd:Au ratio to find the most promising compositions for catalytic activity and selectivity.

7.2.2 Synthesis of Pd@Au@Fe_3O_4 and Au@Pd@Fe_3O_4 Triple-layered Core@shell Nanoparticles and Their Catalytic Applications

Chapter 5 has shown that hollow Fe oxide NPs can be synthesized by taking advantage of the Kirkendall Effect. Shevchenko and co-workers have successfully encapsulated Au NPs inside hollow Fe oxide shell to form hybrid NPs by oxidizing Au@Fe core@shell NPs at high temperatures.[11] The inclusion of Au in Pd NP catalysts can significantly improve their activity and selectivity in many catalytic reactions.[12] As a future plan, I suggest trying to encapsulate Pd@Au or Au@Pd core@shell bimetallic NPs into the hollow Fe oxide NPs to synthesize triple-layered core@shell NPs.

7.2.2.1 Synthesis of Pd@Au@Fe_3O_4 Core@shell Nanoparticles

First, 4.5 nm Pd NPs would be synthesized as reported by Mazumder and co-workers.[13] For example, 75 mg of $Pd(acac)_2$ (acac = acetylacetonate) (0.24 mmol) would be mixed with 15 mL oleylamine in a 50 mL three-neck flask with a condenser under nitrogen at 60 °C for 10 min. 300 mg of borane tributylamine complex in 4.0 mL of oleylamine would be injected into the mixture. The temperature would then be raised to 90 °C and kept at this temperature for 1 h. Following this, the solution would be cooled down to room temperature, and 30 mL of ethanol would be added to wash the Pd NP product. Followed by seperation by centrifugation.

These Pd NPs would be used as seeds, and the Au coating could be achieved by reducing $HAuCl_4 \cdot 3H_2O$ (0.20 mmol) by oleylamine (2.0 mL) onto Pd seeds at 80 °C in 1-octadecene (8.0 mL).[14] Then 0.10 mL of $Fe(CO)_5$ would be injected into the solution and the solution would be kept at 180 °C for 30 min. This would be followed by cooling to 100 °C, and passing air throught the solution for 10 min to oxidize the Fe shell. To create cracks in the Fe_3O_4 shells, a strategy documented by Cheng *et al.* could be followed by etching the Fe_3O_4 shells under nitrogen at 260 °C in benzyl ether mixed with oleylamine and oleic acid for 45 min.[15]

7.2.2.2 Synthesis of Au@Pd@Fe_3O_4 Core@shell Nanoparticles

The potential synthesis of Au@Pd cores follows a method developed by Chen and co-workers.[12] The synthesis begins with the preparation of core@shell Au@Ag NPs by the sequential reduction of $HAuCl_4 \cdot 3H_2O$ and $AgNO_3$ by oleylamine at 150 °C. Then the pure Ag shells are converted into shells made of Ag/Pd alloy by galvanic exchange reaction between the Ag shells and Pd(II) precursors. Finally, the Ag component is completely removed from the solution using a saturated NaCl solution.

To synthesize Au@Pd@Fe_3O_4 NPs, the toluene solution with Au@Pd NPs would be mixed with 1-octadecene (8.0 mL) and oleylamine (2.0 mL) at 80 °C. Then 0.050 mL of $Fe(CO)_5$ would be injected into the solution and keep at 180 °C for 30 min. The solution would be cooled to 100 °C, and air passed through the solution for 10 min. The resulting Fe_3O_4 shells could also be etched by the strategy reported by Cheng and co-workers.[15]

The Pd@Au@Fe_3O_4 and Au@Pd@Fe_3O_4 NPs can be used to catalyze various olefin and alkyne hydrogenation reactions.

Fe or Fe oxide NPs not only could be the supports to help magnetically recover active catalysts, but also have catalytic ability themselves as shown in Chapter 6. In the future, studies of bi- or multimetallic NPs hybridized with Fe or Fe oxide NPs with improved catalytic ability or bifunctional activities will be carried out. The further development of *in situ* XAS techniques will help the rational design of the NPs.

7.3 References

1. Gao, F.; Goodman, D. W. Pd-Au Bimetallic Catalysts: Understanding Alloy Effects from Planar Models and (Supported) Nanoparticles. *Chem. Soc. Rev* **2012**, *41*, 8009–8020.

2. Woo, H.; Park, J. C.; Park, S.; Park, K. H. Rose-like Pd-Fe_3O_4 Hybrid Nanocomposite-Supported Au Nanocatalysts for Tandem Synthesis of 2-pheylindoles. *Nanoscale.* **2015**, *7*, 8356–8360.

3. Zhang, J.; Ma, J.; Fan, X.; Peng, W.; Zhang, G.; Zhang, F.; Li, Y. Graphene Supported Au-Pd-Fe_3O_4 Alloy Trimetallic Nanoparticle with Peroxidase-Like Activities as Mimic Enzyme. *Catal. Comm.* **2017**, *89*, 148–151.

4. Aranishi, K.; Jiang, H.-L.; Akita, T.; Haruta, M.; Xu, Q. One-Step Synthesis of Magnetically Recyclable Au/Co/Fe Triple-layered Core-Shell Nanoparticles as Highly Efficient Catalysts for the Hydrolytic Dehydrogenation of Ammonia Borane. *Nano Res.* **2011**, *4*, 1233–1241.

5. Jiang, H.-L.; Xu, Q. Catalytic Hydrolysis of Ammonia Borane for Chemical Hydrogen Storage. *Catal. Today.* **2011**, *4*, 56–23.

6. Jiang, G.; Zhu, H.; Zhang, X.; Shen, B.; Wu, L.; Zhang, S.; Lu, G.; Wu, Z.; Sun, S. Core/Shell Face-Centered Tetragonal FePd/Pd Nanoparticles as An Efficient Non-Pt Catalyst for the Oxygen Reduction Reaction. *ACS Nano* **2015***, 9,* 11014–11022.

7. Dash, P.; Dehm, N. A.; Scott, R. W. J. Bimetallic PdAu Nanoparticles as Hydrogenation Catalysts in Imidazolium Ionic Liquids. *J. Mol. Catal. A: Chem.* **2008***, 286,* 114–119.

8. Luo, W.; Sankar, M.; Beale, A. M.; He, Q.; Kiely, C. J.; Bruijnincx, P. C. A.; Weckhuysen, B. M. High Performing and Stable Supported Nano-Alloys for the Catalytic Hydrogenation of Levulinic Acid to γ-valerolactone. *Nat. Commun.* **2015**, doi: 10. 1038/ncomms7540.

9. Choudhary, T. V.; Sivadinarayana, C.; Datye, A. K.; Kumar, D.; Goodman, D. W. Acetylene Hydrogenation on Au-Based Catalysts. *Catal. Lett.* **2003***, 86,* 1–3.

10. Ham, H. C.; Stephens, J. A.; Hwang, G. S.; Lim, T. H. Pd Ensemble Effects on Oxygen Hydrogenation in AuPd Alloys: A Combined Density Functional Theory and Monte Carlo Study. *Catal. Today.* **2011***, 165,* 138–144.

11. Shevchenko, E. V.; Bodnarchuk, M. I.; Kovalenko, M. V.; Talapin, D. V.; Smith, R. K.; Aloni, S.; Heiss, W.; Alivisatos, A. P. Gold/Iron Oxide Core/Hollow-Shell Nanoparticles. *Adv. Mater.* **2008***, 20,* 4323–4329.

12. Chen, D.; Li, C.; Liu, H. Ye, F.; Yang, J. Core-Shell Au@Pd Nanoparticles with Enhanced Catalytic Activity for Oxygen Reduction Reaction *via* Core-Shell Au@Ag/Pd Constructions. *Sci. Rep.* **2015**, *5*, 11949.

13. Mazumder, V.; Sun, S. Oleylamine-Mediated Synthesis of Pd Nanoparticles for Catalytic

Formic Acid Oxidation. *J. Am. Chem. Soc.* **2009***, 131,* 4588–4589.

14. Mazumder, V.; Chi, M.; More, K. L.; Sun, S. Synthesis and Characterization of Multimetallic Pd/Au and Pd/Au/FePt Core/Shell Nanoparticles. *Angew. Chem. Int. Ed.* **2010***, 49,* 9368–9372.

15. Cheng, K.; Peng, S.; Xu, C.; Sun, S. Porous Hollow Fe_3O_4 Nanoparticles for Targeted Delivery and Controlled Release of Cisplatin. *J. Am. Chem. Soc*. **2009**, *131*, 10637–10644.